

**3D seismic constraints on the strato-structural evolution of the deep-water Orange Basin, South
Africa**

By

Nombuso Gladys Maduna

A thesis submitted in fulfilment of the requirements for the degree of

Doctor of Philosophy

In the

Faculty of Science

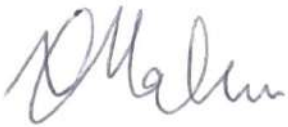
University of the Witwatersrand, Johannesburg



November 2023

Declaration

I declare that this thesis is my own, unaided work. It is being submitted for the Degree of Doctor of Philosophy at the University of the Witwatersrand, Johannesburg. It has not been submitted before for any degree or examination at any other University.



Nombuso Gladys Maduna

Student Number: 863395

Signed on the

30th day of November 2023 at the University of the Witwatersrand, Johannesburg

Abstract

This research utilizes seismic attributes and advanced machine learning methodologies to analyse high-resolution 3D reflection seismic data from the deep-water Orange Basin, located offshore western South Africa. The primary goal is to gain valuable insights into the basin's tectonic setting, depositional environment, and hydrocarbon potential. Significant features are delineated within the basin including (1) a gravitational collapse system in the Mesozoic Late Cretaceous, (2) mass flow features in the Cenozoic, (3) natural gas and fluid escape structures, (4) a large slope-perpendicular submarine canyon cutting Oligocene strata, and (5) multiple slope-parallel, sinusoidal channel features in the Miocene. The Late Cretaceous succession exhibits a gravitational collapse system with a translational and compressional domain detaching on seaward-dipping Turonian shales. Gravitational collapse during margin uplift formed fold-and-thrust belts along the slope characterizing the compressional domain. As they are commonly linked to hydrocarbons, the compressional domain of these systems has been extensively studied, while the translational domain has been poorly constrained due to its structural complexity. In this research, the translational domain is shown to contain a mixture of extensional tectonics (normal faults) up-dip and compressional tectonics (thrusts) down-dip, with extensive oblique-slip faults cutting thrusts perpendicularly during the translation of sediment. Variance and chaos, conventional seismic attributes, were used to manually pick and interpret the >500 regional-scale faults arising from the gravitational collapse system. Fault-net, a convolutional neural network (CNN), was compared with these edge-enhancing seismic attributes for extracting faults from the seismic volume. The CNN offers several notable advantages over conventional seismic attributes, such as automation, accelerated analysis, and improved time-efficiency on large datasets. Analysing the distribution, type, and geometry of faults within the basin gave valuable insights into the potential hydrocarbon system at work. Numerous natural gas and fluid escape features are identified in the seismic volume including an elongated mud volcano, pockmarked surfaces, and polygonal faults. The stability of the evolving margin is influenced by the underlying structure of a Late Cretaceous gravitational collapse system, also referred to as a deep-water fold-and-thrust belt (DWFTB) system. The fault framework within provides primary migration pathways for hydrocarbons. Major seafloor slumping occurs directly above a syncline of the Late Cretaceous DWFTB system. This slumping surrounds a structurally controlled, 4.2 km long elongated mud volcano situated between the translational and compressional domains of the underlying DWFTB system. The late Campanian has the largest accumulation of hydrocarbons evidenced by (1) an anticline with a positive high amplitude anomaly situated at the intersection of the two domains, and (2) >950 pockmarks preserved on the palaeo-surface compared to the 85 pockmarks observed on the seafloor. In addition to tectonics, the onset of stratified oceanographic circulation patterns and climate played a large role in changing depositional trends since the mid-Cenozoic. The Oligocene is characterized by a ~2.3 km wide, >13 km long, slope-perpendicular canyon formed at ~30 Ma during a major sea-level fall by a turbidity current. The Miocene is characterized by a ~14 km wide zone of slope-parallel, sinusoidal channels between water depths of 1 200–1 500 m. The formation and preservation of these features during the Miocene are attributed to the erosive interaction between two distinct water currents: (1) the Antarctic Intermediate Water flowing northwards, and (2) the deep North Atlantic Deep Water bottom currents flowing southwards; and the effects of the Benguela Upwelling System and a dry climate prevailing in southwest Africa all intensifying around 11 Ma. While pre-Miocene hydrocarbons originate from Turonian and Aptian source rocks, the origin of hydrocarbons on the seafloor is likely biogenic, arising from organic-rich sediment in the Miocene.

Dedication

“Yours, O LORD, is the greatness and the power and the glory and the splendour and the majesty, for everything in heaven and on earth belongs to You. Yours, O LORD, is the kingdom, and You are exalted as head over all.”

1 Chronicles 29:11

Acknowledgements

This dissertation would certainly not have been possible without the help of various people and organizations from a financial, academic, mental, spiritual, and emotional perspective. My sincere gratitude is expressed to all these parties involved in the completion of this herculean journey— becoming a Doctor of Philosophy in the field of Geosciences!

First and foremost, I express my gratitude to the South African National Research Foundation (grant UID: 130186) for funding my doctoral (PhD) studies and to the Council for Geoscience for funding my masters (MSc) studies before transitioning to a PhD. My thanks are further extended to the following organizations: (1) Shell South Africa and (2) the Petroleum Agency of South Africa for supplying the 3D reflection seismic dataset used in my research, along with (3) Schlumberger for providing the Petrel seismic interpretation software license, and for their valuable technical support.

I am grateful to have been given the opportunity to study at the prestigious institution of the University of the Witwatersrand, Johannesburg. I was extremely privileged to work with two highly esteemed researchers in my field of Geosciences; my supervisors Prof. Musa Manzi and Dr Zubair Jinnah. I would like to sincerely thank them for their invaluable advice, continuous support, and much-needed patience in supervising my research with knowledge and wisdom. I am furthermore grateful to Julie Bourdeau and others for their insightful comments and suggestions to the research when collaborating on manuscripts.

I would like to thank my colleagues and friends from the School of Geosciences whose diverse perspectives and expertise have broadened my understanding of the field of geosciences. I give special thanks to those of the Wits Seismic Research Centre for the times spent together on various field work and in the seismic lab. The knowledge shared from stimulating scientific discussions, brainstorming sessions, and sleepless nights of problem-solving has been one of the greatest highlights of my academic career. I am also grateful for the contributions made by numerous researchers, scholars, and authors cited in this research who have given a solid foundation for my own research.

I sincerely thank my church family for their prayers and counsel, continually encouraging me to do everything as “unto the Lord” in my daily life which extends to my academic studies. Finally, I would like to express my deepest gratitude to my friends and family who have supported me emotionally. I am extremely grateful to my parents, Makenete and Mamello Maduna, who have made me into what I am today, going above and beyond to provide me with the resources and opportunities necessary for my education. Further thanks are extended to my cousin and deputy parent, Ausi Mary, together with her family for always being there for me. Overall, without the tremendous understanding and encouragement of my family, it would not have been impossible for me to reach this stage in my studies. I am extremely grateful for my best friend and loving husband, Wayne Ngcobo, for his endless patience, his care, and motivating me to push through the most challenging of times.

No matter how big or small the contribution, I am truly grateful for the guidance, encouragement, and support of all individuals and groups involved on this PhD journey including those I have not mentioned. It has been an incredible journey culminating in a successfully completed doctorate.

Table of Contents

Declaration.....	ii
Abstract	iii
Dedication.....	iv
Acknowledgements	v
List of papers	ix
List of figures.....	x
List of tables	xiii
List of abbreviations.....	xiv
1 Introduction.....	1
1.1 Background.....	1
1.2 Location.....	3
1.3 Aims and objective	3
1.4 Thesis structure	4
2 Regional setting.....	7
2.1 Structural framework offshore southwestern Africa.....	7
2.2 Offshore stratigraphy.....	8
2.2.1 Pre-rift	8
2.2.2 Syn-rift.....	9
2.2.3 Post-rift.....	10
2.3 The interplay of tectonic, climatic, and oceanographic processes	11
2.3.1 The role of tectonics on Late Cretaceous sedimentation.....	12
2.3.2 The interplay of tectonics, climate, and oceanic circulation on early Cenozoic sedimentation.....	12
2.3.3 The interplay of tectonics, climate, and oceanic circulation on mid-Cenozoic sedimentation	13
2.4 DWFTB systems	14
2.4.1 Overview of DWFTB systems	14
2.4.2 DWFTB systems of the Orange Basin.....	15
2.5 Hydrocarbon systems of the Orange Basin	17
3 Review of the seismic method and seismic stratigraphy.....	19
3.1 The seismic reflection method	19
3.1.1 Seismic acquisition.....	19
3.1.2 Seismic processing	20
3.1.3 Seismic interpretation	23
3.2 Seismic Stratigraphy.....	25
3.2.1 Background.....	25
3.2.2 Sequence stratigraphic framework	25
3.3 Seismic interpretation using seismic attributes.....	30
3.3.1 Overview of seismic attributes	30
3.3.2 Volumetric attributes.....	32
3.3.3 Surface attributes.....	33

4 Methodology	35
4.1 Seismic acquisition and processing	35
4.2 Seismic interpretation and strategy	37
4.2.1 Seismic interpretation strategy	38
4.2.2 Seismic resolution limit	39
4.3 Data preparation	40
4.3.1 Data loading	40
4.3.2 Realizing and cropping	40
4.4 Volumetric attributes	40
4.4.1 Relative acoustic impedance	40
4.4.2 Structural smoothing	42
4.4.3 Variance and chaos	43
4.4.4 Direct hydrocarbon indicators	43
4.5 Horizon mapping	45
4.5.1 Picking horizons	45
4.5.2 Confidence classification mapping	45
4.5.3 Surface creation	46
4.6 Surface attributes	47
4.6.1 Surface smoothing	48
4.6.2 Anomaly identifier and influential data	48
4.6.3 Edge detection	49
4.7 Fault mapping	50
4.7.1 Fault interpretations	50
4.7.2 Fault interpretations to fault framework modelling	51
4.8 Domain conversion	52
4.8.1 Velocity modelling	52
4.8.2 Orange Basin velocity modelling to depth conversion	53
4.9 Structural modelling	54
4.9.1 Fault framework modelling	55
4.9.2 Boundary definition	56
4.9.3 Horizon modelling and depospace calculation	57
4.9.4 Structural gridding	60
5 Summary of manuscripts	61
5.1 Strato-structural evolution of the deep-water Orange Basin: constraints from 3D reflection seismic data	61
5.2 3D reflection seismic imaging of natural gas/fluid escape features in the deep-water Orange Basin of South Africa.....	62
5.3 A novel approach to fault interpretation using convolutional neural network: a case study of the deep-water Orange Basin, South Africa.....	63
6 Strato-structural evolution of the deep-water Orange Basin: constraints from 3D reflection seismic data	65
7 3D reflection seismic imaging of natural gas/fluid escape features in the deep-water Orange Basin of South Africa.....	91

8 A novel approach to fault interpretation using convolutional neural network: a case study of the deep-water Orange Basin, South Africa	119
9 Discussion.....	151
9.1 The deep-water Orange Basin’s hydrocarbon system.....	151
9.1.1 Elements of a prolific hydrocarbon system.....	151
9.1.2 Natural gas and fluid escape features of the Orange Basin	152
9.2 Seismic attributes and convolutional neural networks	155
9.2.1 Seismic attributes	155
9.2.2 The comparison of edge-enhancement attributes with a fault-net CNN	156
9.3 Evolution of the deep-water Orange Basin	158
9.3.1 Late Cretaceous evolution.....	158
9.3.2 Cenozoic evolution.....	160
9.4 Future considerations and recommendations	161
10 Concluding remarks.....	162
11 References.....	163
Appendices	169

List of papers

This thesis is based on the following manuscripts forming Chapters 6, 7 and 8:

- A. Maduna, NG, Manzi, MS, Jinnah, Z and Bourdeau, JE (2022) Strato-structural evolution of the deep-water Orange Basin: constraints from 3D reflection seismic data. *Solid Earth* 13:1755-1780. <https://doi.org/10.5194/se-13-1755-2022>.
- B. Maduna, NG, Manzi, MSD, Bourdeau, JE and Jinnah, Z (2023) 3D reflection seismic imaging of natural gas/fluid escape features in the deep-water Orange Basin of South Africa. *Marine Geophysical Research* 44, 17:1-28. <https://doi.org/10.1007/s11001-023-09523-2>.
- C. Maduna, NG, Manzi, MSD, Nwaila, G, Zhang, SE, Bourdeau, JE and Jinnah, Z (2023) A novel approach to fault interpretation using a convolutional neural network: a case study of the deep-water Orange Basin, South Africa. Manuscript submitted for publication.

List of figures

Figure 1.1 Location of the Orange Basin study area showing wells and hydrocarbon systems in play, 3D deep-water seismic surveys and gravitational collapse structures.....	2
Figure 2.1 Rifting of Gondwana during the Late Jurassic (Light et al., 1993).	7
Figure 2.2 Tectonic structural framework of south-western Africa (modified after Baby et al., 2018).	8
Figure 2.3 Regional NE-SW seismic line showing the tectonostratigraphy of the Orange Basin (de Vera et al., 2010).	9
Figure 2.4 Orange Basin tectonostratigraphic chart illustrating the principal depositional sequences, their corresponding bounding surfaces, and the margin's evolutionary history, influenced by sea-level variations (Hartwig et al., 2012).	10
Figure 2.5 Integrated chronostratigraphy of the southwest African passive margin from various studies (modified after Baby et al., 2018).	11
Figure 2.6 Oceanic circulation offshore southwest Africa from the Cenozoic till present (modified after Weigelt and Uenzelmann-Neben, 2004). Abbreviations: NADW= North Atlantic Deep Water, BOC= Benguela Oceanic Current, BCC= Benguela Coastal Current, AGC= Agulhas Current, AABW= Antarctic Bottom Water, AAIW= Antarctic Intermediate Water	14
Figure 2.7 Model illustrating gravitational collapse to form Orange Basin DWFTB systems (modified after Dalton et al., 2017a). a) Margin uplift, (b) Downslope sliding of sediment upon a shale detachment surface beginning with gravitational collapse centrally (transitional domain) (c) new thrusts and folds form down-dip following normal faulting up-dip in the extensional domain; (d) Gravitational sliding upon upper system becomes increasingly difficult forcing faults to propagate onto a lower slip surface to redistribute strain; (e) Sediment above the lower slip surface becomes compacted then a second compressional domain develops.	17
Figure 3.1 Illustration of the seismic reflection method as used in marine settings showing the ray path along the surface of layer 3 (modified after Song et al., 2012).	20
Figure 3.2 Schematic illustration of the Fresnel Zone (Fourie and Botha, 2001).	21
Figure 3.3 Illustration of the common midpoint method (modified after Ruddick et al., 2009). (a) A set of source to receiver pathways showing multiple sampling of the same feature to produce a common midpoint gather. (b) Plotted traces from the common midpoint gather in (a) showing the delay to return time (TWT) on the vertical axis with the increase in displacement (x- axis) laterally. (c) common midpoint gathers after the application of a normal moveout correction. (d) The normal moveout-corrected traces are averaged out to create a “stack”.	22
Figure 3.4 Illustration of Kirchhoff pre-stack time migration (a) multiple reflection points on the diffraction curve and (b) summed amplitudes along the diffraction curve (modified after Onajite, 2013).	23
Figure 3.5 Reflection seismic data of the deep-water Orange Basin showing (a) a 3D window displaying the inline, crossline (or xline) and time slice sections, and (b) a 2D interpretation window of the crossline viewed in (a). Common features including the different axes, compass, 3D grid, horizontal scale and seismic colour bar have been annotated. VE= 5.....	24
Figure 3.6 Upper and lower sequence boundary stratal termination patterns (Mitchum et al., 1977).	26
Figure 3.7 Sequence stratigraphic framework regional architecture illustrating the various depositional systems, systems tracts, and stratigraphic surfaces formed during different phases of the relative sea-level cycle (Catuneanu, 2006). SL= sea-level.	27

Figure 3.8 The various internal reflection geometries observed in seismic facies units (Mitchum et al. 1977). .28	28
Figure 3.9 Uninterpreted and interpreted 2D seismic lines of a deep-water gravity flow deposit (Catuneanu et al., 2009). Seismic facies include A- mudflow deposits; B- turbidity flow frontal splay; C- leveed channel and overbank facies; and D- mudflow deposits. Sequence stratigraphic surfaces include: 1- correlative conformity; 2- correlative conformity; 3- maximum regressive surface; and 4- maximum flooding surface.29	29
Figure 3.10 Categorisation of seismic attributes using geological, geophysical, and mathematical properties (Barnes, 2016). Boxes indicate those used in the research.....30	30
Figure 4.1 Map showing seismic survey OB123D-01 and the location of this study’s seismic data within it (refer to Fig. 1.1 for the regional setting).36	36
Figure 4.2 Survey orientation and bin grid schematic used for 3D processing (Kramer and Heck, 2014).....36	36
Figure 4.3 Petrel seismic interpretation workflow.....39	39
Figure 4.4 3D windows showing the application of volumetric attributes comparing (a) the normal seismic volume, (b) the relative acoustic impedance volume, and (c) the structurally smoothed volume. VE= 5.....41	41
Figure 4.5 3D windows comparing the chaos (a) and variance (b) input volumes used for ant tracking. (c) is the passive ant tracked volume produced using chaos as input. (d) is the passive ant tracked volume produced using variance as input. (e) is the aggressive ant tracked volume produced from (c). (f) is the aggressive ant tracked volume produced from (d). VE= 5.42	42
Figure 4.6 Volumetric attributes used as direct hydrocarbon indicators. An inline section of a) sweetness, b) envelope, c) iterative root mean square amplitude, and d) generalised spectral decomposition indicating the presence of hydrocarbons as bright positive high amplitude anomalies (PHAAs) (Maduna et al., 2023a). VE= 5.44	44
Figure 4.7 Picking horizons in reflection seismic data. A crossline section showing (a) the uninterpreted seismic data in TWT, (b) high amplitude reflectors picked as horizons for creating geological surfaces in the stratigraphy, and (c) the stratigraphic units interpreted between each geological surface. Abbreviations: sf= seafloor, Mio= Miocene, Oli= Oligocene, Ma= Maastrichtian, Sa= Santonian, Tu= Turonian, Al= Albian. VE= 5.46	46
Figure 4.8 Horizon mapping workflow shown on the Santonian horizon. (a) 3D auto-tracking, and 2D manual interpretation using a crosshatch technique in areas with low signal-to-noise ratios; (b) validation of horizon interpretation using the confidence classification map with red, green, and blue showing high, intermediate, and low levels of confidence, respectively; and c) the resultant surface created from the horizon interpretation.....47	47
Figure 4.9 Surface creation using the convergent interpolation algorithm illustrated in (a) showing four iterations which increase in resolution, and (b) showing the Santonian horizon created through convergent interpolation after specifying the geometry.....49	49
Figure 4.10 Comparison of the (a) anomaly identifier attribute highlighting all local variations, and the (b) influential data attribute highlighting larger, geometric variations in geometry on the Santonian surface.49	49
Figure 4.11 The dip angle (a) and dip azimuth (b) computed on the Santonian surface. High dip angles (a) are faulted areas on the surface. Dip directions (b) are variable across the surface, however, the primary directions are NE and SW.50	50
Figure 4.12 Edge detection attribute applied on the Santonian surface. Areas where the surface is faulted appear as red and orange, between 0–10 %.....51	51

Figure 4.13 Interpreting faults in reflection seismic data with (a) displaying fault segments picked on a 2D interpretation window, (b) showing the variance time slice used to guide interpretation, and (c) displaying fault interpretations fitting lineaments on the variance time slice. VE= 5.53

Figure 4.14 Illustration of the three main velocity models applied in seismic data showing the interval velocity, linear velocity, and advanced velocity models (modified after Babasafari, 2019).54

Figure 4.15 Chart showing the average interval velocities of Late Cretaceous stratigraphic surfaces from wells in the shallow Orange Basin (modified after Kuhlmann et al., 2010). The surfaces named in bold italics are those identified in the study area.55

Figure 4.16 2D interpretation windows viewing a crossline in (a) the time domain, and (b) depth domain following depth conversion using the interval velocity model. Note how the crossline appears laterally squashed in the depth domain (b) compared to time (a). VE= 5.57

Figure 4.17 Fault modelling process showing (a) original fault interpretations used as input to create (b) a fault framework model with fault relationships defined. Following fault framework modelling, (c) dip and (d) dip azimuth was applied.58

Figure 4.18 All surfaces used in horizon modelling following the creation of a fault framework.59

Figure 4.19 Structural model created using volume-based modelling showing zones at key intervals; (a) the thrust Santonian surface with the fault framework, (b) the Oligocene with canyoning, (c) the Miocene with sinusoidal channels, (d) the seafloor with slumping. VE= 7.5.60

Figure 4.20 3D structural gridded model showing zone layering in the southern section of the study area. VE= 5.61

Figure 9.1 Schematic diagram of the deep-water Orange Basin illustrating the distribution and relationship of natural gas and fluid escape features observed in the study area. The Turonian shales are a thermogenic source rock interval. An explosive hydrocarbon expulsion event in the late Campanian created numerous pockmarks. The Miocene is a biogenic source rock interval and is marked by slope-parallel, sinusoidal channels. An episodic release of hydrocarbons from the Miocene surface created pockmarks on the seafloor. 153

List of tables

Table 2.1 Characteristics of DWFTB systems according to Morley et al. (2011). Fold and thrust style abbreviations: PU=pop-up, BT=break thrusts (associated with folding), I=imbricate thrusts, FBF=fault bend fold, FPF=fault propagation fold, DF (TF)=detachment fold (in thrust faulting), CF=crestral normal faults. Overpressure abbreviations: S=slab-derived fluids, BDC=burial disequilibrium compaction, I=inflationary, C=chemical15	
Table 3.1 The main sequence stratigraphic surfaces found in deep-water marine settings (modified after Catuneanu, 2006).29	
Table 3.2 Methods used in the application of seismic attributes (Barnes, 2016).31	
Table 4.1 Acquisition parameters of the Orange Basin’s seismic survey (Kramer and Heck, 2014).35	
Table 4.2 Dolphin Geophysical pre-processing sequence (Kramer and Heck, 2014).37	
Table 4.3 Seismic processing workflow applied to the deep-water survey (Kramer and Heck, 2014).38	
Table 4.4 Bin grid definitions.....38	
Table 4.5 Parameters used for variance in the study area.....43	
Table 4.6 Passive and aggressive ant tracking parameters.43	
Table 4.7 Parameters used in generalised spectral decomposition45	
Table 4.8 The parameters used in creating a confidence classification map and the description of each.....46	
Table 4.9 Surface smoothing parameters.48	
Table 4.10 Anomaly identifier and influential data parameters.48	
Table 4.11 The parameters defined in creating a fault framework from fault interpretations.56	
Table 4.12 The parameters used in computing horizons using volume-based modeling.....58	
Table 9.1 The advantages and disadvantages of conventional edge-enhancement attributes (variance and chaos) compared to the fault-net convolutional neural network.....157	

List of abbreviations

DWFTB	deep-water fold-and-thrust belt
CNN	convolutional neural network
PASA	Petroleum Agency of South Africa
km	kilometres
m	metres
mbsl	metres below sea level
TWT	two-way travel time
VE	vertical exaggeration
2D	two dimensional
3D	three dimensional
RC	reflection coefficient
ρ	density
v	velocity
f	dominant frequency

1 Introduction

1.1 Background

Studies on the evolution of the southwest African passive margin, driven mainly by the petroleum industry's ever-widening search for hydrocarbons, have increased greatly since the 1960s and 1970s with the advancement of deep-sea technologies. Structural and stratigraphic features in the subsurface are detected through the reflection seismic method which is an integral part of basin analysis in reservoir studies, optimizing the drilling location and production of hydrocarbons. From proximal shelf to distal slope environments the southwest African margin contains features such as submarine channel-canyon systems, deltas, and mass flow deposits driven by gravitational instability (Rogers and Rau, 2006; Bluck et al., 2007; de Vera et al., 2010; Scarselli et al., 2016; Baby et al., 2018). These common depositional and erosional features are identifiable in reflection seismic data. They are often associated with natural gas and fluids with hydrocarbons either being sourced from, matured within, migrated along, or trapped within the structures formed. Since there is an increasing shortage of fossil fuels onshore and in the shallower shelf environments of South Africa (Pretorius et al., 2015), features known to be associated with hydrocarbon in the deep-water marine environments need investigation.

Apart from the considerable presence of diamonds scattered along the southwest African coastline (Corbett and Burrell, 2001; Bluck et al., 2007), the margin (western Namibia and South Africa) has been extensively investigated concerning both established and speculative hydrocarbon systems found in the offshore basins (van der Spuy and Sayidini, 2022). A basin's underlying petroleum system is often indicated by natural gas and fluid escape features appearing on the seafloor as the surface expression of hydrocarbons migrating through the sedimentary column. In seismic data, direct hydrocarbon indicators are shown by bottom simulating reflectors and positive high amplitude anomalies (Løseth et al., 2001; Gay et al., 2003; Hustoft et al., 2010; Ho et al., 2012). Seafloor and buried pockmarks, mud diapirs, mud volcanoes, together with the pipes and chimneys which feed them, are some natural gas and fluid escape features identified in the shallow Orange Basin offshore southwestern Africa (Ben-Avraham et al., 2002; Viola, et al., 2005; Boyd et al., 2011; Hartwig et al., 2012).

The southwest African margin provides a classic example of processes that occur in passive margin settings recording both the pre- and post-rift evolution of the continental margin (Séranne and Anka, 2005). Studying the post-rift evolution of the margin is highly important to the petroleum industry as ~ 35% of all giant hydrocarbon field discoveries are from the post-rift sequences of passive margins, which represents 67% of conventional hydrocarbon discoveries (Levell et al., 2010). Economical hydrocarbon plays have been identified in post-rift sequences along the shallow shelf and deep-water slope environments of the Orange Basin (van der Spuy and Sayidini, 2022). In production along the proximal shelf are the South African Ibubhesi and Namibian Kudu gas fields (Fig. 1.1).

In passive margin settings the downslope contraction and gravitational collapse of sedimentary sequences form shale- or salt-detached gravitational collapse structures in the deep sea (Rowan et al., 2004; Nemcok et al., 2005). A full gravitational collapse system, also referred to as a deep-water fold-and-thrust belt (DWFTB) system (Maduna et al., 2022, 2023), comprises a (1) linked up-dip extensional domain with basinward-dipping listric growth faults, (2) central transitional (or translational) domain with a complex structural framework, and (3)

down-dip compressional domain with folded sedimentary wedges separated by thrust faults (Morley et al., 2011). Distal folds of the compressional domain are known to host hydrocarbons and are therefore significant to the petroleum industry (Krueger and Gilbert, 2009; Morley et al., 2011). The Orange Basin, situated offshore the western South African and Namibian coastlines, contains some of the most excellently preserved DWFTB systems within Late Cretaceous post-rift sequences (Fig. 1.1; de Vera et al., 2010; Mahlalela et al., 2021). Extensive research has been done on the extensional domain and compressional domain of DWFTB systems, due to the straightforward nature of the former and the recognized hydrocarbon potential of the latter. There is however a lack of sufficient data available for the structurally complex transitional/translational domain (Dalton et al., 2017a) and this work aims, in part, to address this.

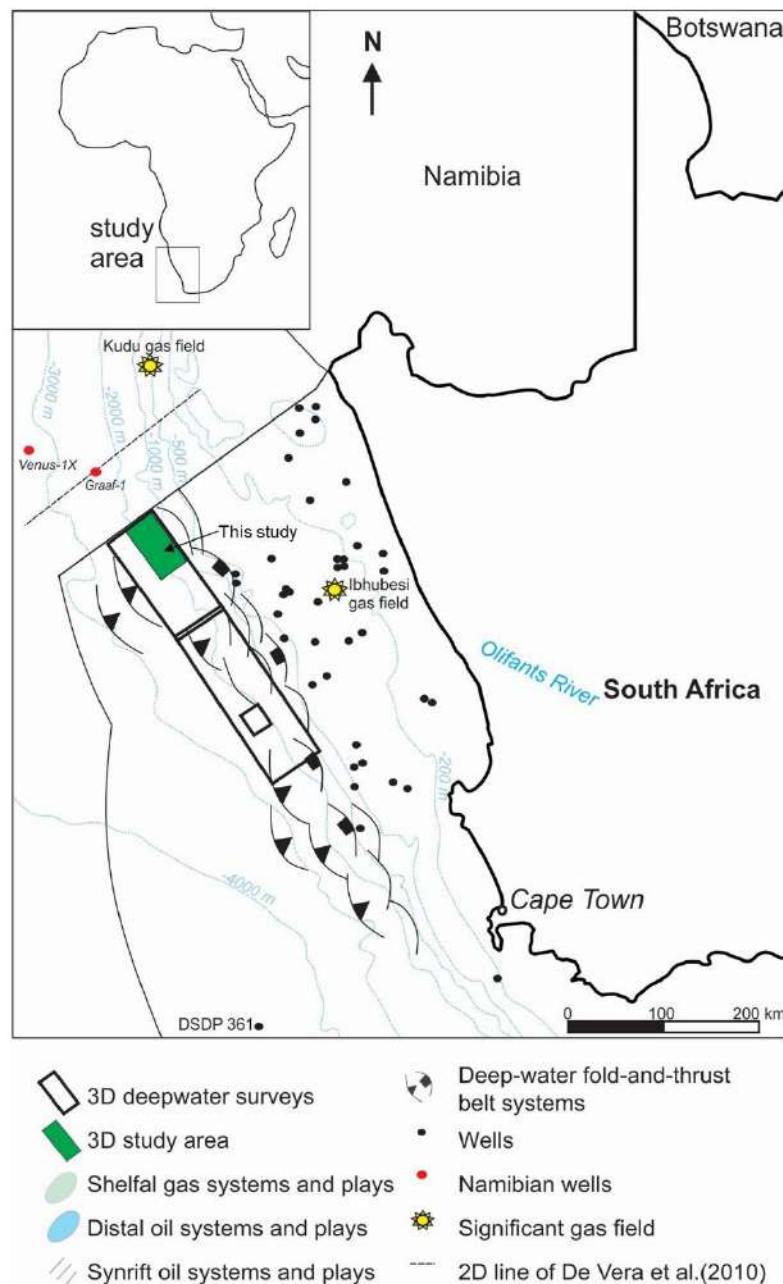


Figure 1.1 Location of the Orange Basin study area showing wells and hydrocarbon systems in play, 3D deep-water seismic surveys and gravitational collapse structures.

The Petroleum Agency of South Africa (PASA) confirms that the Orange Basin remains relatively underexplored due to sparse 3D reflection seismic survey coverage, and despite dense 2D seismic data, only one well has been drilled per 4000 km² in South African waters (PASA, 2017). Notably, in the deep-water environment of Namibia, significant hydrocarbon discoveries were made between 2021 and 2022 from the Venus-1X wildcat and Graaf-1 appraisal wells, situated at depths between 2000–3000 metres below sea level (mbsl) (Fig. 1.1; van der Spuy and Sayidini, 2022). Since the two regions likely share the same underlying geology and petroleum system, the potential for a substantial hydrocarbon find in the South African deep-water area adjacent to these Namibian deep-water discoveries is very high. This research therefore concentrates on the South African deep-water Orange Basin, which borders the Namibian maritime licensing region.

1.2 Location

The study area lies offshore southwestern Africa in the deep-water regions of the Orange Basin (Fig. 1.1). Sediments were deposited into the basin since the Early Cretaceous from the Orange and Olifants rivers (Maslanyj et al., 1992; de Vera et al., 2010). The Orange Basin covers a large ~160 000 km² area in Namibia and South Africa combined and is South Africa's largest basin offshore (Kuhlmann et al., 2010; PASA, 2017). Three 3D seismic surveys were conducted in the South African deep-water extension of the basin; the most recent two surveys were acquired between 2012 and 2014, and the oldest in 2002 (van der Spuy and Sayidini, 2022). A ~1800 km² portion of the northern-most seismic survey (OB123D-01) is used in this research, located adjacent to the Namibian waters (Fig. 1.1). The deep-water study area stretches between water depths of approximately 1000 and 2000 meters along the continental slope.

1.3 Aims and objective

Prior investigations of the Orange Basin primarily concentrated on the 2D seismic interpretation of DWFTB systems, which inherently presents limitations and inadequacies in describing their complete evolution. This research, however, benefits from high-resolution 3D reflection seismic data. A comprehensive understanding of the stratigraphic and structural architecture of the Orange Basin deep-water region, spanning between the Mesozoic and overlying Cenozoic successions, can therefore be established. Understanding the stratigraphic, lithological, morphological, and tectonic evolution of the basin is crucial for determining potential sites for petroleum exploration through basin modelling.

The research aims to:

- Examine the structural relationship and change between the translational and compressional domains of the gravitational collapse system.
- Analyse the depositional elements of the gravitational collapse system together with that of the younger, overlying sedimentary successions.
- Identify natural gas and fluid escape features present and investigate the processes responsible for them.
- Compare conventional methods of seismic interpretation (seismic attributes) with machine learning algorithms for detecting fracture systems in reflection seismic data.

The main goal is to develop a comprehensive model of the Orange Basin's deep-water region, encompassing the evolution of the Cretaceous gravitational collapse system in the Mesozoic to the depositional processes and systems of the Cenozoic. Through this model, the petroleum system of the deep-water Orange Basin can be better comprehended. While it's important to note that each passive margin setting is unique, the analysis of structural and depositional elements in this research may provide valuable insights and serve as an analogue for understanding the evolution of comparable passive margin settings.

1.4 Thesis structure

This thesis is divided into several chapters outlined as follows:

Chapter 1 (Introduction) provides an overview of the motivation behind the research, the location of the study area, the aims and objective, and the structure of the dissertation.

Chapter 2 (Regional setting) is a summary of the geological background and literature review of geological features related to the study area. This chapter is based on the structural framework and stratigraphy of the SW African environment looking at the tectonic, climatic, and oceanographic processes responsible for sedimentation; gravitational collapse structures (DWFTB systems); and hydrocarbon systems of the Orange Basin.

Chapter 3 (Review of the seismic reflection method and seismic stratigraphy) gives the theory of the seismic reflection method and the principles of seismic stratigraphy used in seismic interpretation. The chapter also includes the theory behind seismic attributes used to aid seismic interpretation in [Chapter 4's](#) Methodology.

Chapter 4 (Methodology) details the step-by-step interpretation of seismic data from loading the seismic data to creating a 3D structural model using Schlumberger's Petrel software package. This follows a summary of how the seismic data were acquired and processed by other companies on behalf of Shell (a global group of energy and petrochemical companies).

Chapter 5 (Summary of manuscripts) provides summaries of the three papers produced from this research.

Chapter 6 (Strato-structural evolution of the deep-water Orange Basin: constraints from 3D reflection seismic data) is the first manuscript. Part one of the main findings of the research are presented as an accepted and published paper in the Solid Earth journal. This research utilizes 3D reflection seismic data obtained from the deep-water Orange Basin in South Africa to conduct a comprehensive analysis of features present in the Mesozoic's Late Cretaceous to Cenozoic sedimentary successions. By doing so, it offers valuable insights into the structural styles observed within the Late Cretaceous gravitational collapse system, particularly in the transitional area between the translational domain and the compressional domain. Furthermore, the research sheds light on the tectonic and oceanographic processes that have contributed to mass-scale erosion in the Cenozoic's Tertiary and Quaternary periods.

As the primary author of this paper, the doctoral candidate (Nombuso G. Mauna) carried out the full seismic interpretation of the study and prepared the manuscript. Musa SD Manzi assisted in the practical use of the software and the concepts used in reflection seismic data. Zubair Jinnah assisted with the geological interpretation

of the dataset. The manuscript was reviewed and edited under the guidance of secondary authors and supervisors Musa S.D. Manzi and Zubair Jinnah, together with mentor Julie E. Bourdeau who provided additional insights into the geological interpretation.

Chapter 7 (3D reflection seismic imaging of natural gas/fluid escape features in the deep-water Orange Basin of South Africa) is the second manuscript. Part two of the main findings of the research are presented as an accepted and published paper in Marine Geophysical Research. 3D reflection seismic data from the deep-water Orange Basin, South Africa, are used to image natural gas and/or fluid escape features in the basin to assess its hydrocarbon potential. Several volumetric seismic attributes are used as direct hydrocarbon indicators to identify natural gas and/or fluid escape features associated with the Mesozoic's Late Cretaceous DWFTB system and Cenozoic sequences of the Orange Basin. These features would have otherwise been missed or not fully resolved in a regular 2D seismic survey and without the use of volumetric seismic attributes.

Author contributions are the same as in the first manuscript published in Solid Earth. As the primary author of this paper, the doctoral candidate (Nombuso G. Maduna) carried out the full seismic interpretation of the data using seismic attributes and prepared the manuscript draft. Musa SD Manzi assisted in the practical use of the software and the concepts used in reflection seismic data. Zubair Jinnah assisted with the geological interpretation of the dataset. The manuscript was reviewed and edited under the guidance of secondary authors and supervisors Musa S.D. Manzi and Zubair Jinnah, together with mentor Julie E. Bourdeau who provided additional insights into the geological interpretation.

Chapter 8 (A novel approach to fault interpretation using convolutional neural network: a case study of the deep-water Orange Basin, South Africa) is the third manuscript related to part one of the main findings of the research. The paper is currently under-review. A convolutional neural network (CNN) for segmenting faults is compared against conventional edge-enhancement methods of fault detection using 3D reflection seismic data from the deep-water Orange Basin as a case study. The fault-net CNN used proved to be highly effective in the identification and delineation of faults from the seismic dataset over the chaos and variance seismic attributes.

The doctoral candidate (Nombuso G. Maduna) computed and applied the variance and chaos seismic attributes to the data and wrote the primary aspects related to this method. Nombuso G. Maduna was assisted by Glen Nwaila to carry out the fault-net CNN method of fault extraction on the seismic volume. Steve Zhang wrote the primary aspects related to the deep learning algorithm used. Musa SD Manzi created and facilitated the whole structure of the paper, and furthermore reviewed and edited the paper draft. Julie E. Bourdeau prepared the regional setting and Zubair Jinnah, one of the main author's supervisor, assisted with the geological interpretation of the dataset. All authors were involved in writing the discussion and editing the paper.

Chapter 9 (Discussion) discusses all the main findings of the research which is centred around the three manuscripts produced in [Chapter 6](#), [7](#) and [8](#). Discussion topics cover the evolution and hydrocarbon potential of the deep-water Orange Basin, together with the use of conventional seismic attributes and a CNN. Lastly, recommendations are given for future work in the Orange Basin's deep-water region.

Chapter 10 (Conclusion) gives the overall concluding remarks of the research.

Chapter 11 (References) lists the references used from [Chapters 1–4](#) and [9](#).

Appendix A contains copies of abstracts (peer-reviewed and non-peer-reviewed) submitted and presented at various geological and geophysical conferences covering topics within the PhD research. As primary author, the doctoral candidate (Nombuso G. Maduna) interpreted the seismic data and prepared the abstracts, and furthermore presented the work. Secondary authors Musa S.D. Manzi and Zubair Jinnah reviewed and edited the abstracts as supervisors of the doctoral candidate. The description of conference abstracts presented are listed as follows:

- *From a Cretaceous deep-water fold-and-thrust belt to Cenozoic mass transport systems of the Orange Basin.* This was presented at the 35th International Association of Sedimentology Meeting in 2021.
- *Evolution of the Orange Basin; Cretaceous Deep-water Fold-and-Thrust Belts to Cenozoic Mass Transport Systems.* This was presented both at the European Association of Geoscientists and Engineers Near Surface Geoscience Conference & Exhibition 2021, and the 82nd European Association of Geoscientists and Engineers Annual Conference & Exhibition (<https://doi.org/10.3997/2214-4609.202120156>).
- *Constraining the temporal evolution of the deep-water Orange Basin using high-resolution 3D seismic reflection data.* This was presented at the European Association of Geoscientists and Engineers Near Surface Geoscience Conference & Exhibition 2022.
- *Temporal evolution of the deep-water Orange Basin using high-resolution 3D seismic reflection data.* This was presented at the 17th South African Geophysical Association Biennial Conference & Exhibition in 2022.

Appendix B is a compilation (i–viii) of the picked horizon- to surface-based attributes applied on each stratigraphic surface used in the structural model. This includes the picked horizon in elevation time (a), confidence classification map (b), influential data (c), dip angle (d), dip azimuth (e), and edge detection (f) attributes applied to the Albian (i), early Campanian (ii), late Campanian (iv), Maastrichtian (v), Oligocene (vi), Miocene (vii), and seafloor (viii) surfaces.

2 Regional setting

2.1 Structural framework offshore southwestern Africa

The structure offshore the SW African coastline can be attributed to two significant phases of tectonism. The first phase involved Basin and Range type extension followed by rifting during Gondwana breakup in the Late Jurassic (Fig. 2.1; Maslanyj et al., 1992; Light et al., 1993; Hartwig et al., 2012). Between the Late Cretaceous and early Paleogene, the second phase occurred which is characterized by thermal subsidence and the formation of a passive margin at the onset of drift. During the first phase, the offshore region displayed a structural grain orientated north to south and fracture zones orientated east to west which facilitated the formation of three primary Early Cretaceous depocenters (Fig. 2.2; Light et al., 1993). These depocenters mark the position of the Walvis, Lüderitz, and Orange basins (from youngest to oldest) formed in zones with the greatest subsidence (Fig. 2.2). Additional depocenters accommodated the smaller Cape and Outeniqua basins located offshore southern South Africa (Fig. 2.2).



Figure 2.1 Rifting of Gondwana during the Late Jurassic (modified after Light et al., 1993).

The basins, situated between the Agulhas-Falkland Fracture Zone in the south and the Rio Grande Fracture Zone in the north, enabled dextral strike-slip motion during rifting (Figs. 2.1 and 2.2; Séranne and Anka, 2005). The second phase of drift is associated with the development of a spreading oceanic ridge (Séranne and Anka, 2005). This subdivided the margin into distinct basin, slope, and shelf environmental settings (Light et al., 1993). The continental shelf of southwest Africa comprises a mostly flat ($<1^\circ$) outer shelf region, a middle shelf, and a steep rocky inner shelf at water depths of about 200–500 m, 30–200 m, and 20 m, respectively (Rogers and Rau, 2006). The shelf break occurs at water depths between 400–500 m (Rogers and Rau, 2006; Compton and Wiltshire, 2009). Moderate seismic activity is experienced along the South African margin, with earthquakes accountable for triggering turbidites along the lower slope as observed on the eastern margin (Rogers and Rau, 2006).

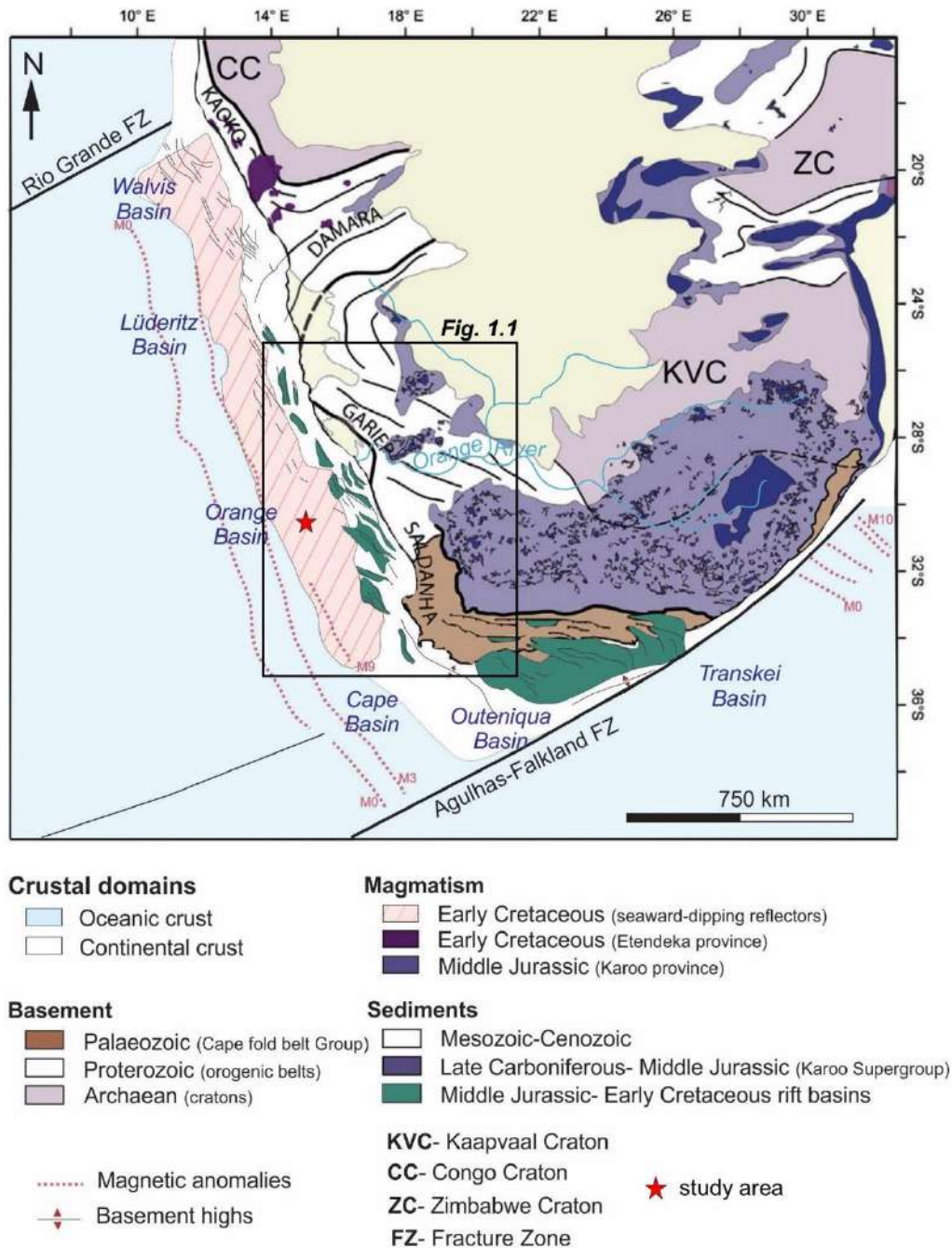


Figure 2.2 Tectonic structural framework of south-western Africa (modified after [Baby et al., 2018](#)).

2.2 Offshore stratigraphy

2.2.1 Pre-rift

As reflected on by [Mohammed et al. \(2017\)](#), very little is known of the pre-rift configuration of passive margin settings and the role it plays in basin evolution. In reflection seismic data, the offshore intra-continental basement of SW Africa is similar to the intricate onshore Pan African Gariep Belt (Proterozoic to early Palaeozoic in age) in that it is acoustically transparent, and lacks internal reflections ([Mohammed et al., 2017](#)). A 30 km wide section of the basement forms a pronounced N-S boundary zone of flexure, known as the hinge line, separating the margin

into distinct onshore and offshore morphologies (Clemson et al., 1997; Aizawa et al., 2000; Mohammed et al., 2017). The hinge line has several perpendicular segment boundaries which indicate different times of rifting during the break-up of Gondwana (Clemson et al., 1997). The thickness of the continental crust (from the Moho to the top of the basement rocks) gradually decreases from ~45 km inland to ~25 km at a location that is 100 km offshore the western coastline (Séranne and Anka, 2005).

2.2.2 Syn-rift

Gondwana break-up initially began between 170 and 150 Ma as the west (South America and Africa) separated from the east (Australia, Antarctica, India, and New Zealand) (Viola et al., 2012). This was accompanied by ~183–174 Ma doleritic and basaltic intrusions of the Karoo Large Igneous Province (Hastie et al., 2014). The separation of Africa and South America (west Gondwana) began around 144 Ma followed by ENE–WSW extension and rifting with the opening of the South Atlantic Ocean at ~134 Ma (Viola et al., 2012).

The upper portion of the basement is characterized by seaward-dipping reflectors (Fig. 2.3) that are believed to have originated from a significant subaerial, basaltic extrusive event linked to continental rifting (Menzies et al., 2002; Séranne and Anka, 2005; Granado et al., 2009). These seaward-dipping reflectors constitute a thick package, measuring over 3 km in thickness (Baby et al., 2018) and are approximately the same age as the ~135 Ma Parana-Etendeka Large Igneous Province (Koopman et al., 2016). The M3 magnetic anomaly (Fig. 2.2) is the earliest indication of mid-oceanic ridge activity and oceanic crust formation at ~127 Ma (Séranne and Anka, 2005).

The synrift sequence is predominantly characterized by isolated half grabens filled with alternating layers of clastic and volcanic deposits (Jungslager, 1999). This Late Jurassic to late Hauterivian syn-rift sequence consists of siliciclastic and volcanoclastic sediments, clearly demarcated by a regional break-up unconformity from the post-rift clastic sediments situated above (Figs. 2.3 and 2.4; Light et al., 1993; Granado et al., 2009).

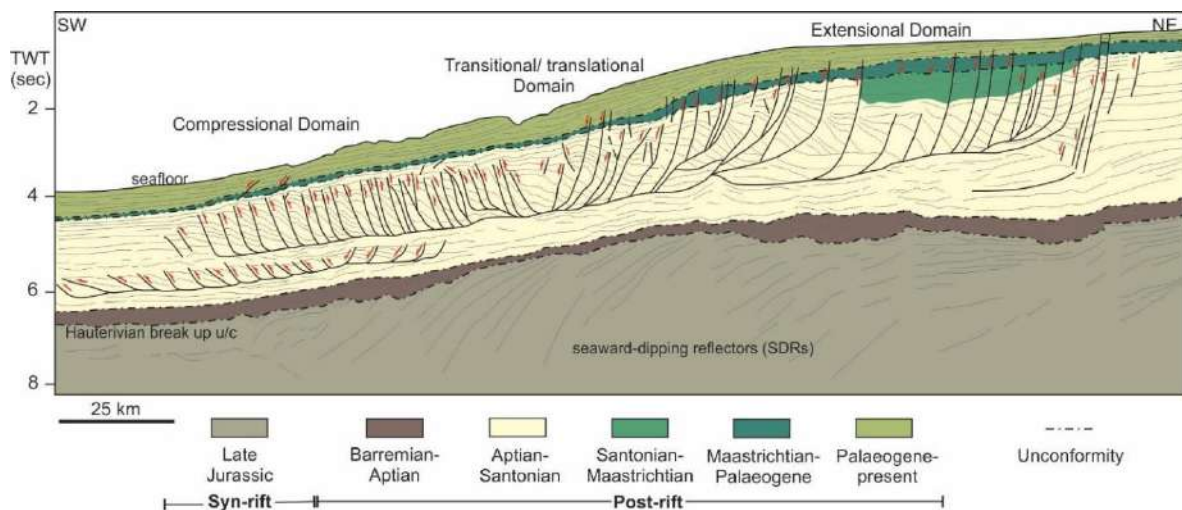


Figure 2.3 Regional NE-SW seismic line showing the tectonostratigraphy of the Orange Basin (de Vera et al., 2010).

2.2.3 Post-rift

The Olifants and Orange rivers have deposited post-rift clastic sediments into the Orange Basin ever since ~130 Ma (Figs. 2.3 and 2.4; Maslanyj et al., 1992; Granado et al., 2009; de Vera et al., 2010). These clastic sediments form the current post-rift megasequence, with a central basin thickness of 5.6 km and 3 km in the north and south, respectively (Dalton et al., 2017a). Numerous authors including Emery et al. (1975), Brown et al. (1995); Holtar and Forsberg. (2000), Paton et al. (2008), Granado et al. (2009), de Vera et al. (2010), Kuhlmann et al. (2010), Dalton et al. (2017a), and Baby et al. (2018) have described the southwest African margin's post-rift megasequence, subdividing the stratigraphy into various depositional units, each delineated by unconformities and/or maximum flooding surfaces shown in Fig. 2.5.

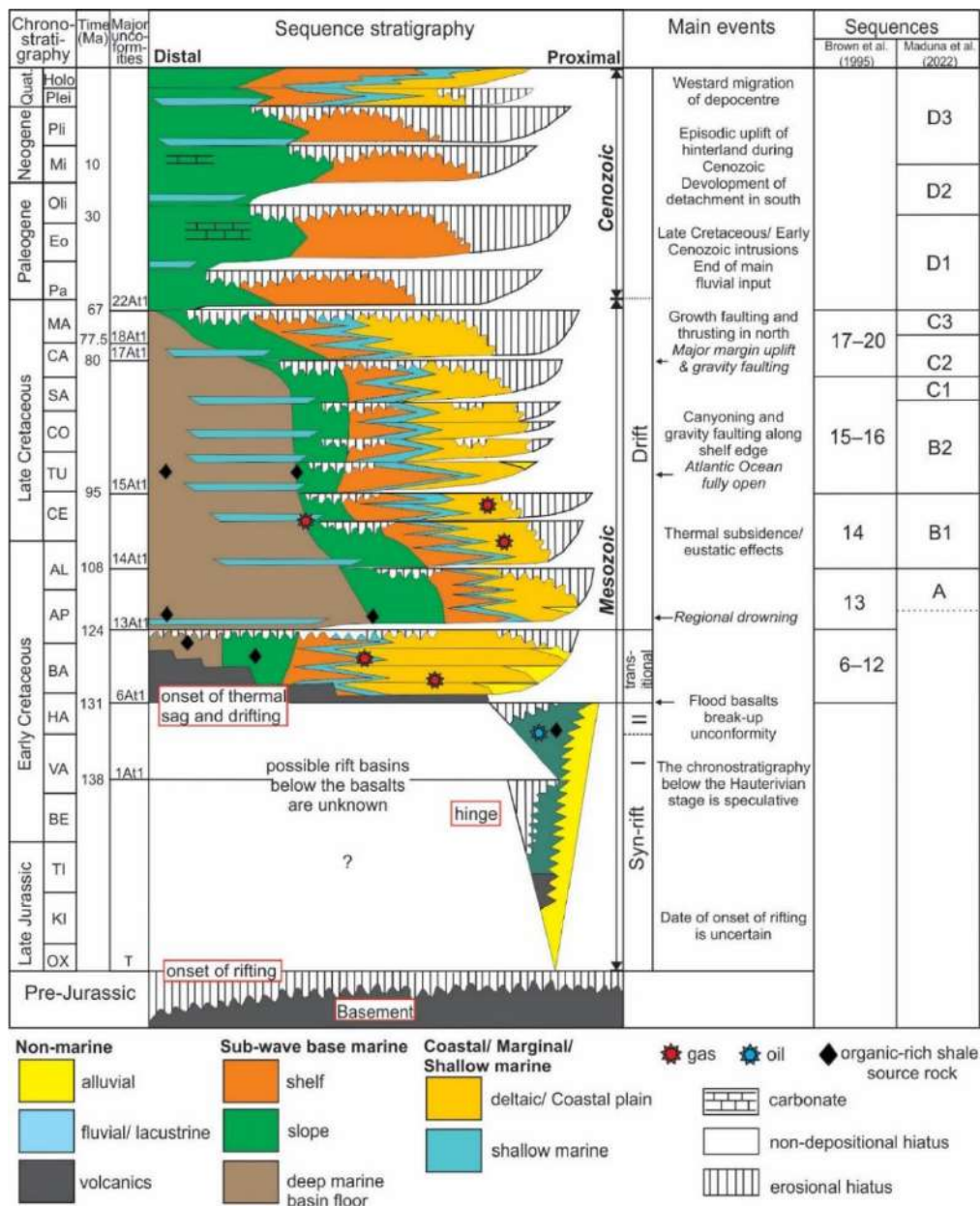


Figure 2.4 Orange Basin tectonochronostratigraphic chart illustrating the principal depositional sequences, their corresponding bounding surfaces, and the margin's evolutionary history, influenced by sea-level variations (Hartwig et al., 2012).

The number of depositional units, the age of their bounding surfaces, and nomenclature used varies between different studies as shown in Fig. 2.5. The most popularly used nomenclature for bounding surfaces in the Late Cretaceous was developed by Soeker (now called PetroSA) (Brown et al., 1995; PASA, 2017). These are the 6At1 Hauterivian, 13At1 Aptian, 14At1 Albian, 15At1 Turonian, possibly 16Dt Santonian, 17At1 early Campanian, 18At1 late Campanian, and 22At1 Maastrichtian surfaces (Fig. 2.5). Unconformity surfaces recognised in the Cenozoic sedimentary succession of the Orange Basin are in the Oligocene and Miocene (Baby et al., 2018). Dalton et al. (2017a) categorized the post-rift sedimentary succession into three distinct megasequences: (1) Early Cretaceous (early drift), (2) Late Cretaceous (late drift), and (3) the Cenozoic. Black shales and claystones dominate in the Early Cretaceous, while interbedded heterolithic claystones and shales dominate in the late drift and Cenozoic megasequences.

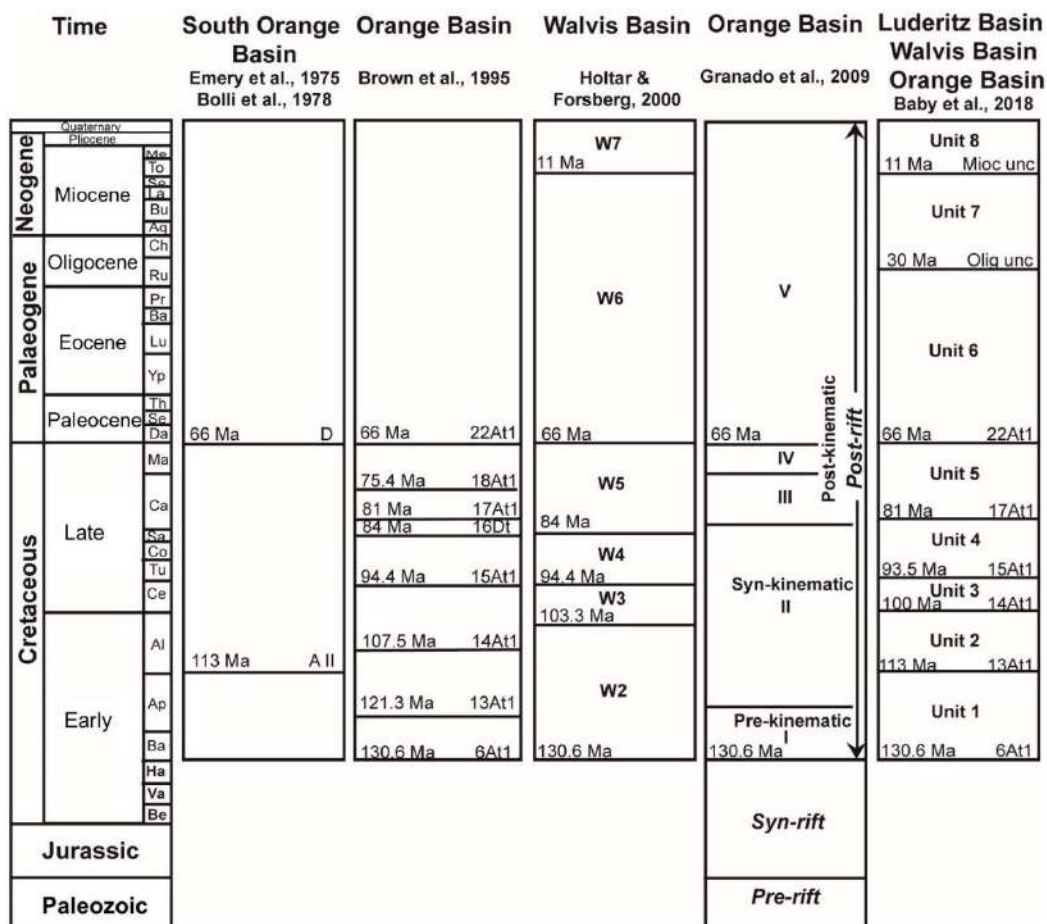


Figure 2.5 Integrated chronostratigraphy of the southwest African passive margin from various studies (modified after Baby et al., 2018).

2.3 The interplay of tectonic, climatic, and oceanographic processes

The southwest African margin's tectonic history is primarily based on shallow marine, coastal and interior land studies (Cockburn et al., 2000; Bluck et al. 2005; Bluck et al., 2007; Braun et al., 2014). The post-rift succession of the margin records multiple instances of uplift and denudation, leading to the inversion of extensional faults, crustal thinning, and intensifying gravitational processes within the Orange Basin (Fig. 2.4; Granado et al., 2009; Brown et al., 2014; Wildman et al., 2015). The interplay of oceanographic processes and climate in the Cenozoic

has strongly influenced depositional trends in the Orange Basin's post-rift succession (Fig. 2.6; Weigelt and Uenzelmann-Neben, 2004). Two major uplift events are recorded in southwest Africa's post-rift sedimentary succession; one in the Late Cretaceous leading to the spectacular formation of DWFTB systems, and another in the Oligocene accompanied and followed by significant changes in climate and oceanic circulation (Séranne and Anka, 2005; Paton et al., 2008; Wigley and Compton, 2006; Kuhlmann et al., 2010; Baby et al., 2018; Baby et al., 2020).

2.3.1 The role of tectonics on Late Cretaceous sedimentation

Compared to the arid climate and resultant low sedimentation rates ($\times 1\,000\text{ km}^3/\text{Myr}$) of the Early Cretaceous between 134–113 Ma, the Late Cretaceous had a wetter climate with increased sedimentation rates ($\times 10\,000\text{ km}^3/\text{Myr}$) recorded between ~110–80 Ma (Baby et al., 2020). The increase in Late Cretaceous sedimentation is correlated with a major erosional event of the continental margin supported by onshore thermochronological data where the rate of erosion is estimated to have increased from 0 m at the hinge line to ~1 000 m in the inner margin (Hirsch et al., 2010; Kuhlmann et al., 2010; Baby et al., 2018; Baby et al., 2020). High rates of sedimentation ($>30,000\text{ km}^3/\text{Myr}$) are observed in the Orange Basin between 93.5–81 Ma (Baby et al., 2020). A period of uplift is identified along the southwest African margin constrained between ~81 Ma (late Campanian) and 66 Ma (late Maastrichtian) marked by the extensive 22At1 erosional unconformity at its terminus (Figs. 2.4 and 2.5; Hirsch et al., 2010; Baby et al., 2018). The deposition of sediment upon an already unstable slope during this time created large-scale DWFTB systems as the southwest African margin tilted along-strike between 23° S to 35° (Fig. 2.3; Kuhlmann et al., 2010; Baby et al., 2018). The Late Cretaceous to Eocene greenhouse age had low pole to equator temperature differences and well-stratified oceans (Spicer and Corfield, 1992; Miller et al., 2005). Consequently, sedimentation was primarily influenced by tectonics, with oceanic circulation and climate having minimal to no impact (Light et al., 1993; Séranne and Anka, 2005; Uenzelmann-Neben et al., 2017).

2.3.2 The interplay of tectonics, climate, and oceanic circulation on early Cenozoic sedimentation

Low rates and volumes of sedimentation are recorded in the Palaeogene period with values below $1\,000\text{ km}^3/\text{Myr}$ (Baby et al., 2020). The southwest African margin has undergone marine transgressions and regressions of at least +170 m in the Eocene to -120 m in the late Pleistocene as observed for the Namibian coastline according to Bluck et al. (2005) and Bluck et al. (2007). The most significant of these is speculated to be the Oligocene sea-level lowstand corresponding to global sea-level fall (Dingle et al., 1983; McMillan, 2003; Wigley and Compton, 2006). The Oligocene sea-level fall is believed to have moved the southwest African shoreline 100–170 km west from its present-day location rejuvenating the Orange River and exposing shelf sediments (Miller, 2008). Controversy surrounds the true depth that sea level fell by; postulated to be 500 metres below sea level (mbsl) (Siesser and Dingle, 1981; Dingle et al., 1983). The margin, however, lacks substantial evidence to support a sea-level fall of this magnitude beyond the shelf break, i.e., no wave-cut platform, beach terrace, nor major incision into shelf sediments extending from the Orange River is evident at 500 mbsl (Miller, 2008). A large portion of younger Late Cretaceous sequences were eroded making it difficult to reconstruct a complete sea-level curve for this period (McMillan, 2003; Hirsch et al., 2010).

The significant decline in local sea levels during the Oligocene to late Miocene was attributed to an estimated 290–345 m tectonic uplift event caused by the African superswell underneath the southern African plate (Séranne and Anka, 2005; Baby et al., 2018). This is evidenced by tilted topsets in the Walvis Basin and the 350 m elevation difference of the late Eocene and Oligocene coastlines in the northern Orange Basin (Paton et al., 2008; Baby et al., 2018). The effect of uplift was further intensified by the major growth of continental ice which accumulated in Antarctica from the late Eocene at ~34 Ma then rapidly grew in the Oligocene (Lear et al., 2000). This major growth of ice coincided with a decline in atmospheric carbon dioxide levels and the opening of oceanic gateways as continents continued their migration, marking the change from greenhouse to icehouse climates (Uenzelmann-Neben et al., 2017). The formation of the Antarctic Circumpolar Current and Atlantic Meridional Overturning Circulation currents is attributed to the Drake Passage which opened in the early Oligocene (DeConto and Pollard, 2003; Uenzelmann-Neben et al., 2017).

Ever since the early Oligocene, the west African margin has experienced increased rates of continental erosion due to the tropical to humid equatorial change in climate resulting in the large Congo deep-sea fan offshore (Séranne and Anka, 2005). In contrast, the SW African margin entered a more arid climate in the Palaeogene with very low denudation rates (0.5- 1m/My) in the Neogene attributed to the Namibian desert and later intensification of the mid-Miocene initiation of the cool Benguela Current (Cockburn et al., 2000; Séranne and Anka, 2005; Wigley and Compton, 2006). The aridification of southwest Africa is believed to have prevented significant large-scale erosion of the southwest African margin despite the high topographic gradient and extension of the Orange River catchment during the Oligocene (Séranne and Anka, 2005).

2.3.3 The interplay of tectonics, climate, and oceanic circulation on mid-Cenozoic sedimentation

Sedimentation and facies distribution offshore southwest Africa has strongly been affected by climate and oceanographic processes since the mid-Miocene (Weigelt and Uenzelmann-Neben, 2004, 2007a). Although an increase in sedimentation rates is recorded along southwestern Africa between the late Miocene to Pliocene times, the seismic profiles of rivers along the margin barely show any evidence of uplift due to the greater effect of ocean currents (Baby et al., 2020). The intensification of the Antarctic Circumpolar Current and Atlantic Meridional Overturning Circulation in the mid-Miocene formed thermally stratified, bottom water currents in the western South Atlantic including the deep south-flowing Antarctic Bottom Water current, south-flowing North Atlantic Deep Water current, and the north-flowing Antarctic Intermediate Water current (Fig. 2.6; Weigelt and Uenzelmann-Neben, 2004, 2007a).

The development of these stratified bottom and deep-water masses resulted in the change from warm-water carbonate deposition to cold water upwelling of the Benguela Current around ~15 Ma until ~1.5 Ma (following the Oligocene to Miocene uplift event) (Wigley and Compton, 2006; Weigelt and Uenzelmann-Neben, 2007b). The Benguela Current directs surface waters in a northerly direction as the eastern boundary of the South Atlantic's subtropical gyre offshore the SW African coastline (Peterson and Stramma, 1991; Diester-Haass et al., 1992). Since terrigenous sediment supply was low because of the arid climate, deposition was mostly dominated by slope-parallel bottom currents during the Miocene (Baby et al., 2018). The mouth of the Orange River is characterized by a late Pleistocene to Holocene wave-dominated delta thinning seawards and northwards terminating around Elizabeth Bay in Namibia (Rogers and Rau, 2006). According to Spaggiari et al. (2006) and

Bluck et al. (2007), higher sedimentation rates are implied during the Pleistocene to Holocene with the delta being extensively reworked by intense wave action driven by strong northerly winds.

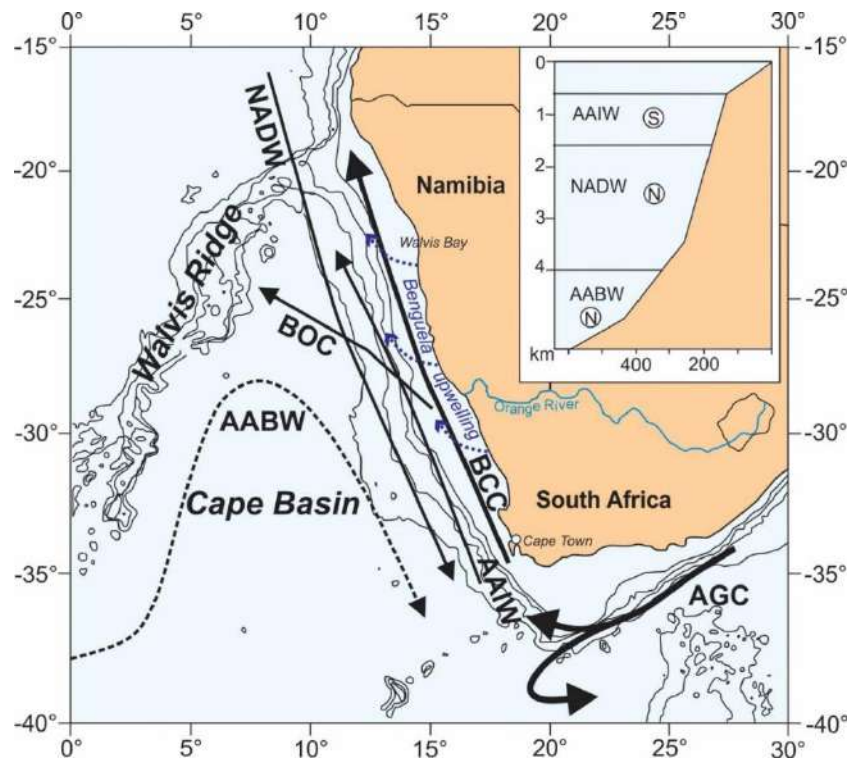


Figure 2.6 Oceanic circulation offshore southwest Africa from the Cenozoic till present (modified after Weigelt and Uenzelmann-Neben, 2004). Abbreviations: BOC= Benguela Oceanic Current, BCC= Benguela Coastal Current, AGC= Agulhas Current, NADW= North Atlantic Deep Water, AABW= Antarctic Bottom Water, AAIW= Antarctic Intermediate Water.

2.4 DWFTB systems

2.4.1 Overview of DWFTB systems

In very deep sedimentary basins with high sedimentation rates, the gravitational collapse of sediment may occur to form gravity collapse structures referred to as DWFTB systems (Morley et al., 2011). Gravitational collapse encompasses two primary mechanisms: (1) gravity spreading, involving the flattening of sediment laterally due to its own weight, and (2) the sliding of sediment masses along a weak, dipping detachment surface that lost cohesion (Rowan et al., 2004; Morley et al., 2011). In passive margin settings, well-developed DWFTB systems are interconnected tripartite systems, comprising a compressional, transitional/translational, and extensional domain (Fig. 2.3; Rowan et al., 2004; Krueger and Gilbert, 2009). Listric faulting separates convex-upward growth strata in the up-dip extensional domain (Fig. 2.3; Butler and Paton, 2010). The continued supply of sediment up-dip in the extensional domain eventually leads to gravitational collapse with down-dip compression along a basal shale or salt detachment surface forming fold-and-thrust belts (King and Morley, 2017). The transitional/translational domain is generally a poorly studied region in between the extensional and compressional zones. This is due to poor seismic imaging of its structurally complex internal geometry (e.g., Butler and Paton, 2010).

Numerous researchers have classified DWFTB systems based on their tectonic setting, basal detachment lithology, and the type of stress field the system is under (Rowan et al., 2004, Hamilton and de Vera, 2009; Krueger and Gilbert, 2009). Combining these, Morley et al. (2011) proposed a robust classification of DWFTB systems shown in Table 2.1. Type 1 systems are driven by near-field stresses and are mostly found in passive margin settings with either shale (Type 1a) or salt (Type 1b) detachments or associated with large deltas. Type 2 systems are driven by both near- and far-field (Type 2a) or predominantly far-field (Type 2b) stresses in continental convergent zones (Type 2a and 2bi) and accretionary prisms (Type 2bi). The basal detachment strength of DWFTBs in near-field stress driven systems is known to be weaker than those formed by far-field stress driven systems and display smaller wedge-taper angles attributed to the lithology and high pore fluid pressures of the detachment (Table 2.1; King and Morley, 2017). In seaward dipping detachments such as the Orange Basin, however, the wedge-taper angle is not strongly a result of the detachment's lithology or overpressure but more the dip which is secondary to fault strength.

Table 2.1 Characteristics of DWFTB systems according to Morley et al. (2011). Fold and thrust style abbreviations: PU= pop-up, BT= break thrusts (related to folding), FBF= fault bend fold, FPF= fault propagation fold, I= imbricate thrusts, DF (TF)= detachment fold (in thrust faulting), CF= crestal normal faults. Overpressure abbreviations: S= slab-derived fluids, BDC= burial disequilibrium compaction, I= inflationary, C= chemical.

	Type 1			Type 2 (Shale detachments)		
	Type 1a (Shale detachment)	Type 1b (Salt detachment)	Type 1 (Large deltas)	Type 2a	Type 2bi	Type 2bii
Tectonic setting	Passive margins			Continental convergent zones	Continental convergent zones	Accretionary prisms
Stress type	Near Field			Near and far field	Predominantly far field	
Dip direction of detachment	Oceanward	Oceanward	Landward	Landward		
Propagation of DWFTB	Oceanward	Landward propagation can be important	Oceanward , lateral migration of DWFTB	Oceanward		
Fold and thrust style	I, FPF, FBF, F(TF)	DF, I, FPF, PU, CF	DF, I, PU, CF, FBF, FPF	DF (TF), I, FPF, FBF	DF (TF), I, FPF, FBF	
Inversion of DWFTB-related growth faults	No	Yes, in deepwater	Uncertain, probably no	Deepwater no, nearshore yes	No	Deepwater no, nearshore yes
Duration	1's my–10's my	Episodic up to ~100my	<40 my?	<15 my?	<15 my?	10's my–100 my+
Overpressure	BDC, C	BDC, C	BDC, I, C	BDC, I, C	BDC, I, C	BDC, I, C, S
Critical taper	3°<	0–3°	2–3°	3–8°	3–11°	4–11°

2.4.2 DWFTB systems of the Orange Basin

The impressive formation of DWFTB systems offshore southwest Africa is attributed to sea-level fall in the late Campanian due to seaward tilting and major margin uplift (Fig. 2.3; Paton et al., 2008; Hirsch et al., 2010; de

Vera et al., 2010; Kuhlmann et al., 2010; Baby et al., 2018). The Orange Basin contains Type 1a, near-field stress-driven DWFTB systems (Morley et al., 2011) with all extensional, transitional, and compressional domains observed along a roughly east-west transect (Fig. 2.3; de Vera et al., 2010). Sediment from the upper parts of the extensional domain undergo reworking in the proximal settings of fully developed DWFTB systems giving rise to various mass flow deposits including slides and slumps (Kuhlmann et al., 2010; Dalton et al., 2017a). Deformation in the Orange Basin is confined to the sedimentary section through gravitational instability and is underlain by three main offshore dipping shale detachment surfaces (Morley et al., 2011). These are Cenomanian-, Turonian-, and Aptian-aged maximum flooding surfaces composed of thin, over-pressured basal shale (Brown et al., 1995; Dalton et al., 2015) the properties of which are extensively reviewed in Morley et al. (2011). The lateral movement of sediment is contained within a set of sidewall faults within the extensional domain, aligned in a parallel manner to the direction of sediment transport (de Vera et al., 2010; Scarselli et al., 2016). Folds and thrusts of the compressional domain are 60 km wide in a ~3 km thick section with 1–5 km spacings between imbricate thrusts (Fig 2.3; de Vera et al., 2010; Morley et al., 2011).

Up-dip extension should equal down-dip compression in linked DWFTB systems but has been found to not be the case in some systems such as in the Gulf of Mexico (Vázquez-Meneses, 2005), Spanish Pyrenees and the Orange Basin (Dalton et al., 2017b). Approximately 5% of strain is missing between the extensional (length of 25 km) and compressional (length of 16 km) domains of an Orange Basin's DWFTB system (Rowan et al., 2004; Butler and Paton, 2010; de Vera et al., 2010; Dalton et al., 2015). Based on Dalton et al.'s (2017b) findings, the 5% missing strain is attributed to second-order compressional features in the extensional domain, which could be applicable to various DWFTB systems. The absence of a compressional domain in the far outer regions of certain DWFTB systems (e.g., elsewhere the Orange Basin; Dalton et al., 2015) may additionally indicate an internal redistribution of strain. According to Butler and Paton (2010) and de Vera et al. (2010) the transitional zone results from the central shift in contact between the extensional and compressional domains, and therefore contains features overprinted by both tectonics. Other researchers such as Corredor et al. (2005), Krueger and Gilbert (2009) and Dalton et al. (2017a), however, suggest the zone to be a package of mostly undeformed sediment.

Gravitational collapse in a sedimentary basin is strongly controlled by the stratigraphic setting and the detachment surface's properties (Rowan et al., 2004; Dalton et al., 2017a). The presence of three over-pressurized shale detachment surfaces in the Orange Basin played a significant role in DWFTB formation in the Orange Basin (de Vera et al., 2010; Kuhlmann et al., 2010; Dalton et al., 2017a). Localized variations in slip potential along a detachment are caused by changes in detachment thickness, lithology, and overpressure (Dalton et al., 2017a). In Fig 2.7, Dalton et al. (2017a) presented a model for the growth of these gravitational collapse structures in the Orange Basin with multiple shale detachment surfaces. Margin uplift (Fig 2.7a) caused DWFTB formation with gravitational collapse initiating in the transitional domain (Fig 2.7b) as initially proposed by Dalton et al. (2015). Proximally, normal faults in the extensional domain eventually led to fold and thrust belt formation in the distal, down-dip compressional domain upon an initial shale detachment surface (Fig 2.7b). With deformation progressing through time gravitational sliding continued upon an upper shale detachment surface (Fig 2.7c). Once the upper DWFTB system could no longer accommodate gravitational slip, faults propagated downwards to another shale detachment surface at depth (Fig 2.7d) and formed underlying DWFTB (Fig 2.7e). The order of the formation of the upper and lower DWFTB system may be controversial; rather than strain being redistributed

upwards into younger sequences, Dalton et al. (2017a) suggest strain was redistributed downwards forming a later set of DWFTB systems in older sedimentary sequences.

2.5 Hydrocarbon systems of the Orange Basin

When organic matter is deposited and buried in an anoxic marine environment it may mature into petroleum over millions of years (Pepper and Corvi, 1995). Petroleum is a fossil fuel composed of a mixture of hydrocarbons (hydrogen and carbon) in the solid, oil or gaseous phase, and may include elements of oxygen, nitrogen, sulfur and trace metals in decreasing amounts. The terms “petroleum” and “hydrocarbon” are thus often used interchangeably. The maturation of petroleum depends on temperature and pressure increases through time starting with the formation of kerogen followed by oil then lastly gas (van der Spuy, 2003). Globally, 60% of discovered hydrocarbon provinces have been found within major Jurassic and Cretaceous source rocks in the Mesozoic, and 15% in the Cenozoic (Levell et al., 2010). Source rocks of passive margins fall within the same period (e.g., Toarcian, Aptian, Turonian, and Lower Eocene shales) and are found to extend to whole sets of basins within the Atlantic Ocean.

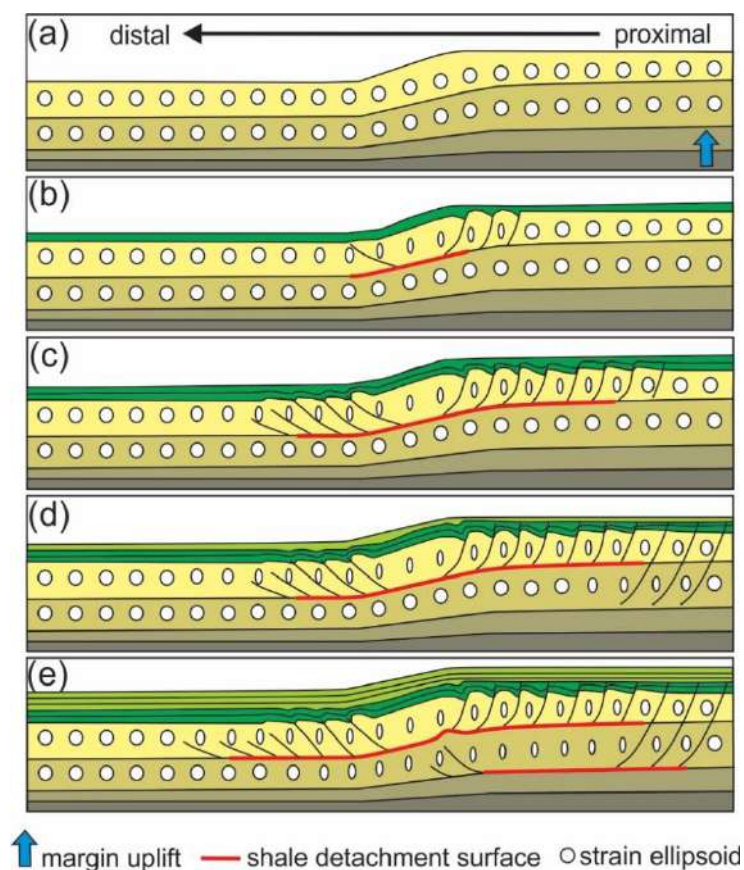


Figure 2.7 Model illustrating gravitational collapse to form Orange Basin DWFTB systems (modified after Dalton et al., 2017a). a) Margin uplift, (b) Downslope sliding of sediment upon a shale detachment surface beginning with gravitational collapse centrally (transitional domain) (c) new thrusts and folds form down-dip following normal faulting up-dip in the extensional domain; (d) Gravitational sliding upon upper system becomes increasingly difficult forcing faults to propagate onto a lower slip surface to redistribute strain; (e) Sediment above the lower slip surface becomes compacted then a second compressional domain develops.

The deep Barremian gas, Albian gas, Late Cretaceous deep-water slope turbidite oil/gas, and shallow Late Cretaceous gas plays are currently being appraised in the Orange Basin (PASA, 2017). Source rocks of the Orange

Basin include the syn-rift Hauterivian deposits of the Late Jurassic–Neocomian, and the transitional to early post-rift Barremian–Aptian and Turonian deposits of the Early Cretaceous (Aldrich et al., 2003; van der Spuy, 2003). The Hauterivian source rock is composed of high-quality, oil-prone lacustrine shales found within syn-rift half grabens producing the commercial A-J oil syn-rift system in the shallow Orange Basin offshore the South African margin (Jungslager, 1999; van der Spuy, 2003; van der Spuy and Sayidini, 2022). The late Barremian to early Aptian shallow sea environment provided the ideal anoxic conditions for the generation of petroleum (van der Spuy, 2003) to produce the commercial multi-trillion cubic feet Ithubesi and Kudu gas fields located offshore South Africa and Namibia, respectively (Fig. 1.1; PASA, 2017). Natural gas reservoirs of the Ithubesi gas field occur within Albian–Cenomanian fluvial channel-fill sandstones following the trend of underlying grabens while those of Kudu gas field occur within Barremian aeolian sandstones stratigraphically trapped by basement volcanics (Paton et al., 2008; Kuhlmann et al., 2010). The results from a 300 m thick interval in the DSDP 361 well (Fig. 1.1) show a total organic carbon content up to 25% with a hydrocarbon indicator of 800 mg HC/g according to van der Spuy (2003) and Paton et al. (2008). Some wells in the Orange Basin show evidence for a wet gas shale source rock in Cenomanian–Turonian sediments corresponding to a gas-prone maximum flooding event in the Late Cretaceous (Aldrich et al., 2003; van der Spuy, 2003; Kuhlmann et al., 2010). The comparison between shallow and deep-water wells (e.g., DSDP 361; Fig. 1.1) show that source rocks become increasingly oil-prone in distal deep-water environments while gas is concentrated along the proximal shelf (Jungslager, 1999; van der Spuy, 2003).

The geochemical analyses of samples collected from the Orange Basin's seafloor indicate both a biogenic and mostly thermogenic origin of hydrocarbons, with the thermogenic source possibly derived from early Aptian shales (Jungslager, 1999; Kuhlmann et al., 2010). Petroleum migrates from the organic-rich source rock in which it formed into porous reservoir rocks. In seismic sections common features associated with fluid and gas migration indicative of hydrocarbons include bright spots, flat spots, wipe-out zones, gas chimneys, natural gas and fluid escape features (e.g., craters, mounds, mud volcanoes, pockmarks) and bottom simulating reflectors (Jungslager, 1999; Kuhlmann et al., 2010). These are found in the shallow and deep, undrilled, and high-risk regions of the Orange Basin (PASA, 2017).

3 Review of the seismic method and seismic stratigraphy

3.1 The seismic reflection method

The seismic method is a geophysical method involving the propagation of elastic waves through the subsurface from a seismic source and the reflection and refraction of waves due to changes in density and velocity recorded by receivers (Sengbush, 1983). A seismic source may generate two primary types of waves: (1) body waves including P- (compressional) and S- (shear) waves, and (2) surface waves including L- (Love) and R- (Rayleigh) waves (Cox et al., 2020). P-waves have high velocities with backwards and forwards particle motion travelling parallel to the wave direction through solids, liquids, and gases. S-waves travel only through solids in a side-to-side manner perpendicular to the wave travel direction thus causing a shearing effect. L-waves are side-to-side particle motions perpendicular to wave propagation causing the earth's surface to shift horizontally. R-waves have dispersive velocities and frequencies due to their complex vertical and horizontal rolling particle motion.

Although the seismic method is believed to have first begun in the past century to understand the internal structure of the earth through earthquake monitoring, the most basic use of sound reflection dates to 450 BC as the earliest written record by Heroditus (Veekan, 2007; Veekan, 2013). Here, people avoided possible threats in tunnels (such as loose rocks) using the echoed return signal of sound waves through rocks. Modern seismic surveys use multi-component receivers to measure all waves since S-waves are also known to give important information of the subsurface (Dondurur, 2018). The seismic reflection method has been invaluable in exploration since the 1960s and 70s, particularly offshore in the oil industry's search for hydrocarbons and are the most used surveys while refraction is used where more detailed velocities are needed to image deep structures or obtain the near surface information (Cox et al., 2020).

3.1.1 Seismic acquisition

Figure 3.1 illustrates the typical layout of the reflection seismic survey in marine settings involving a ship-towed transmitter and linked array of hydrophones (Song et al., 2012). A sound wave generating device, usually an array of airguns in marine settings, transmits acoustic (seismic) energy that propagates through the water column and stratigraphic layers. Air bubble pulses of compressed air from different-sized airguns are released at set time intervals into the water from a navigating ship (Ruddick et al., 2009; Song et al., 2012). The pulses or source wavelet resemble a radio antenna in the water column created from the difference in time of shots fired and the strong reflection of sound from the sea's surface. Once this transmitted energy encounters a contrast in physical properties (a product of density and compressional velocity termed an acoustic impedance) between different layers, a fraction of the energy is reflected back from the surface and received by an array of hydrophones tuned to the same transducer generated from the outgoing signal (Song et al., 2012). Hydrophones record the amplitude and arrival time of reflected signals therefore giving information of their depth and distance behind the acoustic source (Fig. 3.1; Ruddick et al., 2009). The reflected energy is defined by the reflection coefficient (RC) as follows:

$$RC = \frac{\rho_2 V_2 - \rho_1 V_1}{\rho_2 V_2 + \rho_1 V_1} \quad (3.1)$$

Where ρ = density, V = compressional velocity.

In Eq. 3.1, $\rho_2 V_2$ is the underlying layer's acoustic impedance reflecting the interface and $\rho_1 V_1$ is the overlying layer's acoustic impedance the reflecting interface, e.g., the surface between layer 2 and layer 3 in Fig. 3.1. The RC value lies between -1 and +1 meaning that the rest of the seismic signal is transmitted downwards and thus able to reach great depths at which hydrocarbon reservoirs may be found.

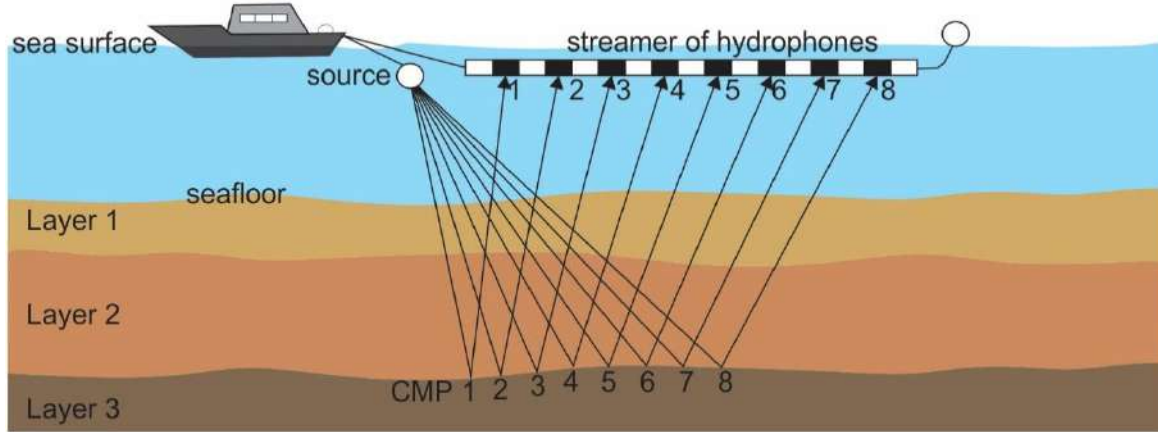


Figure 3.1 Illustration of the seismic reflection method as used in marine settings showing the ray path along the surface of layer 3 (modified after Song et al., 2012).

3.1.2 Seismic processing

To produce a seismic section as representative to the subsurface image as possible, the seismic data need to be processed to remove noise artefacts and distortions produced during acquisition (Onajite, 2013). Dondurur (2018) categorizes the general steps used in seismic processing into: (1) data preparation involving demultiplexing and trace editing; (2) data correction involving amplitude correction, noise attenuation, static corrections, and velocity analysis; (3) data reduction involving common midpoint stacking and multiple attenuation; and (4) data enhancement involving deconvolution, migration, filtering, and scaling. Since seismic data are obtained from a variety of geological settings with different acquisition parameters, the steps used in seismic processing differs from dataset to dataset (Cox et al., 2020). All processing steps are however designed to aid the accurate and efficient interpretation of data through noise removal, minimizing artifacts and improving the resolution.

Hydrophones receive a hyperbolic pattern of returns equivalent to the wavelet generated by the source (Ruddick et al., 2009). The wavelet's seismic resolution limit, defined as the ability to seismically detect different objects, is explained by the Rayleigh criterion (Sheriff and Geldart, 1995). Both vertical and horizontal (lateral) resolutions are considered in seismic data processing which, to note, decrease with increasing velocities and depth (Onajite, 2013). Yilmaz (2001) gives the dominant wavelength (λ) of seismic waves by:

$$\lambda = \frac{v}{f} \quad (3.2)$$

Where v = average velocity, f = dominant frequency.

The vertical resolution limit needs to be generally $\frac{1}{4}$ of the wavelength of the dominant frequency in Eq. 3.2 to distinguish between different reflectors at depth in the seismic section (Sheriff and Geldart, 1995). According to Yilmaz (2001), the $\frac{1}{4}$ wavelength criterion may be too much especially if the RC value is small resulting in an indiscernible reflection event. A $\frac{1}{8}$ dominant wavelength may also be used, defining the Widess criteria (Widess,

1973). Thinner units or beds in the seismic data may be resolved using the Widess criteria as reviewed by Manzi et al. (2013). Modern digital seismic systems with peak frequencies of 50 Hz and higher may improve the vertical resolution to 8 m or less showing that higher frequencies produce greater vertical seismic resolution limits (Ruddick et al., 2009). The difference in time of the seismic wavelets and the presence of wavelet side lobes may cause confusion as multiple reflectors overlap resulting in constructive or destructive interference. The amplitude of the interfering reflectors is fine-tuned and built up in constructive interference while in destructive interference the amplitude is degraded and thus discarded from the output (Dondurur, 2018).

The horizontal seismic resolution is described in terms of the Fresnel Zone shown in Eq. 3.3 and illustrated in Fig. 3.3. This is the radius over which reflected waves interfere with each other constructively, occurring when the path lengths of reflected waves differ by less than half the dominant period in the “first” Fresnel Zone region (Sheriff, 1996; Ruddick et al., 2009; Onajite, 2013). Beyond this region the interference of waves may either be constructive or destructive (Sheriff, 1996). As the radius of the Fresnel Zone decreases, the horizontal resolution increases. The Fresnel Zone's radius is dependent on the wavelength, and for an unmigrated section with a zero offset, this relationship is described by Yilmaz (2001) as:

$$R = \frac{V}{2} \sqrt{\frac{t_0}{f}} \quad (3.3)$$

Where V= average velocity, t= two-way time, and f= dominant frequency.

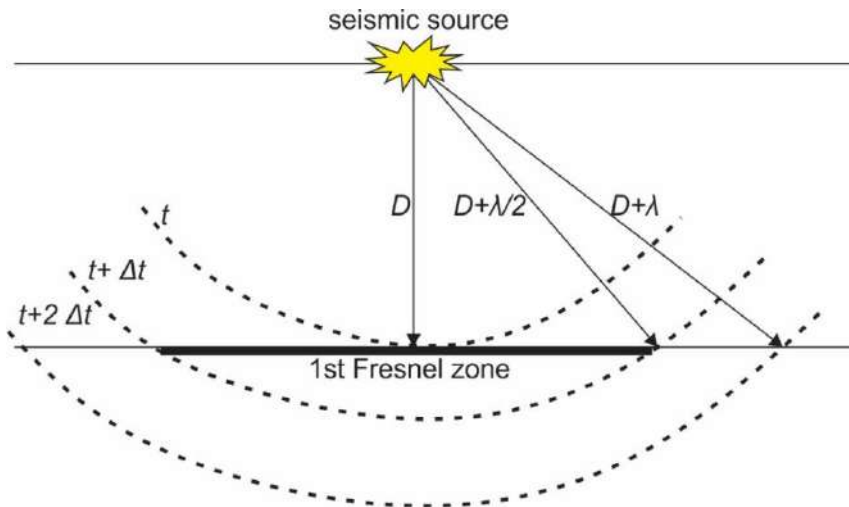


Figure 3.2 Schematic illustration of the Fresnel Zone (Fourie and Botha, 2001).

For high-resolution, migrated seismic data Herron (2011) states that the horizontal resolution may be equal to as small as ½ the wavelength. Other factors to consider in relation to horizontal resolution include the bin size, trace spacing, and aperture width (Lebedeva-Ivanova et al., 2018). In 3D seismic data acquisition, bins are rectangular cells found centrally within a surficial area between an inline and crossline termed a bin grid (Dondurur, 2018). The size of the inline and crossline bins for a single source array are usually ½ of the group interval and ½ streamer separation, and ¼ of the streamer separation in flip-flop acquisition for dual source arrays, respectively.

In seismic processing seismic traces are edited, noise-filtered and corrected for the decay of wave amplitude with distance. The common midpoint method is then used to enhance the signal-to-noise ratio by sorting common

midpoint gathers (in order of the increase in offset) from seismic traces (Fig. 3.3; cf. Yilmaz, 2001; Song et al., 2012). The common midpoint is the common offset point between the receiver and source. In 2D seismic processing the common midpoint methodology is used to obtain a near vertical signal of reflection and the speed of sound as the acoustic signal moves through different layers (Song et al., 2012). The offset in distance and travel time of the reflected traces corresponding to each common midpoint is corrected for through the normal moveout correction, making the delay time of each seismic trace equivalent to a vertical traverse where $x=0$ (Fig. 3.3c; Ruddick et al., 2009). These are then all added together to form a stacked section (Fig. 3.3d) representing the response a sound wave would generate as it travels downwards vertically from the source and is reflected along the same traverse to a coincident receiver.

Equivalent to the common midpoint common midpoint method for 3D seismic processing (in swath shooting with straight lines), is the creation of common cell stacks as traces of data are sorted and collected into common cell gathers called bins (cf. Yilmaz, 2001). 3D seismic processing otherwise follows much of the same basic principles used in 2D seismic processing. The common midpoint methodology only works for reflections of horizontal layers while dipping layers have problematic azimuthal variations of the normal moveout (Yilmaz, 2001). This effect is corrected for in the seismic section through the process of migration either before (pre) or after (post) stacking in either the time or depth domain.

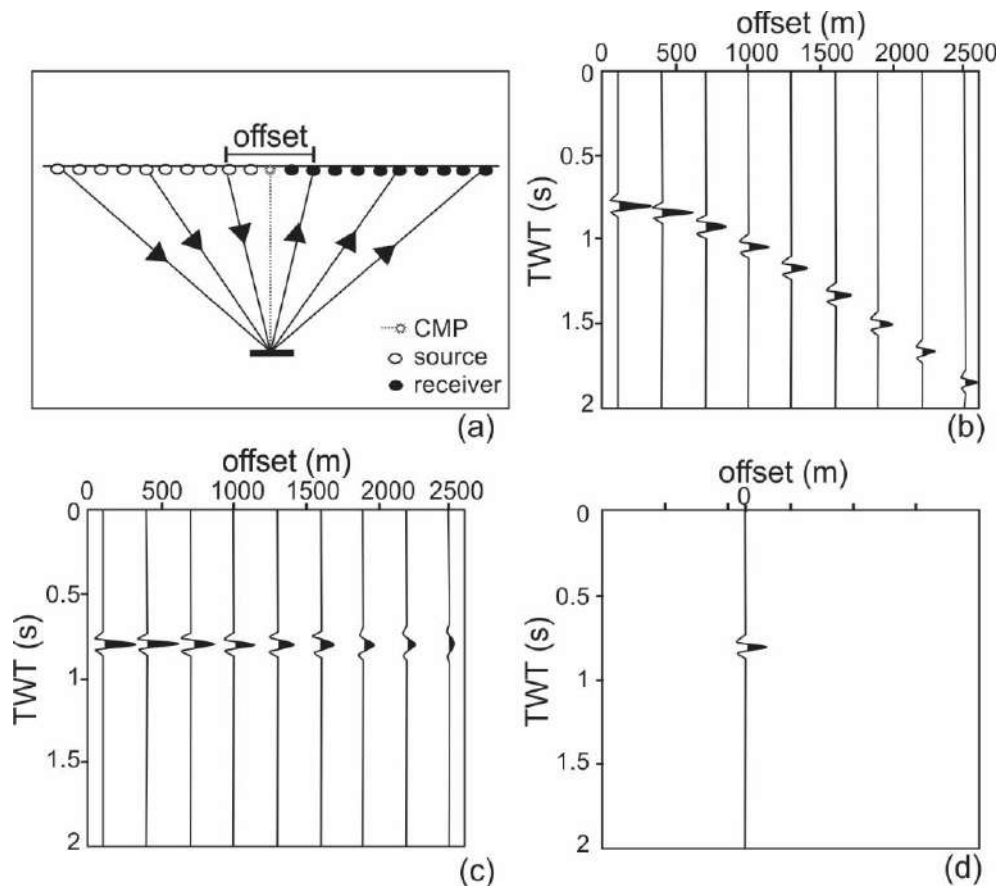


Figure 3.3 Illustration of the common midpoint method (modified after Ruddick et al., 2009). (a) A set of source to receiver pathways showing multiple sampling of the same feature to produce a common midpoint gather. (b) Plotted traces from the common midpoint gather in (a) showing the delay to return time (TWT) on the vertical axis with the increase in displacement (x - axis) laterally. (c) common midpoint gathers after the application of a normal moveout correction. (d) The normal moveout-corrected traces are averaged out to create a “stack”.

Seismic migration is an image processing technique that collapses the in-line aspect of the Fresnel Zone within the seismic section (Ruddick et al., 2009). By suppressing diffracted energy, the effects of dipping reflectors and wave propagation are removed to obtain a more accurate subsurface image of the reflection events (Dondurur, 2018). Migration techniques are classified into many types: (1) Kirchhoff migration method, (2) finite-difference migration, and (3) reverse migration are the most commonly used methods in seismic processing (Onajite, 2013). The most popularly used migration technique in offshore data processing in the time domain is Kirchhoff pre-stack time migration (Fig. 3.4). Kirchhoff migration is an algorithm based on the integral form of the scalar wave equation (Dondurur, 2018). It uses Huygens principle together with geometry to collapse diffraction and reposition reflectors to their correct geological positions (Onajite, 2013; Dondurur, 2018).

The amplitude of diffraction hyperbolas generated from reflectors in the subsurface (each consisting of multiple contiguous point sources) are added together as a summed amplitude at the peak of the diffraction hyperbola (Fig. 3.4). This apex is considered the true location of the reflector in the output field of the migrated trace (Fig. 3.4). Two important parameters need to be considered for Kirchhoff migration: (1) migration aperture width; controlling the accuracy and quality of the migrated output and how long the diffraction summation algorithm runs for, and (2) velocity model; the algorithm is sensitive to velocity errors so a slight departure from the true velocity field may result in over- or under-migration.

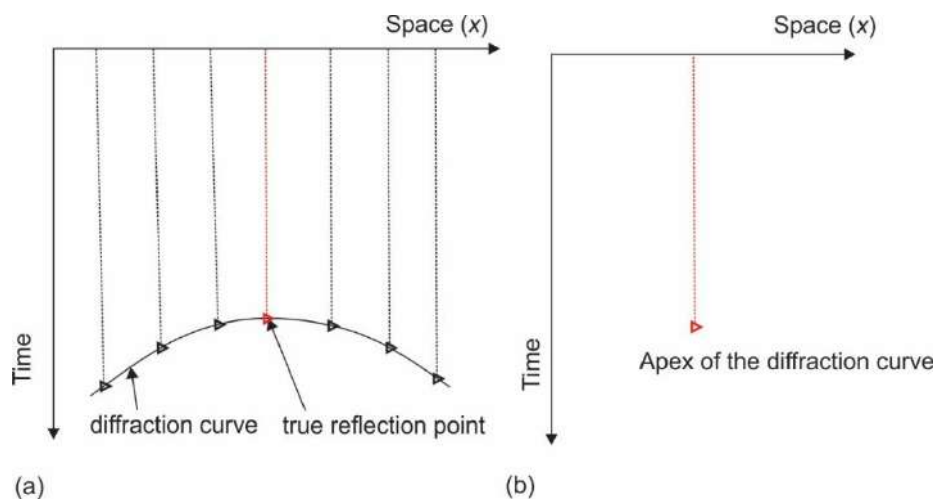


Figure 3.4 Illustration of Kirchhoff pre-stack time migration (a) multiple reflection points on the diffraction curve and (b) summed amplitudes along the diffraction curve (modified after Onajite, 2013).

The seismic section produced at the end of processing is usually plotted along the vertical axis in the time domain known as two-way time (TWT) travel with the common midpoint plotted along the horizontal axis (Ruddick et al., 2009). To obtain the true thickness of seismic units the TWT may be converted to depth using velocity-depth functions obtained during normal moveout correction. Usually, a constant 1500 m/s sound speed is given to sea water so 1000 ms TWT correlates to ~ 750 m water depth. Using a two-colour palette scheme, the seismic traces are placed one on top of another as positive (peak) and negative (trough) reflectors in the seismic section.

3.1.3 Seismic interpretation

Once reflection seismic data have been processed, interpretation may take place. The interpretation of seismic data includes many steps and applications which depend on the level of detail the interpreter wants to achieve.

Prior to computer-generated software, reflection seismic data were interpreted on paper (Cox et al., 2020). Today, various computer-based software platforms may be used for seismic interpretation. These software packages display various intersections. A 3D seismic volume appears as orthogonal slices with three principal directions; two of which are vertical sections (inlines and crosslines) and one a horizontal section (time/depth slices) through the earth illustrated in Fig. 3.5 Inlines (y-axis) are acquired parallel to the direction of boat movement while crosslines (x-axis), also known as xlines, are acquired perpendicular to these. Time or depth slices (z-axis) are horizontal sections created from the seismic volume. Additional vertical sections may be created from a 3D seismic volume in any orientation called arbitrary polylines. Arbitrary polylines can be used to verify the consistency of an interpretation, e.g., determining the continuation of a surface beyond a fault plane otherwise not clearly resolved on the inline and crossline section.

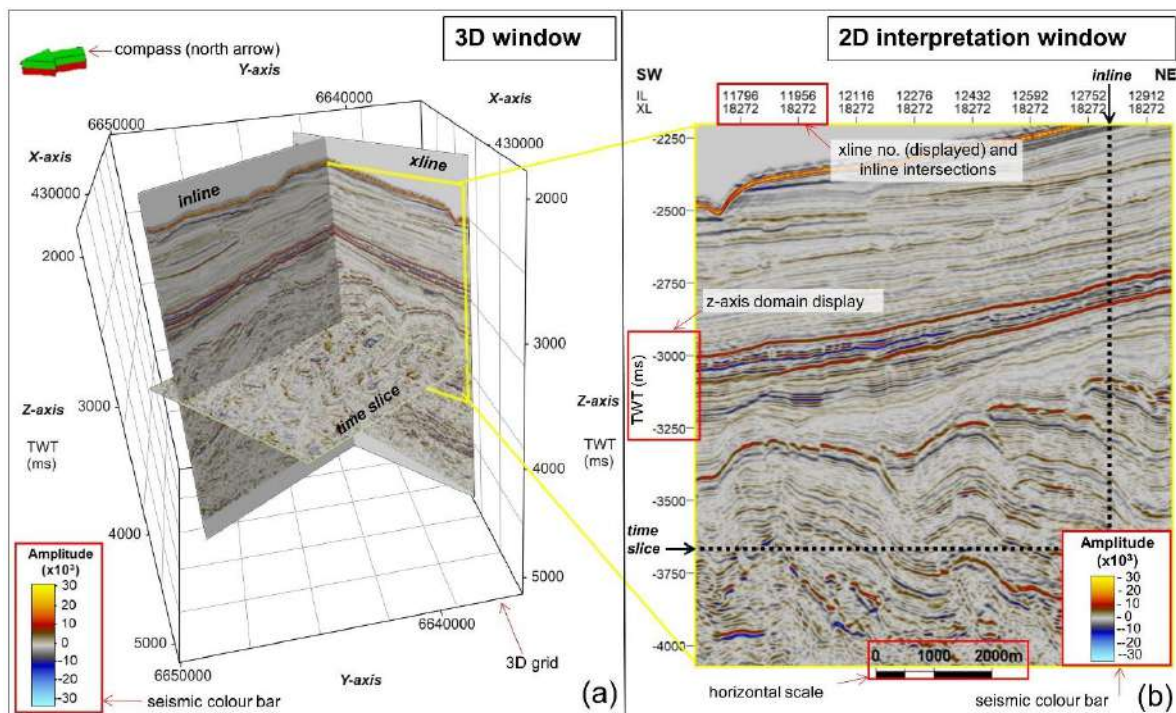


Figure 3.5 Reflection seismic data of the deep-water Orange Basin showing (a) a 3D window displaying the inline, crossline (or xline) and time slice sections, and (b) a 2D interpretation window of the crossline viewed in (a). Common features including the different axes, compass, 3D grid, horizontal scale and seismic colour bar have been annotated. VE= 5.

Genetically related strata, called stratigraphic units, are separated from each other by stratigraphic surfaces upon which reflectors terminate against through downlap, onlap, toplap, erosional truncation, or concordance (Mitchum et al., 1977). The first step in seismic interpretation is identifying stratigraphic surfaces marking important geological events. These stratigraphic surfaces often (but not always) appear as high amplitude reflections dominant throughout the study area. The vertical displacement of a continuous reflector (i.e., stratigraphic surface) and the abrupt termination of a seismic event are the main criteria for identifying faults in a seismic section (Duru et al., 2018). Stratigraphic surfaces may be picked in 2D and 3D on the vertical inline, crossline and additional arbitrary lines using two principal methods: (1) manual interpretation, and (2) auto-tracking. Manual interpretation involves clicking key points or dragging a freeform curve along a stratigraphic surface of interest to create a horizon interpretation. Faults may be manually picked in the same manner by clicking points between the observed

hanging wall and footwall blocks of a discontinuity. Auto-tracking is a quick essential tool in picking horizons. Auto-tracking automatically extrapolates selected high or low amplitude horizons throughout the seismic data then where the tracking criteria cannot be satisfied, auto-tracking stops. This occurs either when the quality of the surface decreases in a particular section (low signal-to-noise ratio) or when the tracker detects discrepancies on the surface caused by fault displacement, sharp changes in dip, or stratigraphic events such as a change in facies, channels, and eroded or merged surfaces (Veekan, 2017). Well ties, if present, may help resolve such features during seismic interpretation, together with the application of seismic attributes. The following section outlines the seismic stratigraphic concepts used in seismic interpretation.

3.2 Seismic Stratigraphy

3.2.1 Background

The interpretation of reflection seismic data reveals important geological information pertaining to the history, depositional facies, and stratigraphy of a sedimentary basin. Based on the observations of [Vail et al. \(1975\)](#) and [Vail et al. \(1977\)](#) together with the latter's published sea-level chart, the concept of seismic stratigraphy was first introduced by [Mitchum et al. \(1977\)](#). Seismic stratigraphy is the study of cyclical changes in sedimentation patterns arising from the interplay of accommodation and sedimentation ([Catuneanu, 2006](#); [Catuneanu et al., 2009](#)). It is based on the view that the formation of sequences at all levels of stratigraphic cyclicity is driven mainly not only by eustasy but also tectonics, together termed as relative sea-level. Stratigraphic cyclicity is also controlled by climate, sediment supply and loading (leading to compaction) and other autogenic processes affecting sediment supply such as fluvial avulsion and delta lobe switching ([Catuneanu et al., 2009](#)).

The concept of seismic stratigraphy has greatly evolved since the 1970s due to the petroleum industry's persistent search for hydrocarbons in deeper parts of sedimentary basins ([Veeken, 2013](#)). The significance of seismic stratigraphy today lies in the fact that two different scales of observation are used in exploring sedimentary basins including (1) the well-control approach, and (2) the seismic method used particularly where well-control is limited or lacking ([Cross and Lessenger, 1988](#); [Veeken, 2007](#)). Although seismic data covers a large areal extent enabling one to define sequences and sequence sets, smaller scale stratal units such as laminae and beds are often poorly resolved. To incorporate other forms of data such as outcrop and core/well log data covering the smaller details of strata in more detail, the more generic term "sequence stratigraphy" evolved in the 1980's ([Catuneanu, 2006](#); [Catuneanu et al., 2009](#)).

3.2.2 Sequence stratigraphic framework

Seismic analysis involves subdividing genetically related strata into seismic sequences or packages based on their reflected termination patterns and interpreting the environmental setting and lithofacies (seismic facies) of these according to their internal arrangement pattern ([Figs. 3.6 and 3.7](#); [Mitchum et al., 1977](#)). Seismic sequences are interpreted as depositional sequences expressing the lithology of the features that formed them, with each bound by an unconformity or correlative conformity surface ([Fig. 3.8](#)). These chronostratigraphic surfaces are identified by their continuity and the way in which seismic strata terminate against them. The genetically related stratigraphic units between chronostratigraphic (or just stratigraphic) surfaces are termed systems tracts; a stack of sediment

deposited during a specific phase of the relative sea-level cycle and therefore used in sequence stratigraphic analysis to describe changes in relative sea level (Catuneanu, 2006; Veeken, 2013). The four major tracts recognised in sequence stratigraphy illustrated in Fig. 3.7 include the highstand systems tract with sea-level rise, falling stage systems tract with sea-level fall, lowstand systems tract with the beginning of sea-level rise, and transgressive systems tract with continued sea-level rise (Catuneanu, 2002; Catuneanu, 2006).

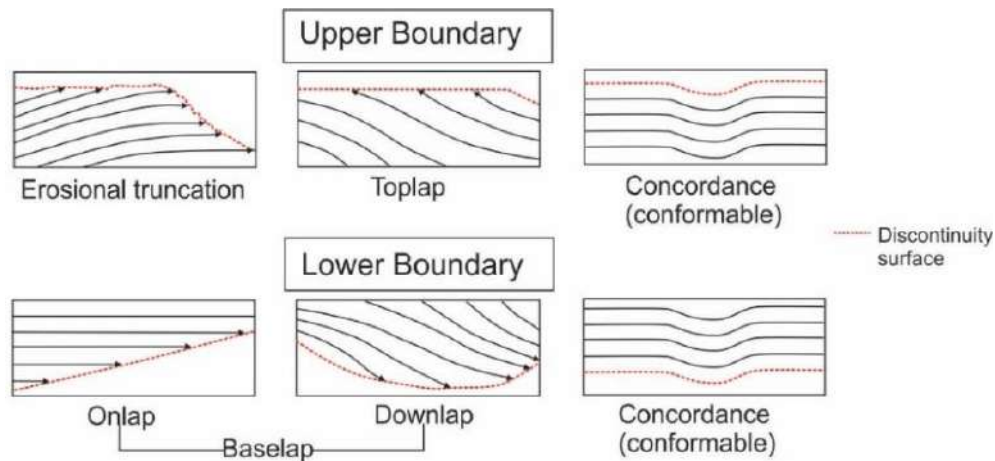


Figure 3.6 Upper and lower sequence boundary stratal termination patterns (Mitchum et al., 1977).

3.2.2.1 Stratal terminations

Stratal terminations include onlap and downlap terminating above a discontinuity surface, toplap and truncation terminating below a discontinuity surface, and offlap occurring in a conformable sequence as summarised by Catuneanu (2006) and shown in Figs. 3.6 and 3.7. Erosional truncation refers to the scouring of topsets in a package of strata as the older strata is eroded. This is the most common and reliable criteria in identifying a channel. In toplap strata terminate at an inclined angle against an overlying discontinuity surface usually if erosion is affecting a prograding shelf. Onlap forms with transgression where progressively younger horizontal or inclined strata overstep each other terminating against a surface of greater inclination, while offlap forms during a forced regression where younger strata progressively shift offshore to expose a portion of the older, underlying strata. Downlap may give the main direction of sediment supply as inclined strata terminate in a down-dip direction. The term baselap is used when onlap cannot be distinguished from downlap due to deformation.

3.2.2.2 Seismic facies analysis

Seismic facies analysis allows one to differentiate between adjacent seismic facies or units based on their internal reflection patterns (Mitchum et al., 1977). Adjacent seismic facies units differ to each other according to varying seismic reflection parameters which include the interval velocity, amplitude, continuity, configuration, and frequency. All these parameters apart from interval velocity may be observed visually within the seismic section without special computer adjustments to the data (Cross and Lessenger, 1988). Internal reflection geometries relate to the depositional environment and lithofacies of each seismic unit and include chaotic, parallel, subparallel, prograding, divergent, and reflection-free patterns (Fig. 3.8; Mitchum et al., 1977). Progradational configurations include sigmoid, oblique tangential, shingled, oblique parallel, complex sigmoid oblique, and hummocky clinoforms.

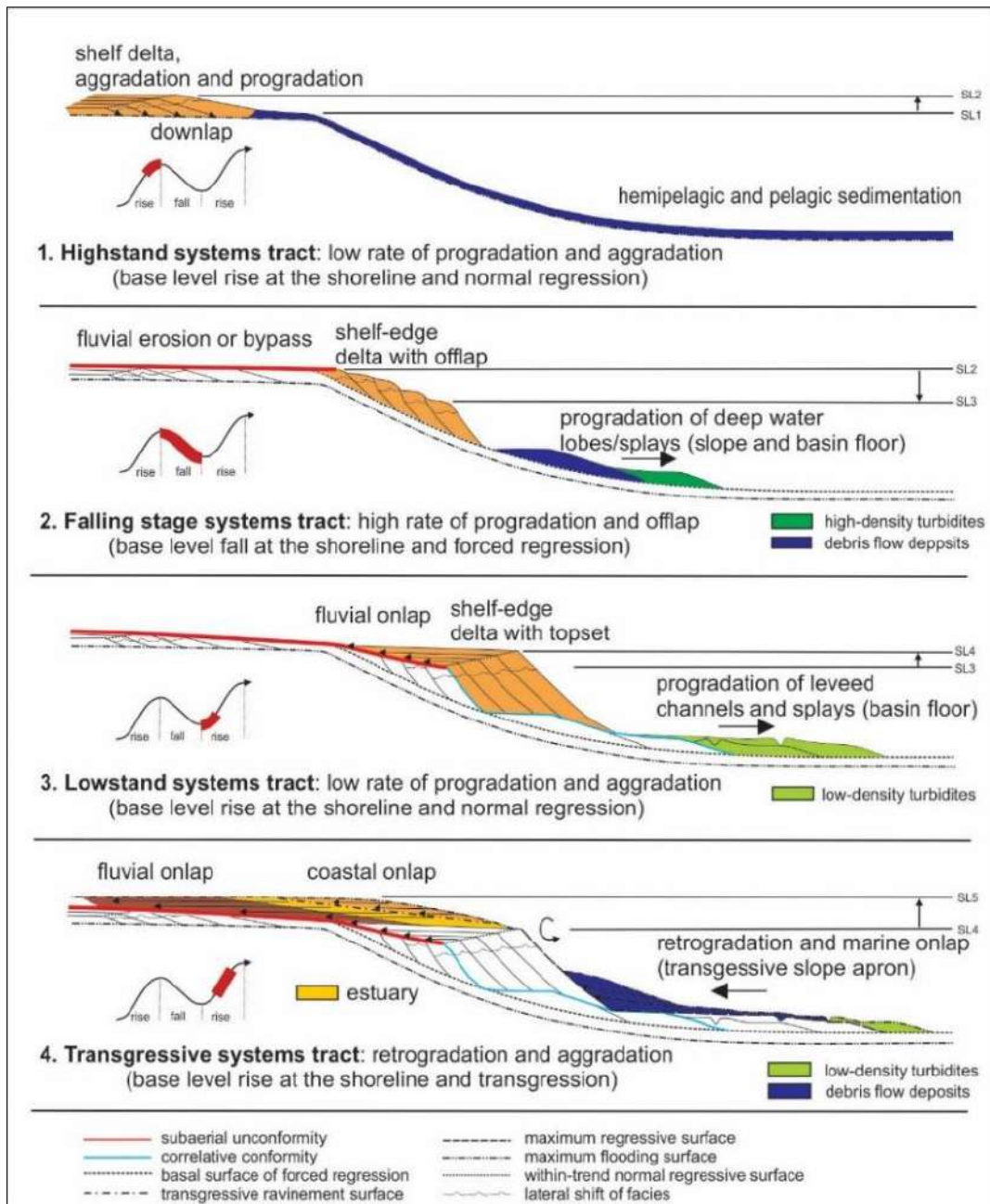


Figure 3.7 Sequence stratigraphic framework regional architecture illustrating the various depositional systems, systems tracts, and stratigraphic surfaces formed during different phases of the relative sea-level cycle (Catuneanu, 2006). SL= sea-level.

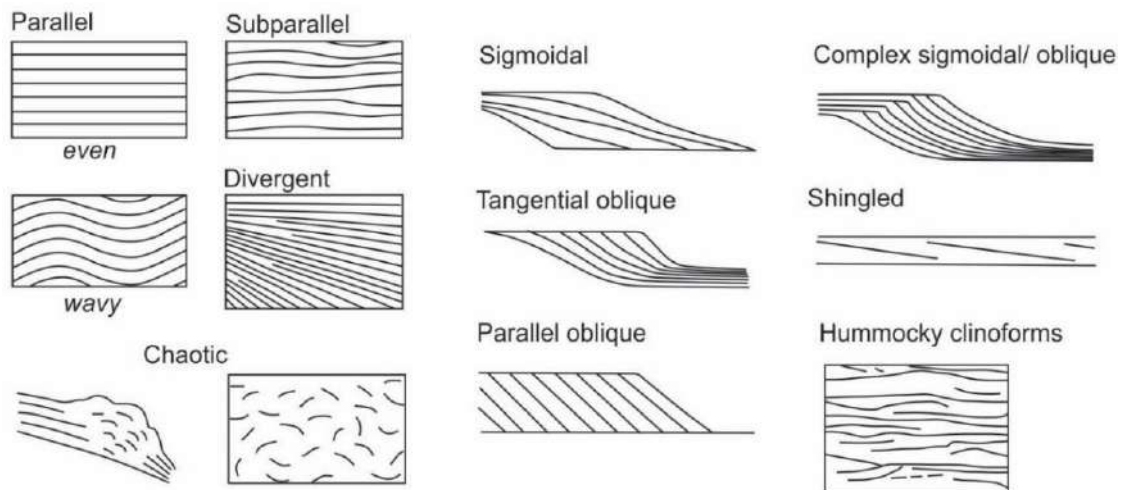


Figure 3.8 The various internal reflection geometries observed in seismic facies units (Mitchum et al. 1977).

3.2.2.3. Stratigraphic surfaces

Changes through time in depositional regimes are marked by stratigraphic surfaces which are created through the interplay between sea-level fluctuations and sedimentation (Catuneanu, 2006). According to Catuneanu (2006), the identification of stratigraphic surfaces is based on several criteria involving facies analyses and a basic understanding of how the depositional environment the surface, and the facies units it separates, originated. Due to the abrupt vertical change in physical properties from one substrate to another, stratigraphic surfaces appear well on seismic data due to a significant contrast in acoustic impedance between them. Stratigraphic surfaces formed in deep-water marine settings include the two mappable correlative conformity surfaces which are (1) the mappable maximum flooding surface, and (2) the cryptic maximum regressive surface summarised in Table 3.1 and shown in Fig. 3.9 (Catuneanu, 2002; Catuneanu et al., 2009). A proper sequence stratigraphic framework for deep-water settings is difficult to construct since only four of the seven types of stratigraphic surfaces form (Table 3.1; Catuneanu et al., 2009). This is due to the physical disconnection of the deep-water environment to its fluvial and shallower-water counterparts, arising from extended periods of non-deposition or shelf edge to upper slope erosion and sediment instability.

In Catuneanu et al. (2009) the sequence stratigraphic framework for a deep-water marine setting is given in Fig. 3.9 which is the 2D seismic interpretation of a gravity flow deposit reflecting a full cycle in relative sea-level changes. In seismic facies analysis the chaotic internal reflectors of 'A' represent a mudflow deposit formed in early stages of forced regression; strong parallel internal reflectors of 'B' represent a turbidity flow frontal splay formed at the end of forced regression, high amplitude (sandy channel fill) and transparent (overbank deposits) internal reflectors of 'C' represent normal regression lowstand conditions and early transgression, chaotic internal reflectors of 'D' represent mudflow deposits of late transgression. The sequence stratigraphic surfaces present include (1) the two 'CC' surfaces marking the change between forced and normal regression (and hence stacking patterns of strata), and (2) the maximum regressive surface marking the change between lowstand normal regression and transgression which is often difficult to map within an undifferentiated succession of deposits, and (3) the maximum flooding surface representing the change from transgression to highstand normal regression.

Table 3.1 The main sequence stratigraphic surfaces found in deep-water marine settings (modified after Catuneanu, 2006).

Surface	Description	Nature of contact	Marine Facies		Depositional trends	Stratal terminations
			Below	Above		
<i>Maximum regressive surface</i>	Marks change from shoreline regression to transgression; Replaced by MFS in distal marine	Conformable (few exceptions)	Fining upward in deep water; Coarsen-upward in shallow water	Fining-upward	Above: transgression Below: normal regression	Above: marine onlap Surface: onlap, downlap
<i>Maximum flooding surface</i>	Marks end of shoreline transgression	Conformable or scoured	Fining-upward	Coarsen-upward	Above: normal regression Below: transgression	Below: truncation Above: downlap Surface: onlap, downlap
<i>Correlative conformity</i>	Reflects paleo-seafloor at the end of a forced regression; correlates with subaerial unconformity	Conformable	Coarsen-upward	Coarsen-upward on shelf	Above: normal regression Below: forced regression	Above: downlap Surface: downlap

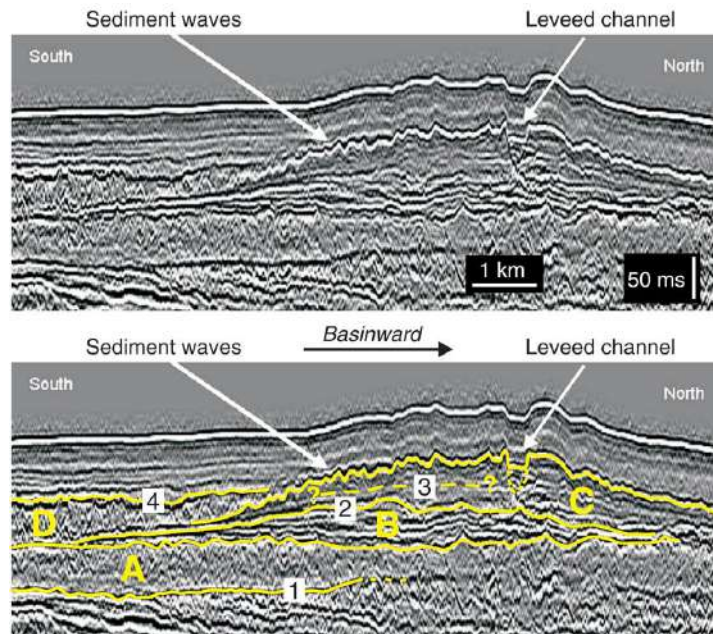


Figure 3.9 Uninterpreted and interpreted 2D seismic lines of a deep-water gravity flow deposit (Catuneanu et al., 2009). Seismic facies include A- mudflow deposits; B- turbidity flow frontal splay; C- leveed channel and overbank facies; and D- mudflow deposits. Sequence stratigraphic surfaces include: 1- correlative conformity; 2- correlative conformity; 3- maximum regressive surface; and 4- maximum flooding surface.

3.3 Seismic interpretation using seismic attributes

3.3.1 Overview of seismic attributes

To aid horizon/surface and fault mapping seismic attributes may be applied to a seismic dataset. Seismic attributes enhance subtle aspects of the conventional seismic data (Chopra and Marfurt, 2005, 2007). They act as filters focussing the attention of one specific component in the dataset by removing others (Barnes, 2016). Since seismic data may be described in a variety of different ways, hundreds of attributes exist (Fig. 3.10) usually based on the seismic measurement of time, amplitude, and frequency (Cox et al., 2020). Extractable properties of the seismic dataset are considered attributes including reflection terminations, inversion associated with acoustic impedance, complex-trace attributes, the prediction of pore pressures, and amplitude variation with offset (Chopra and Marfurt, 2005, 2007). Seismic attribute analysis is widely known to have begun in the 1960s and 70s with the advancement of computer technology. An early form of seismic attribute analysis, however, occurred as far back as the 1930s before digital records were available whereby early geophysicists correlated travel times to reflections observed in the field on paper records (Chopra and Marfurt, 2005).

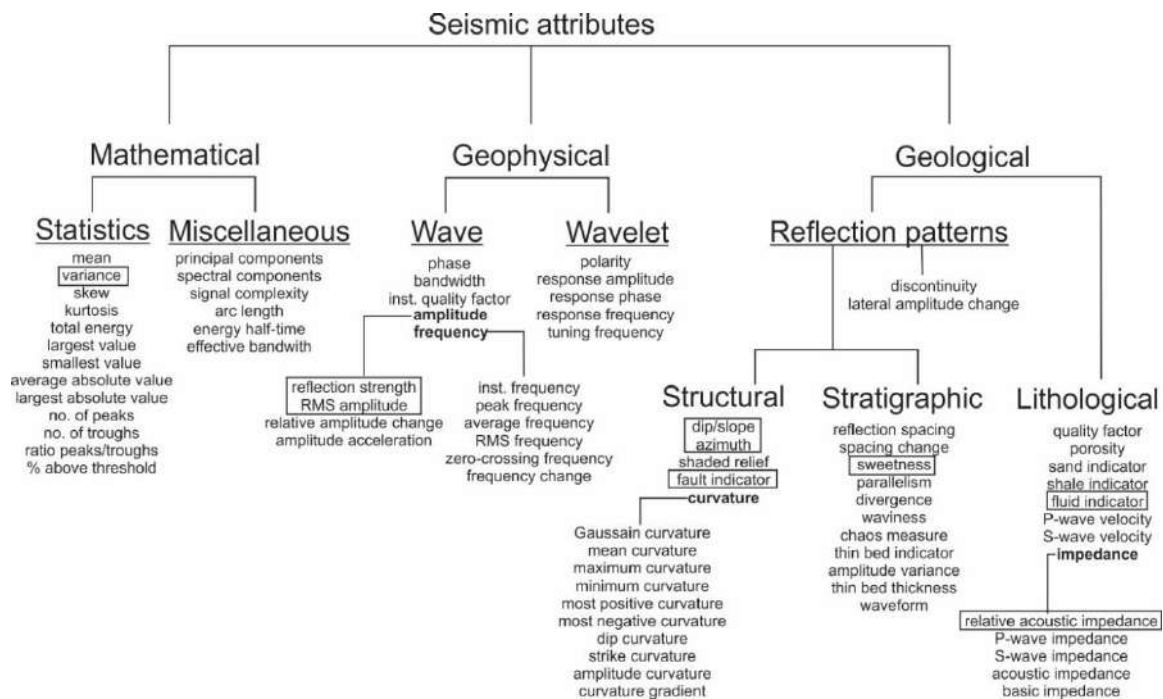


Figure 3.10 Categorisation of seismic attributes using geological, geophysical, and mathematical properties (Barnes, 2016). Boxes indicate those used in the research.

Seismic attributes may be applied on both pre-stack and post-stack seismic data (Barnes, 2016). While pre-stack attributes are obtained through geophysical inversion methods, post-stack attributes use statistics, filters and transforms to gain the stratigraphic and structural properties of the seismic data. According to Barnes (2016) post-stack attributes fall short when it comes to obtaining the lithological properties of the seismic data which are best described and imaged using pre-stack seismic data and attributes. The analysis of seismic attributes reveal significant physical and geological properties in seismic data such as a basin's structure, stratigraphy, and reservoir characteristics through the enhancement of faults, thin bed tuning and bright spot identification, to name a few (Chopra and Marfurt, 2005; Brown, 2011).

Chopra and Marfurt (2005) review several major classification schemes of seismic attributes from the past four decades and provide their own. Liner et al. (2004) who subdivided seismic attributes into general, specific, and composite (or meta-attribute) categories. General attributes are applicable from one basin to another as they are based on well-defined physical or morphological parameters related to the geology seen in the seismic data. Specific attributes are not based on a common geological or physical principle, meaning that what is applicable in one basin may not necessarily be so in all basins. Composite attributes include those that display multiple attributes at a time, and those formed from combining the neural nets and geostatistics of a specific physical or geological variable.

Barnes (2016) categorises seismic attributes into geological, geophysical, and mathematical properties shown in Fig. 3.10 applied in a variety of different methods summarised in Table 3.2. A seismic attribute may however fall into more than category combining different filters. Geological and geophysical seismic attributes are the most useful as they are easier to quantify, interpret and relate to the geology, while mathematical attributes may lack significant geological importance. Numerous seismic attributes exist that can be applied on an interpreted horizon/surface, or on a full seismic volume using various software. Volumetric attributes may be applied from the onset of seismic interpretation while surface attributes (also known as horizon-based attributes) may only be applied once a stratigraphic horizon has been interpreted sufficiently (Brown, 2011). Seismic attributes used in this research are shown in boxes of Fig. 3.10 and discussed below.

Table 3.2 Methods used in the application of seismic attributes (Barnes, 2016).

Method	Description	Attributes
<i>Statistics</i>	Mathematical attributes usually represented as maps	Mean value, root mean square (RMS) amplitude, total energy, variance, smallest and largest value, no. of peaks, total energy, % above threshold
<i>Map computations</i>	Applied on interpreted seismic horizons to measure the difference in structural properties	Discontinuity, dip, azimuth, curvature, shaded relief
<i>Complex trace analysis</i>	Many attributes are derived from the differentiation, averaging and combination of the seismic data's amplitude and phase	Reflection strength, instantaneous phase, instantaneous frequency, bandwidth, amplitude change, dip, azimuth, curvature, parallelism, quality factor, thin-bed indicator
<i>Response attributes</i>	A further subset of complex trace attributes	Apparent polarity, response amplitude, response phase, response frequency, sweetness
<i>Correlation, semblance, principal component analysis</i>	Measure structural and stratigraphic attributes by comparing the resemblance of adjacent seismic traces	Discontinuity, dip, azimuth, curvature, parallelism
<i>Dip scanning, plane-wave destruction, gradient squared tensor</i>	Applies 3D derivatives in an averaging window	Dip, azimuth, curvature, continuity
<i>Spectral decomposition</i>	Geophysical attributes recording time-varying spectral properties	Frequency components, mean frequency, peak spectral frequency, bandwidth, tuning thickness
<i>Pattern recognition</i>	Applied to seismic waveforms and sets of attributes	Waveform maps, attribute classes or seismic facies
<i>Miscellaneous</i>	Measured through specific methods	Relative acoustic impedance, arc length, energy half-time, zero-crossing frequency, quality factor

3.3.2 Volumetric attributes

3.3.2.1 Data conditioning

Although seismic processing attempts to remove the effect of noise introduced during acquisition, seismic data may require more conditioning during interpretation to filter out unwanted artifacts. Noise and the presence of geological features (e.g., buried channels) may appear as low continuity regions usually indicative of faulting (Hale, 2013). Caution is required in seismic interpretation as these areas may be erroneously interpreted as a fault network. In this research the data were conditioned using the volumetric attribute of structural smoothing. Structural smoothing enhances the resolution (signal-to-noise ratio) of seismic data by using a Gaussian filter with mean and median filters to smooth the input signal (Randen, 2000).

3.3.2.2 Edge enhancement attributes

Edge-enhancement attributes are filters that identify sharp edge contrasts in seismic data indicative of discontinuities in the subsurface and are therefore structural attributes. Several edge-enhancement attributes are provided by interpretation software such as coherence, variance, chaos, semblance, entropy, and gradient magnitude (Hale, 2013). The focus in this research are the variance and chaos attributes. Variance uses a coherency analysis to measure the local variation of points in the seismic signal and, regardless of high or low amplitude regions, will give the same response for the same seismic signature (Silva et al., 2015). Chaos measures the lack of the seismic signal's organization through statistical analysis of the dip and azimuth orientations (Silva et al., 2015).

Edge-enhancement attributes are often used in the ant tracking workflow. Ant tracking, so called after the similar swarm intelligence behaviour pattern observed in ant colonies from nature (Silva et al., 2015), is a powerful algorithm used in fault interpretation. Ant colonies use trail pheromones to lead members of the same species towards a food source thus optimizing the search. In much the same way, virtual ants placed as seeds in a seismic volume use virtual pheromones to capture the trail of discontinuities in fault zones. Ant tracking enhances the fault networking system and may be used as the input for automatic fault extraction to produce fault patches. Many studies use different inputs in creating an ant tracked volume and may re-run the input edge-enhancement attributes (e.g., variance, chaos) multiple times depending on the interpreter's preference (cf. Silva et al., 2015; Qi et al., 2019; Mahlalela et al., 2021).

3.3.2.3 Relative acoustic impedance

The stratigraphic information (horizons) of seismic data may be enhanced using a variety of different attributes (Fig. 3.10). Relative acoustic impedance is one such volumetric attribute most effective in enhancing the seismic stratigraphy. Relative acoustic impedance is an impedance attribute applied on post-stack seismic data with the benefit of not requiring the input of wells, velocities, pre-stack seismic data or any other components (Barnes, 2016). Even though it is an easy attribute to generate, it must be used cautiously in seismic interpretation. This is because it is an approximation rather than the true estimate of the low frequency information and does not prove the removal of the seismic source wavelet which obscures the earth's reflectivity. Since the original seismic data are recoverable through differentiation (albeit with a slight error) and the attribute does not fragment the data, relative acoustic impedance may be regarded as more of a transformation (Barnes, 2016). It uses a recursive inversion algorithm whereby low frequencies are enhanced by high frequencies as the phase of the seismic trace

is rotated by 90°. For recursive inversion to be effective, seismic data must have high signal-to noise ratios, have a zero-phase and a broad bandwidth.

Relative acoustic impedance is derived from regular acoustic impedance (Z) which is defined by the two rock properties of density and compressional wave velocity (Barnes, 2016). Acoustic impedance is most valuable in inferring porosities and may be applied to datasets containing both seismic and well log data to create impedance logs through the process of inversion. High porosities reduce the density and compressional wave velocity of rocks. If pore spaces become infilled with gas rather than water or oil, the compressional wave velocity and resultant acoustic impedance drop significantly. Together these properties serve as direct hydrocarbon indicators. Distinguishing between economic and non-economic gas saturations is not possible, however. Impedance logs provide information on both low and high frequencies. High frequencies record stratigraphic detail and are recovered from seismic data, while low frequencies give absolute porosities from the background trend of impedance and are recovered from well data. If poststack seismic data alone are available, this background trend is non-existent, and the term “relative acoustic impedance” is more applicable.

3.3.2.4 Direct hydrocarbon indicators

Volumetric attributes used to identify and enhance natural gas/fluid flow features are known as direct hydrocarbon indicators. Direct hydrocarbon indicators of interest include the root mean square amplitude, sweetness, generalised spectral decomposition, and envelope. Relative acoustic impedance may also be considered as a direct hydrocarbon indicator as it is a measure of porosity (Barnes, 2016; Azevedo and Pereira, 2019). Direct hydrocarbon indicators highlight acoustic impedance contrasts in sandstone reservoirs with hydrocarbons appearing as bright, positive high amplitude anomalies (Koson et al., 2014).

The most widely used attribute for the detection of hydrocarbons is envelope (also known as magnitude, reflection strength, or instantaneous amplitude). Envelope is the total instantaneous energy of the complex trace independent of the phase (Brown, 2011). Closely correlated to envelope is the sweetness volumetric attribute often used to identify features that change the overall signature of energy in the seismic data such as coarse-grained sandstone reservoirs (Koson et al., 2014). The root mean square amplitude (iterative), a smoother scaled estimation of envelope, computes the root mean square iteratively over instantaneous trace samples in a vertical window specified by the user (Koson et al., 2014). In seismic data high root mean square amplitudes possibly represent coarse-grained facies (e.g., Maselli et al., 2019). Generalised spectral decomposition involves the deconstruction of the seismic data back to its original waveforms and tuning the seismic data to specific frequencies (Chopra and Marfurt, 2005; Koson et al., 2014). The fine tuning of frequencies enables generalised spectral decomposition to detection subtle variations in flow barriers or lithology.

3.3.3 Surface attributes

Surface attributes provide more information on the stratigraphic and structural elements of a basin and are therefore highly effective in fault mapping and understanding reservoir characteristics (Cox et al., 2020). Different seismic interpretation software may offer different surface attributes, and as such those outlined in this section are specific to the interpretation software used in the research. Prior to creating a geological surface (and hence prior to surface attributes) a confidence classification map may be run on that picked horizon. The operation shows the

degree of confidence in horizon picks by combining the histogram equalization of the root mean square amplitude (thick slice volume amplitude) and the surface stability index. Once sufficient and satisfactory interpretation has taken place on an interpreted horizon, surface attributes may be applied. Surface smoothing, anomaly identifier, influential data, and edge detection surface attributes are briefly explained below. The advantages and specifics of each surface attribute used are explained further in [Chapter 4](#)'s Methodology.

Surface smoothing reduces inconsistencies produced from picking by levelling out any anomalous points. It is most useful in areas that have low signal-to-noise ratios that required manual interpretation over auto-tracking. The anomaly identifier and influential data attributes are very similar; the former highlights points along the surface that are geometrically different from their surrounding area, and the latter highlights areas of rapid 3D geometric change. Edge detection is a surface attribute that combines dip and azimuth properties to identify sharp boundaries (edges) along a surface ([Randen et al., 2000](#)). Edge detection is used to enhance discontinuities by operating like a smoothing filter, but with the opposite effect where edges are sharpened regardless of their orientation ([Brown, 2011](#)).

4 Methodology

The study area is a portion of a 3D seismic survey owned by Shell (a global group of energy and petrochemical companies) called OB123D-01 in the deep-water Orange Basin (Figs. 1.1 and 4.1). Seismic data acquisition and processing were conducted by the Dolphin Geophysical Polar Duchess and the Netherlands Global Processing Team, respectively, while this research dealt solely with seismic interpretation. The seismic data were obtained from the Petroleum Agency of South Africa's database in the processed form. The first section summarises the acquisition and processing steps given in Kramer and Heck's (2013) Orange Basin Shell report. From there on (Chapter 4.2 onwards) the steps used in seismic data interpretation employed in this research are explained in detail.

Table 4.1 Acquisition parameters of the Orange Basin's seismic survey (Kramer and Heck, 2014).

Recording	
<i>Recording format</i>	SEG-D
<i>Record length</i>	7168 ms
<i>Recording filter delay</i>	None
<i>Sample rate</i>	2 ms
<i>Low cut filter hydrophone, slope</i>	4.4 Hz, 12 dB / octave
<i>Low cut filter geophone, slope</i>	Not applicable
<i>High cut filter both, slope</i>	214 Hz, 341 dB / octave
Source	
<i>Source type</i>	Dual source
<i>Number of source arrays</i>	2
<i>Number of sub-arrays</i>	3
<i>Shot point interval</i>	25 m (flip/flop)
<i>Array separation</i>	100 m
<i>Array length</i>	15 m
<i>Source volume</i>	4100 cu in
<i>Number of airguns / arrays</i>	30
<i>Operating pressure</i>	2000 psi
<i>Source depth</i>	8 m
<i>Nominal common midpoint fold</i>	80
Sercel SSAS Sentinel, Sercel Seal-428	
<i>Number of streamers</i>	8
<i>Group interval</i>	12.5 m
<i>Group length</i>	12.5 m
<i>Number of hydrophones / groups</i>	1
<i>Number of geophones / groups</i>	1
<i>Streamer length</i>	7950 m
<i>Streamer separation</i>	200 m
<i>Number of groups / streamers</i>	636
<i>Streamer depth</i>	10–15 m linear slant
<i>Nearest offset</i>	222 m

4.1 Seismic acquisition and processing

The 3D reflection seismic survey was conducted by Dolphin Geophysical Polar Duchess between the 25th of October 2012 and the 22nd of February 2013 in the deep-water Orange Basin using conventional streamers with sparse geometry (Kramer and Heck, 2014). The seismic data covered a total area of ~8200 km² (Figs. 1.1 and

5.1). The survey was orientated ~NNW to SSE with an azimuth of 36.6° anticlockwise using the central meridian 15° map projection in UTM Zone 33S. Table 4.1 lists the acquisition parameters used in the survey.

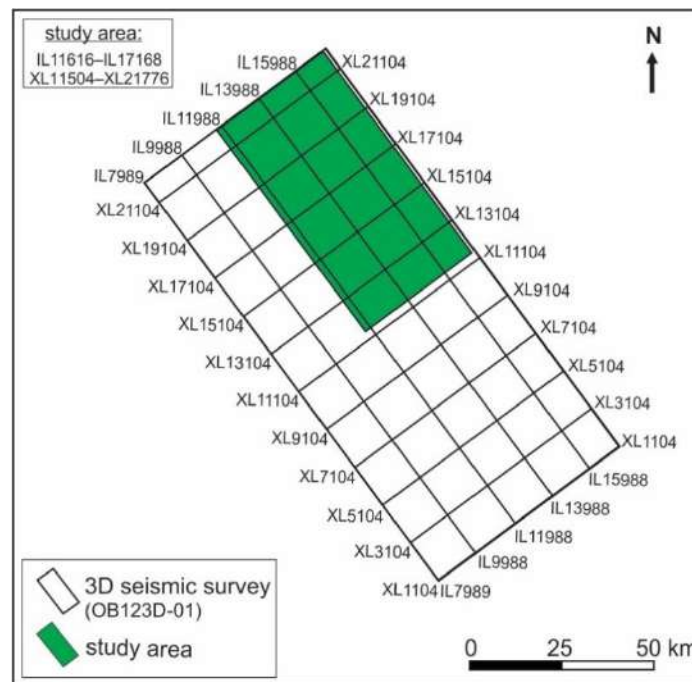


Figure 4.1 Map showing seismic survey OB123D-01 and the location of this study's seismic data within it (refer to Fig. 1.1 for the regional setting).

The raw data were first pre-processed on board by the Dolphin Geophysical team from field tape. Table 4.2 shows the summarised workflow. More details of these processing steps may be found in Dolphin Geophysical Orange Basin 3D Pre-stack Time Migration report (Kramer and Heck, 2014). Using their proprietary SIPMAP software, the Global Processing team (Rijswijk, Netherlands) commenced with full seismic processing. Table 4.3 shows the full seismic processing workflow which involved Kirchhoff pre-stack depth migration following 3D surface-related multiple elimination. The initial acquisition grid was 6.25 x 50 m for the inline and crossline, respectively. The final grid size following pre-stack depth migration was 25 x 25 m for the crossline and inline cells, respectively. The bin grid schematic and definitions are shown Fig. 4.2 and Table 4.4.

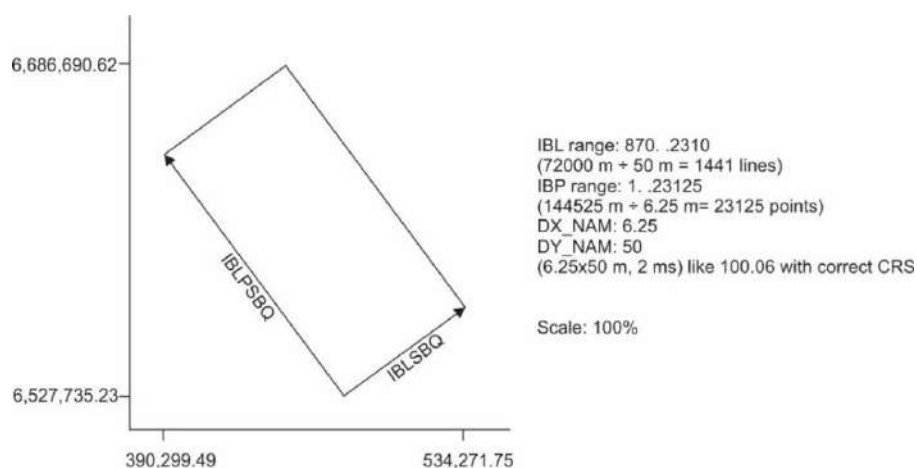


Figure 4.2 Survey orientation and bin grid schematic used for 3D processing (Kramer and Heck, 2014).

Table 4.2 Dolphin Geophysical pre-processing sequence (Kramer and Heck, 2014).

Dolphin processing centre	
1	Input SEG-D, nav-merge and apply trace edits and interpolation
2	Designature and zero-phasing
3	Low-cut 2.5Hz, 18dB/octave
4	Anti-alias (100Hz)
5	Resample 2 to 4ms
6	Seismic interference removal on common channels, FX method
7	Shot and channel domain FX swell noise removal 0-30Hz
8	Tau-P linear noise removal
9	K-filter and alternate trace drop
10	Gun and cable static (using actual depths and average water velocity)
11	2D surface-related multiple elimination
12	Velocity picking at 2x2km grid
13	Radon demultiple (common midpoint domain)
14	Dip moveout
15	Velocity analysis on 1x1 grid
16	Output of dip moveout gathers (last processing step on board)
17	Receive data (dip moveout gathers)
18	Restore data
19	Fold quality control
20	DMA (a residual demultiple process with no clear SIPMAP version)
21	Inner and outer mutes. Inner mute starts at seabedx2, and is 1 km at Tmax
22	Partial Stack (discard re-shoot lines)
23	Stack
24	Interpolation to 12.5 (inline) x 25 (xline) and a 25x25 stacked volume
25	FX deconvolution denoising
26	Kirchhoff PTM (4km operator)
27	Output to SEG-Y (raw)
28	Scaling and filtering
29	Muting/tapering
30	Output to SEG-Y (filtered)

4.2 Seismic interpretation and strategy

The ~1 800 km² study area's seismic dataset was acquired between water depths of 1 000 and 2 000 mbsl along the South African continental slope (Fig. 1.1). The volume of seismic data used in this research was interpreted using the Petrel software from Schlumberger (Chapters 6 and 7) then later compared with a convolutional neural network (CNN) in deep-learning called fault-net (Chapter 8). The seismic interpretation workflow used is shown in Fig. 4.3 involving (1) loading seismic data, (2) applying volume-based attributes, (3) horizon mapping, (4) surface attributes, (5) fault mapping, (6) velocity modelling and depth conversion, then finally (7) structural modelling. All the processes and steps used for seismic interpretation are found within the seismic interpretation and structural modelling tabs of Petrel.

Table 4.3 Seismic processing workflow applied to the deep-water survey (Kramer and Heck, 2014).

Dolphin Geophysical Polar Duchess team	
1	Conversion from SEG-D and navigation merge
2	Output to SEG-Y
Global Processing team	
3	Conversion from SEG-Y to Shell's proprietary software (SIPMAP) format
4	Spherical spreading correction
5	Despike
6	Swell noise attenuation
7	Resample to 4 ms
8	Denoise
9	Linear noise attenuation
10	Deghosting
11	Seismic interference attenuation
12	Zero phasing
13	2D surface-related multiple elimination prediction
14	3D surface-related multiple elimination prediction
15	LSQ matched subtraction
16	Multiplicity scaling for Kirchhoff migration
17	Phase deabsorption
18	RMO analysis
19	RMO velocity model inversion and anisotropy scanning
20	Pre-migration signal enhancement
21	Kirchhoff pre-stack time migration
22	Residual radon demultiplex
23	Amplitude deabsorption
24	RMO correction
25	(Angle) stack
26	Time variant scaling (additional output volumes)
27	Archiving

Table 4.4 Bin grid definitions.

Inline/track	Crossline/bin	Easting/x	Northing/y
320	932	478892.85	6532018.86
23040	932	394228.92	6646018.94
320	3492	530273.17	6570177.25
23040	3492	445609.23	6684177.34

4.2.1 Seismic interpretation strategy

The seismic volume was interpreted using the seismic-to-sequence stratigraphic approach originally proposed by Mitchum et al. (1977) explained in Chapter 3.2. Nine stratigraphic surfaces (or markers) were identified in this research based on their continuity and dominant high-amplitude reflections using the classification of Catuneanu (2006) (Table 3.1). These stratigraphic markers are the Mesozoic's Late Cretaceous (1) Albian, (2) Turonian, (3) Santonian, (4) early Campanian, (5) late Campanian, and (6) Maastrichtian surfaces; and the Cenozoic's (7) Oligocene and (8) Miocene surfaces, together with the (9) seafloor. Surface names were assigned according to their approximate geological ages which were derived from the comparison of seismic sections in previous Orange Basin studies (some with published well data) including Brown et al. (1995), Paton et al. (2008), de Vera et al. (2010), Kuhlmann et al. (2010), Hartwig et al. (2012), Dalton et al. (2017), and Baby et al. (2018). While the

terminology for both stratigraphic markers and sequences may vary across different studies, the assigned ages for each generally exhibit consistency.

The Late Cretaceous surfaces correspond to the 14At1, 15At1, 16Dt1, 17At1, 18At1, 22At1 (respectively) stratigraphic intervals recognised throughout the SW African margin (Figs. 2.4 and 2.5; Brown et al., 1995; PASA, 2017). The Oligocene and Miocene stratigraphic surfaces are recognised in Baby et al. (2018). All seismic interpretations were done in the time domain as the study area contained no well logs at the present time of research to accurately tie the stratigraphic information to proper geological times. To estimate the rough thickness of seismic sequences, however, a generalised depth conversion was performed, utilizing average interval velocities derived from well logs obtained in the shallower areas of the Orange Basin, as employed in Kuhlmann et al.'s (2010) study (see Chapter 4.8).

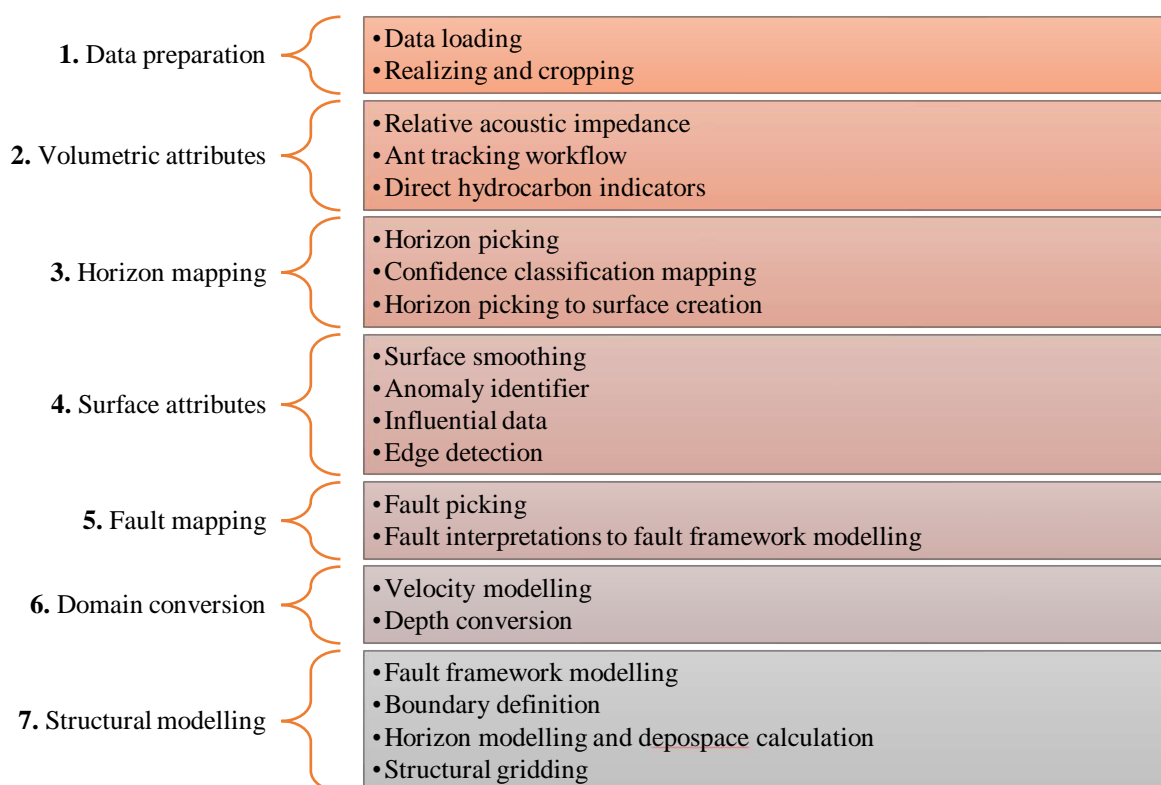


Figure 4.3 Petrel seismic interpretation workflow.

4.2.2 Seismic resolution limit

The Orange Basin has ~20 Hz dominant frequency and a 2 400 m/s average velocity (cf. Kuhlmann et al., 2010; Scarselli et al., 2016). According to Eq. 3.2, the vertical seismic resolution limit is 30 m and 60 m for the $\frac{1}{4}$ and $\frac{1}{2}$ dominant wavelength criteria, respectively (Yilmaz, 2001) for a 120 m wavelength. For migrated, high-resolution seismic data obtained from the marine environment, the horizontal resolution may be as high as half the wavelength ($\lambda/2$) (Herron, 2011). In this research, the horizontal resolution limit is therefore 60 m, or equal to the original inline and crossline bin sizes (Dondurur, 2018). Features in the seismic data smaller these two resolution limits would not be effectively resolved without the use of seismic attributes.

4.3 Data preparation

4.3.1 Data loading

The Orange Basin's 3D seismic survey (OB123D-01) was imported as a SEG-Y file using preset parameters and the WGS_1984_UTM_ZONE_33S co-ordinate reference system (CRS).

4.3.2 Realizing and cropping

A time/depth slice is only created once the seismic volume has been "realized" in Petrel. Realizing creates a physical copy of the dataset with the z-component time slice upon which all seismic attribute applications and interpretations can be efficiently done. Since the seismic volume was too large (~8 200 km²) to be effectively managed by the software and workstation, a manageable portion of interest (~1 800 km²) from the full seismic survey was cropped out (Fig. 4.1). Cropping is a valuable tool for interpreting large sets of seismic data as large datasets require a lot of computational power, memory, and a long run-time to compute processes such as the application of attributes. The cropped volume was exported in SEG-Y format and used to create a new project which forms the basis of the present research. Fig. 3.5 is a small portion of the ~1 800 km² dataset illustrating the display of seismic data in a 3D and 2D interpretation window.

4.4 Volumetric attributes

Volumetric attributes were applied in the initial stage of seismic interpretation to aid horizon and fault mapping (Fig. 4.3). The volumetric attributes applied include (1) relative acoustic impedance to enhance stratigraphic features, (2) structural smoothing for preconditioning, (3) variance and chaos edge-enhancement attributes, and (4) direct hydrocarbon indicator attributes of envelope, sweetness, root mean square amplitude (iterative), and generalised spectral decomposition. Algorithms were first run on a smaller portion of the seismic volume to test the most suitable parameters to be used on the full seismic dataset. This is because the application of attributes is a time-consuming process requiring a lot of disc memory.

4.4.1 Relative acoustic impedance

Relative acoustic impedance removes random long wavelength trends in the seismic data by integrating the seismic trace then applying a high-pass Butterworth filter. Relative acoustic impedance was most useful in enhancing the continuity of thin beds (horizons) that otherwise look completely discontinuous in the original seismic volume. Compared to the original seismic volume (Fig. 4.4a), low frequencies in the relative acoustic impedance volume are more consistent giving the data an enhanced look with boosted amplitudes (Fig. 4.4b). The only parameter required in generating a relative acoustic impedance volume is a low-cut frequency on the original seismic volume which was set at 10.0 in this research. Overall, the enhanced relative acoustic impedance volume made it easier to identify unconformity surfaces and delineate structures particularly in areas where the resolution was too low.

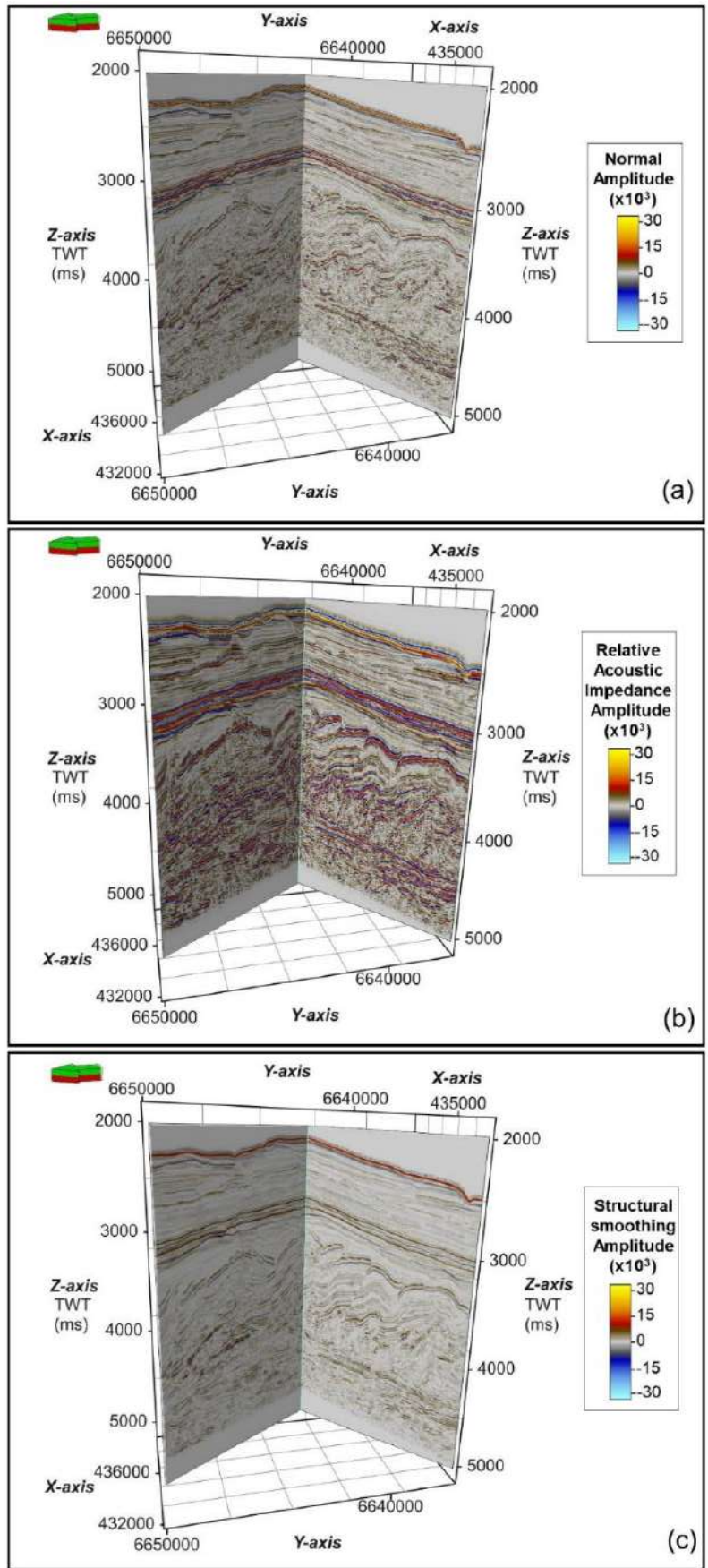


Figure 4.4 3D windows showing the application of volumetric attributes comparing (a) the normal seismic volume, (b) the relative acoustic impedance volume, and (c) the structurally smoothed volume. VE= 5.

4.4.2 Structural smoothing

Prior to the application of most volumetric attributes, the seismic data were conditioned through structural smoothing (Fig. 4.4c). Structural smoothing combines median and mean filters to improve the signal-to-noise ratio of the seismic data. It is also a structural attribute that was used at the start of the ant tracking workflow (Fig. 4.5) to correctly enhance discontinuities without the effect of noise. Parameters that need defining include the type of filter to be used, and size of the orientation windows (sigma X, Y and Z). The “dip-guided with edge enhancement filter” was used in this research to visually enhance edges. Here, two half filters are run: (1) chaos is first run on both, then (2) a Gaussian filter is applied to the filter with the least chaos. Sigma X, Y, and Z were all 1.5.

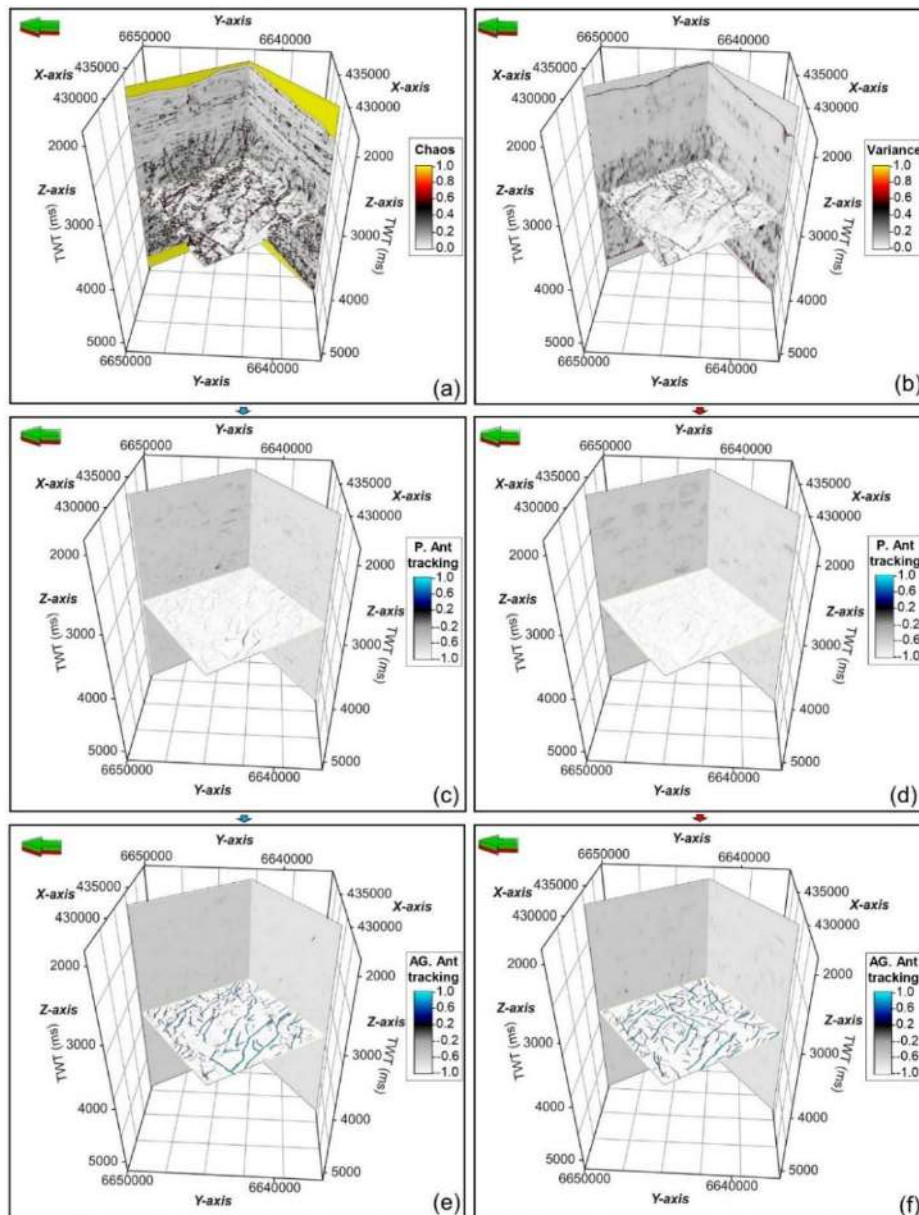


Figure 4.5 3D windows comparing the chaos (a) and variance (b) input volumes used for ant tracking. (c) is the passive ant tracked volume produced using chaos as input. (d) is the passive ant tracked volume produced using variance as input. (e) is the aggressive ant tracked volume produced from (c). (f) is the aggressive ant tracked volume produced from (d). VE= 5.

4.4.3 Variance and chaos

Variance and chaos are edge-enhancement attributes typically used in the ant tracking workflow (Fig. 4.5). In this research the variance and chaos attributes were compared to determine which volumetric attribute enhanced faults better (Fig. 4.5ab) and created a better ant tracked volume (Fig. 4.5cdef). Table 4.5 shows the parameters used in creating a variance volume using the structurally smoothed volume as input. The only parameter required for chaos was sigma X, Y, and Z (size of orientation windows); all of which were set at 1.5. Both large- and small-scale discontinuities are visible in the chaos volume from faults to fractures and other stratigraphic features (Fig. 4.5a). Variance, on the other hand, only enhanced larger-scale discontinuities (faults) and thus appears less “chaotic” (Fig. 4.5b).

Table 4.5 Parameters used for variance in the study area.

Variance parameters	
<i>Inline range (filter length)</i>	3
<i>Crossline range (filter length)</i>	3
<i>Vertical smoothing (in samples)</i>	25
<i>Dip correction</i>	On
<i>Scale of inline</i>	1.5
<i>Range of crossline</i>	1.5
<i>Vertical scale</i>	1.5
<i>Plane confidence threshold</i>	0.6
<i>Dip-guided smoothing</i>	Off

Once the data were conditioned and pre-processed, passive ant tracking was run for both the inputted variance and chaos volumes (Fig. 4.5cd). Aggressive ant tracking was then applied upon the previously generated passive ant tracked cube (Fig. 4.5ef). Both passive and aggressive ant tracking use system-generated parameters shown in Table 4.5. Undesirable dips and azimuths may be filtered out of the ant tracked volume using the stereonet plot. Overall, ant tracking is seen better on the time slice than on the vertical inline and crossline sections (Fig. 4.5cdef). Since the quality of reflection seismic data in this research is high, not much conditioning and pre-processing was required. Variance on its own, without ant tracking, was enough to enhance the large, regional-scale discontinuities necessary for the research in plan section.

Table 4.6 Passive and aggressive ant tracking parameters.

	Passive ant tracking	Aggressive ant tracking
<i>Initial ant boundary</i>	7	5
<i>Ant track deviation</i>	2	2
<i>Ant step size</i>	3	3
<i>Illegal steps allowed</i>	1	2
<i>Legal steps required</i>	3	2
<i>Stop criteria (%)</i>	5	10

4.4.4 Direct hydrocarbon indicators

Additional volumetric attributes were applied at different points within the horizon and fault mapping workflow (Fig. 4.3) to identify and enhance natural gas/fluid flow features. These are the envelope, sweetness, root mean square amplitude (iterative), and generalised spectral decomposition volumetric attributes (Fig. 4.6). Natural gas/

fluid appears as high amplitude reflections or bright spots in these seismic volumes. The only parameter required in the computation of envelope and sweetness volumetric attributes (Fig. 4.6ab) was the length of the Hilbert transform (also called quadrature amplitude) filter window which was set at 33 for both. The parameters used in the calculation of the root mean square amplitude (iterative) are a vertical window length of 11 (no. of samples) with an iteration of 1. Generalised spectral decomposition was calculated using the correlation algorithm which measures the similarity between the constructed wavelet and each trace with (only positive correlations are kept). The parameters used for the generalised spectral decomposition volumetric attribute are shown in Table 4.7.

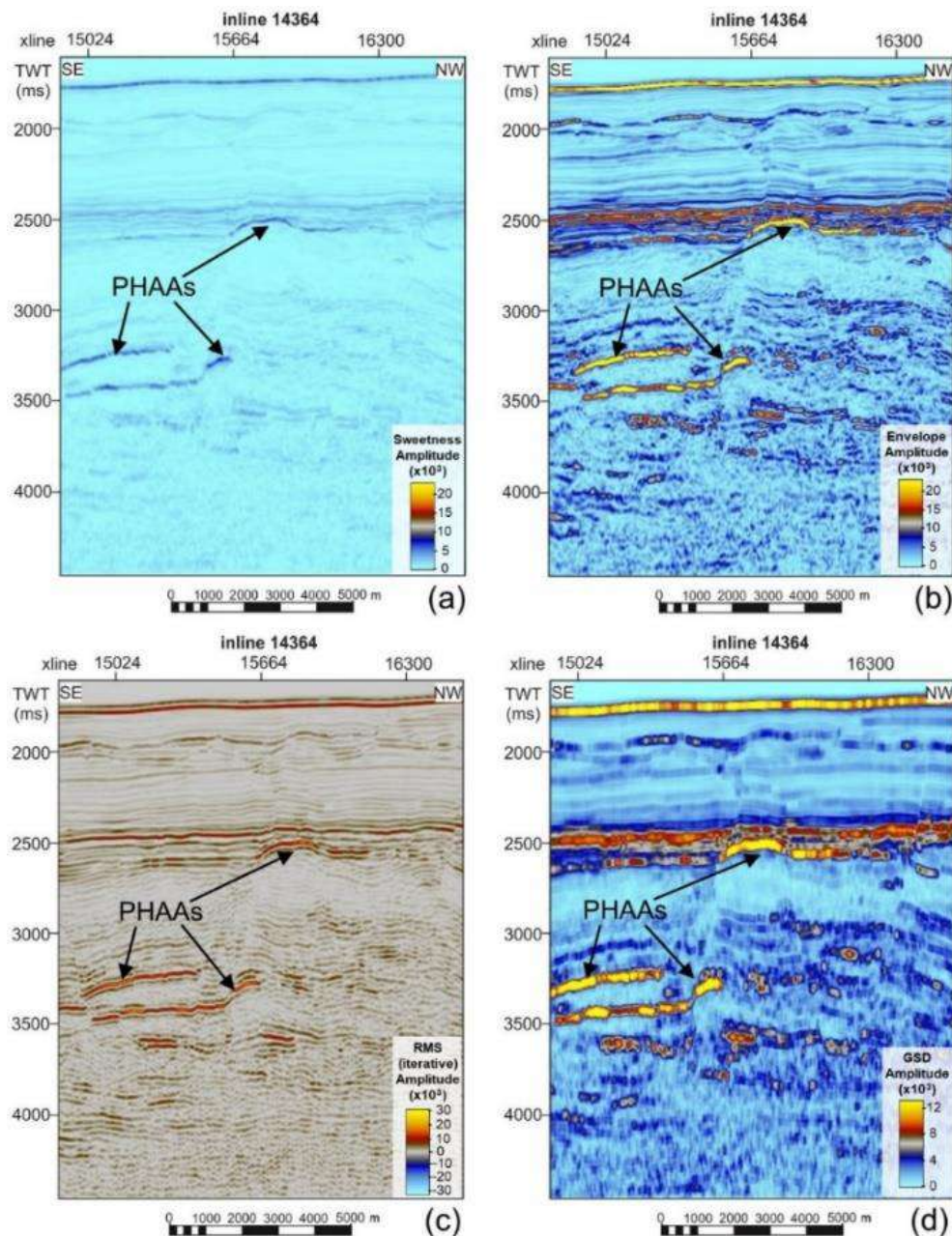


Figure 4.6 Volumetric attributes used as direct hydrocarbon indicators. An inline section of a) sweetness, b) envelope, c) iterative root mean square amplitude, and d) generalised spectral decomposition indicating the presence of hydrocarbons as bright, positive high amplitude anomalies (PHAAs) (Maduna et al., 2023a). VE= 5.

Table 4.7 Parameters used in generalised spectral decomposition.

Generalised Spectral Decomposition Parameters	
<i>Algorithm</i>	correlation
<i>Frequency</i>	30
<i>No. of cycles</i>	2.0
<i>Phase (in degrees)</i>	90
<i>Max filter length</i>	0.5
<i>Method of computation</i>	Sample by sample calculation

4.5 Horizon mapping

Nine stratigraphic surfaces of interest were “picked” to create horizon interpretations. The steps used in horizon interpretation to surface creation for 3D modelling is explained in the following section using the Santonian stratigraphic surface as an example for each step. [Appendix B](#) is an overall compilation of the (a) picked horizon, (b) confidence classification map, (c) influential data, (d) dip angle, (e) dip azimuth, and (f) edge detection operations applied to the Albian (i), early Campanian (ii), late Campanian (iv), Maastrichtian (v), Oligocene (vi), Miocene (vii), and seafloor (viii) surfaces.

4.5.1 Picking horizons

Multiple window views may be opened and worked on at the same time to correctly interpret the seismic section ([Fig. 3.5](#)). This helps guide real-time horizon and fault picking without the constant need of changing through different views. A combination of auto-tracking and manual interpretation was used to pick surfaces of interest in the seismic volume ([Fig. 4.7a](#)). To validate the picked interpretations, the confidence classification horizon-based attribute was applied to each horizon ([Fig. 4.7b](#)) prior to making a surface for use in modelling ([Fig. 4.8](#)). Since the quality of most of the seismic volume is high, seeded 2D and 3D auto-tracking was used mostly. In areas with low signal-to-noise ratios where auto-tracking was no longer possible (e.g., [Fig 4.7b](#)), 2D manual interpretation was done using a cross-hatched technique ([Fig. 4.7a](#)).

4.5.2 Confidence classification mapping

Prior to making a surface from a horizon interpretation, a confidence classification horizon-based attribute was applied ([Fig. 4.7b](#)). Red values correspond to high levels of confidence, green to intermediate values of confidence, and blue to low values of confidence in horizon picking. [Fig. 4.7b](#) shows that low confidence regions were often areas where the signal-to-noise ratio of the horizon was low, or where the topography was unstable due to faulting. If a horizon was mapped with a low degree of confidence (blue) mostly, it was re-picked to get the optimum confidence level (green and mostly red). The parameters used in creating a confidence classification map are tabulated in [Table 4.8](#).

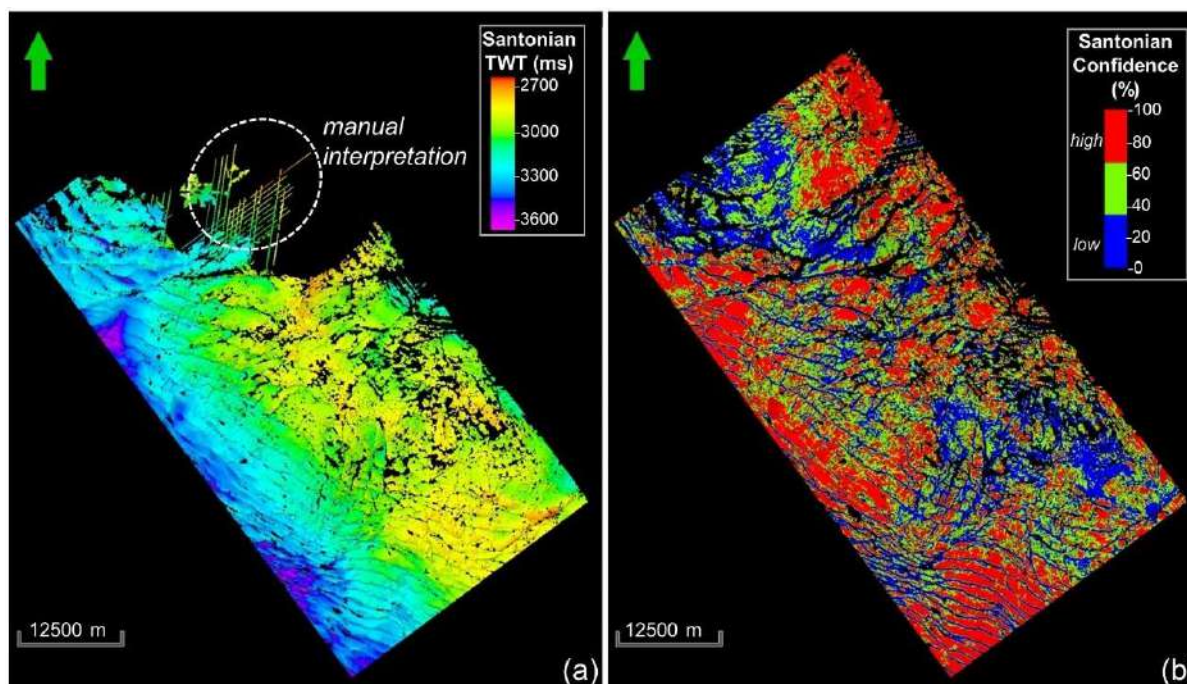


Figure 4.7 Horizon mapping workflow shown on the Santonian horizon. (a) 3D auto-tracking, and 2D manual interpretation using a crosshatch technique in areas with low signal-to-noise ratios; (b) validation of horizon interpretation using the confidence classification map with red, green, and blue showing high, intermediate, and low levels of confidence, respectively; and c) the resultant surface created from the horizon interpretation.

Table 4.8 The parameters used in creating a confidence classification map and the description of each.

Parameters		Description
<i>Combined confidence map</i>	Combined method	Combines the calculation of the surface stability index and the thick slice volume amplitude
<i>Stability window radius</i>	3	The radius of the moving window that is used to define points of the horizon interpretation that are included in the interpretation
<i>No. of nodes</i>	20	The size of the surface that is created from the data used to estimate the confidence map
<i>Smooth surface</i>	Yes	The surface that is used is smoothed prior to computation
<i>Seismic cube</i>	Uninterpreted seismic volume (TWT)	The thick slice volume amplitude method requires the seismic cube the horizon interpretation was picked on
<i>Sample window</i>	5	How many values above and below the pick are used in the computation of the root mean square

4.5.3 Surface creation

The picked horizons were made into geological surfaces (Fig. 4.8). If an interpreted horizon was changed, the corresponding surface could also be edited by updating the input data and re-running the surface. A limitation in horizon mapping is the software's inability to pick overturned surfaces and hence a gain of ground caused by low angle thrust faulting. This was a major limitation in the current research since about half the study area is dominated by large-scale thrust faulting (in the DWFTB system's compressional domain; see Chapter 6).

The interpolation or gridding algorithm used for all surfaces was convergent (Fig. 4.8). The trend extrapolation method used preserved the trend of the data in extrapolated areas. Convergent interpolation is used for both

geophysical (seismic) and geological data (well logs). It is the most common surface gridding and smoothing algorithm as it is computed fast and requires minimal input data and parameters to be defined. It can therefore work with just seismic data alone if the data quality is good. Key to its performance is that data do not need searching or sorting, as in other traditional methods. It is a control point-orientated algorithm built in stages with each iteration adding more resolution upon the previous surface derivative.

The convergent interpolation algorithm is illustrated in Fig. 4.8a showing four (4) iterations. Each iteration is run with a factor resolution change of 2 starting with an initial coarse grid (1) and finishing with a smooth grid, high in resolution (4). The red points show the initial input data, and the areas beyond them are additional nodes added to the geometry. The edges of the created surface (4) are shown to follow the implied trend given by the initial input data points. There are three sequential steps in each iteration of the algorithm: (1) refine, (2) snap, and (3) smooth. Refining changes the grid resolution, snapping grids or re-grids the data, and smoothing minimizes the grid curvature using a constrained biharmonic operator.

In the geometry of the output surface the position and size of the grid created were automatically obtained from the inputted horizon interpretation. The size of the grid cells in the X and Y directions were both set at increments of 50. A boundary may be created around the input data using a convex spline. The specific number of nodes to be extended by from the input data may be defined. In this research, the number of nodes applied to each horizon was extended by 3 nodes. An example of a created surface (Santonian) is shown in Fig. 4.9b after defining all parameters used in convergent interpolation and the geometry.

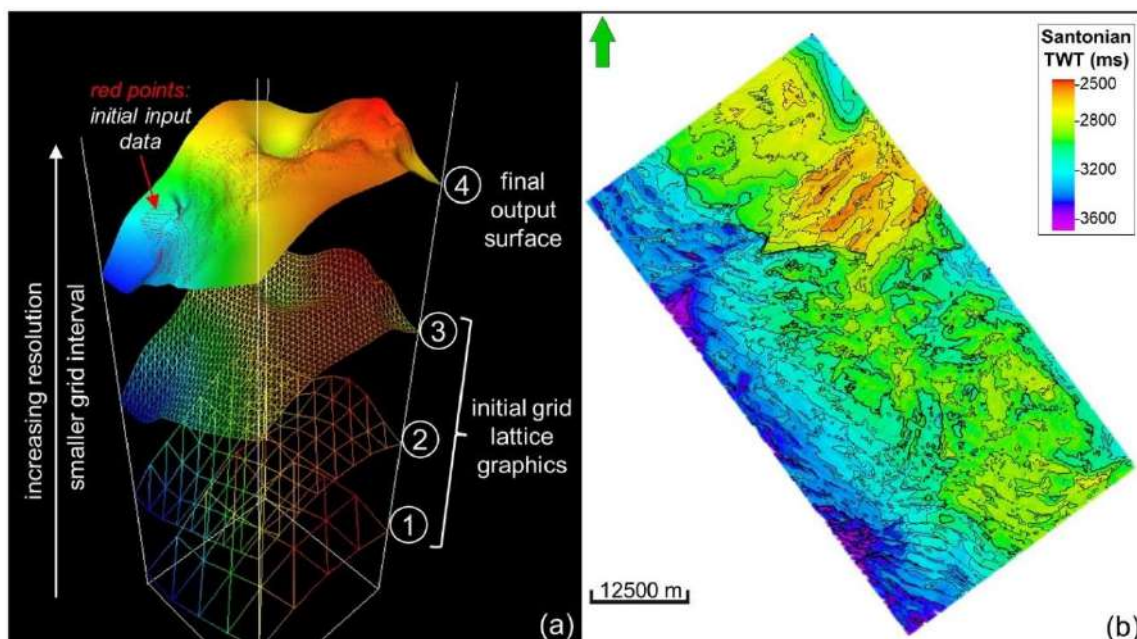


Figure 4.8 Surface creation using the convergent interpolation algorithm illustrated in (a) showing four iterations which increase in resolution, and (b) showing the Santonian horizon created through convergent interpolation after specifying the geometry.

4.6 Surface attributes

Surface attributes were applied once sufficient horizon interpretation was done to understand the reservoir characteristics and fault framework of the deep-water Orange Basin study. The surface attributes applied include

surface smoothing, anomaly identifier, influential data, and edge detection explained below together with their parameters.

4.6.1 Surface smoothing

Following surface creation, the surface smoothing structural operation was applied on all surfaces. Depending on the level smoothing required for each surface, the number of iterations (passes) run were different between each. Low iterations of 2 were applied to all surfaces, except the Albanian surface at depth on which 4 iterations were run. The rest of the parameters used in surface smoothing are tabulated in [Table 4.9](#).

Table 4.9 Surface smoothing parameters.

Parameters		Description
<i>Region half-width (I direction)</i>	2	The radius in surface nodes over which smoothing is applied
<i>Region half-width (J direction)</i>	2	The radius in surface nodes over which smoothing is applied
<i>Averaging method</i>	Combo smooth	Applies a median smooth followed by a mean smooth upon the median smooth
<i>Boundary treatment</i>	Smooth edges	Smoothing is extended across the edge of the boundary

4.6.2 Anomaly identifier and influential data

The anomaly identifier and influential data attributes highlight points and areas that are geometrically very different to their surroundings in 3D. Both attributes create a property on the data with high positive (red) and corresponding negative (blue) values implying large variations in geometry. Since these two attributes are similar, they share the same parameters. The parameters used in this research are tabulated in [Table 4.10](#).

Table 4.10 Anomaly identifier and influential data parameters.

Parameters		Description
<i>Search region</i>	4	Distance in cell nodes that the search radius is applied over
<i>Horizon equalization</i>	Yes	It stretches the data to provide an even range in the results. It removes the effect of end-member points within the data and helps identify subtle variations in the data
<i>Clamp to P5 and P95 values</i>	Yes	Values below the 5th percentile value or above the 95th percentile value will be reset to the 5th and 95th percentile values, respectively. The dataset is less skewed towards the extreme end-member values.

In this research, unlike anomaly identifier which appears slightly noisy ([Fig. 4.9a](#)), influential data ([Fig. 4.9b](#)) is more effective in highlighting regional-scale variations rather than local-scale variations in geometry. In [Fig. 4.9b](#) the influential data attribute is shown to enhance areas with a great magnitude of displacement between the hanging wall and footwall portions of the Santonian surface; the kilometre-scale, NE-SW trending faults spanning the south and west of the study area are well enhanced. Since influential data creates a cleaner output surface compared to the similar anomaly identifier attribute, it was used on all surfaces to correctly interpret the regional-scale fault framework.

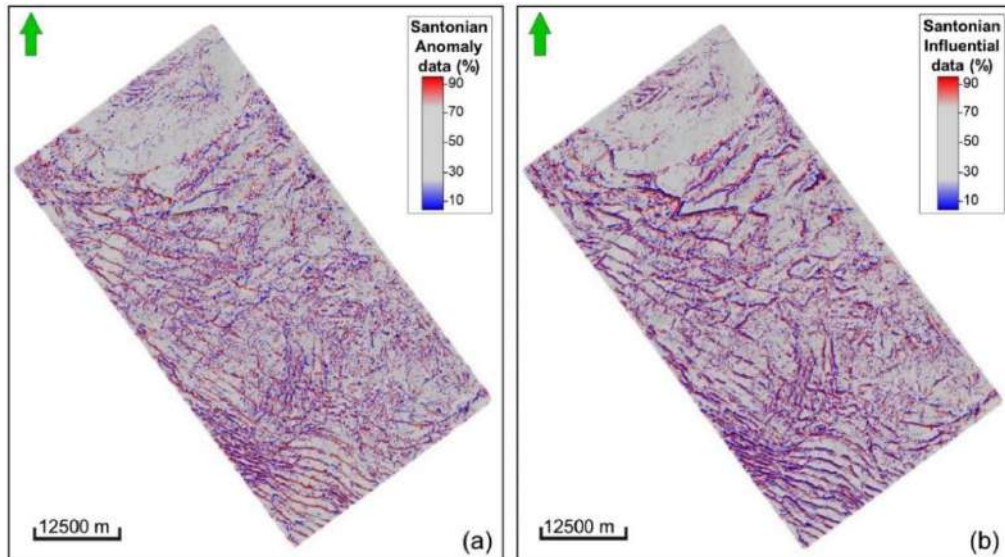


Figure 4.9 Comparison of the (a) anomaly identifier attribute highlighting all local variations, and the (b) influential data attribute highlighting larger, geometric variations in geometry on the Santonian surface.

4.6.3 Edge detection

Fig. 4.10 shows the dip and dip azimuth applied to the Santonian surface. Dip (Fig. 4.10a) emphasizes faults well but reveals minimum information on the rest of the surface. Dip azimuth (Fig. 4.10b) shows a wide range in the direction the surface is dipping, however, distinguishing individual faults is difficult. Edge detection, combining both dip and dip azimuth, enhanced discontinuities on each surface. The only parameter required for edge detection was whether to pre-smooth or not pre-smooth the data before the operation is run. In this research, all surfaces were pre-smoothed using a combination of median followed by a mean smoothing filter (Fig.4.11).

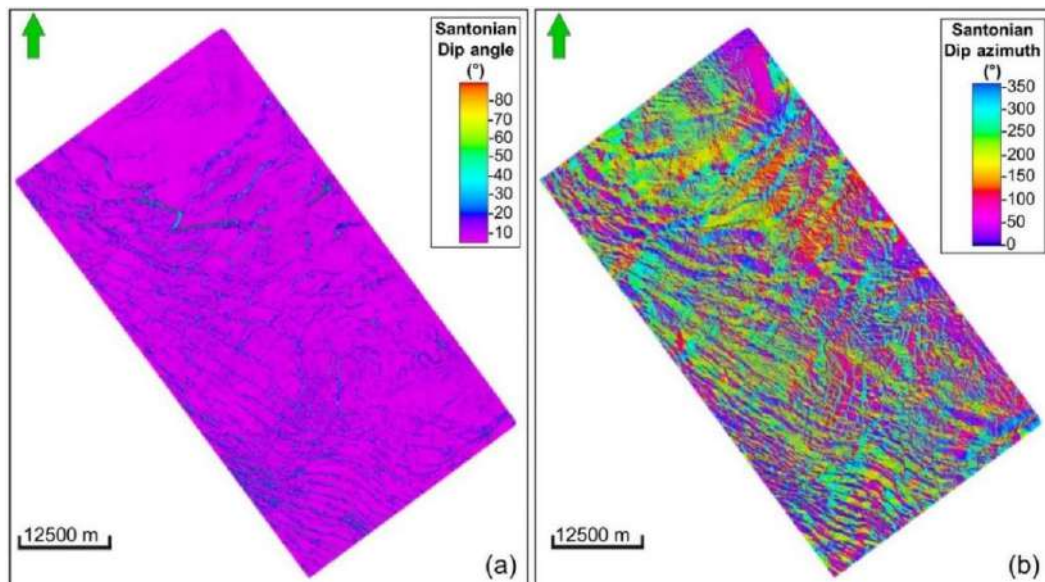


Figure 4.10 The dip angle (a) and dip azimuth (b) computed on the Santonian surface. High dip angles (a) are faulted areas on the surface. Dip directions (b) are variable across the surface, however, the primary directions are NE and SW.

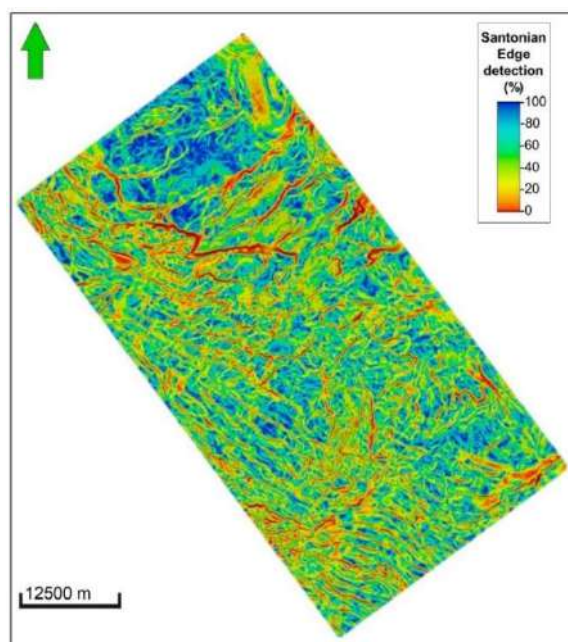


Figure 4.11 Edge detection attribute applied on the Santonian surface. Areas where the surface is faulted appear as red and orange, between 0–10 %.

4.7 Fault mapping

To understand the regional structural framework of the study area, only the most extensive and prominent faults were mapped out belonging to a particular network or system (Fig. 4.12a; see Chapter 6). Besides the observation of upthrown and downthrown blocks, evidence of fault displacement was implied when auto-tracking abruptly stopped along the chosen reflection being picked. The most favourable edge-enhancement attribute used in fault mapping was variance (Figs. 4.5b and 4.12bc). Although all surface attributes are structural operations, influential data was most advantageous at enhancing discontinuities for fault mapping (Fig. 4.9b).

4.7.1 Fault interpretations

Fault interpretations are created in like manner as horizon interpretations, drawn as vertical lines rather than horizontal picks on a vertical seismic section (Fig. 4.12a). Fault interpretations were digitised in segments along a seismic section to form the entire length of a fault. Caution is required when picking; choosing the correct seismic section for interpretation is vital in ensuring the true extent of a fault is mapped out. If the seismic section was orientated parallel or near parallel the trend of a fault, the fault trace was poorly, if at all, resolvable. Seismic sections therefore needed to be orientated perpendicular or normal to the fault plane being interpreted.

The horizontal extent of some faults often appeared to be meandering, i.e., changing directions at different intervals. For this reason, besides the given inline and crossline, arbitrary polylines of variable orientations were added to the seismic data to perpendicularly intersect faults along their trace. Although Petrel does offer automated fault interpretation, not all fault interpretations created through auto-picking honoured the full trace of the fault. Faults were therefore best manually interpreted. In general, automated methods in fault extraction still have a long way to go in seismic interpretation software.

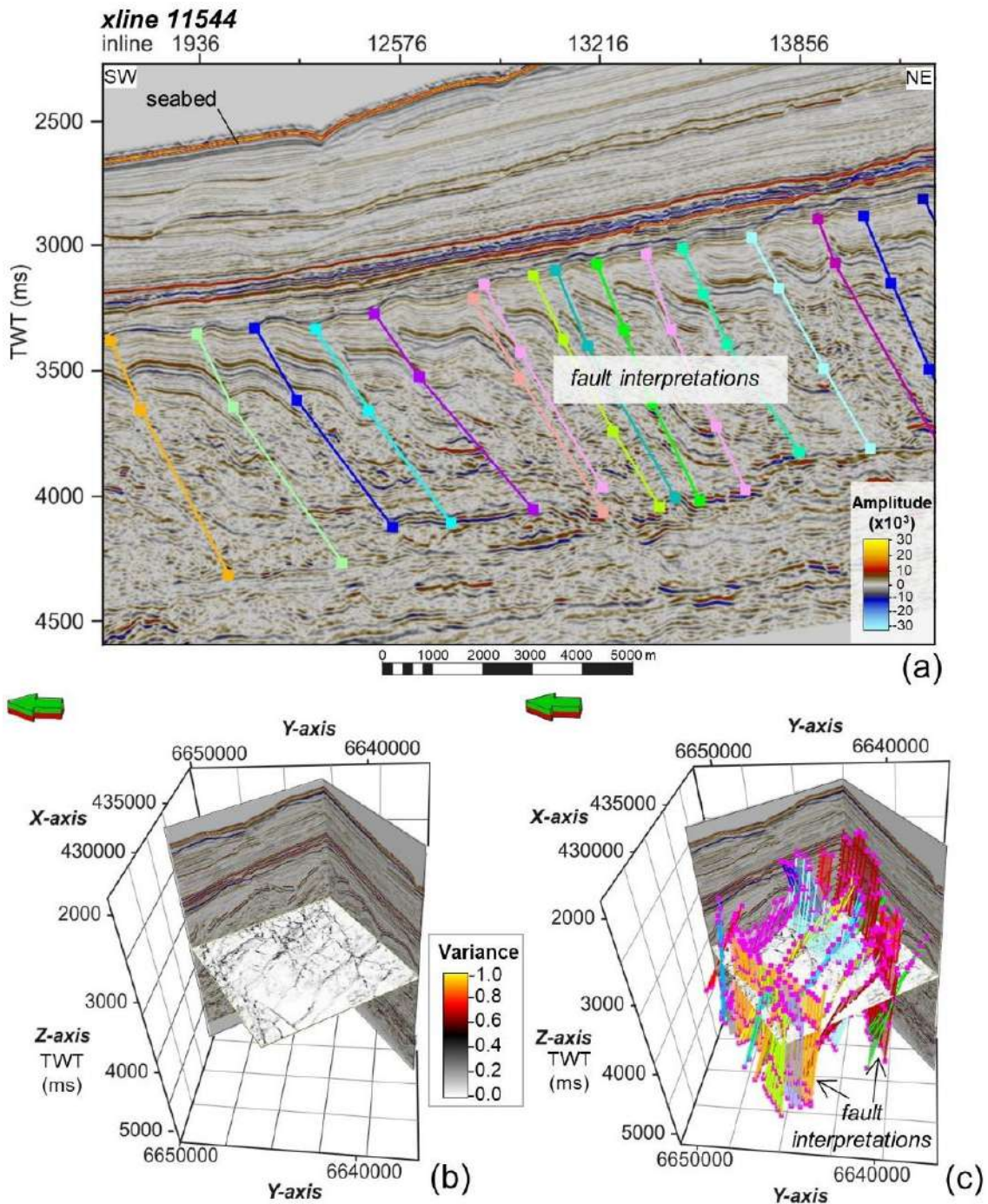


Figure 4.12 Interpreting faults in reflection seismic data with (a) displaying fault segments picked on a 2D interpretation window, (b) showing the variance time slice used to guide interpretation, and (c) displaying fault interpretations fitting lineaments on the variance time slice. VE= 5.

4.7.2 Fault interpretations to fault framework modelling

Fault interpretations are used as input in creating a fault framework; the first step in creating a structural model. Prior to creating a structural model, however, the interpreter needs to decide whether the model will be created in time (TWT= two-way time) or depth since changing between the two domains will no longer be possible whilst modelling.

4.8 Domain conversion

Seismic sections are initially recorded in time. To portray the true thickness and dips of sedimentary units and fault planes at depth (respectively), the seismic profile needs to be converted from the time to the depth domain (Pandey et al., 2013). Domain conversion requires a velocity model of rocks to describe the variation of velocity in space. The velocity model is used to convert the seismic data from one domain to another. Although the final structural model was created in the time domain, depth conversion was necessary to obtain the approximate depth of features and thickness of stratigraphic units in the Orange Basin study area. The following section describes different velocity models, the velocity model chosen, and velocities assigned to this orange Basin research together with depth conversion.

4.8.1 Velocity modelling

Three main functions are recognised in velocity modelling being the interval velocity, linear velocity, and advanced linear velocity illustrated in Fig. 4.13 (Duru et al., 2018; Babasafari, 2019). The functions for each velocity model are outlined below where, V = average velocity, K = gradient/compaction factor, Z = depth and T = time, unless otherwise stated:

- **Interval velocity model ($V = V_0 = V_{int}$):** At each location velocity is constant through each zone.
- **Linear velocity model- depth ($V = V_0 + K \cdot Z$):** Velocity changes vertically by a factor of K giving room for heterogeneity. Z is depth (distance in length units from datum), V_0 is the reference velocity (where $Z = 0$), and K is the velocity gradient. V_0 is lower than the velocities in the layer and may be negative in extreme cases resulting in increasing velocities with depth. If $K = 0$, the linear velocity model is equivalent to the interval model.
- **Advanced linear velocity model ($V = V_0 + K \cdot (Z - Z_0)$):** More advanced than the linear velocity model in that $Z = Z - Z_0$; this the distance between a point and the top of the zone. V_0 is the velocity at the top of the zone (reference velocity). If $K = 0$, the advanced velocity model is equivalent to the interval velocity model.

Petrel offers three additional velocity modelling functions; the linear velocity model in time, and the average/interval cube model, and average property model explained below:

- **Linear velocity model- time ($V = V_0 + K \cdot T$):** Works the same as the linear velocity model in depth ($V = V_0 + K \cdot Z$) except it converts depth (Z) to time (T). To obtain the same results, the K factor needs to be 4 in the modelling process for the linear instantaneous and average velocity in time functions.
- **Average/ interval cube:** Uses a velocity cube which may contain the average velocity from datum, interval, or instantaneous velocity.
- **Velocity property model:** Uses a velocity property which can only contain average velocity from datum.

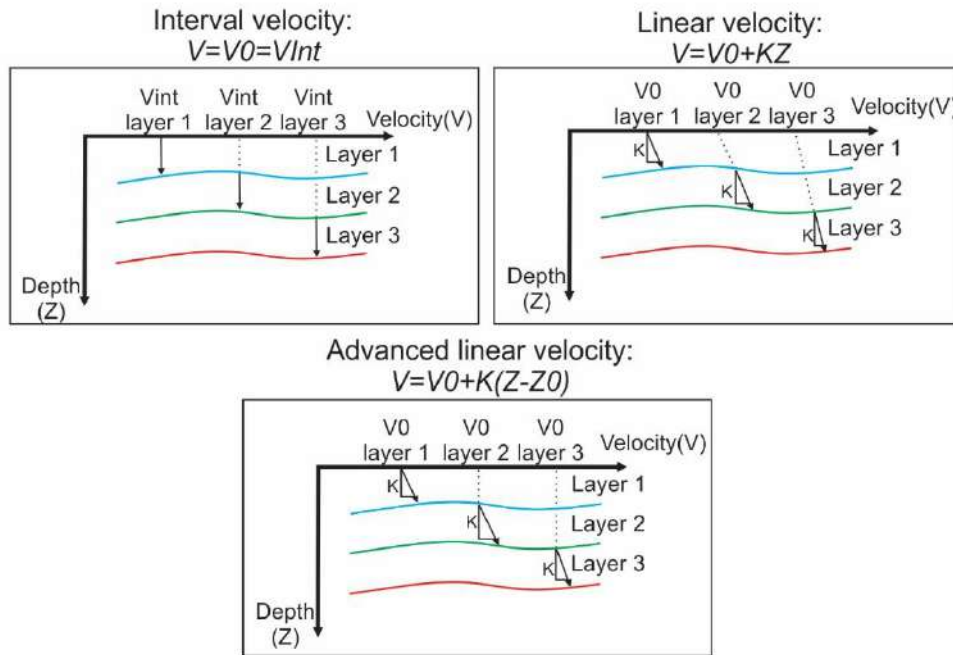


Figure 4.13 Illustration of the three main velocity models applied in seismic data showing the interval velocity, linear velocity, and advanced velocity models (modified after Babasafari, 2019).

4.8.2 Orange Basin velocity modelling to depth conversion

Seismic velocities are dependent on several parameters: shear modulus (μ), bulk modulus (k), and Lamé's lambda constant (λ), and mass density (ρ); all of which are dependent on several rock properties (Kuhlmann et al., 2010). Rock properties include lithology, porosity, gas and oil pore filling, matrix, rock structure, pressure with depth, temperature, and compaction degree. Since no wells currently exist in the deep-water study area, seismic velocities assigned to each surface used were inferred from other Orange Basin research in the shallow waters, namely Kuhlmann et al. (2010) who compiled a chart of the average interval velocities per well for each major surface recognised in Late Cretaceous sequences (Fig. 4.14).

To remove the structural ambiguity presented by time, the correct velocity model needed to be chosen for depth conversion in the research. Both the interval ($V = V_0 = V_{int}$) and linear (depth) ($V = V_0 + K \cdot Z$) velocity models were tested. Since the K values for the linear velocity model were unknown, they were assigned using trial and error as in Tigli (2016); the K values used lay between +0.5 and -0.2 defining the uppermost and lowermost limits, respectively. Since the interval velocity model had fewer variables, thus leaving less room for erroneous calculations, it was the final model chosen for depth conversion (Fig. 4.15). The seafloor, Oligocene, Maastrichtian (22At1), and Albian (14At1) surfaces (so named in this research) were used as input, and assigned velocities of 1800, 2000, 2000, and 4500 m/s, respectively as an average of the velocities in Kuhlmann et al. (2010) shown in Fig. 4.14.

A time to depth domain conversion using the active velocity model was then carried out on the seismic volume, all horizon interpretations, surfaces, and fault interpretations. The depth values of the depth converted seismic

volume (Fig. 15b) are typical for sequences of the same age seen in other Orange Basin studies such as de Vera et al. (2010) (refer to Fig. 2.3). Compared to the seismic volume in time (Fig. 15a), however, the depth converted seismic volume appears distorted as it is vertically stretched and horizontally compressed (Fig. 15b). Due to the distortion, the depth-converted seismic volume was not used, therefore all interpretations and modelling were carried out in the time domain. If, however, well logs were available, velocity modelling and depth conversion would have been carried from the beginning, making all interpretations in the depth domain. The dips quoted of fault planes and surfaces are all approximate values as they are in the time domain.

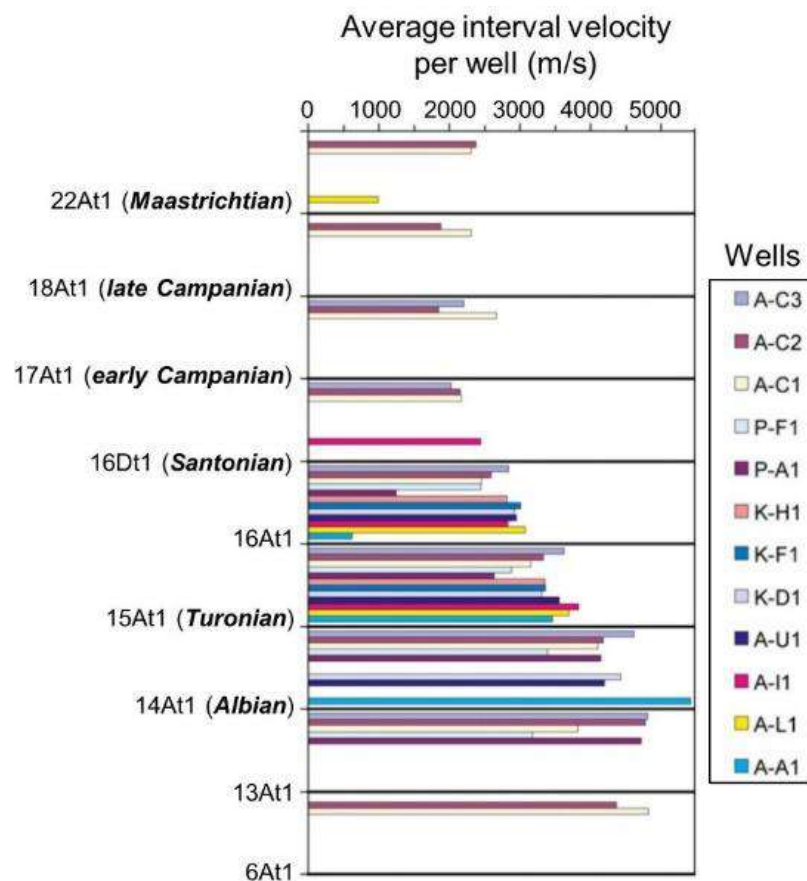
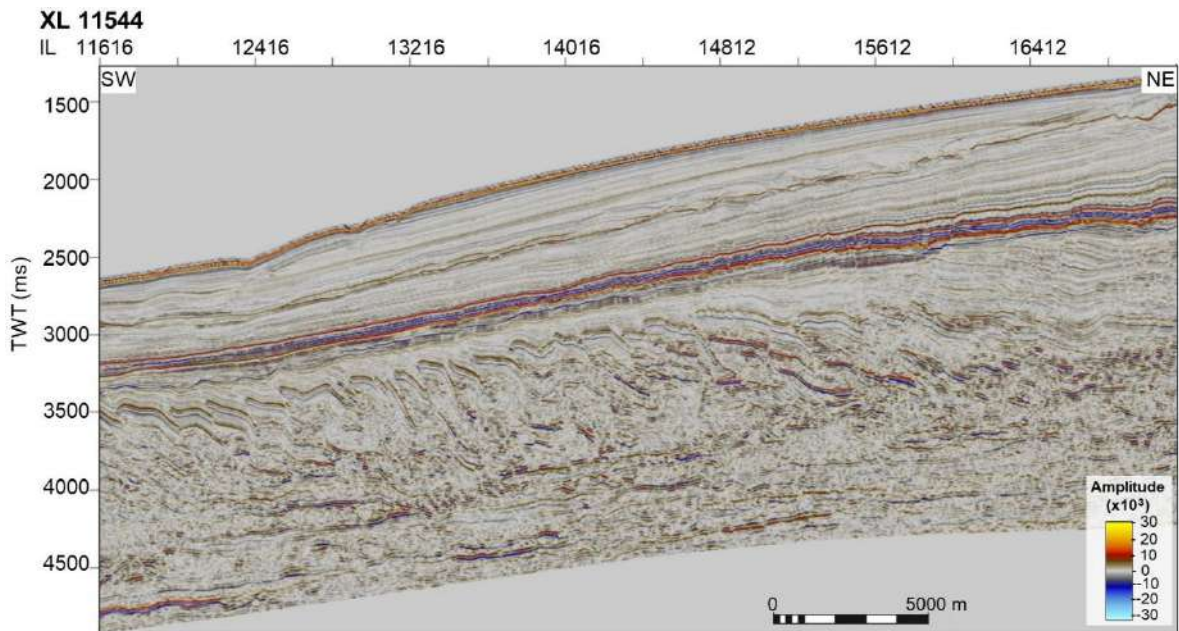


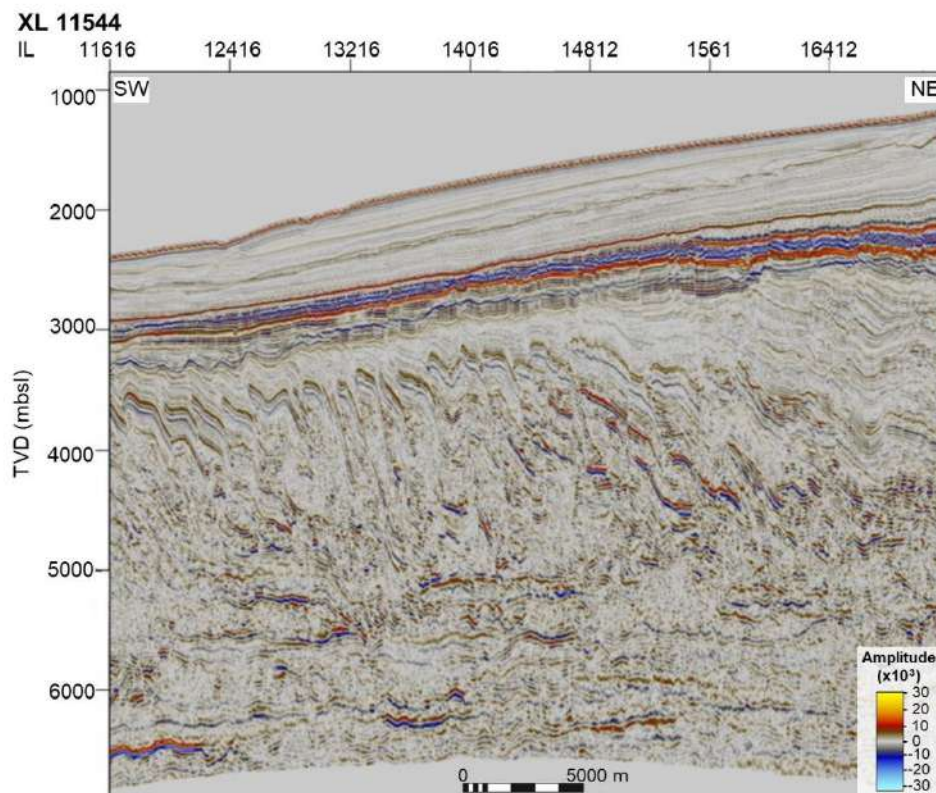
Figure 4.14 Chart showing the average interval velocities of Late Cretaceous stratigraphic surfaces from wells in the shallow Orange Basin (modified after Kuhlmann et al., 2010). The surfaces named in bold italics are those identified in the study area.

4.9 Structural modelling

Once all horizon and fault interpretations are complete, a structural model may be created. The process of structural modelling used in this research included (1) fault framework modelling, (2) boundary definition, (3) horizon modelling, (4) depospace calculation, and (5) structural gridding. The structural model may either be created in the time or depth domain. If depth conversion is required, it needs to be done prior to building a structural framework since a structural model cannot be depth converted. All the modelling steps used in structural modelling are explained in the following section.



(a)



(b)

Figure 4.15 2D interpretation windows viewing a crossline in (a) the time domain, and (b) depth domain following depth conversion using the interval velocity model. Note how the crossline appears laterally squashed in the depth domain (b) compared to time (a). $VE= 5$.

4.9.1 Fault framework modelling

Fault interpretations (Fig. 4.16a) were modelled into smooth, gridded surfaces (Fig. 4.16b) bound by a tip loop defining the edge of each fault. Intersecting fault relationships were semi-automatically defined in terms of which is the major and minor fault, if they are truncated or not, and whether the truncation is below or above the

intersecting fault. The general parameters used for each fault interpretation are shown in [Table 4.11](#). Petrel had the following limitations in fault modelling:

- (1) Offset scissor faults could not be modelled. The solution was to split the fault into two separate fault interpretations for the fault framework.
- (2) Defining fault relationships was not a fully automated process. Some fault relationships therefore needed to be manually forced.

Table 4.11 The parameters defined in creating a fault framework from fault interpretations.

Parameters		Description
<i>Grid interval</i>	500 m	Fault gridding interval
<i>Smoothing</i>	2	The number of smoothing passes applied
<i>Tip loop style</i>	Convex hull	The shape of the tip loop
<i>Extrapolation distance</i>	50 m	The distance the tip loop is extrapolated beyond the input
<i>Gridding plane</i>	Plane 1	The plane on which gridding takes place; plane 1 is default

A quality control check was performed to validate the fault framework model from a geological and geometric perspective. If a fault did not model well, either the fault interpretation was tweaked, a fault relationship was redefined, or a parameter or two (mostly the grid interval) was changed to produce a more desirable outcome. If a fault interpretation was changed, the fault framework was automatically updated (an invaluable process offered in Petrel).

Since over 500 faults were picked in the seismic volume, faults were added in manageable portions to the fault framework, enabling a more efficient way to edit the many fault relationships. Dip and dip azimuth were added to the fault framework. Since the structural model was created in the time domain, the average interval velocity was required to allow for some form of geometric calculation. An average interval velocity of 2 400 m/s was used as reported for the Orange Basin through seismic refraction studies and well logs ([Kuhlmann et al., 2010](#)).

4.9.2 Boundary definition

The geometry of the structural framework needs to be defined through “boundary definition”. Boundary/geometry definition creates a new structural model and determines the area and resolution of surfaces. The geometry of the structural framework was obtained from the seismic volume that all horizon and fault interpretations were made upon. The boundary definition parameters were automatically obtained from the selected seismic volume giving information on the origin, width, height, and rotation of the lattice. The geometry was automatically coarsened by a factor of 1 (i.e., the seismic volume’s lattice was multiplied by 1) to allow faster initial model building by using a relatively low number of nodes retrieved from objects in the input tree. The seismic volume was rotated 36.6° counter-clockwise ([Fig. 4.1](#)). The resolution of the model was defined by the grid increment of the I and J axes set at 125.

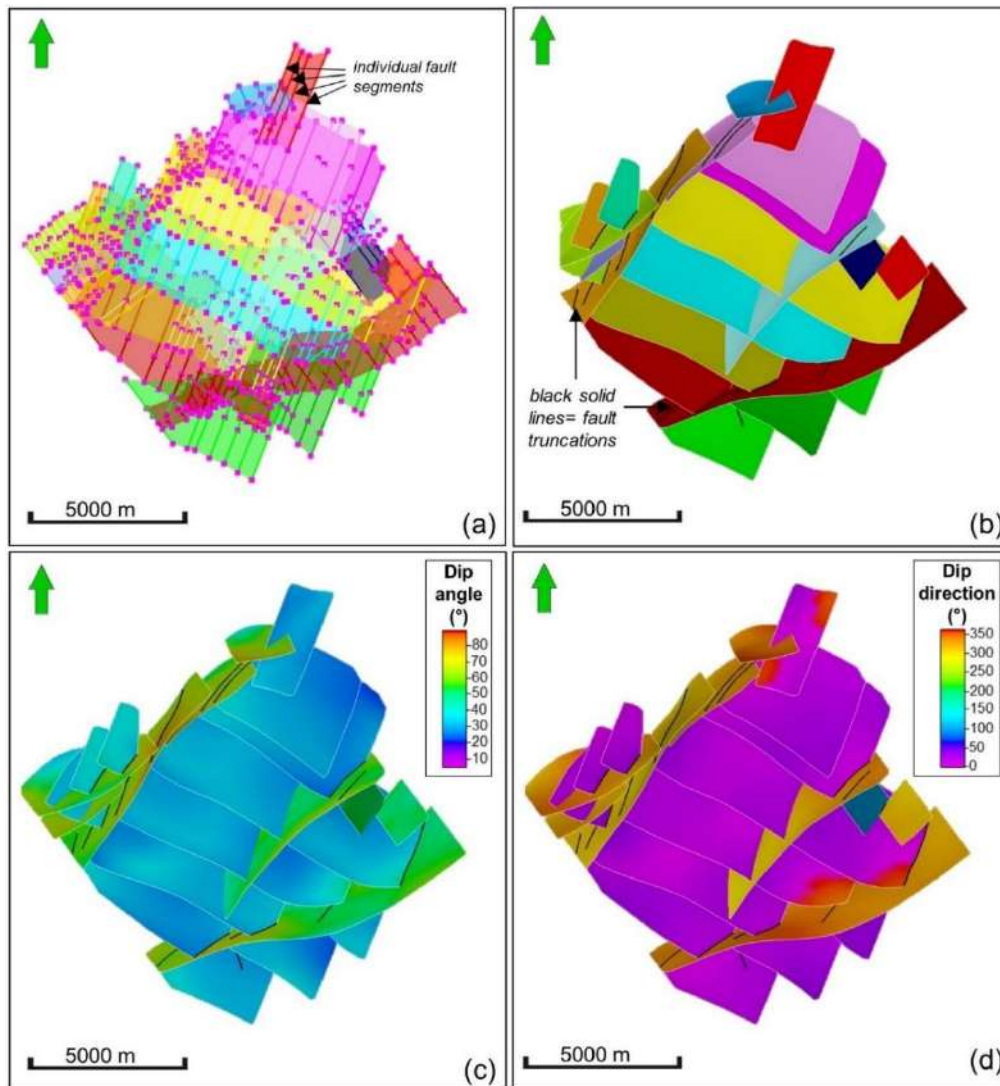


Figure 4.16 Fault modelling process showing (a) original fault interpretations used as input to create (b) a fault framework model with fault relationships defined. Following fault framework modelling, (c) dip and (d) dip azimuth was applied.

4.9.3 Horizon modelling and depospace calculation

After the geometry was defined, surfaces/horizons were added to the structural model using volume-based modelling (VBM). VBM is an algorithm that uses implicit modelling to compute surfaces based on the depositional sequence rather than treating them as discrete surfaces (Zhang et al., 2022). The surfaces used in horizon modelling include (from oldest to youngest) the (1) Albian surface, (3) Santonian surface, (4) early Campanian surface, (5) late Campanian surface, (6) Maastrichtian surface, (7) Oligocene surface, (8) Miocene surface, and (9) the seafloor surface (Fig. 4.17). The second oldest surface, the Turonian, was not included as it was too thin or absent in many areas to properly map.

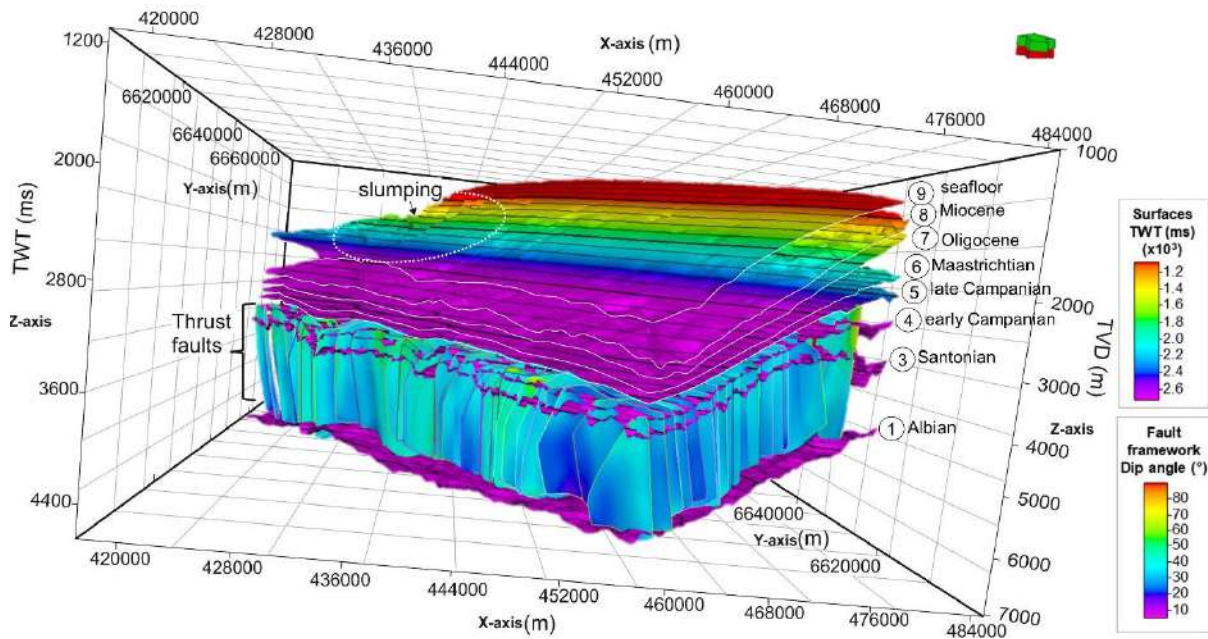


Figure 4.17 All surfaces used in horizon modelling following the creation of a fault framework.

Surfaces made from horizon interpretations were modelled to fit and honour the faults in the fault framework by having gaps indicating fault displacement along the surface. Each surface was smoothed and assigned a specific horizon type (conformable, erosional, base, or discontinuous) to establish the relationship between them. Assigning a horizon type automatically set the sequence order; each conformable surface bound by an unconformable surface was given a separate number. The parameters used in computing horizons for the structural model that worked in this research are tabulated in [Table 4.12](#).

Table 4.12 The parameters used in computing horizons using volume-based modeling.

Index	Horizon	Sequence	Horizon type	Smoothness
1	Seafloor	1	Conformable	35
2	Miocene	1	Erosional	35
3	Oligocene	2	Erosional	35
4	Maastrichtian	3	Conformable	35
5	Late Campanian	3	Conformable	35
6	Early Campanian	3	Erosional	35
7	Santonian	4	Conformable	35
8	Albian	4	Conformable	35

Once the parameters used in computing horizons were set, other settings for the VBM algorithm needed defining. The complexity/size of horizon modelling was set at “very complex” to efficiently handle the ~500 faults in the fault framework. Large thickness variations between surfaces were allowed to accommodate surfaces that often merged into one. The convergent interpolation method was used to calculate the thickness trend. Since the thickness of layers varies laterally, the vertical resolution enhancement was set identify very thin layers. A coarsening factor of 8 was applied to control the level of detail of points far from input data. A quality control check may be applied to the modelled horizons to identify locations that are problematic in the structural

framework. If problems exist in the model either the fault framework needs to be edited, or parameters and settings in horizon modelling itself need to be reassessed. Zones are created from refined models through VBM (Fig. 4.18).

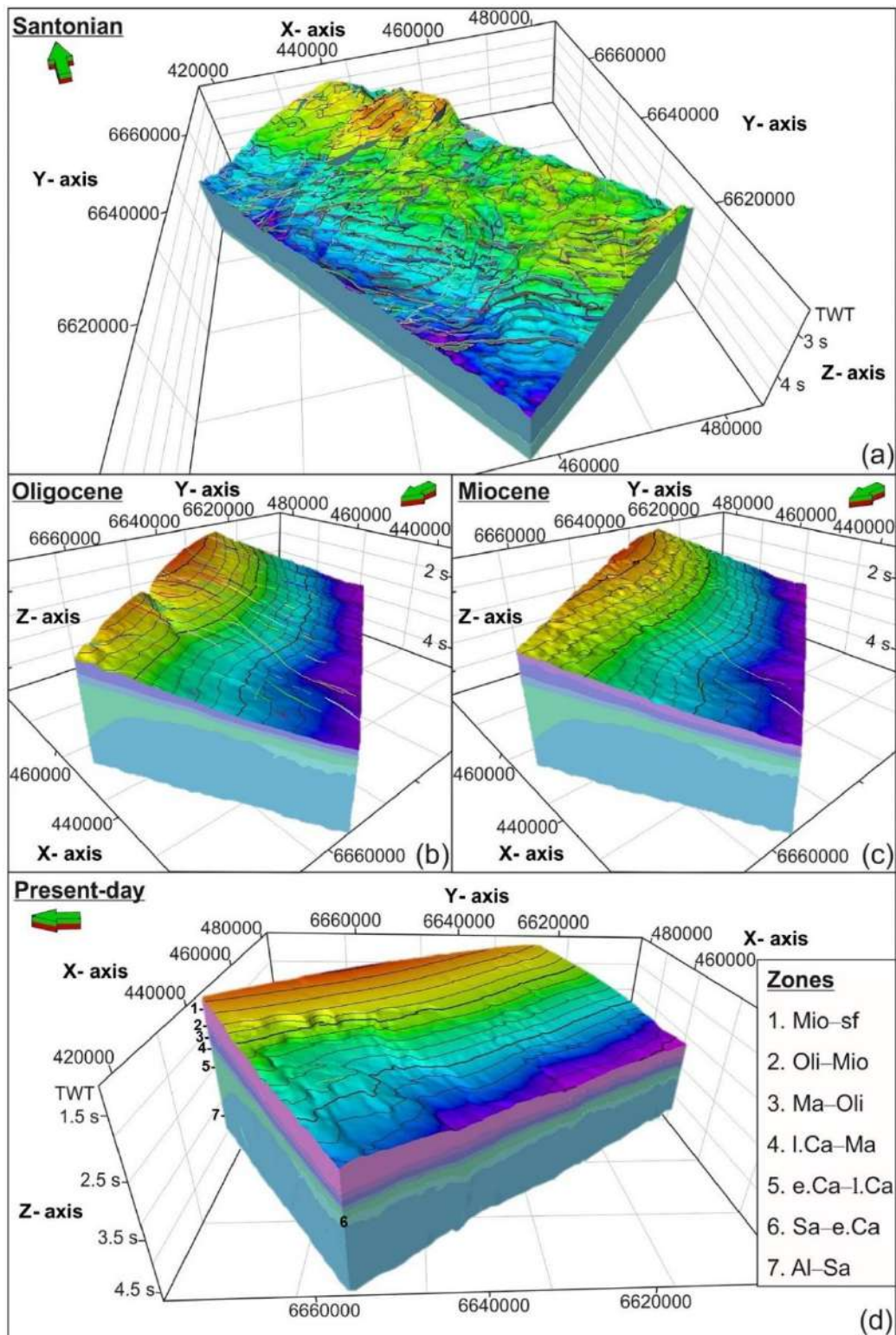


Figure 4.18 Structural model created using volume-based modelling showing zones at key intervals; (a) the thrust Santonian surface with the fault framework, (b) the Oligocene with canyoning, (c) the Miocene with sinusoidal channels, (d) the seafloor with slumping. VE= 7.5.

Following computation and refining of a volume-based model, a depospace (depositional space) calculation can be run. Depospace calculation uses the geometry of the structural model (VBM) to create a virtual depositional space that is physically consistent with the chronostratigraphic environment during deposition. The interval of the structural model included in depospace calculation lay between the Albian (base) and the seafloor (top) surfaces or horizons.

4.9.4 Structural gridding

Using the internal depositional space created through depospace calculation, a stairstepped grid in structural gridding can be made. A structural framework with applied geometry conditions and defined zones is used as input to construct a stairstepped corner point grid. In generating a structural grid, structural framework horizons to be included in the grid need to be specified. The vertical interval of the grid was set between the seafloor (stratigraphically highest) and Albian (stratigraphically deepest) surfaces and set to include grid regions and fault block properties. The stratigraphic zone layering method was used for all zones (Fig. 4.18). Fig. 4.19 shows a southern portion of the model using zone layering once structural gridding was run. The discussion of the overall evolution of the deep-water Orange Basin is presented in Chapter 9, combining all manuscripts produced from researching the Orange Basin deep-water study area (Chapters 6, 7 and 8).

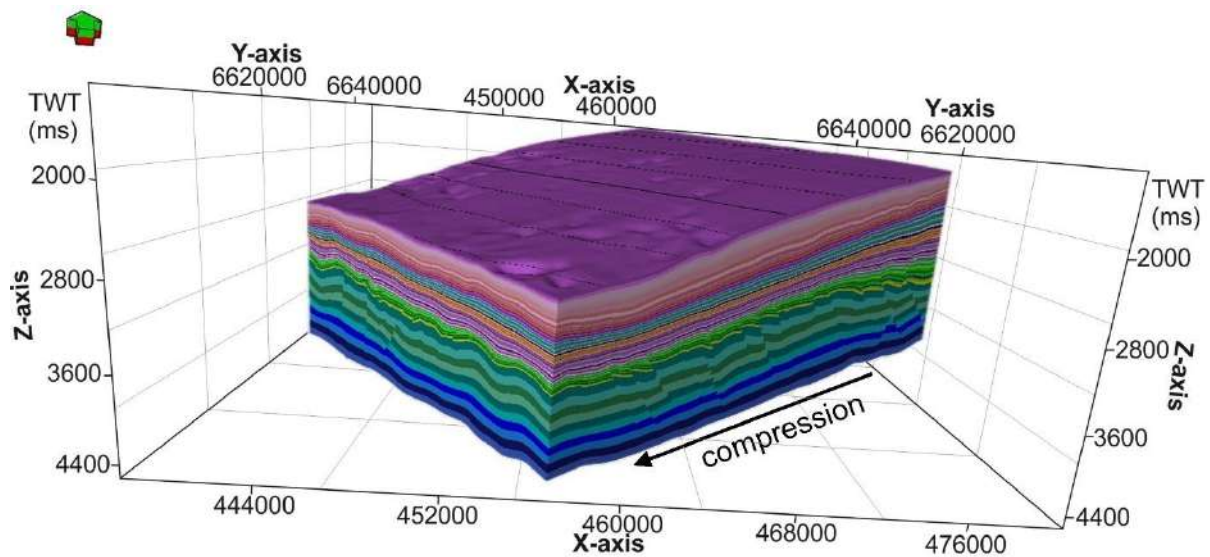


Figure 4.19 3D structural gridded model showing zone layering in the southern section of the study area. VE= 5.

5 Summary of manuscripts

The primary objective of basin analysis is to comprehend the evolution of a basin, which revolves around key factors such as the tectonic setting responsible for its formation, the depositional environment it underwent, and the assessment of the presence, accumulation, and distribution of hydrocarbons within the basin. Three manuscripts produced from this research attempt to constrain these elements for the deep-water Orange Basin study area using high-resolution 3D reflection seismic data. The seismic volume for all manuscripts is situated along the SW African's continental slope of between water depths of 1000 to 2000 mbsl, covering an area of ~1 800 km². Each manuscript produced from the research is summarised below.

5.1 Strato-structural evolution of the deep-water Orange Basin: constraints from 3D reflection seismic data

The temporal evolution of the deep-water, South African Orange Basin is given through 3D reflection seismic data. The seismic data show the delineation of the Mesozoic's Late Cretaceous to Cenozoic deposits of the deep-water Orange Basin. Detailed mapping of key stratigraphic surfaces, structural elements (faults), and geomorphological features have helped to unravel the basin's depositional setting through time. Significant features include (1) a kilometre-scale, gravitational collapse system of deep-water fold-and-thrust belts (DWFTBs), well-imaged in the Late Cretaceous succession, (2) a large (~2.3 km wide, >13 km long) slope-perpendicular submarine canyon in the Oligocene, and (3) a condensed, ~14 km wide zone of crosscutting, sinusoidal channels orientated parallel to the slope in the Miocene.

Gravitational collapse structures, known as DWFTB systems, are common in passive margin settings such as the Orange Basin offshore SW Africa. The Late Cretaceous succession of deep-water Orange Basin is dominated by the translational and compressional domains of an extensive DWFTB system that extends far beyond the ~1 800 km² seismic dataset. The down-dip compressional domain is characterized by landward-dipping DWFTBs detaching the seaward-dipping Turonian shale detachment surface at depth. This is linked to an up-dip translational domain via extensive oblique-slip faults reaching up to ~ 20 km in length. The oblique-slip faults accommodated the downslope translation of sediment segmenting thrust sheets along strike. The translational domain is postulated to be a central region containing overprinted features of both compressional and extensional tectonics as it has a combination of thrust, normal and oblique-slip faults with cross-cutting relationships. The observation of stratal changes in fold geometry shows deformation (due to downslope gravitational collapse and contraction) began in the Coniacian and ended in the early Campanian. Smaller, localized sets of DWFTBs occur in stratigraphically younger sediments underlying the compressional domain of the main, kilometre-scale DWFTB system. These are metre-scale DWFTBs detaching the Albian shale detachment surface in smaller regions. The existence of numerous over-pressurized shale detachment surfaces has resulted in a diverse array of geometries within the overlying kilometre-scale DWFTB system. The Late Cretaceous DWFTB system has been and will continue to be a crucial factor in the ongoing evolution of the margin. For example, in the region directly above a large ~7 km wide syncline in the compressional domain of the DWFTB system, a major slump scar of the same size is found on the seafloor reflecting margin instability.

In the Oligocene a large canyon is detected, attributed to major sea-level fall (possibly beyond the shelf break) at ~30 Ma recognised throughout the SW African margin. The canyon is roughly perpendicular to the slope showing

a slight northwest transport direction. It is interpreted to have been formed by the erosive action of a downslope turbidity current which was deflected northwards by the initiation of a later northward-flowing ocean current. Slope-parallel, crosscutting, and sinusoidal channels are found between 1200 to 1500 m water depths in the Miocene. The channels are interpreted to have been formed by the erosive interaction of the north-flowing Antarctic Intermediate Water and deeper south-flowing North Atlantic Deep Water slope-parallel bottom currents. The development and growth of these ocean bottom currents led to cold water upwelling. The preservation of the Miocene channels is thus attributed not only to interaction of the concurrent Antarctic Intermediate Water and North Atlantic Deep Water bottom currents, but also the intensification of the Benguela upwelling system at ~ 11 Ma under an arid SW African climate. Both the Oligocene canyon and Miocene channels are confined to the region above the translational domain of the Late Cretaceous DWFTB system. Normal and oblique-slip faults of the translational domain propagated upwards to terminate at the Oligocene and Miocene stratigraphic surfaces, while thrust faults of the compressional domain terminate at the stratigraphically younger early Campanian surface.

The study shows major structural differences between the two Late Cretaceous domains imaged in the Mesozoic, and their relation to the overlying Cenozoic succession. From these observations, a conceptual model describing the evolution of the deep-water Orange Basin is created. Late Cretaceous to Oligocene sedimentation was controlled by tectonics, while the deposition of mid-Miocene to present-day sedimentary sequences was primarily controlled by climatic and oceanographic processes.

5.2 3D reflection seismic imaging of natural gas/fluid escape features in the deep-water Orange Basin of South Africa

Using high-resolution 3D reflection seismic data many features indicative of natural gas/fluid leakage have been imaged in the deep-water Orange Basin offshore South Africa. These features would have otherwise been missed or not fully resolved in a regular 2D seismic survey. They have been enhanced by various attributes, some of which are direct hydrocarbon indicators which reveal the presence of hydrocarbons as positive high amplitude anomalies. The most effective direct hydrocarbon indicators include the envelope, generalised spectral decomposition, sweetness, and iterative root mean square volumetric attributes applied to the seismic dataset. The occurrence of natural gas and fluid escape features is strongly influenced by the proximal translational domain and distal compressional domain of a deep-water fold -and-thrust belt (DWFTB) system in the Late Cretaceous described in [Maduna et al. \(2022\)](#).

Hydrocarbons originated from both thermogenic and biogenic sources with the former stemming from the proven Aptian and speculated Turonian source rocks, and the latter from organic-rich sediments in the Cenozoic attributed to the Miocene Benguela Upwelling System. Faults, pipes, and chimneys serve as conduits for the upward migration of hydrocarbons with most initiating from the Turonian shales at depth. The surface expression of hydrocarbon migration is shown by an elongated mud volcano piercing the seafloor, and pockmarks on the present-day seafloor and late Campanian palaeo-seafloor surface. All these features indicate moderate to high gas and fluid expulsion rates since they penetrate the palaeo- and present-day seafloors.

Gas/fluid migration features on the seafloor are associated with mass wasting; the elongated mud volcano is surrounded by a large slump system, while most pockmarks occur together with slides. The base of internal deformation for both mass wasting systems is along the Oligocene and Miocene surfaces. The full slump system covers an areal extent $>26 \times 19$ km, with the ~ 7 km wide slump scar identified in [Maduna et al. \(2022\)](#) forming part of it. Margin instability to form this large geomorphological feature is driven by high rates of sedimentary volcanism as it is centred around a 4.2 km long elongated mud volcano with a deep-seated conduit rooting from the Turonian shales. The mud volcano is tectonically controlled as it is situated along the axis of a Late Cretaceous anticline and separating the translational domain and the compressional domain of the DWFTB system. Numerous $\sim 2\text{--}4$ km slides occur together with the simple cone-shaped seafloor depressions called pockmarks.

While only 85 pockmarks occur on the seafloor, an extensive population of over 950 well-preserved pockmarks are imaged on the late Campanian palaeo-seafloor. Seafloor pockmarks are mainly found directly above or following the same trend as those on the buried late Campanian surface. There are no visible pipes/faults connecting the pockmarks between the two surfaces meaning that the conduits for fluid migration are below the seismic vertical resolution limit of 60 m or 30 m. Three distinctive shapes and sizes of pockmarks are observed on the late Campanian surface in this research categorised into giant (>1500 m diameter), crater ($\sim 700\text{--}900$ m diameter), and simple (<500 m diameter) pockmark groups. There are 8 giant and >900 simple pockmarks found throughout the study area unconfined to a specific region. Simple pockmarks occur along faults, in linear belts seemingly unrelated to faults, as conjoined composite clusters, and otherwise random distributions with some occurring within giant pockmarks. There are ~ 20 crater pockmarks situated mostly above the translational domain (south and southeast of the study area). Crater pockmarks are centrally located within polygonal faults which post-date them.

The largest hydrocarbon accumulations are shown by direct hydrocarbon indicators at the intersection of translational and compressional domains of the Late Cretaceous gravitational collapse system in the late Campanian. Here, sediments within a late Campanian anticline appear as a positive high amplitude anomaly. Large, irregular pockmarks occur in the same vicinity on both the late Campanian and seafloor surfaces. The widespread presence and distribution of natural gas and fluid escape features suggest that there are significant hydrocarbon reservoirs that remain untapped in the deep-water Orange Basin.

5.3 A novel approach to fault interpretation using convolutional neural network: a case study of the deep-water Orange Basin, South Africa

A convolutional neural network (CNN) for automatic fault extraction is compared against conventional seismic attributes for fault detection using high-resolution 3D reflection seismic data from the deep-water Orange Basin as a case study. Approximately 500 faults were manually picked from the seismic volume by [Maduna et al. \(2022\)](#) aided by the application of seismic attributes within Schlumberger's Petrel seismic interpretation software. Volume-based attributes of variance and chaos were initially applied to the seismic dataset to enhance edges and thus delineate faults. Fault-net, a convolutional neural network (CNN) within deep machine learning, was developed and used as a comparative method to delineate faults automatically from the seismic volume through a task called image segmentation.

Faults are displacements of otherwise continuous rock layers. They are important structures in the exploration of hydrocarbons as gas and fluids migrate through the pathways created by them. Apart from creating primary gas/fluid migration pathways, the analysis of the fault framework system provides valuable insights pertaining to the source rock, trapping mechanisms, and reservoir characteristics of a basin's hydrocarbon system. Seismic attributes have long been used as the conventional method of delineating faults from reflection seismic data, highlighting features of interest by removing others through mathematical applications. The rising influx of large seismic datasets acquired within current state-of-the-art surveys has boosted the growth of deep machine learning algorithms called CNNs which mimic human vision (the convolutional layer) to automatically interpret features within seismic data.

The correct interpretation of the type, geometry, distribution, extent, and relationship characteristics of faults is an essential task within basin analysis to optimize drilling locations and understand the potential risks involved in hydrocarbon exploration. Faults identified in the deep-water study area originate from the translational domain and the compressional domain of a Late Cretaceous DWFTB system. The fault framework system is a complex mesh of extensional (normal faults), compressional (thrust faults), and translational (normal to thrust faults accompanied by crosscutting oblique-slip faults) tectonics. Most faults initiate from the Turonian shale detachment surface which is also a source rock interval. Anticlinal folds of the compressional domain provide structural traps that are possibly Santonian and late Campanian (where thrust faults of the compressional domain terminate) in age. Potential sandstone reservoirs are sediments between the Turonian to Santonian, and Santonian to late Campanian stratigraphic markers.

Prior to applying the edge-enhancing and CNN methods to the dataset, the seismic volume was first conditioned using structural smoothing to increase the quality of the data. The fault-net CNN proved itself to be highly effective and advantageous compared against the conventional seismic attributes such as chaos and variance. Although the input data was conditioned in the same way for both methods, the edge-enhanced seismic volumes suffer from noise-induced loss of performance particularly at depth. Other setbacks with conventional methods include the high computation power and long run times required. In contrast, the fault-net CNN may take a few hours to weeks for model training. Once the model is trained it may take a few hours to run the model, get results, and apply post-processing over the input seismic data. The fault-net CNN is an effective tool to automatically segment faults from the seismic dataset significantly reducing the time and subjectivity associated with manual interpretation using conventional methods. The benefits of CNNs far outweigh the limitations allowing for a more accurate interpretation of subsurface structures.



Strato-structural evolution of the deep-water Orange Basin: constraints from 3D reflection seismic data

Nombuso G. Maduna¹, Musa S. D. Manzi¹, Zubair Jinnah¹, and Julie E. Bourdeau²

¹School of Geosciences, University of the Witwatersrand, Johannesburg, PBag 3, WITS, 2050, Republic of South Africa

²Geological Survey of Canada, 601 Booth Street, Ottawa, Ontario, K1A 0E8, Canada

Correspondence: Nombuso G. Maduna (nombuso.maduna@gmail.com)

Received: 9 April 2022 – Discussion started: 10 May 2022

Revised: 14 October 2022 – Accepted: 24 October 2022 – Published: 18 November 2022

Abstract. Deep-water fold-and-thrust belt (DWFTB) systems are gravity-driven collapse structures often found in passive margin settings and are comprised of a linked up-dip extensional domain, central transitional/translational domain, and down-dip compressional domain. Many Late Cretaceous DWFTB systems occur along the SW African passive margin with multiple, over-pressurized, seaward-dipping shale detachment surfaces accommodating gravitational slip. In this study we use 3D reflection seismic data to constrain the strato-structural evolution of the translational and compressional domains of a Late Cretaceous DWFTB system and the overlying Cenozoic deposits in the Orange Basin, South Africa. The stratigraphy and structure of the Late Cretaceous DWFTB system is shown to have controlled fundamental sedimentary processes and the stability of the evolving margin. The compressional domain exhibits large-scale landward-dipping DWFTBs with thrust faults detaching the main Turonian shale detachment surface at depth and terminating at the early Campanian surface. A major ~ 7 km wide seafloor slump scar reflecting margin instability occurs directly above a syncline of the same width from the buried DWFTB system's compressional domain. The translational domain is imaged as a complex region displaying overprinted features of both extensional and compressional tectonics with the downslope translation of sediment comprising listric normal and then thrust and oblique-slip faults distally. Thrust sheets are segmented along strike by extensive oblique-slip faults which extend from the translational domain into the down-dip compressional domain. Smaller, localized fold-and-thrust belts are found directly below the kilometre-scale DWFTB system in the down-dip compressional domain detaching a lower, Albian shale detachment

surface which corresponds to an older gravitational collapse. The upward propagation of normal and oblique-slip faults with progressive sedimentation is hindered by the Oligocene or Miocene stratigraphic markers corresponding to mass erosional processes in the Cenozoic. A large (~ 2.3 km wide), roughly slope-perpendicular Oligocene submarine canyon formed by turbidity currents is attributed to a major sea-level fall at ~ 30 Ma. Oceanographic circulation is shown to have held a significant control on the deposition of mid-Miocene to present-day sedimentary sequences. Between 1200 to 1500 m water depths along the upper continental slope well-preserved extensive slope-parallel, sinusoidal channel-like features occur on the Miocene stratigraphic marker. The channels are confined within a ~ 14 km wide zone at the interface of the upper northward-flowing Antarctic Intermediate Water (AAIW) and deeper southward-flowing North Atlantic Deep Water (NADW) currents. The erosive interaction of these oppositely flowing bottom currents combined with the effects of the Benguela Upwelling System (BUS), all of which formed or intensified at ~ 11 Ma, are responsible for the creation and preservation of the extensive slope-parallel channels. This study shows the difference in structural styles of the translational and compressional domains of a Late Cretaceous DWFTB system and the processes responsible for mass-scale erosion in the Cenozoic.

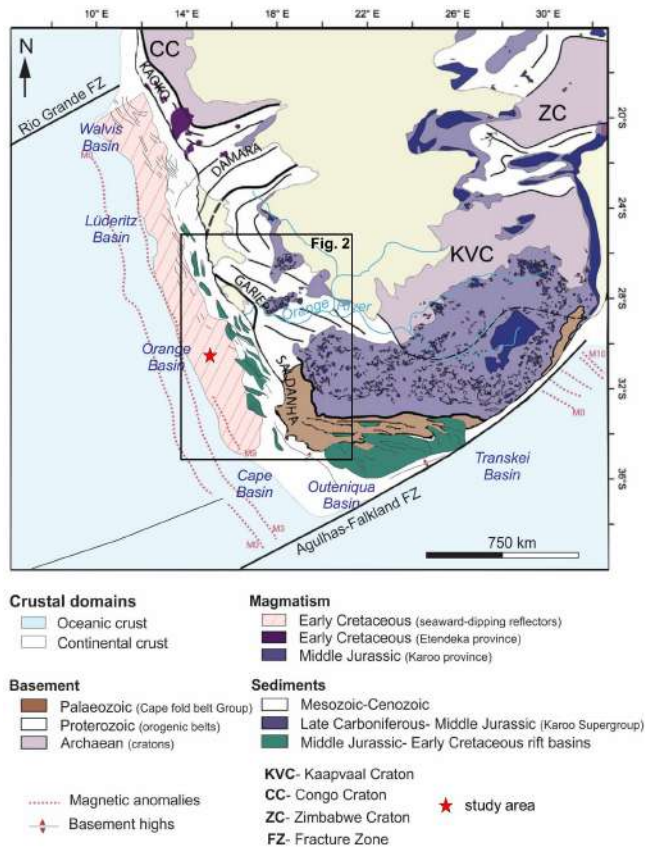


Figure 1. Tectonic structural framework showing the crustal components of southern Africa and major basinal depocentres offshore of the SW African margin (adapted from Baby et al., 2018).

1 Introduction

The southwest African margin is a prime site for the study of processes in passive margin settings. From shallow to deep-water environments, the margin not only records the Late Jurassic to Early Cretaceous break-up of Gondwana but also its post-rift evolution (Fig. 1; Séranne and Anka, 2005). The gravitational collapse and subsequent contraction of sedimentary sequences in the deep ocean formed deep-water fold-and-thrust belts (DWFTBs), distal sedimentary wedges of interrelated folds and thrust faults over a sloping detachment surface (Fig. 2; Rowan et al., 2004; Nemčok et al., 2005). DWFTBs form part of a linked tripartite system consisting of a (1) down-dip compressional domain (within which DWFTBs form), (2) central transitional/translational domain, and (3) up-dip extensional domain with proximity to the coastline (Fig. 3; Rowan et al., 2004; Corredor et al., 2005; de Vera et al., 2010; Morley et al., 2011). The advancement in deep-water drilling technology by the petroleum industry over the last 2 decades has promoted interest in the study of DWFTBs, as their anticlines are known to host vast reserves of hydrocarbons (e.g. Bilotti and Shaw, 2005; Corredor et al., 2005).

Well-preserved DWFTB systems are found within the Orange Basin, which is located offshore of South Africa and Namibia (Figs. 2a and 3; Butler and Paton, 2010; de Vera et al., 2010; Scarselli et al., 2016; Mahlalela et al., 2021). The use of 2D reflection seismic data acquired in the Orange Basin has allowed certain key elements of its evolution to be constrained through several studies (e.g. Light et al., 1993; Clemson et al., 1997; de Vera et al., 2010; Dalton et al., 2015, 2017; Collier et al., 2017; Baby et al., 2018). These studies describe events within the late stages of continental break-up, affecting the stratigraphy, structure, and hydrocarbon potential of the basin, with later studies including the formation of gravitational collapse structures (DWFTB systems). The observations are however limited for the South African region of the Orange Basin, particularly in the distal deep-water environment, which has been poorly explored in contrast to the Namibian extent. Directly adjacent to the South African maritime border (and hence this present study), significant light oil discoveries from deep-water wells drilled between 2000–3000 m below sea level (m b.s.l.) have been reported in Namibia (Fig. 2; van der Spuy and Sayidini, 2022). Although there is extensive 2D legacy seismic data coverage, the deep-water Orange Basin in South Africa remains largely under-explored due to the sparsity of wells (Fig. 2) and both 2D and 3D seismic data coverage (van der Spuy and Sayidini, 2022). According to the Petroleum Agency of South Africa (PASA hereafter), only 38 exploration wells have been drilled with one well per 4000 km², most of which are confined to the shelf environments below 1000 m b.s.l. (Fig. 2; PASA, 2017; van der Spuy and Sayidini, 2022). Dense 2D legacy seismic data coverage is confined to the shelf, while the more distal, deep-water environment has fewer seismic lines that are spaced farther apart. Furthermore, only three 3D seismic surveys have been conducted in the deep-water environment (van der Spuy and Sayidini, 2022).

There is a great paucity of data for the central transitional/translational domain of gravity collapse structures both offshore of SW Africa and worldwide due to its structural complexity and how it has previously been poorly seismically imaged (mainly 2D), thus making it difficult to interpret (e.g. Butler and Paton, 2010). In stark contrast, there is extensive knowledge on the up-dip extensional and down-dip compressional domains, which are well-studied due to the simplicity of the former and known hydrocarbon potential of the latter (e.g. Butler and Paton, 2010; de Vera et al., 2010; Scarselli et al., 2016; Mahlalela et al., 2021). An examination of the translational domain in a buried DWFTB system is done in this study using one of the existing deep-water 3D reflection seismic surveys (Fig. 2). We define its relationship to the down-dip compressional domain and assess how both domains have structurally affected the younger deposits following progressive sedimentation. We also look at the along-strike change in stratigraphy and structure of both domains along the margin. From these observations we create a model describing not only the evolution of one DWFTB

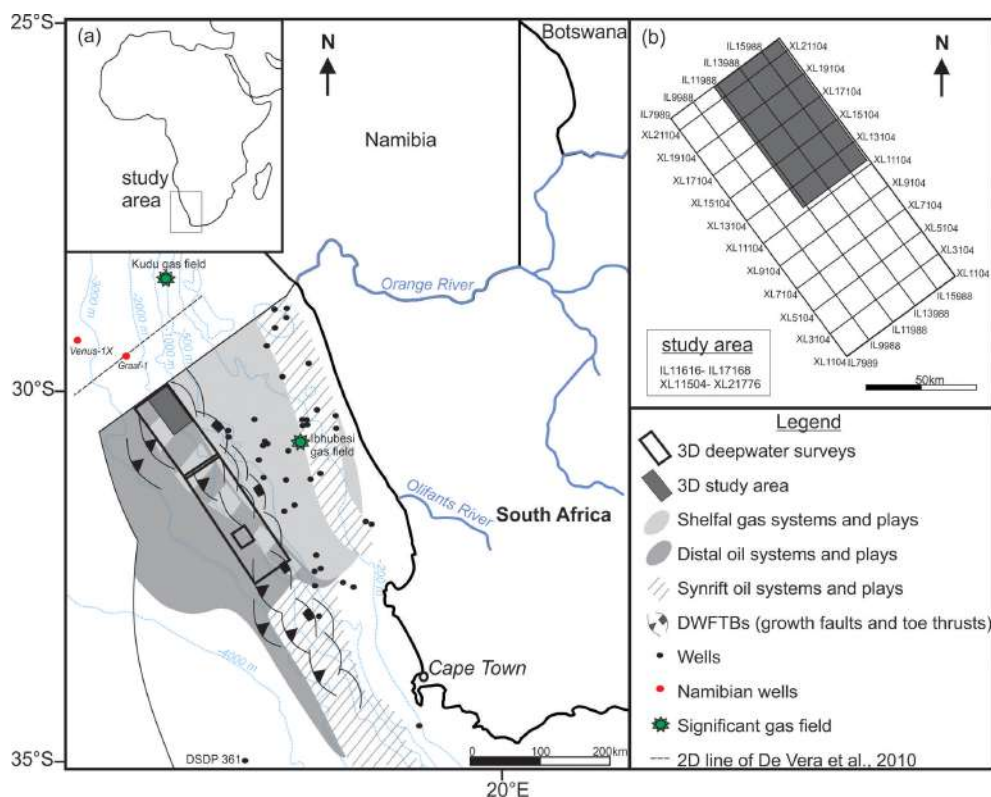


Figure 2. Simplified map of the Orange Basin study area offshore of the SW African coastline. (a) Known and predicted petroleum systems and plays and the position of gravitational structures and wells within the South African licensing area (adapted from Jungslager, 1999). (b) Location of the present study within the full 3D seismic survey.

system but also that of the overlying sediments and their erosional features primarily affected by global oceanographic circulation.

2 Regional setting

2.1 Offshore structural framework

As in all margins, very little is known of the SW African margin's configuration prior to rifting (Mohammed et al., 2017). What is known is that the pre-rift basement forms a 30 km wide, N–S-orientated zone of pronounced flexure induced by thermal subsidence in the continental lithosphere (Light et al., 1993; Clemson et al., 1997; Mohammed et al., 2017; Baby et al., 2018). This zone, known as the hinge line, has separated regions of subsidence with regions of stasis or uplift ever since the Mesozoic, forming a critical boundary of the margin's offshore and onshore morphologies (Light et al., 1993; Clemson et al., 1997; Aizawa et al., 2000). The hinge line forms a N–S structural grain offset by several E–W-orientated segment boundaries having partitioned the timing of rifting in continental break-up (Clemson et al., 1997). The E–W-orientated segment boundaries are fracture zones, which accommodated the zipper-like, south to north

development of Early Cretaceous depocentres in zones of greatest subsidence (Light et al., 1993; Baby et al., 2018). From oldest to youngest these depocentres mark the position of the Outeniqua, Cape, Orange, Lüderitz, and Walvis basins contained between the Rio Grande Fracture Zone to the north and the Aghulhas–Falkland Fracture Zone to the south (Fig. 1; Séranne and Anka, 2005). By analogy of the southern Outeniqua Basin, rifting and continental break-up likely began around the Middle Jurassic (~160 Ma) up until ~131 Ma in the Early Cretaceous (Dingle et al., 1983; Collier et al., 2017). This first stage of margin deformation (extension and rifting) was followed by continental drift with the onset of a spreading oceanic ridge subdividing the margin into well-defined shelf, slope, and basinal environmental settings (Fig. 1; Light et al., 1993; Séranne and Anka, 2005).

2.2 Offshore stratigraphy

The syn-rift succession comprises sediments deposited during extension and rifting of the margin, while the post-rift succession comprises sediments deposited since continental drift until present (Fig. 4; e.g. de Vera et al., 2010). Sedimentation and facies distribution were tectonically controlled in the deposition of the syn-rift succession (Light et al., 1993), which forms a megasequence of Late Jurassic to Early Cre-

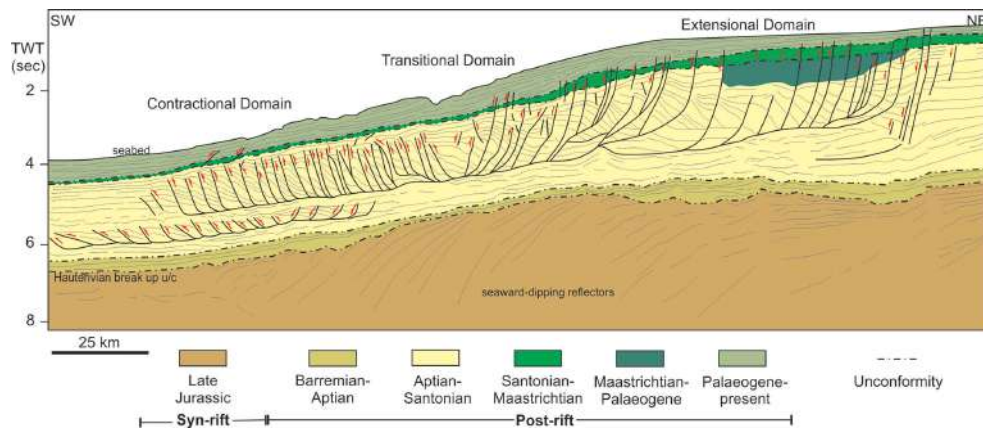


Figure 3. Two-dimensional profile of the Orange Basin showing structures with the up-dip extensional, central transitional (or translational), and down-dip compressional domains of a Cretaceous DWFTB system upon the Late Jurassic syn-rift sequence (de Vera et al., 2010).

taceous (late Hauterivian) siliciclastic and volcanoclastic sediments (Fig. 4, Paton et al., 2008; Dalton et al., 2017). The syn-rift succession is a classic example of a volcanic rifted margin setting as it is characterized by seaward-dipping reflectors (SDRs) reflecting a large subaerial, basaltic extrusive event associated with the break-up of the margin (Maslanyj et al., 1992; Menzies et al., 2002; Baby et al., 2018). The SDRs form a thick (>3 km) package (Baby et al., 2018) comparable in age to the Paraná–Etendeka Large Igneous Province at ~135 Ma (Koopmann et al., 2016; Collier et al., 2017). Sedimentation and facies distribution were tectonically controlled during the rifting phase, hence the presence of these SDRs together with rotated and eroded extensional fault blocks in the syn-rift succession (Maslanyj et al., 1992; Light et al., 1993; Granado et al., 2009). The oldest evidence of mid-oceanic ridge (MOR) activity and the transition to oceanic crust occurs at the M3 magnetic anomaly (Fig. 1), between the Hauterivian and Barremian sequences at 127 Ma (Séranne and Anka, 2005; Collier et al., 2017). Overall, the syn-rift succession is comprised of isolated half grabens filled with interbedded clastics and volcanics (Jungslager, 1999). The change from subaerial conditions during rifting to an open marine environment with continental drift occurs at ~131 Ma with the initial deposition of the post-rift succession above the regional, late Hauterivian break-up unconformity (Figs. 3 and 4; Menzies et al., 2002; Granado et al., 2009; de Vera et al., 2010).

The Orange Basin covers an extensive area of approximately 160 000 km², including the Namibian extension, making it South Africa's largest offshore basin both aerially and volumetrically (Kuhlmann et al., 2010; PASA, 2017). The basin has acted as the depocentre for sediments deposited from the Olifants and Orange rivers and their ancestral equivalents since the Early Cretaceous (Fig. 1; Maslanyj et al., 1992; Paton et al., 2008; de Vera et al., 2010). The ~131 Ma to present-day post-rift clastic sediments currently reach a central thickness of 3 km in the south and 5.6 km in

the north of the Orange Basin (Maslanyj et al., 1992; Paton et al., 2008; Granado et al., 2009; Dalton et al., 2017). Dalton et al. (2017) subdivided the post-rift succession into three megasequences: (1) early drift (Early Cretaceous), (2) late drift (Late Cretaceous), and (3) Cenozoic. The early drift megasequence is comprised of black shales and claystones. The late drift (within which most DWFTB systems are found) and Cenozoic megasequences are comprised of interbedded heterolithic shales and claystones. The post-rift stratigraphy of the Orange Basin has been well-described by many authors (e.g. Emery et al., 1975; Brown et al., 1995; Paton et al., 2008; Granado et al., 2009; de Vera et al., 2010; Kuhlmann et al., 2010; Dalton et al., 2017; Baby et al., 2018), who subdivided the succession into several stratigraphic units (sequences) separated by key stratigraphic markers or bounding surfaces (Fig. 4).

2.3 Gravitational collapse structures

Gravitational processes in the Orange Basin have been enhanced by several phases of uplift and denudation, responsible for crustal thinning and the inversion of extensional faults recorded in the SW African margin's Cretaceous post-rift stratigraphic succession (Granado et al., 2009; de Vera et al., 2010; Hirsch et al., 2010; Hartwig et al., 2012; Wildman et al., 2015; Baby et al., 2020). This resulted in the impressive formation of DWFTB systems observed throughout the SW African margin (Fig. 1). DWFTB systems are mass transport deposits consisting of a linked up-dip extensional domain, central transitional/translational, and down-dip compressional domain, which are often well-preserved in passive margin settings (Fig. 3; Rowan et al., 2004; Bilotti and Shaw, 2005; Krueger and Gilbert, 2009). The extensional domain is characterized by convex-upward growth strata separated by listric normal faulting up-dip, adjoining the transitional domain down-dip (Fig. 3; Butler and Paton, 2010). With the continual supply of sediment up-dip in passive mar-

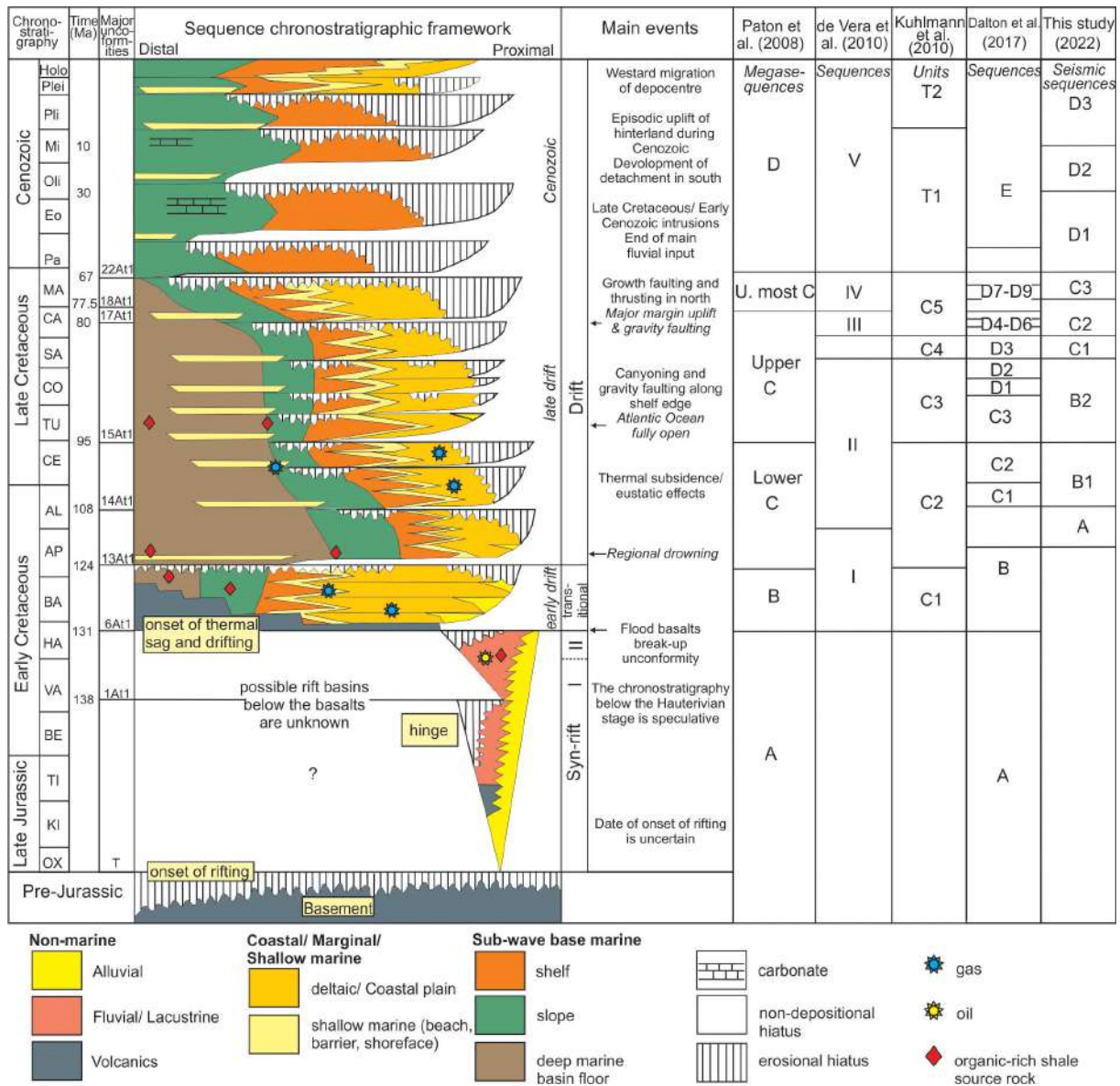


Figure 4. Tectonochronostratigraphic chart of the Orange Basin showing the major depositional sequences, their bounding surfaces, and the evolution of the margin through fluctuations in global and local sea level (Brown et al., 1994; PASA, 2017).

gins, normal faulting within the extensional domain eventually leads to down-dip compression along the basal detachment and the subsequent formation of fold and thrust belts in the compressional domain (Fig. 3; King and Morley, 2017). The anticlines of distal folds in the compressional domain are known to host vast accumulations of hydrocarbons as proven previously in the Niger Delta (Bilotti and Shaw, 2005; Corredor et al., 2005) and recently in the northern Orange Basin of Namibia (van der Spuy and Sayidini, 2022). To form gravity collapse structures in passive margin settings, a very deep sedimentary basin with high rates of sedimentation upon a dipping slope is required (Krueger and Gilbert, 2009). Once enough overburden material has

accumulated in the basin, combined with a lack of cohesion, gravitational sliding occurs along a weak, sloping detachment layer (Rowan et al., 2004; Morley et al., 2011). This gravity sliding process, together with the lateral flattening of sediment under its own weight in gravity spreading, results in gravitational collapse and the subsequent formation of DWFTBs (Morley et al., 2011). The combination of episodic margin uplift and thermal subsidence along the SW African margin resulted in downslope gravitational sliding and spreading forming DWFTB systems in the Orange Basin (de Vera et al., 2010). Trigger mechanisms for gravitational collapse and slope instability offshore of SW Africa include earthquake activity (seismicity) and rapid rates of sedimen-

tation causing elevated internal pore fluid pressures (Séranne and Anka, 2005; Kuhlmann et al., 2010).

Various classification schemes have been proposed for DWFTB systems based on the type of stress field, tectonic setting, and basal detachment lithology which the system is under (e.g. Rowan et al., 2004; Krueger and Gilbert, 2009). Morley et al. (2011) classified DWFTB's into Type 1 near-field stress-driven systems occurring predominantly in passive margin settings and Type 2 far-field together with mixed near- and far-field stress-driven systems occurring predominantly in active margin settings. Type 1a systems are comprised of seaward- or landward-dipping basal shale detachments, while Type 1b is comprised of seaward-dipping basal salt detachments. The Orange Basin DWFTB systems are classified as Type 1a, near-field stress-driven systems containing multiple shale detachment surfaces (Morley et al., 2011). The multiple detachments surfaces upon which gravitational sliding occurs include the Aptian, Turonian, and Campanian seaward-dipping shales (Séranne and Anka, 2005; Dalton et al., 2015). The most significant, regional shale detachment surface is Turonian-aged while others are more locally developed (de Vera et al., 2020). The shales correspond to maximum flooding surfaces, marking the end of a marine transgression (Baby et al., 2018), and are associated with high fluid overpressures and source rock intervals (van der Spuy et al., 2003; de Vera et al., 2010; Kuhlmann et al., 2010). The widespread occurrence of subsurface and surface gas/fluid escape features is indirect evidence of overpressurized conditions (Morley et al., 2011). Fluid overpressures are mainly formed by the combined effects of volumetric expansion involved in hydrocarbon generation and maturation, tectonic stresses, and disequilibrium compaction (Rowan et al., 2004; Bilotti and Shaw, 2005).

2.4 Palaeoceanography

According to Uenzelmann-Neben et al. (2017), oceanic circulation since the Albian to Paleocene/early Eocene created a proto-Antarctic Circumpolar Current (ACC), not strong enough to affect sedimentation in the western South Atlantic. Since the Eocene–Oligocene boundary, however, a major change in oceanic circulation patterns occurred with the onset the Antarctic Circumpolar Current (ACC) and Atlantic meridional overturning circulation (AMOC) after the opening of the Drake Passage in the early Oligocene (~31–28 Ma). With the intensification of the AMOC and strong ACC, southern sourced bottom and deep-water currents formed in the mid-Miocene which were responsible for the change in sedimentation offshore of SW Africa. The bottom and deep-water currents offshore of western South Africa include the Antarctic Intermediate Water (AAIW), the North Atlantic Deep Water (NADW), and the deep Antarctic Bottom Water (AABW). The interplay of these currents, together with the Benguela Current offshore of South Africa has affected sedimentation along the SW African margin

since the mid-Cenozoic (Weigelt and Uenzelmann-Neben, 2004, 2007a; Uenzelmann-Neben et al., 2017).

The Benguela Current drives surface water circulation offshore of SW Africa in a northerly direction as the eastern portion of the South Atlantic subtropical gyre (Peterson and Stramma, 1991). Changes in the growth of Antarctic ice sheets, reflected in oxygen isotope data, have influenced long- and short-term variations within the current and its associated upwelling system (Diester-Haass et al., 1992). The extension of the Benguela Current starts from Cape Point (34° S) in the south and ends at the Angola–Benguela front in Cape Frio (18° S) to the north. At 28° S, the current separates into an oceanic and a coastal branch referred to as the Benguela Oceanic Current (BOC) and Benguela Coastal Current (BCC), respectively. Through geostrophic flow, the BOC transports warm waters from the Agulhas Current (in the south) northwards and westwards, whereas the BCC transports colder waters from the proximal wind-dominated coastal region northwards, eventually encountering the warm Angola Current in the north (Stramma and Peterson, 1989).

During the middle to late Miocene, palaeoceanographic studies record a sharp drop in oceanic CaCO₃ concentrations, termed the “carbonate crash”, in all equatorial regions of major oceans including the Atlantic offshore of SW Africa (see Diester-Haass et al., 2004). The carbonate crash offshore of SW Africa was caused by an increase in clastic input from the Orange River during sea-level regressions resulting in terrigenous dilution. This was followed by an increase in biogenic activity during the late Miocene to early Pliocene, referred to as the “biogenic bloom” (Hermoyian and Owen, 2001; Diester-Haass et al., 2004). In concordance with the global cooling trends recognized in the mid-Miocene (13 Ma), surface ocean water temperatures are shown to have dropped significantly offshore of SW Africa as Antarctic ice sheets expanded, thus intensifying southeasterly trade winds triggering the inflow of cold waters (Zachos et al., 2001; Rommerskirchen et al., 2011). An increase in total organic carbon content and benthic foraminifera accumulation is recorded from core samples taken from the Cape Basin's Ocean Drilling Program (ODP) sites 1085, 1086, and 1087, forming a depth transect across the upper continental slope of the SW African margin (Rommerskirchen et al., 2011). These high palaeo-productivity rates are attributed to upwelling of the Benguela Current in the southern Atlantic intensifying at ~11 Ma (Diester-Haass et al., 2004; Rommerskirchen et al., 2011).

3 Data and methods

Three 3D seismic surveys have been conducted in the deep-water South African Orange Basin: one acquired in 2002, imaging low-resolution data and two large, higher-resolution surveys acquired between 2012 and 2014 (van der Spuy and

Table 1. Acquisition parameters of the seismic survey (Kramer and Heck, 2014).

Recording	
Recording format	SEG-D
Record length	7168 ms
Recording filter delay	None
Sample rate	2 ms
Low-cut filter hydrophone, slope	4.4 Hz, 12 dB per octave
Low-cut filter geophone, slope	Not applicable
High-cut filter both slope	214 Hz, 341 dB per octave
Source	
Source type	Dual source
Number of source arrays	2
Number of sub-arrays	3
Shot point interval	25 m (flip/flop)
Array separation	100 m
Array length	15 m
Source volume	0.0672 m ³
Number of airguns/arrays	30
Operating pressure	2000 psi
Source depth	8 m
Nominal common mid-point (CMP) fold	80
Sercel SSAS Sentinel, Sercel Seal-428	
Number of streamers	8
Group interval	12.5 m
Group length	12.5 m
Number of hydrophones/groups	1
Number of geophones/groups	1
Streamer length	7950 m
Streamer separation	200 m
Number of groups/streamers	636
Streamer depth	10–15 m linear slant
Nearest offset	222 m

Sayidini, 2022). This study uses the northernmost 3D seismic dataset bordering the Namibian maritime licensing region (Fig. 2). Following seismic acquisition by the Dolphin Geophysical *Polar Duchess* ship (Table 1), seismic processing was carried out by the Netherlands Global Processing Team (Table 2) on behalf of Shell Global Solutions International. In this study we interpreted the processed seismic data obtained from Shell.

3.1 Seismic acquisition and processing

Shell Global Solutions International commissioned a 3D reflection seismic survey between 2012 and 2013 in the deep-water Orange Basin (Kramer and Heck, 2014). The survey was designed in a \sim NNW to SSE orientation, covering a total area of \sim 8200 km² (Fig. 2b). Dual-airgun arrays were used with a source volume of 0.0672 m³ towed at 8 m depth with a 25 m shot point interval, and a 7950 m long streamer with a 12.5 m group interval and 12.5 m group length. The data were recorded at a 2 ms sample rate for a total record length of 7168 ms. A low-cut frequency of 4.4 Hz at a 12 dB Oct⁻¹ slope and a high-cut frequency of 214 Hz at a 341 dB Oct⁻¹ slope were used during data acquisition,

giving a dominant frequency of 50 Hz after the application of an anti-aliasing filter. The full survey acquisition parameters are summarized in Table 1. Pre-processing from field tape seismic data was first carried out onboard by the Dolphin Geophysical *Polar Duchess* ship. This involved data conversion from SEG-D to SEG-Y output, and, thereafter, the Netherlands Global Processing Team carried out the rest of the processing workflow, as summarized in Table 2. Processing was carried out at 4 ms from SEG-Y field tape datum through surface-related multiple elimination (SRME) using 3D SRME and anisotropic Kirchhoff pre-stack depth migration (PreSDM) (Table 2).

3.2 Seismic interpretation

In this study we geologically interpret a \sim 1800 km² seismic portion of interest (Fig. 2b) using the Petrel Schlumberger software. The seismic volume lies along the continental slope offshore of western South Africa, between water depths of 1000 to 2000 m b.s.l. (Fig. 2). The seismic interpretation workflow included (1) loading the SEG-Y seismic data involving importing, realizing, and cropping; (2) applying volumetric-based attributes of structural smoothing and variance; (3) horizon and fault mapping through picking horizons and faults of interest and generating surfaces from them; (4) applying horizon-based attributes of influential data and edge detection; (5) velocity modelling and depth conversion; and (6) the creation of a 3D geological model with modelled faults and surfaces in the structural framework. Since no well log data were available for the correlation of stratigraphic sequences at the time of this study, seismic interpretation was carried out in the time domain.

3.2.1 Seismic resolution limit

With an average velocity of 2400 ms⁻¹ reported for the Orange Basin (see Kuhlmann et al., 2010) and a dominant frequency of \sim 20 Hz for the study, the vertical seismic resolution limit given for the half and quarter dominant wavelength criteria (Yilmaz, 2001) is 60 and 30 m, respectively. Since the data are migrated the horizontal resolution is given by the dominant wavelength (i.e. 120 m). Geological features smaller than the vertical and horizontal resolution limits are indistinguishable. It is only through the application of seismic attributes that features lower than the resolution limit may be detected. For example, Manzi et al. (2013) identified small-scale structures in one of the Witwatersrand gold mines using seismic attributes.

Table 2. Processing workflow of the seismic survey (Kramer and Heck, 2014).

Dolphin Geophysical <i>Polar Duchess</i> team	
1	Conversion from SEG-D and navigation merge
2	Output to SEG-Y
Global Processing Team	
3	Conversion from SEG-Y to Shell's proprietary software (SIPMAP) format
4	Spherical spreading correction
5	Despike
6	Swell noise attenuation
7	Resample to 4 ms
8	Denoise
9	Linear noise attenuation
10	Deghosting
11	Seismic interference attenuation
12	Zero phasing
13	2D surface rendered multiple elimination (SRME) prediction
14	3D SRME prediction
15	Least-squares (LSQ)-matched subtraction
16	Multiplicity scaling for Kirchhoff migration
17	Phase de-absorption
18	Residual moveout (RMO) analysis
19	RMO velocity model inversion and anisotropy scanning
20	Pre-migration signal enhancement
21	Kirchhoff pre-stack migration
22	Residual radon demultiplex
23	Amplitude de-absorption
24	RMO correction
25	(Angle) stack
26	Time variant scaling (additional output volumes)
27	Archiving

3.2.2 Structure delineation using seismic attributes

Seismic attributes are mathematical measurements derived from the information provided by seismic data. They are often used to enhance important geological and physical properties of the seismic data by delineating faults, resolving thin beds, and identifying bright spots that could indicate hydrocarbon reservoirs (Chopra and Marfurt, 2005, 2007; Brown, 2011). Seismic attributes are dependent on the signal-to-noise (S/N) ratio of the data and therefore need to be conditioned using various filters. Schlumberger's Petrel software offers a wide variety of seismic attributes which may be applied to the whole volume or to interpreted horizons. Volumetric attributes may be applied from the onset of seismic interpretation to the entire volume while horizon-based attributes are only applicable once sufficient interpretation has taken place on a surface of interest (Brown, 2011).

Structural smoothing was first applied to the full seismic volume to condition the data. It is used to increase the S/N ratio by smoothing the seismic data's input signal through local averaging with a Gaussian filter (Randen et al., 2000). Using the structurally smoothed volume as input, the vari-

ance attribute was applied to enhance fault discontinuities throughout the seismic section. Variance is an edge enhancing attribute that measures local deviations from the seismic signal in the form of a coherency analysis (Silva et al., 2005) and is used in many studies to highlight faulted areas in place of the similar chaos attribute (e.g. Maselli et al., 2019).

To further enhance fault continuities and visualize 3D geometric variations, horizon-based attributes of edge detection and influential data were applied to the surfaces of interest. Horizon-based attributes were used in conjunction with the surface smoothing structural operation which filters out anomalous peaks from picking. Edge detection extracts an edge model to enhance discontinuities by combining the dip and dip azimuth properties and normalizing these to the local noise of the surface (Randen et al., 2000). Influential data generates a property on the data object that highlights areas of rapid 3D geometric variation which is key to ensuring sensible geometric form.

3.2.3 Seismic interpretation strategy

This study's seismic volume images the compressional and translational domains of a Late Cretaceous DWFTB system

together with the overlying Cenozoic successions. The variance time slice shown in Fig. 5a cuts through both domains of the DWFTB system at a level where most structures may be seen in plan view at 3424 ms two-way time (TWT). Combining this with the plan view of all faults dip orientations in Fig. 5b was integral in aiding 3D seismic interpretation. Figure 5c combines all observations in plan section to give a generalized overview of the structural framework and shows the position of regional sections Figs. 6, 7, and 8. These regional sections are used to describe the seismic stratigraphy and structural framework observed in and above the Late Cretaceous DWFTB system. Figure 6 is a full crossline section of the study area, showing a portion of the translational domain and, more importantly, the compressional domain (Fig. 5). The regional section lies roughly perpendicular to the DWFTBs giving a clear view of their internal geometry and surroundings. Figures 7 and 8 are inline sections showing the along-strike component of the compressional and translational domains, respectively, and are orientated perpendicular to NE–SW-trending faults (Fig. 5).

The seismic volume was interpreted using the classical approach implemented by Mitchum et al. (1977), who first introduced the concept of seismic stratigraphy whereby the sequence stratigraphic framework is characterized by stratal termination patterns (i.e. downlap, onlap, toplap erosional truncation, and concordance) between each seismic facies or sequence. Stratigraphic markers are bounding surfaces that separate each sequence and are created through the interplay of base sea-level fluctuations and sedimentation marking the change in depositional regimes (Catuneanu, 2006). In deep-water marine settings surfaces separating each seismic sequence, based on the difference in internal configuration patterns, include the maximum flooding surface (MFS), correlative conformity (CC), and maximum regressive surface (MRS) (Catuneanu, 2006; Catuneanu et al., 2009). Continuous, dominant high-amplitude reflections were picked as key stratigraphic markers in this study and named using the classification and terminology of Catuneanu (2006), as summarized in Table 3. Unconformity surfaces developed through erosion or prolonged periods of non-deposition (Catuneanu, 2002) are also identified in this study, often combining with MFSs, CCs, and MRSs. Nine key stratigraphic markers were identified in the seismic section, coinciding with those recognized throughout the Orange Basin in previous studies (Fig. 4; Brown et al., 1995; Paton et al., 2008; de Vera et al., 2010; Kuhlmann et al., 2010; Hartwig et al., 2012; Dalton et al., 2017; Baby et al., 2018). The geological ages used for stratigraphic markers in this study were postulated from the comparison of the aforementioned past studies and published well data. Figure 3 shows that although the nomenclature used for stratigraphic markers (and stratigraphic sequences) differs between various studies, the actual ages assigned to each are generally consistent.

To derive the approximate thickness of seismic sequences, a generalized depth conversion was carried out using aver-

Table 3. Diagnostic attributes of the main sequence stratigraphic surfaces in deep-water marine settings (Catuneanu, 2006).

Stratigraphic surface	Description	Nature of contact	Marine Facies		Depositional trends	Stratigraphic surface
			below	above		
Maximum regressive surface (MRS)	Marks change from shoreline regression to transgression; replaced by MFS in distal marine	Conformable (few exceptions)	Fining upward in deep water; Coarsening upward in shallow water	Fining upward	Above: transgression Below: normal regression	Above: marine onlap Surface: onlap, downlap
Maximum flooding surface (MFS)	Marks end of shoreline transgression	Conformable or scoured	Fining upward	Coarsening upward	Above: normal regression Below: transgression	Below: truncation Above: downlap Surface: onlap, downlap
Correlative conformity	Reflects the palaeo-seafloor at the end of forced regression; correlates with the subaerial unconformity	Conformable	Coarsening upward	Coarsening upward on shelf	Above: normal regression Below: forced regression	Above: downlap Surface: downlap

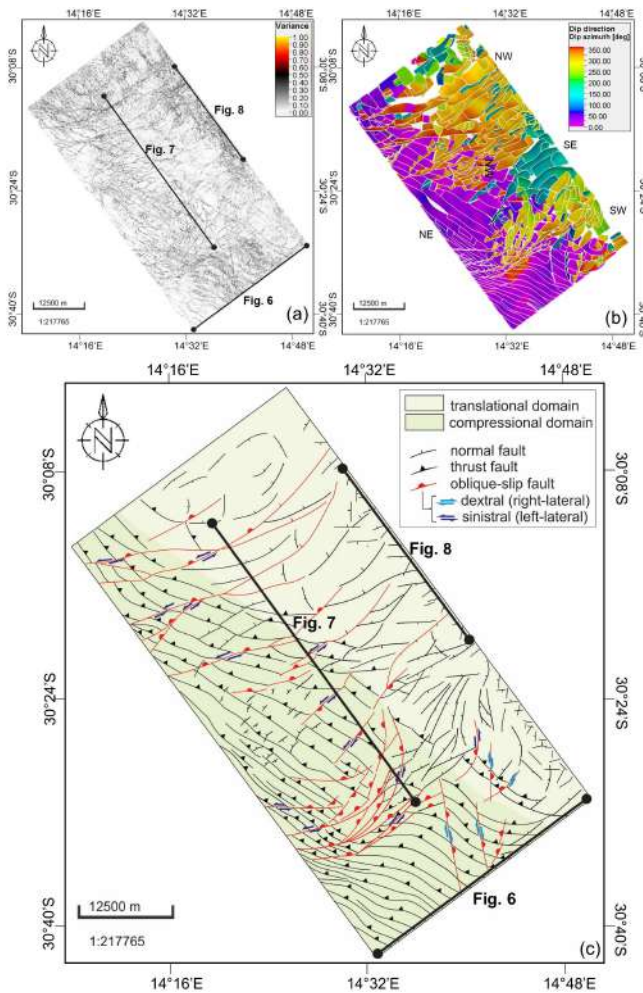


Figure 5. Structural framework showing the translational and compressional domains imaged in the study area. (a) Uninterpreted variance time slice at -3424 ms (imaged within sequence B2 covering depths approximately between -3200 to -5000 m) showing the fault continuities. (b) The dip azimuth of various faults. (c) The interpretation of the structural framework in plan view using (a) and (b) including fault displacement characteristics observed in plan section.

age interval velocities from well logs acquired in the shallower reaches of the Orange Basin used in Kuhlmann et al. (2010). Velocities of 1800, 2000, 2000, and 4500 ms^{-1} were assigned to the seafloor, Oligocene, Maastrichtian, and Albian surfaces (named in this study), respectively, to create an interval velocity model for depth conversion in Petrel.

4 Results

4.1 Seismic stratigraphy

In the Cretaceous we identified and named the Albian, Turonian, Santonian, early Campanian, late Campanian, and

Maastrichtian unconformity surfaces. These surfaces correspond to the 14At1, 15At1, possibly 16Dt, 17At1, 18At1, and 22At1 MFSs and unconformity surfaces, respectively, according to the offshore of stratigraphic nomenclature developed by PetroSA (previously Soeker) (Fig. 4; Brown et al., 1995; PASA, 2017). In the Cenozoic succession we identified the Miocene and Oligocene unconformity surfaces which were also recognized by Baby et al. (2018). The surfaces are markers that divide the entire seismic succession into nine stratigraphic sequences, explained from the regional sections shown in Figs. 6, 7, and 8. The sequences were further grouped into four main megasequences (A–D) reflecting three major phases of margin evolution as described by Dalton et al. (2017): early drift (A), late drift (B1–C3), and Cenozoic (D1–D3) (Fig. 4). Older stratigraphic markers and sequences (below the Albian) were left uninterpreted in the regional sections shown in Figs. 6, 7, and 8, as their full sedimentary package lay mostly below the vertical limit of seismic data.

4.1.1 Early to late drift megasequences (A and B1–C3)

Sequence A in this study is a 400–700 m thick succession that forms a portion of the early drift megasequence. It is characterized by low-to-medium-amplitude, chaotic (Fig. 8), sub-parallel to mounded, internal reflections (Figs. 6 and 7). The upper stratigraphic marker of the sequence is the medium-amplitude Albian surface. Sequences B1 to C3 are grouped as the late drift megasequence. Sequence B1 downlaps the Albian surface as a 0–500 m thick unit characterized by deformed, medium-to-high-amplitude, chaotic, and mounded internal reflectors (Figs. 6, 7, and 8). The upper bounding surface of sequence B1 is the medium-to-high-amplitude undulatory and irregular Turonian surface. The Turonian surface often merges with the deeper Albian surface in the translational domain (Fig. 8).

Sequence B2 forms a sedimentary wedge that thickens from 900–1700 m seawards (down-dip direction), with the greatest thickness in the central region of the entire seismic volume, as shown in Figs. 6 and 7. Sequence B2 is characterized by deformed, medium-to-high-amplitude seismic reflections downlapping the Turonian surface. The internal geometry of the unit in the compressional domain appears as stacked, steeply NE-dipping reflections (Fig. 6) which flatten towards the translational domain to become parallel with the underlying and overlying sequences (Fig. 8). The steeply dipping reflections are folded into asymmetric anticlines distinctly separated by imbricate thrusts creating fold-and-thrust belts (Sect. 4.2; Figs. 6 and 9). The upper bounding surface of sequence B2 is the Santonian surface that defines the main crest of the kilometre-scale DWFTBs. It is a thick, high-amplitude surface conformable to the folded geometry of the unit. Figure 9 shows the Santonian surface in 3D and the underlying sequences. The horizon-based attribute of dip angle was computed for the surface to enhance the morphology of

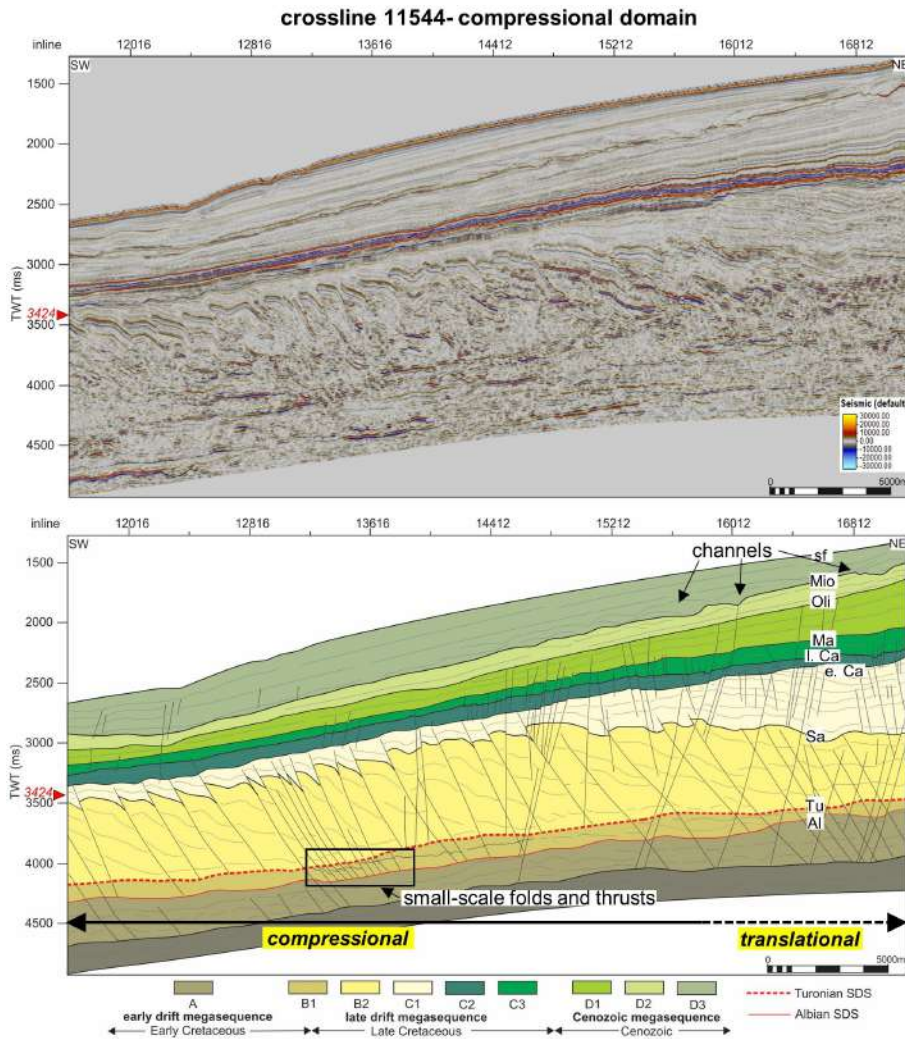


Figure 6. Uninterpreted and interpreted sections of crossline 11 544 showing a portion of the translational and compressional domains and position of time slice 3424. The crossline lies roughly perpendicular to the compressional domain DWFTBs giving a view of their structure in comparison to the translational domain. Abbreviations: Al – Albian; Tu – Turonian; Sa – Santonian; Ma – Maastrichtian; Oli – Oligocene; Mio – Miocene; sf – seafloor; SDS – shale detachment surface. Vertical exaggeration: 5.

the fold crests dipping between 0–15°. In the NW portion of Fig. 7, towards the translational domain (see Fig. 5), a large 6.3 km wide syncline is imaged in sequence B2. To the SE the rest of the sequence appears as a shallow and very broad anticline.

Onlapping the Santonian surface is sequence C1, a sedimentary wedge that thins from 1000 m in the translational domain to 120 m in the distal contractional domain (Fig. 6). It is characterized by low-amplitude, concave-upward sag geometries that onlap and downlap the Santonian surface (Figs. 6, 7, and 8). In the more distal region of compressional domain, however, the reflectors have stacked conformably with the underlying sequence (SW portion of Fig. 6). The early Campanian upper bounding surface of sequence C1 erosionally truncates the unit (Figs. 6 and 7). Sequence C2 is a ~ 200 m thick unit of thin, wavy to parallel, high-frequency,

high-amplitude seismic reflectors (Figs. 6, 7, and 8). Reflectors are initially wavy at the base of the sequence, due to folding above the underlying thrust planes, then gradually straighten to parallel continuous reflections at the top of sequence C2 (Figs. 6 and 7). The sequence’s late Campanian upper bounding surface is a thick, very high in amplitude surface, and appears conformable. Above this lies sequence C3, a seaward-thinning wedge of sediment decreasing from 200–90 m (Figs. 6, 7, and 8). The internal geometry of sequence C3 consists of thick, parallel, very high-amplitude seismic reflectors, including that of its upper Maastrichtian bounding surface which appears conformable.

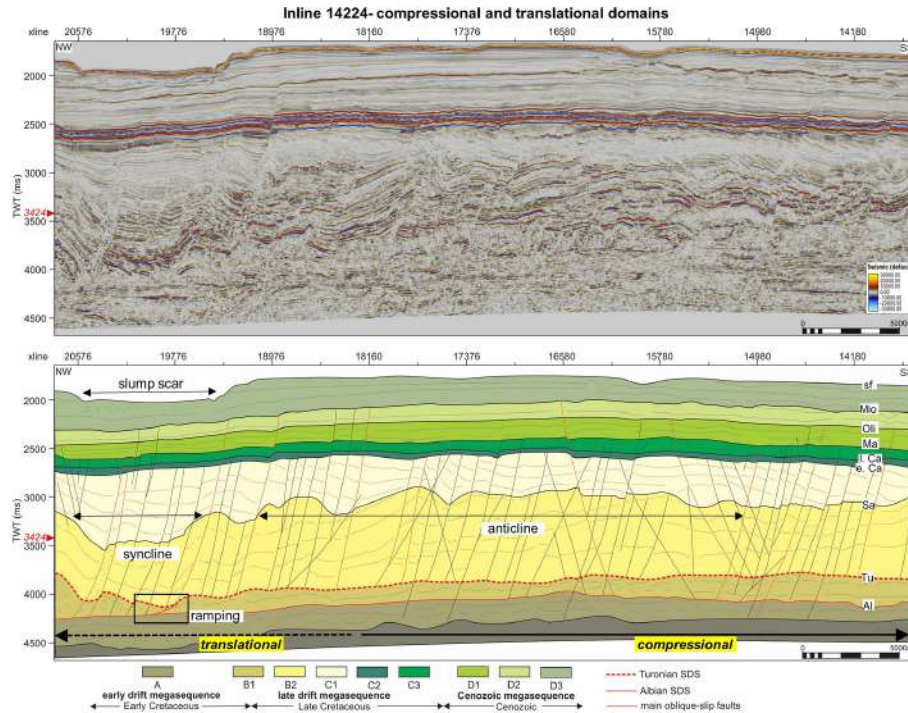


Figure 7. Uninterpreted and interpreted sections of inline 14224 showing the compressional domain and position of time slice 3424. The section lies roughly along-strike the DWFTBs giving a view of the oblique-slip faults that crosscut them. Present-day slumping is evident above a Late Cretaceous syncline. Abbreviations: A – Albian; Tu – Turonian; Sa – Santonian; Ma – Maastrichtian; Oli – Oligocene; Mio – Miocene; sf – seafloor; SDS – shale detachment surface. Vertical exaggeration: 5.

4.1.2 Cenozoic (D1–D3)

Influential data and edge detection horizon-based attributes were used to enhance the 3D geometric variation in erosional features observed upon the Oligocene and Miocene Cenozoic stratigraphic markers (Fig. 10). The lowermost Cenozoic sequence corresponds to the D1 and forms a 450–100 m seaward-thinning wedge (Fig. 6). It is characterized by low-amplitude, parallel seismic reflections which downlap the Maastrichtian surface mostly in the translational domain (Fig. 8). Sequence D1 (and a small upper portion of the underlying C3 in the translational domain, Fig. 8) is erosionally truncated by a SE–NW-trending submarine canyon running perpendicular to the slope (Fig. 10a, b). From the observation of the transitional domain regional section (Fig. 8), the canyon is situated above a ~ 1.3 km wide horst from the Late Cretaceous B2 sequence with opposite dipping normal faults. The horst forms a large antiformal anticline with chaotic internal reflectors observable in sequence B2 and outlined in Fig. 8. The canyon is ~ 2.3 km wide with a visible length of 13 km, which extends beyond the seismic dataset (Fig. 10a, b). Onlapping against the walls of the canyon and overlying the Oligocene surface is the 100–200 m thick D2 sequence (Fig. 8). It comprises low-amplitude, parallel reflectors with some chaotic sections. More than one erosional event is evident both before and after the main Oligocene unconformity

surface as reflectors within sequences D1 and D2 have been erosionally truncated.

The Miocene stratigraphic marker is a medium-to-high-amplitude surface which cuts the upper D2 reflectors (Figs. 8 and 11c, d). It is an irregular unconformity surface characterized by a series of multiple NW–SE-trending, sinusoidal crosscutting channels (Fig. 11c, d). Individual channels are ~ 500 m in width with a long axis trending parallel to the slope and hence continental margin. The channels form a ~ 14 km wide zone in the upper continental slope between ~ 1200 – 1500 m b.s.l. (Fig. 2). The large extent of crosscutting and overlapping makes it difficult to differentiate between individual channels and their lateral extents. Sequence D3 is the youngest Cenozoic, and therefore uppermost, sequence. It forms a 100–350 m seaward thickening wedge (Fig. 6) characterized by medium-to-low-amplitude, mounded to parallel reflectors. Basal sediments of sequence D3 are mounded in geometry for approximately 80 m, whereas earlier sediments were deposited continuously in a parallel manner (Figs. 6 and 7). The youngest stratigraphic marker, the seafloor, is a very high-amplitude and thick surface. Slumping, characterized by chaotic internal reflectors, is evident on the present-day seafloor (seen in the northwest in Fig. 7 and a portion of Fig. 9). The slump scar is ~ 7 km in width, sitting directly above the region of a large Late Cretaceous syncline (B2 sequence) (Fig. 7).

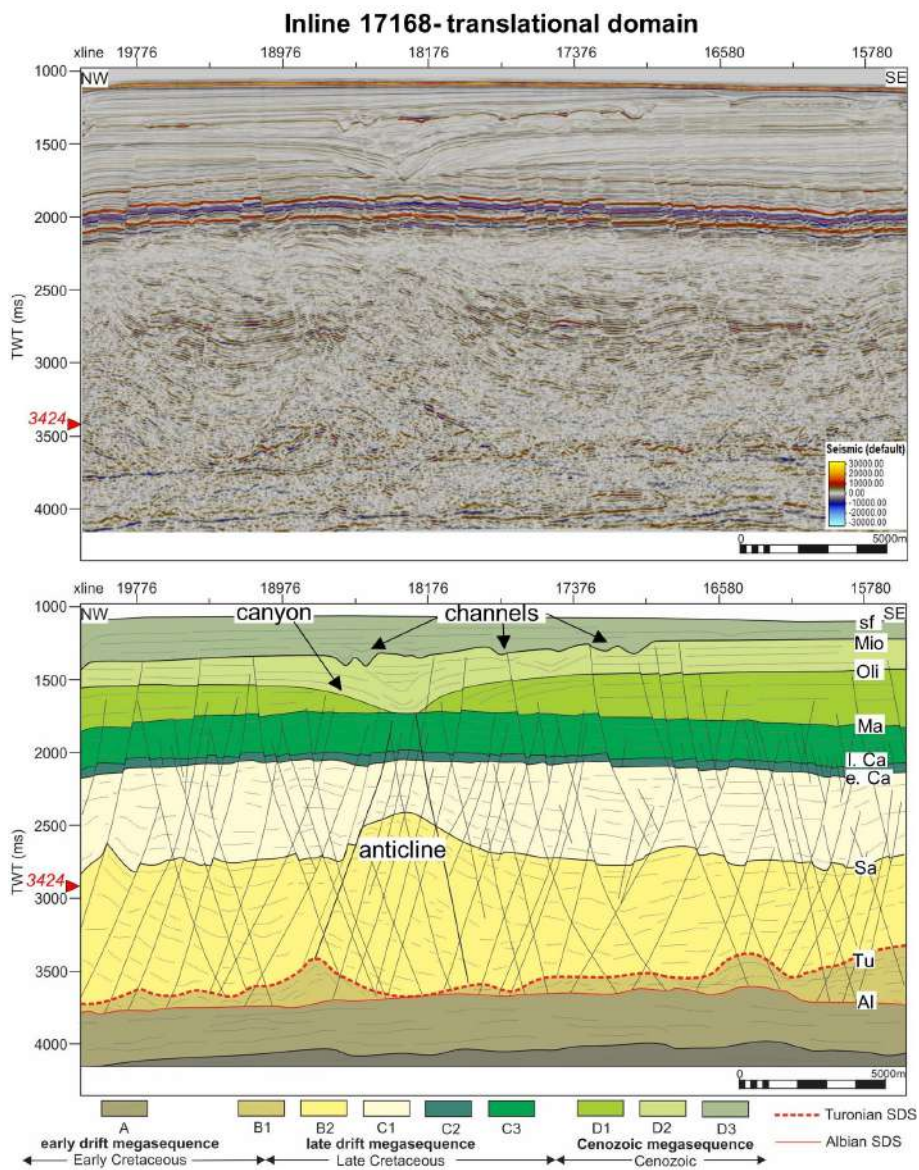


Figure 8. Uninterpreted and interpreted sections of inline 17 168 showing the translational domain and position of time slice 3424. Normal faults extend to the Albian surface at depth and upwards into the Cenozoic megasequence with some terminating at Oligocene or Miocene unconformity surfaces. Abbreviations: A – Albian; Tu – Turonian; Sa – Santonian; Ma – Maastrichtian; Oli – Oligocene; Mio – Miocene; sf – seafloor; SDS – shale detachment surface. Vertical exaggeration: 5.

4.2 Structural framework

The sedimentary succession comprises several sedimentary packages displaced by a complex structural framework of faults, as shown in Figs. 5 and 11. Since the seismic volume is heavily faulted (over 500 manually picked), the only faults included in the structural framework in Figs. 5b and 11a were large, first-order faults greater than ~2 km laterally. Faults terminate at either the early Campanian, Oligocene, or Miocene surfaces and originate from Turonian or deeper Albian surfaces depending on their location with respect to

the DWFTB system. Upon closer inspection, and the use of the variance seismic attribute, it is evident that some faults extend past the lower Albian surface for both the compressional (Figs. 6a and 7) and the translational domains (Fig. 8). As explained previously, Fig. 5a shows the variance attribute in TWT at time slice 3424 ms, which was used to enhance the lateral continuity of faults. The position of the variance time slice is shown on the regional sections (Figs. 6, 7, and 8). Using the regional sections (Figs. 6, 7, and 8) and Figs. 5 and 11, the structural framework is described in relation to the compressional and translational domains in the following

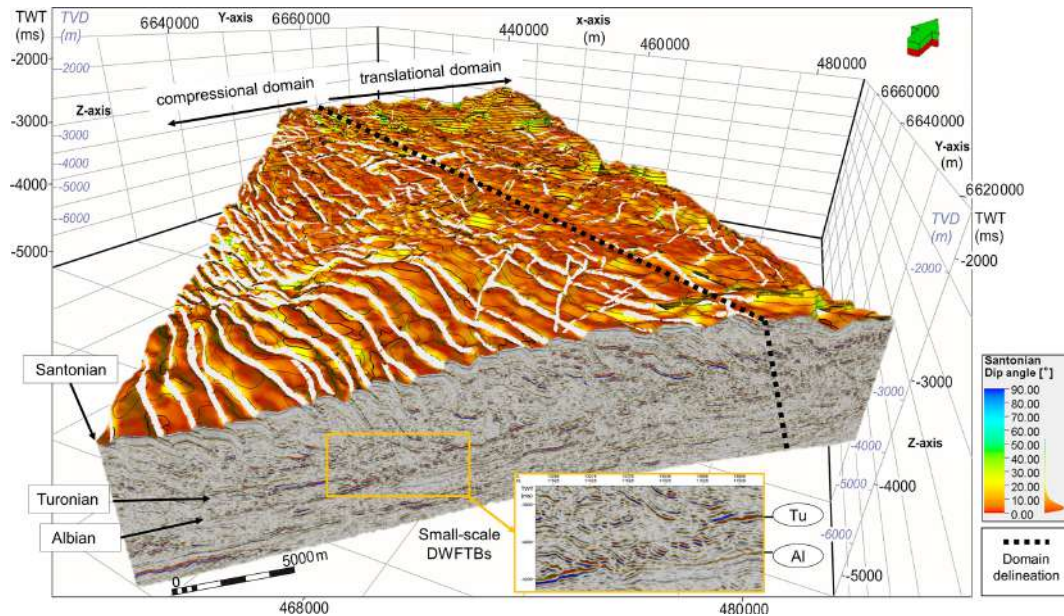


Figure 9. Three-dimensional view of a crossline showing an extensive, kilometre-scale DWFTB system detaching the Turonian slip surface, the Santonian horizon (in dip angle) defining the crest of the large folds, and an underlying localized set of secondary, small-scale DWFTBs upon the Albian slip surface. Vertical exaggeration: 5.

subsections as the geometry and displacement characteristics of each domain differ greatly.

4.2.1 Compressional domain

DWFTBs occur down-dip in the compressional domain with slip mainly upon the Turonian seaward-dipping surface (Figs. 6, 7, and 9). Imbricate thrust faults detach mostly against the Turonian surface, with some extending to the Albian surface at depth and fewer continuing to greater depths. Thrust faults terminate either just below or at the early Campanian surface within the C1 late drift sequence (Fig. 6). Faults are relatively equally spaced between 1.6–2 km, with average displacements of 250 m (Fig. 6). Thrust faults strike NW–SE and dip between 22–45° NE with generally lower dip angles where they detach from the Turonian or Albian surfaces at depth (Figs. 6 and 11a, b). Thrust sheets are segmented and displaced by extensive oblique-slip normal faults measuring up to ~20 km in length (Figs. 5, 7, and 12a, b). Figure 7 is a distal inline section (see Fig. 5c) showing a few normal, oblique-slip, and thrust faults extending past the Turonian to the Albian surfaces at depth. In Fig. 7 the upward vertical extent of oblique-slip faults terminates along the Maastrichtian to Miocene surfaces, while normal faults terminate between the Campanian (early and late) to Maastrichtian surfaces.

Oblique-slip faults strike NE–SW (Figs. 5 and 11a, c) with average dip-slip offsets of ~80 m (Fig. 7). The strike-slip displacement between each thrust sheet segmented is variable showing mainly sinistral (left-lateral) motion. They

dip on average between 40–70° mostly to the NW with the few dipping SE in the south showing right-lateral dextral slip motion (Figs. 5 and 11a, c). In the compressional domain, the concave upwards, NW-dipping oblique-slip faults display a roughly oval-shaped pattern or geometry in plan section (Figs. 5 and 11a). This central zone forms a very broad anticline in sequence B2 (Turonian to Santonian stratigraphic markers) observed SE of the syncline previously mentioned in Fig. 7 (see Fig. 5a, c for location). Down-dip, this central zone is not as heavily faulted as its surroundings but contains smaller ~2 km length normal faults dipping both NW and SE with some displaying overlapping or step-like, en-echelon-type geometries (Fig. 5). Up-dip, thrust segmenting oblique-slip faults have the greatest strike-slip offsets (~250 m) towards the translational domain (Fig. 5c). Along-strike, sinistral oblique-slip displacements decrease proximally towards the translational domain compared to the down-dip compressional domain until only normal dip-slip motion occurs where a few thrust sheets are present (Fig. 5). A deviation from the sinistral motion of displacement is seen S of the study area, as occurring just outside the oval-shaped region in plan section shown in Figs. 5a and c and 11a. Here, the oblique-slip faults dip to the west and southeast and show dextral (right-lateral) slip motion in contrast to those in the rest of the study area (Fig. 5). This more structurally complex region has smaller localized sets of fold-and-thrust belts occurring below the kilometre-scale DWFTB system (Figs. 6 and 9). The smaller-scale DWFTBs occur within sequence B1, detaching from the Albian surface. The smaller set of secondary DWFTBs is less well-defined and weakly

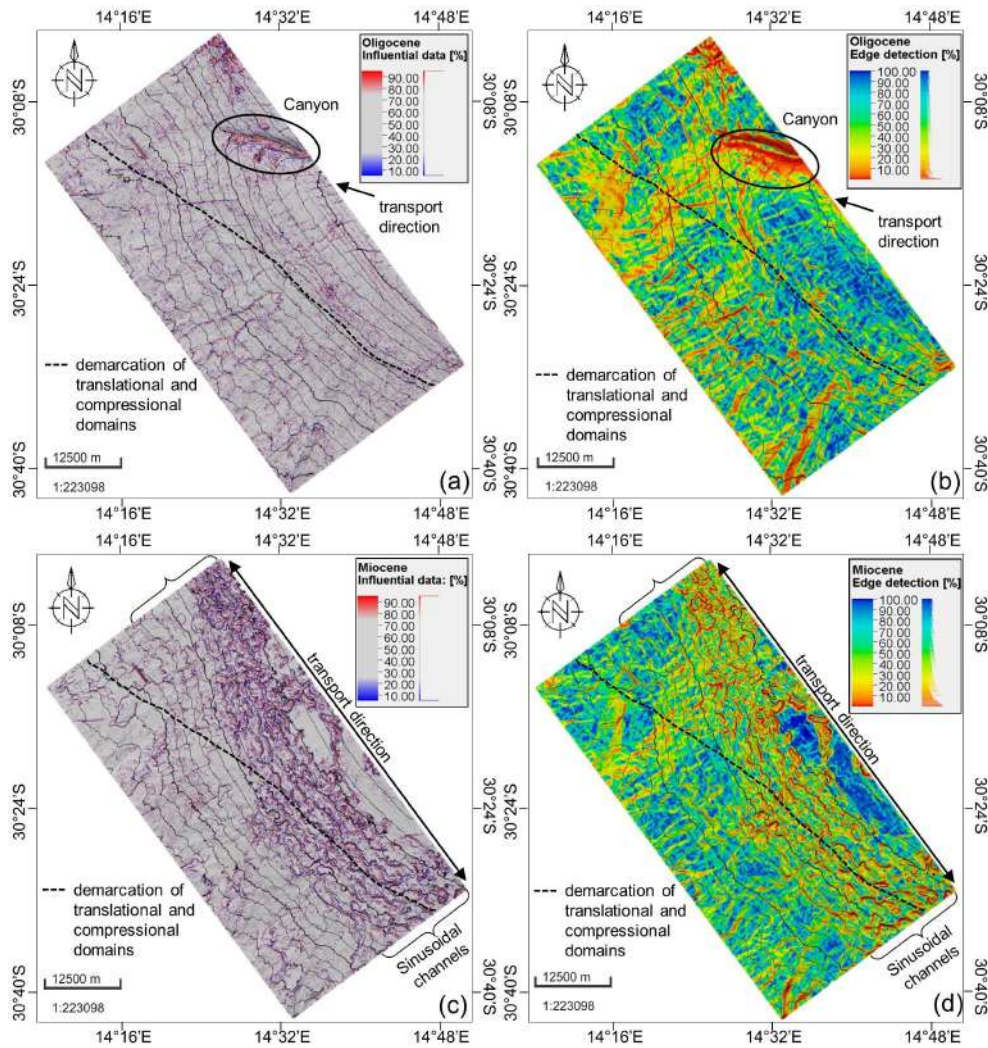


Figure 10. Cenozoic horizons showing the canyon-channel systems. Oligocene canyon formed by a downslope turbidity current viewed using the (a) influential data and (b) edge detection attributes. Miocene sinusoidal channels formed by an along-strike bottom current viewed using the (c) influential data and (d) edge detection attributes. Vertical exaggeration: 5.

folded with smaller thrust spacings of ~ 250 m and displacements below the seismic resolution limit compared to those of the overlying kilometre-scale DWFTBs. Similar sets of clear, small-scale DWFTBs are found in other portions of the compressional domain between the Albian and Turonian surfaces.

4.2.2 Translational domain

From east to west the translational domain is characterized mainly by normal faults, followed by laterally extensive oblique-slip faults and a few segmented thrust faults in the down-dip direction (Figs. 5, 6, and 11a). Most normal and oblique-slip faults in the proximal translational domain extend from the Albian surface, at depth, and terminate between the late Campanian to Miocene surfaces (Fig. 8). The greatest dip-slip fault displacements of normal and oblique-

slip faults occur within sequence B2, between the Turonian to Santonian surfaces for both the compressional and translational domain, with offsets reaching up to 80 m (Figs. 6, 7, and 8). Normal faults observed in the study area have shorter lateral extents in comparison to thrust and oblique-slip faults, reaching up to 13 km (Fig. 5). Like oblique-slip faults, they dip $50\text{--}70^\circ$ on average, with a NE–SW orientation perpendicular to thrust faults of the compressional domain (Figs. 5 and 11a, c). Along individual fault planes, dip angles as low as $\sim 30^\circ$ may occur at depth, while the higher dip angles occur in stratigraphically higher sequences (Fig. 11 c).

In the north of the study area, laterally extensive NW-dipping normal faults (>5 km) form conjugate pairs with laterally shorter normal SE-dipping faults (<2 km length) (compare Fig. 5 with Fig. 8). The overarching dominant fault directions are evident in Fig. 5b, as compared to those seen

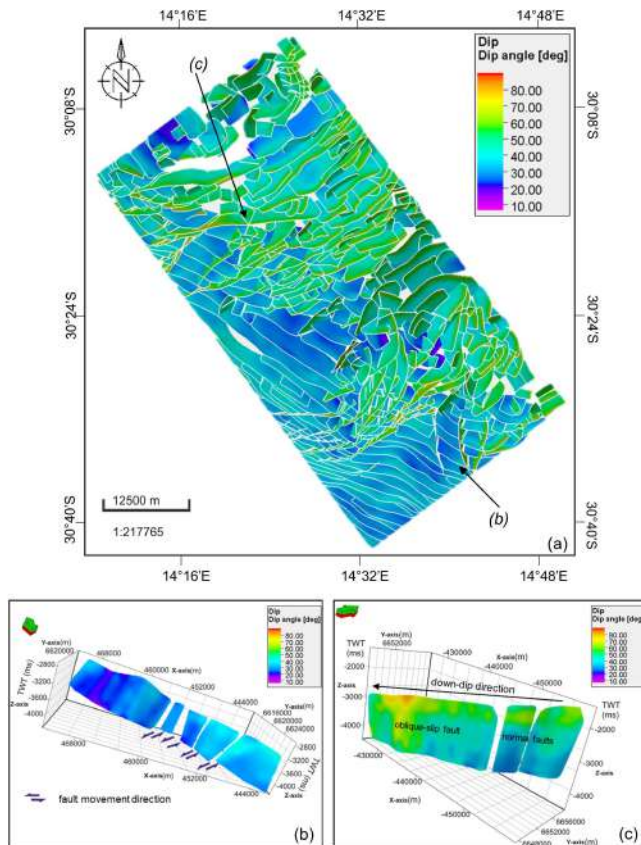


Figure 11. Structural framework faults interpreted in the study area showing (a) plan view of all dipping faults; (b) segmented shallow-dipping thrust fault showing left lateral (sinistral) slip motion of displacement in 3D; and (c) steeply dipping normal and oblique-slip fault extending between both the translational and down-dip compressional domains in 3D.

in the interpretation of the regional section (Fig. 8) since all faults, regardless of their lateral length, were interpreted in the 2D seismic sections. The centre of the translational domain to the east of the study area then becomes dominated by SE-dipping normal faults (Fig. 5b). In the south, SW-dipping faults dominate (Fig. 5b). Second-order normal faults (those that originate from a large first-order fault) are common in the late drift to early Cenozoic megasequences. These attach to the main faults at acute angles with intersections in megasequence C (Fig. 8). Due to their small vertical and lateral extent (<2 km), they were not included in the structural framework shown in Figs. 5b and 11a given that this study focusses on the regional-scale structures affecting basin evolution.

5 Discussion

5.1 Stratigraphy of the Late Cretaceous SW African margin

The architectural stratigraphy of the deep-water Orange Basin is explained primarily from regional section Fig. 6 because of its perpendicular orientation to the SW African palaeo- and current coastline, which was also parallel to the direction of sediment transportation. Terrigenous sediments observed in the Orange Basin were transported offshore by the Orange and Olifants river systems and their ancestral equivalents (Fig. 1). To understand the full stratigraphic framework of the SW African margin we present our interpretations of the deep-water Orange Basin stratigraphy and discuss what has been observed from previous Orange Basin studies from shallow to deep-water environments.

5.1.1 Influence of multiple shale detachment surfaces

Key surfaces in the Late Cretaceous megasequence are the Albian and Turonian stratigraphic markers upon which small-scale and large-scale DWFTB systems are found, respectively. The sequence between these two stratigraphic markers (sequence B1 in this study) is comprised of organic-rich shales as revealed from well log data recovered from DSDP 367 and well A calibrated by Baby et al. (2018) in the Orange Basin. The Albian and Turonian markers are MFSs corresponding to the 14At1 and 15At1 shales (Fig. 4; Brown et al., 1995), upon which gravitational sliding occurs (Fig. 6). These shale detachment surfaces are also proven source rock intervals in the basin and are thus of great significance for hydrocarbon potential (Fig. 4; van der Spuy, 2003). Subtle ramps in the early drift (sequence A) and beginning of the late drift megasequence (sequence B1) have linked these multiple levels of basal slip giving rise to a complex range of geometries both within and above the DWFTB systems (e.g. Fig. 7).

Two important factors controlling gravitational collapse within a basin include the stratigraphy of the margin and thickness of the detachment surface (Rowan et al., 2004; Dalton et al., 2017). In the Orange Basin these factors vary due to the presence and distribution of multiple basal overpressurized shale detachment surfaces (de Vera et al., 2010; Kuhlmann et al., 2010; Dalton et al., 2017). Once enough overburden material has accumulated in the basin, combined with a lack of cohesion along a weak, sloping detachment surface, gravitational sliding occurs (Rowan et al., 2004; Morley et al., 2011). Rapid sedimentation rates with resultant high internal pore fluid pressures, seismicity, downslope undercutting, and tilting glide planes are the main trigger mechanisms responsible for slope failure leading to gravitational collapse (Séranne and Anka, 2005; Rogers and Rau, 2006; Kuhlmann et al., 2010).

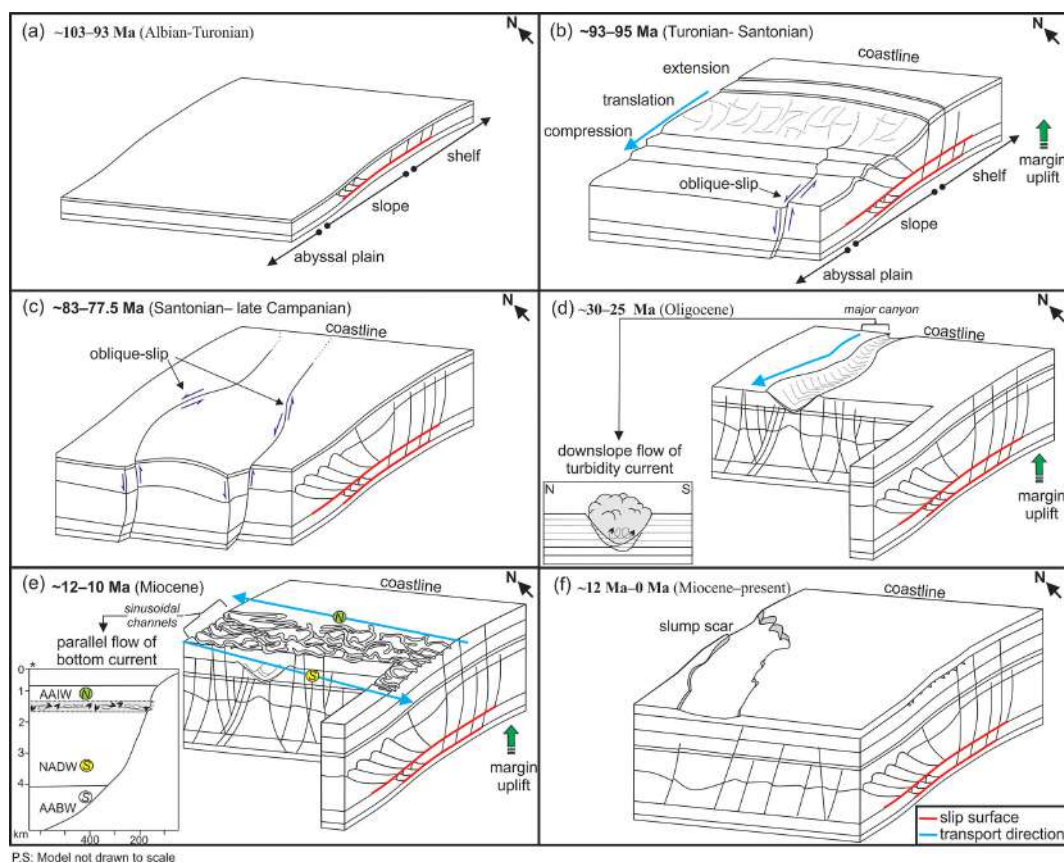


Figure 12. Temporal model of the evolution of the deep-water Orange Basin from the Late Cretaceous DWFTB system to the mass transport complexes of the Cenozoic. For a detailed explanation the reader is referred to Sect. 5.4. Insert diagram in panel (e), denoted by *, is modified after Weigelt and Uenzelmann-Neben (2004).

Dalton et al. (2017) present a model for the temporal evolution of a gravity collapse system in the Orange Basin containing multiple shale detachment surfaces whereby (1) gravitational collapse initiates in the translational domain (according to Dalton et al., 2015) upon an initial upper detachment surface, followed by up-dip extension and then down-dip compression; (2) once the initial detachment surface can no longer accommodate sliding (e.g. due to thinning of the detachment surface or possibly a change in shale overpressures), the gravitational system will lock and deformation will cease; (3) stress and strain is redistributed as extensional faults penetrate to a stratigraphically lower shale detachment surface; (4) once the shales are sufficiently compacted (Dalton et al., 2015), a compressional zone forms down-dip upon this lower shale detachment surface; (5) if more shale detachment surfaces exist at depth, even older gravitational collapse systems will form following locking and fault renewal with increasing strain. This model implies a downward rather than upward propagation of faults accounting for the formation of underlying smaller DWFTB systems upon an older shale detachment surface. In this study, however, we propose the smaller, localized folds and thrusts observed below the

main, kilometre-scale Late Cretaceous DWFTB system simply represent an older gravitational collapse system in older sediments.

5.1.2 The Late Cretaceous DWFTB system

The strongly mounded geometry in sequence B1 reflects basin floor sediments of the translational domain (Fig. 8; Baby et al., 2018). Due to the loss of seismic resolution with depth in very poorly seismically imaged areas, the geometry of basin floor turbidite sediments may be erroneously misinterpreted as smaller-scale DWFTBs upon the Albian shale detachment surface. Careful inspection was therefore required to properly differentiate between one type of mass flow or transport system from another, especially within the poorly imaged B1 sequence. Overlying the Turonian shale detachment surface is a much larger-scale DWFTB system within late drift sequences B2 and C1, showing that major gravitational collapse began during the Turonian. The folded anticlines of the gravitational system are antiformal as the stratigraphic sequence does not appear to be refolded, and subsequently associated synclines are synformal. The major basal shale detachment surface is the Turonian as shown

throughout the seismic volume (Figs. 6, 7, and 8) and recognized throughout the Orange Basin (e.g. Paton et al., 2008; de Vera et al., 2010; Scarselli et al., 2016), while the Albian is minor with smaller, localized fold and thrust faults detaching it in a few areas.

The downslope compression of sediment from the up-dip extensional (not imaged) and translational domains thickened and strongly folded sequence B2 during gravitational sliding, with the greatest thickness shown to have occurred at the onset of compression (Figs. 6 and 9). The irregularity and discontinuous nature of the Turonian surface is likely caused by the thinning out of the surface under the weight of the thick overlying B2 sequence as it slid seawards with progressive deformation. The large thickness of sequence B2 indicates high sedimentation rates during the Coniacian to early Campanian. In comparison, the overlying sequence C1 is thinner, weakly folded, and has smaller thrust displacements suggesting a syn-kinematic relationship whereby thrusting was still active and contemporaneous with the deposition of these Santonian to early Campanian sediments. In the translational domain the onlap and downlap of sequence C1 upon the Santonian surface (shown well to the northeast in Fig. 6 and northwest in Fig. 7) indicate a localized increase in accommodation space above the translational domain during the downward compression and translation of sediment (Fig. 6). Onlap may also imply lower sedimentation rates relative to deformation which is evidenced by the dramatic thinning of Santonian sediments seawards (Fig. 6). Downslope thrusting is proposed to have ended by the end of the late Campanian. This is shown through the change in configuration patterns of sequence C2 from weakly folded reflections at the base of the sequence to unfolded, parallel reflections at the top of the sequence (see Fig. 6). This observation correlates with that of a DWFTB system observed directly north of the study area in the Namibian Orange Basin (Fig. 1) where the estimated end of gravitational deformation is also postulated within Campanian sediments (~ 83 Ma) from the analysis of growth stratal patterns (Fig. 1; de Vera et al., 2010). The early Campanian sediments, sequence C2, are interpreted to have been deposited under normal to moderate rates of sediment supply as reflections are conformable and continuous and the proximal to distal thickness of the sequence does not change considerably. Sequence C3's late Campanian to Maastrichtian sediments thin seawards with the distal decrease in sediment supply. The Santonian, early Campanian, late Campanian, and Maastrichtian surfaces correspond to the 16Dt, 17At1, 18At1, and 22At1 stratigraphic markers (erosional or non-depositional surfaces) (Fig. 4; Brown et al., 1995; PASA, 2017).

The Early Cretaceous post-rift megasequence retrogradationally reflects the change from subaerial conditions during the emplacement of the SDRs (syn-rift succession) to an open marine environment with a narrow oceanic basin between the late Hauterivian and Albian (de Vera et al., 2010; Baby et al., 2018). As the margin continued to deepen with

retrogradation during the late Albian to early Turonian, a well-defined depositional profile with shelf, slope, and basinal elements began to form (Light et al., 1993; Baby et al., 2018). The Late Cretaceous post-rift megasequence is comprised of aggradational to progradational packages reflecting increased sedimentation rates and a decrease in subsidence from the early Turonian to late Maastrichtian (~ 93.5 – 66 Ma) attributed to the late Campanian sea-level fall with major uplift and seaward tilting of the margin which eroded and transported sediments to the Orange Basin as supported by thermochronometric data (Paton et al., 2008; Granado et al., 2009; de Vera et al., 2010; Kuhlmann et al., 2010; Hirsch et al., 2010; Baby et al., 2020). This period in time records the greatest flux in sedimentation offshore of the SW African margin with the Orange Basin showing lower rates and volumes between 81 and 66 Ma (Baby et al., 2020). The Maastrichtian stratigraphic marker (22At1) is a maximum regressive surface and transgressive ravinement surface as it separates the Cenozoic retrogradational megasequence from the underlying Late Cretaceous progradational megasequence (Fig. 4, Baby et al., 2018).

5.2 Structure of the Late Cretaceous DWFTB system

The kinematics, geometry, and displacement characteristics of structures seen within the translational and compressional domains imaged in this study differ greatly from each other. We discuss the structural variability of the two domains imaged to assess the strato-structural evolution of the Orange Basin from the Late Cretaceous DWFTB system to overlying Cenozoic deposits.

5.2.1 Compressional and transitional tectonics

The structural framework reveals a gradational change between translational and compressional tectonics, with normal and oblique-slip faults dominating proximally and thrust and oblique-slip faults dominating distally (Figs. 5b, 11a). Landward-dipping imbricate thrust faults with seaward-verging folds are recognized in the compressional domain (Figs. 5, 6, 9, and 11a). The NW–SE-orientated thrust faults dip gently landwards, detaching the Turonian shale detachment surface and terminating at the early Campanian surface (Fig. 6). A few thrust faults reach the Albian shale detachment surface at depth and even extend past into stratigraphically lower sequences (Figs. 6 and 8). This shows that renewed faulting caused by gravitational deformation in the Late Cretaceous DWFTB system occurred preferentially along the older pre-existing planes of weakness. Most normal and oblique-slip faults in the proximal region detach the Albian shale detachment surface at depth and terminate in stratigraphically younger Cenozoic sediments at either the late Campanian, Oligocene, or Miocene surfaces (e.g. Fig. 8). In like manner as the thrust faults terminating at the early Campanian surface in the distal compressional re-

gion, it is possible that normal and oblique-slip faults in the proximal region initially terminated at this stratigraphically lower surface. With the subsequent deposition of overlying sediments, however, faults were renewed to propagate upwards into stratigraphically younger sequences, accommodating further increments in strain. This supports the idea that once formed, a fault or fracture will always represent a mechanical zone of weakness to be exploited (Viola et al., 2012).

Oblique-slip faults, formed from the combination of tension and shearing during the down-dip translation of sediment, crosscut thrust sheets orthogonally and thus post-date them. We interpret en-echelon-type and stair-stepped geometries of the small normal faults observed in the centre of the compressional domain imaged in Figs. 5 and 11a to be indicative of lower rates of tensional shear. This is because they are relatively small (~ 2 km in length laterally) in comparison to the kilometre-scale oblique-slip faults they are bound within, which indicate higher rates of tensional shear. The outer oblique-slip faults accounting for the oval geometry observed in plan view in Fig. 5 are shown to have rotated the Turonian to Santonian (sequence B2) sediments (Fig. 7). The observed strike-slip offset for each oblique-slip fault represents the hanging wall and footwall blocks of each thrust sheet since hanging wall and footwalls have the opposite sense of motion (Benesh et al., 2014). The downslope vertical shortening of oblique-slip faults from the translational to compressional domains is shown from regional section Fig. 8 (translational) to Fig. 7 (compressional) and furthermore illustrated in Fig. 11c. Over and above the decrease in basin thickness from proximal to distal settings, explained previously in Sect. 5.1, we attribute this shortening to the decrease in tension and shearing during the downslope translation of sediment. Other DWFTB systems exhibiting similar behaviour to that observed in this study are found in the Niger Delta, containing multiple shale detachment surfaces and oblique-slip faults segmenting thrust sheets along strike (Rowan et al., 2004; Benesh et al., 2014).

5.2.2 Extensional tectonics

Although the extensional domain is not imaged in this study, other studies of DWFTB systems in the Orange Basin may be used to address the structural framework in the extensional domain; see, e.g., Paton et al. (2008), de Vera et al. (2010), and Scarselli et al. (2016). Down-dip compression is linked to the up-dip extension domain as shown from fully imaged DWFTB systems in the Orange Basin (Fig. 3; de Vera et al., 2010). Listric growth faults dip seaward in the extensional domain, while thrust faults dip landward in the compressional domain and thus display an overall an arcuate geometry in 3D (de Vera et al., 2010; Scarselli et al., 2016). The same geometry may be deduced in this study which lies directly south of the DWFTB system observed by de Vera et al. (2010) and shown in Fig. 3. The unimaged extensional

domain of the DWFTB system in the study likely lies along the continental shelf.

5.2.3 Geometry of structural framework

Looking at the overall structural framework, the dominant azimuthal dip direction in a clockwise direction changes from NE- to NW-dipping to SE- to SW-dipping faults (Fig. 5b). Normal and oblique-slip faults dip steeply with NE–SW-orientated strikes in contrast to the gently dipping orthogonal NW–SE thrusts, formed by down-dip contraction. Most structural lineaments and the elongation of plutons and igneous intrusions along the SW African margin are orientated parallel to the regional NW–SE foliation trend of the margin, with the exception of a few complexly faulted regions (Wildman et al., 2015). Thrust faults imaged in this Orange Basin study follow this same NW–SE predominant trend. We deduce the same for the up-dip extensional domain based on other DWFTB systems in the region (e.g. Fig. 3; de Vera et al., 2010; Scarselli et al., 2016). Normal and oblique-slip faults, however, trend orthogonally to the thrust faults (Figs. 5, 11a) and regional foliation of the margin (Fig. 1). Notably, oblique-slip faults are orientated parallel to the deep-seated, underlying Rio Grande and Aghulhas–Falkland fracture zones which accommodated dextral slip motion during rifting of the SW African margin (Fig. 1; Light et al., 1993; Séranne and Anka, 2005). Most oblique-slip faults in the study, however, segment thrust sheets in a sinistral mode of motion apart from the region in the south (Fig. 5a, c). The left-lateral sinistral sense of motion (Fig. 5c) may indicate gravitational collapse initiated in the south and moved northwards, with each subsequent thrust sheet moving seawards. The oblique-slip faults acted as planes for the lateral displacement of each thrust sheet.

In the southern region of the studied volume, the kinematics and geometry of the structural framework differ. Here, right-lateral dextral slip motion of thrust sheets is observed, which is associated with opposite SW-dipping normal and oblique-slip faults (Fig. 5). The change in geometry and sense of movement may represent the outer oblique-slip faults of another gravitational collapse system south of the studied volume. This is shown and described by Scarselli et al. (2016) north of the present study between 350–1300 m water depths along the upper continental slope of Namibia. Both 2D and 3D reflection seismic data reveal a fuller DWFTB system including the up-dip extensional domain with seaward-dipping listric growth faults and connected sidewall faults rotating Late Cretaceous sediments to form rollover anticlines in gravitational collapse systems. The outer oblique-slip faults described centrally in this study are analogous to the sidewall faults they described for each megaslide complex showing lateral downslope motion with gravitational collapse. The megaslides occur adjacent to each other with opposite N- and S-dipping sidewall faults, forming horst structures separating each megaslide. This too de-

scribes and accounts for the change in geometry and kinematics of the structural framework in the south of the present study. Notably, however, most of the main outer oblique-slip faults in the study dip in the same NW or N direction. Only the northern outer oblique-slip fault is shown in Fig. 7 (see location of regional line in Fig. 5b), which is where a Late Cretaceous syncline and seafloor slump scar is found.

5.2.4 Translational domain implications

There are two different schools of thought in what the translational domain represents:

1. A zone caused from the central shift in contact between extensional and compressional tectonics containing overprinted features of both (Butler and Paton, 2010; de Vera et al., 2010). This was proposed due to the crosscutting relationships observed in the distal parts of the extensional domain.
2. A fixed package of mostly undeformed rock representing a short wavelength change from extensional to compressional tectonics (Bilotti et al., 2005; Corredor et al., 2005; Krueger and Gilbert, 2009; Dalton et al., 2017).

In previous Orange Basin studies, the transitional/translational domain was interpreted as a relatively narrow region (~ 10 km in length perpendicular to the slope) considering the massive extent of a complete (roughly ~ 220 km) DWFTB system (Corredor et al., 2005; Krueger and Gilbert, 2009; de Vera et al., 2010; Dalton et al., 2017). In this study, the true extent of the translational domain cannot be constrained since the linked up-dip extensional domain is not imaged. Nevertheless, what is observed is that the translational domain reaches and is greater than ~ 20 km in width, as observed in the north of the studied volume. We therefore propose a third model for what the translational domain represents: a zone displaying overprinted features of both extensional and compressional tectonics, depicting a long wavelength change between the up-dip and down-dip domains with the downslope translation of sediment accommodated by extensive oblique-slip faults.

Overlapping compressional and extensional tectonics may be described in terms of the misbalance in strain observed in other Orange Basin studies. In linked DWFTB systems, the amount of extension should equal the amount of compression; this is however not the case as reflected through the approximate 5 % missing strain observed in favour of extension accounted for in second-order, compressional structures within the extensional domain itself (Butler and Paton, 2010; de Vera et al., 2010; Dalton et al., 2015). The lack of a down-dip compressional domain in the outer reaches of some of these systems, as noted by Dalton et al. (2015) for the Orange Basin, is proof that the 5 % missing strain is accommodated for internally. In like manner, the overlapping and crosscutting relationships observed in the transitional domain are the

system redistributing strain internally. In response to up-dip extension, down-dip compression occurs and with progressive deformation oblique-slip faults act as lateral ramps to accommodate strain with the growth formation of each subsequent thrust sheet. Further small-scale extension occurs within each individual thrust sheet to accommodate strain with gravitational collapse as evidenced by the en-echelon- and step-type normal faults in the compressional domain.

5.3 Cenozoic stratigraphy of the SW African margin

5.3.1 Canyon-channel systems

One of two major features recognized in the Cenozoic megasequence is a large SE-to-NW-orientated canyon which defines the Oligocene erosive surface (Figs. 8, 10a, b). The canyon eroded the underlying early Oligocene (sequence C3, which downlaps the Maastrichtian surface) to late Campanian (sequence D1) sediments (Fig. 8). Sequence D2, the sedimentary infill of the canyon, onlaps against the main Oligocene erosional surface and ensuing erosional surfaces. The Oligocene canyon is interpreted as having been formed by the erosive action of a turbidity current with downslope canyoning possibly deflected by a strong northward-flowing oceanic current since its orientation is not perfectly perpendicular to the continental slope. Turbidity currents are episodic sediment gravity-driven flows that always flow downslope, unless the local morphology (such as the presence of marginal troughs) forced slope-parallel flow (Shanmugam, 2008; Shumaker et al., 2016). The infill of the canyon (sequence D2) displays some chaotic internal reflections possibly diagnostic of a turbidite (Fig. 8).

The second major feature in the Cenozoic are the extensive margin-parallel sinusoidal and overlapping channels, defining the Miocene erosive surface (Figs. 8, 10b, c). These erosional features are interpreted to have been formed by sub-circular water and/or sediment motions flowing parallel to the margin (i.e. erosive deep-water bottom currents) due to their margin-parallel orientation. Supporting this interpretation is the fact the channels are confined between specific isobaths along the palaeo-slope with the base of the overlying sequence D3 displaying mounded geometries indicative of mass flow (Figs. 8, 10c, d). The margin-parallel sinusoidal channels are in contrast to the roughly slope-perpendicular Oligocene canyon proposed to have been formed by a turbidity current (Fig. 10). A bottom current that remains active over prolonged periods of time (i.e. millions of years) will affect sedimentation on the ocean floor, from the winnowing of fine-grained sediments to large-scale erosion and deposition of coarse-grained sediments (Shanmugam, 2008; Rebesco et al., 2008). Strong bottom currents preserve slope-parallel erosional features reflecting the contoured flow of either a thermohaline-, wind-, or tidal-driven (baroclinic currents) deep-water bottom current (Shanmugam, 2008). Temperature and/or salinity differences in bodies of water along

the continental slope cause vertically stratified water layers of different densities resulting in baroclinic or geostrophic flow.

Chaotic internal reflections of sequence D3 and the depression of the seafloor characterize a major slump scar reflecting margin instability in Fig. 7. Internally, slumps are highly deformed due to their rotational movement upon a concave-upward glide plane (Shanmugam, 2017). The slump scar is located directly above a syncline within Late Cretaceous sediments (sequence B1) showing the underlying structural control of the Late Cretaceous DWFTB compressional domain. Faults from the gravitational system, however, are not shown to reach the seafloor but rather terminate along the Miocene stratigraphic marker unless their displacements are below the seismic resolution limit (Fig. 7). Notably, both the Oligocene and most of the Miocene canyon-channel systems are located above the transitional domain. The position of the Oligocene canyon initially appears to be fault controlled since it occurs directly above two opposite dipping faults, forming a horst and graben feature in Fig. 8. In 3D, however (see Fig. 5), both the Oligocene canyon and Miocene channels do not appear to be influenced by the underlying tectonics of the Late Cretaceous since they do not follow the trend of underlying faults. Rather, the vertical propagation of faults in the transitional domain was hindered by the mass flow deposits overlying the Oligocene and Miocene stratigraphic markers.

5.3.2 Role of tectonics and oceanographic circulation on Cenozoic sedimentation

The SW African margin is characterized mainly by retrogradational sequences in the Cenozoic (e.g. Baby et al., 2018) with elevated sedimentation rates occurring in the Oligocene between ~ 30 – 25 Ma (Baby et al., 2020). The Oligocene stratigraphic marker corresponds to a major event recognized in literature and seen throughout the African shelf (Fig. 4; Siesser and Dingle, 1981; Miller et al., 1995; Séranne and Anka, 2005). It was caused by margin uplift resulting in a relative sea-level fall (possibly beyond the shelf break which is a topic of controversy in literature) and is evidenced by; tilting topsets in the Walvis Basin, and a 350 m difference in elevation between the late Eocene and Oligocene shorelines of the northern Orange Basin at ~ 30 Ma, as observed in the shallower reaches of the SW African margin (Hirsch et al., 2010; Baby et al., 2018). Along the coast, well data from Saldanha Bay record sea levels as low as -100 m during the Oligocene (Roberts et al., 2017). The early Miocene corresponds to a sea-level lowstand caused by tectonic uplift attributed to the African superswell (Fig. 3; Séranne and Anka, 2005; Wigley and Compton, 2006; Hirsch et al., 2010). Following this, a major decrease in the supply of siliciclastic sediment is recorded along the SW African margin at ~ 11 Ma, accounting for the Miocene stratigraphic marker (Figs. 6, 7, 8, and 10; Baby et al., 2018). The decrease in sediment supply in the Miocene is attributed to the aridification of the Namibian

margin at ~ 17 – 15 Ma and the lack of margin uplift thus reducing river flooding (e.g. Siesser, 1980). Controls other than tectonics and the morphology of the margin need to be considered to fully understand the stratigraphy of the Cenozoic megasequence, particularly for the mid-Miocene till present as no major uplift event is recognized for the SW African margin during this time (e.g. Siesser and Dingle, 1981).

The Miocene sinusoidal channels in this study were formed by the interaction of parallel flowing bottom currents together with upwelling-induced erosion in the south which both began at around the same time (see Sect. 2.4 for a full overview; Weigelt and Uenzelmann-Neben, 2004, 2007a). Based on the sequence stratigraphic interpretation of sediments in the Cape Basin, Weigelt and Uenzelmann-Neben (2004, 2007b) propose upwelling to have initiated at around ~ 14 Ma up until ~ 1.5 Ma, and therefore earlier than the ~ 11 Ma suggested by Diester-Haass et al. (2004) and Rommerskirchen et al. (2011). Together with the onset of the Benguela upwelling system (BUS), the dramatic change in late Miocene to Plio-Pleistocene sedimentation is attributed to the strong influence of slope-parallel deep and bottom water currents formed at ~ 10 Ma when terrigenous sediment sourced from the Orange and Olifants river systems was negligible (Weigelt and Uenzelmann-Neben, 2004, 2007a). The bottom and deep-water currents offshore of western South Africa include the upper warm northward-flowing Antarctic Intermediate Water (AAIW) surface waters down to ~ 1500 m water depths; the North Atlantic Deep Water (NADW) between ~ 1500 to 4000 m water depths; and the deep Antarctic Bottom Water (AABW) beyond 4000 m water depths (Weigelt and Uenzelmann-Neben, 2004). Since the position of the channels occurs along the upper continental slope between ~ 1200 to 1500 m, the specific bottom water currents responsible for them are the upper northbound AAIW and deeper southbound NADW. The wide ~ 14 km wide zone of sinusoidal scouring along the Miocene stratigraphic marker (Fig. 10c, d) therefore marks the intersection of these concurrent flows. The present-day flow of bottom currents is still strong enough to erode the slope as seen off Cape Columbine (South Africa) with pole-ward current speeds of 16.1 cm s^{-1} (Compton and Wiltshire, 2009). The slope-parallel channels indicate that current speeds were even greater in the Miocene, strong enough to erode the slope and occurring over a prolonged period with their preservation linked to the lack of terrigenous input from the onshore Olifants and Orange rivers.

Along the outer shelf of northern Namibia, Hopkins and Cartwright (2021) similarly identified a closed ~ 40 by 50 km kidney shaped depression that eroded late Miocene sediments. The feature was likely formed by the erosive action of bottom currents associated with the intensification of the late Miocene BUS as evidenced from the orientation of its entry point and the reflection geometry of infilling sediment aligned parallel to the margin. Other possible mechanisms given for the feature included: (1) sea-level fall with

margin uplift and (2) slumping or gravitational collapse, both of which were rejected since there is no evidence for a dramatic sea-level fall recorded during this time (e.g. Siesser and Dingle, 1981) and sediment has not been remobilized. Furthermore, no visible channel feeds into the feature and no faults are found beneath it. The configuration of infilling sediments are downlapping clinoforms interpreted as diagnostic of contourites. Contourites are indicative of high sedimentation rates and many of their depositional systems have been discovered in major oceans worldwide whose bottom currents are shown to have largely been initiated around the Eocene–Oligocene boundary at ~ 32 Ma and then later reactivated or newly formed in the Miocene, reflecting the global change in oceanic circulation (Rebesco et al., 2014).

Compared to the western South African margin, the Namibian margin has thicker Miocene to Pliocene sedimentary sequences, gradually thickening northwards, which is attributed to the dramatic northerly intensification of the BUS between both SW African margins (Weigelt and Uenzelmann-Neben, 2007a). We relate the reworked sediments overlying the Miocene stratigraphic marker (sequence D3) to sediment drifts transported by the erosive action of the BUS, AAIW, and NADW (Figs. 6 and 8). In Weigelt and Uenzelmann-Neben (2004), the interaction of the AAIW and NADW is shown to have formed slumps in the late Cenozoic succession of the Cape Basin. Likewise, in this study, the seafloor slump scar observed in Fig. 7 may possibly have been triggered by the AAIW and NADW, causing mass movement above the weakest zone, directly above a syncline from the Late Cretaceous DWFTB system with fault reactivation. Although faults extending from the Albian shale detachment surface do not appear to reach the seafloor slump scar, it is possible that fault displacements in the younger Cenozoic sediments are simply below the seismic resolution limit. Elsewhere along the western South African margin many Cenozoic to seafloor slumps have been identified strongly influenced by the underlying structural framework of DWFTB systems (e.g. Paton et al., 2008; Hirsch et al., 2010).

5.4 Strato-structural evolutionary model of the deep-water Orange Basin

Using the stratigraphic and structural observations made in the present study, combined with previous literature on the tectonics and stratigraphy of the Orange Basin (e.g. Weigelt and Uenzelmann-Neben, 2004; 2007a; Séranne and Anka, 2005; Paton et al., 2008; Granado et al., 2009; Wigley and Compton, 2006; de Vera et al., 2010; Hirsch et al., 2010; Kuhlmann et al., 2010; Scarselli et al., 2016; Baby et al., 2018), we present a model in Fig. 12 illustrating the temporal evolution of the deep-water Orange Basin. Late Cretaceous ages were assigned based on the major unconformities shown in Fig. 4 (Brown et al., 1995; PASA, 2017). Cenozoic ages are assigned and processes are based on the major unconfor-

mities observed offshore of SW Africa formed by tectonic uplift (Oligocene) and oceanic currents (Miocene onwards) (Weigelt and Uenzelmann-Neben, 2004, 2007a, b; Baby et al., 2018). The following sequence of events is proposed from the formation of a Late Cretaceous DWFTB system to overlying Cenozoic canyon-channel systems and slumps in the deep-water Orange Basin:

- a. ~ 103 – 93 Ma (Albian–Turonian):
 - Following the full opening of the Atlantic Ocean (Fig. 4), well-defined shelf, slope, and abyssal plain environments developed along the margin and gravitational collapse formed small-scale folds and thrusts detaching the Albian shales.
- b. ~ 93 – 85 Ma (Turonian–Santonian):
 - With margin uplift, listric normal faulting in the up-dip extensional domain led to the formation of fold-and-thrust belts in the down-dip compressional domain with faults detaching the Turonian shale detachment surface. Thrusting was accommodated by perpendicularly orientated oblique-slip faults extending from the translational domain.
- c. ~ 85 – 77.5 Ma (Santonian–late Campanian):
 - With progressive sedimentation, oblique-slip faults continued to act as lateral ramps for thrust sheets to redistribute strain caused by continued down-dip compression and deformation.
- d. ~ 30 – 25 Ma (Oligocene):
 - A major sea-level fall following margin uplift led to the formation of a large Oligocene canyon as sediments were eroded by a downslope turbidity current (Figs. 8 and 10a, b).
- e. ~ 12 – 10 Ma (Miocene):
 - Following margin uplift, multiple crosscutting and sinusoidal channels in the Miocene formed by the slope-parallel erosive action of the concurrent NADW and AAIW ocean currents together with intensification of the BUS (Figs. 6, 8, and 10c, d).
- f. ~ 12 Ma– 0 Ma (Miocene–present):
 - Slope instability triggered by ocean currents formed Cenozoic to present-day seafloor slumps (Fig. 7).

6 Conclusions

In this study, we provide insight into the kinematics, geometry, and displacement characteristics of structures observed

within and above the compressional and translational domains of a Late Cretaceous DWFTB system in the Orange Basin using 3D reflection seismic data. These insights permitted a greater understanding of the mechanisms responsible for deformation, sedimentation, and accommodation following gravitational collapse in the Late Cretaceous to Cenozoic megasequences of the basin. Although no two DWFTB systems may be exactly alike, the observations drawn add to the limited understanding of what occurs in the translational domains of passive margin settings. The following major conclusions have been drawn:

1. The translational domain of is a zone containing overprinted features of both the extensional and compressional tectonics.
 - The downslope translation of sediment is accommodated by oblique-slip faulting extending from the translational to the down-dip compressional domains segmenting thrust sheets along-strike orthogonally. The difference and changes in slip along each oblique-slip fault reflects the way in which differential movement is accommodated for between the footwall and hanging wall blocks of the thrust sheets.
2. The morphology of the margin (i.e. slope steepness) and sedimentation rates controlled structural and depositional elements of the Late Cretaceous Orange Basin.
 - The Cenozoic canyon-channel systems occur mainly above the Late Cretaceous DWFTB system's translational domain. Normal and oblique-slip fault propagation from the translational domain is hindered by mass flow deposits of the Oligocene and Miocene shown by faults terminating at their stratigraphic markers.
3. Mid-Cenozoic sedimentation and canyon-channel systems were controlled by slope-parallel ocean currents.
 - The orientation of the Oligocene canyon, formed with sea-level fall, is slightly deflected to the north possibly reflecting the initiation of a northward-flowing current.
 - During the mid-Miocene slope-parallel oceanic currents, together with the lack of sediment supply, were the main factors controlling sedimentation patterns with the Miocene erosional features, representing the zone where the northward-flowing AAIW and southward-flowing NADW intersected.

Data availability. The data are the property of Shell and may be purchased through the PASA online geoportal at https://geoportal.petroleumagencyrsa.com/Storefront/Viewer/index_map.html (last access: 9 November 2022).

Author contributions. NGM conducted the research and wrote the paper draft; MSDM and ZJ supervised the main author's research; MSDM, ZJ, and JEB reviewed and edited the paper.

Competing interests. The contact author has declared that none of the authors has any competing interests.

Disclaimer. Publisher's note: Copernicus Publications remains neutral with regard to jurisdictional claims in published maps and institutional affiliations.

Acknowledgements. We would like to thank the National Research Foundation of South Africa (grant UID: 130186) and the Council for Geoscience for funding the first author's research. Our thanks are also extended to Shell South Africa and the Petroleum Agency of South Africa for providing the 3D reflection seismic data. We are grateful to Schlumberger for providing the Petrel software license and their support. We are furthermore grateful for the insights Vuyolwethu Mahlalela provided and to our colleagues and friends from the Wits Seismic Research Centre for the scientific discussions had and invaluable inputs provided. The authors would also like to thank two anonymous reviewers and Chris Elders (Curtin University) for their constructive comments which have greatly improved this paper. The editorial team of EGU sphere is also thanked for editorial handling.

Financial support. This research has been supported by the National Research Foundation (grant no. MND200623535561).

Review statement. This paper was edited by CharLotte Krawczyk and reviewed by Chris Elders and two anonymous referees.

References

- Aizawa, M., Bluck, B., Cartwright, J., Milner, S., Swart, R., and Ward, J.: Constraints on the geomorphological evolution of Namibia from the offshore stratigraphic record, *Commun. Geol. Surv. Namibia*, 12, 337–346, 2000.
- Baby, G., Guillocheau, F., Morin, J., Ressouche, J., Robin, C., Broucke, O., and Dall'Asta, M.: Post-rift stratigraphic evolution of the Atlantic margin of Namibia and South Africa: Implications for the vertical movements of the margin and the uplift history of the South African Plateau, *Mar. Petrol. Geol.*, 97, 169–191, <https://doi.org/10.1016/j.marpetgeo.2018.06.030>, 2018.
- Baby, G., Guillocheau, F., Braun, J., Robin, C., and Dall'Asta, M.: Solid sedimentation rates history of the Southern African continental margins: Implications for the uplift history of the South African Plateau, *Terra Nova*, 32, 53–65, <https://doi.org/10.1111/ter.12435>, 2020.
- Benesh, N. P., Plesch, A., and Shaw, J. H.: Geometry, kinematics, and displacement characteristics of tear-fault systems: An exam-

- ple from the deep-water Niger Delta, AAPG Bull., 98, 465–482, <https://doi.org/10.1306/06251311013>, 2014.
- Bilotti, F. and Shaw, J. H.: Deep-water Niger Delta fold and thrust belt modeled as a critical-taper wedge: The influence of elevated basal fluid pressure on structural styles, AAPG Bull., 89, 1475–1491, <https://doi.org/10.1306/06130505002>, 2005.
- Brown, A. R.: Interpretation of three-dimensional seismic data, American Association of Petroleum Geologists and the Society of Exploration Geophysicists, Tulsa, Oklahoma, USA, 646 pp., ISBN-13: 978-0-89181-374-3, 2011.
- Brown, L. F., Benson, J. M., Brink, G. J., Doherty, S., Jollands, A., Jungslager, E. A. H., Keenan, J. H. G., Muntingh, A., and van Wyk, N. J. S.: Sequence Stratigraphy in Offshore South African Divergent Basins: An Atlas on Exploration for Cretaceous Lowstand Traps by Soekor (Pty) Ltd, AAPG Studies in Geology 41, AAPG, 191 pp., ISBN: 0-89181-049-8, 1995.
- Butler, R. W. H. and Paton, D. A.: Evaluating lateral compaction in deepwater fold and thrust belts: How much are we missing from “nature’s sandbox”?, GSA Today, 20, 4–10, <https://doi.org/10.1130/GSATG77A.1>, 2010.
- Catuneanu, O.: Sequence stratigraphy of clastic systems: concepts, merits, and pitfalls, J. Afr. Earth Sci., 35, 1–43, [https://doi.org/10.1016/S0899-5362\(02\)00004-0](https://doi.org/10.1016/S0899-5362(02)00004-0), 2002.
- Catuneanu, O.: Principles of Sequence Stratigraphy, Elsevier, Amsterdam, 375 pp., ISBN-10: 0-444-51568-2, 2006.
- Catuneanu, O., Abreu, V., Bhattacharya, J. P., Blum, M. D., Dalrymple, R. W., Eriksson, P. G., Fielding, C. R., Fisher, W. L., Galloway, W. E., Gibling, M. R., Giles, K. A., Holbrook, J. M., Jordan, R., Kendall, C. G. S. C., Macurda, B., Martinsen, O. J., Miall, A. D., Neal, J. E., Nummedal, D., Pomar, L., Posamentier, H. W., Pratt, B. R., Sarg, J. F., Shanley, K. W., Steel, R. J., Strasser, A., Tucker, M. E., and Winker, C.: Towards the standardization of sequence stratigraphy, Earth-Sci. Rev., 92, 1–33, <https://doi.org/10.1016/j.earscirev.2008.10.003>, 2009.
- Chopra, S. and Marfurt, K. J.: Seismic attributes – A historical perspective, Geophysics, 70, 3SO–28SO, <https://doi.org/10.1190/1.2098670>, 2005.
- Chopra, S. and Marfurt, K. J.: Seismic Attributes for Prospect Identification and Reservoir Characterization, SEG and EAGE, 481 pp., <https://doi.org/10.1190/1.9781560801900>, 2007.
- Clemson, J., Cartwright, J., and Booth, J.: Structural segmentation and the influence of basement structure on the Namibian passive margin, J. Geol. Soc., 154, 477–482, <https://doi.org/10.1144/gsjgs.154.3.0477>, 1997.
- Collier, J. S., McDermott, C., Warner, G., Gyori, N., Schnabel, M., McDermott, K., and Horn, B. W.: New constraints on the age and style of continental breakup in the South Atlantic from magnetic anomaly data, Earth Planet. Sc. Lett., 477, 27–40, <https://doi.org/10.1016/j.epsl.2017.08.007>, 2017.
- Compton, J. S. and Wiltshire, J. G.: Terrigenous sediment export from the western margin of South Africa on glacial to interglacial cycles, Mar. Geol., 266, 212–222, <https://doi.org/10.1016/j.margeo.2009.08.013>, 2009.
- Corredor, F., Shaw, J. H., and Bilotti, F.: Structural styles in the deep-water fold and thrust belts of the Niger Delta, AAPG Bull., 89, 753–780, <https://doi.org/10.1306/02170504074>, 2005.
- Dalton, T. J. S., Paton, Douglas, A., Needham, T., and Hodgson, N.: Temporal and spatial evolution of deepwater fold thrust belts: Implications for quantifying strain imbalance, Interpretation 3, SAA59–SAA70, <https://doi.org/10.1190/INT-2015-0034.1>, 2015.
- Dalton, T. J. S., Paton, D. A., and Needham, D. T.: Influence of mechanical stratigraphy on multi-layer gravity collapse structures: insights from the Orange Basin, South Africa, Geol. Soc. Lond. Sp. Publ., 438, 211–228, <https://doi.org/10.1144/SP438.4>, 2017.
- de Vera, J., Granado, P., and McClay, K.: Structural evolution of the Orange Basin gravity-driven system, offshore Namibia, Mar. Petrol. Geol., 27, 223–237, <https://doi.org/10.1016/j.marpetgeo.2009.02.003>, 2010.
- Diester-Haass, L., Meyers, P. A., and Rothe, P.: The Benguela Current and associated upwelling on the southwest African Margin: a synthesis of the Neogene-Quaternary sedimentary record at DSDP sites 362 and 532, Geol. Soc. Lond. Sp. Publ., 64, 331–342, <https://doi.org/10.1144/GSL.SP.1992.064.01.22>, 1992.
- Diester-Haass, L., Meyers, P. A., and Bickert, T.: Carbonate crash and biogenic bloom in the late Miocene: Evidence from ODP Sites 1085, 1086, and 1087 in the Cape Basin, southeast Atlantic Ocean, Paleoceanography, 19 pp., <https://doi.org/10.1029/2003PA000933>, 2004.
- Dingle, R. V., Siesser, W. G., and Newton, A. R.: Mesozoic and Tertiary Geology of Southern Africa, A.A. Balkema, Rotterdam, 262–316, 1983.
- Emery, K. O., Uchupi, E., Bowin, C. O., Phillips, J., and Simpson, E. S. W.: Continental margin off Western Africa: Cape St. Francis (South Africa) to Walvis Ridge (South-West Africa), AAPG Bull., 59, 3–59, <https://doi.org/10.1306/83D91C09-16C7-11D7-8645000102C1865D>, 1975.
- Granado, P., Vera, J. D., and McClay, K. R.: Tectonostratigraphic evolution of the Orange Basin, SW Africa, Trabajos de Geología, 29, 321–328, 2009.
- Hartwig, A., Anka, Z., and di Primio, R.: Evidence of a widespread paleo-pockmarked field in the Orange Basin: An indication of an early Eocene massive fluid escape event offshore South Africa, Mar. Geol., 332, 222–234, <https://doi.org/10.1016/j.margeo.2012.07.012>, 2012.
- Hermoyian, C. S. and Owen, R. M.: Late Miocene-early Pliocene biogenic bloom: Evidence from low-productivity regions of the Indian and Atlantic Oceans, Paleoceanography, 16, 95–100, <https://doi.org/10.1029/2000PA000501>, 2001.
- Hirsch, K. K., Scheck-Wenderoth, M., van Wees, J.-D., Kuhlmann, G., and Paton, D. A.: Tectonic subsidence history and thermal evolution of the Orange Basin, Mar. Petrol. Geol., 27, 565–584, <https://doi.org/10.1016/j.marpetgeo.2009.06.009>, 2010.
- Hopkins, A. and Cartwright, J.: Large scale excavation of outer shelf sediments by bottom currents during the Late Miocene in the SE Atlantic, Geo-Mar. Lett., 41, 1–15, <https://doi.org/10.1007/s00367-021-00708-5>, 2021.
- Jungslager, E. H.: Petroleum habitats of the Atlantic margin of South Africa, Geol. Soc. Lond. Sp. Publ., 153, 153–168, <https://doi.org/10.1144/GSL.SP.1999.153.01.10>, 1999.
- King, R. C. and Morley, C. K.: Wedge geometry and detachment strength in deepwater fold-thrust belts, Earth-Sci. Rev., 165, 268–279, <https://doi.org/10.1016/j.earscirev.2016.12.012>, 2017.
- Koopmann, H., Schreckenberger, B., Franke, D., Becker, K., and Schnabel, M.: The late rifting phase and continental break-up of the southern South Atlantic: the mode and timing of volcanic rifting and formation of earliest oceanic crust, Geol. Soc. Lond. Sp. Publ., 420, 315–340, <https://doi.org/10.1144/SP420.2>, 2016.

- Kramer, E. A. J. and Heck, L.: Orange Basin 3D Pre-processing and preSDM 2013. Shell Global Solutions International B.V., Netherlands, Rijswijk, 39 pp., SR.14.13246, 2014.
- Krueger, A. and Gilbert, E.: Deepwater fold-thrust belts: Not all the beasts are equal, AAPG Search and Discovery Article, 30085, <https://www.searchanddiscovery.com/documents/2009/30085krueger/index.htm> (last access: 9 November 2022), 2009.
- Kuhlmann, G., Adams, S., Campher, C., van der Spuy, D., di Primio, R., and Horsfield, B.: Passive margin evolution and its controls on natural gas leakage in the southern Orange Basin, blocks 3/4, offshore South Africa, *Mar. Petrol. Geol.*, 27, 973–992, <https://doi.org/10.1016/j.marpetgeo.2010.01.010>, 2010.
- Light, M. P. R., Maslanyj, M. P., Greenwood, R. J., and Banks, N. L.: Seismic sequence stratigraphy and tectonics offshore Namibia, *Geol. Soc. Lond. Sp. Publ.*, 71, 163–191, <https://doi.org/10.1144/GSL.SP.1993.071.01.08>, 1993.
- Mahlalela, V., Manzi, M. S. D., Jinnah, Z., Bourdeau, J. E., and Durrheim, R. J.: Structural characteristics and 3D seismic detection of gas migration pathways in the deep-water Orange Basin, South Africa, *Mar. Geophys. Res.*, 42, 1–17, <https://doi.org/10.1007/s11001-021-09428-y>, 2021.
- Manzi, M. S. D., Hein, K. A. A., King, N., and Durrheim, R. J.: Neoproterozoic tectonic history of the Witwatersrand Basin and Ventersdorp Supergroup: New constraints from high-resolution 3D seismic reflection data, *Tectonophysics*, 590, 94–105, <https://doi.org/10.1016/j.tecto.2013.01.014>, 2013.
- Maselli, V., Kneller, B., Taiwo, O. L., and Iacopini, D.: Sea floor bedforms and their influence on slope accommodation, *Mar. Pet. Geol.*, 102, 625–637, <https://doi.org/10.1016/j.marpetgeo.2019.01.021>, 2019.
- Maslanyj, M. P., Light, M. P. R., Greenwood, R. J., and Banks, N. L.: Extension tectonics offshore Namibia and evidence for passive rifting in the South Atlantic, *Mar. Petrol. Geol.*, 9, 590–601, [https://doi.org/10.1016/0264-8172\(92\)90032-A](https://doi.org/10.1016/0264-8172(92)90032-A), 1992.
- Menzies, M. A., Klemperer, S. L., Ebinger, C. J., and Baker, J.: Characteristics of volcanic rifted margins, in: *Volcanic Rifted Margins*, *Geol. Soc. Am. Spec. Paper*, 362, 1–14, <https://doi.org/10.1130/0-8137-2362-0.1>, 2002.
- Miller, D. E., Yates, R. J., Jerardino, A., and Parkinson, J. E.: Late Holocene coastal change in the southwestern Cape, South Africa, *Quaternary Int.*, 29/30, 3–10, [https://doi.org/10.1016/1040-6182\(95\)00002-Z](https://doi.org/10.1016/1040-6182(95)00002-Z), 1995.
- Mitchum, R. M., Vail, P. R., and Thompson, S.: Seismic stratigraphy and global changes of sea level: Part 2. The depositional sequence as a basic unit for stratigraphic analysis: Section 2. Application of seismic reflection configuration to stratigraphic interpretation, *AAPG Memoir*, 26, 53–62, 1977.
- Mohammed, M., Paton, D., Collier, R. E. L., Hodgson, N., and Negonga, M.: Interaction of crustal heterogeneity and lithospheric processes in determining passive margin architecture on the southern Namibian margin, *Geol. Soc. Lond. Sp. Publ.*, 438, 177–193, <https://doi.org/10.1144/SP438.9>, 2017.
- Morley, C. K., King, R., Hillis, R., Tingay, M., and Backe, G.: Deep-water fold and thrust belt classification, tectonics, structure and hydrocarbon prospectivity: A review, *Earth-Sci. Rev.*, 104, 41–91, <https://doi.org/10.1016/j.earscirev.2010.09.010>, 2011.
- Nemčok, M., Schamel, S., and Gayer, R.: Thrustbelts: Structural architecture, thermal regimes and petroleum systems, 1st Edn., Cambridge University Press, 1–541, <https://doi.org/10.1017/CBO9780511584244>, 2005.
- Paton, D. A., van der Spuy, D., di Primio, R., and Horsfield, B.: Tectonically induced adjustment of passive-margin accommodation space, influence on the hydrocarbon potential of the Orange Basin, South Africa, *Bulletin*, 92, 589–609, <https://doi.org/10.1306/12280707023>, 2008.
- PASA (Petroleum Agency South Africa): Information and opportunities, Petroleum Agency South Africa, Cape Town, South Africa, PASA [data set], https://www.petroleumagencyrsa.com/images/pdfs/Pet_exp_opp_broch_2017bw1.pdf (last access: 9 November 2022), 2017.
- Peterson, R. G. and Stramma, L.: Upper-level circulation in the South Atlantic Ocean, *Prog. Oceanogr.*, 26, 1–73, [https://doi.org/10.1016/0079-6611\(91\)90006-8](https://doi.org/10.1016/0079-6611(91)90006-8), 1991.
- Randen, T., Monsen, E., Signer, C., Abrahamsen, A., Hansen, J. O., Sæter, T., and Schlaf, J.: Three-dimensional texture attributes for seismic data analysis, in: *SEG Technical Program Expanded Abstracts 2000*, *SEG Technical Program Expanded Abstracts 2000*, Paper presented at the 2005 SEG Annual Meeting, Calgary, Alberta, 6–11 August 2000, 668–671, <https://doi.org/10.1190/1.1816155>, 2000.
- Rebesco, M., Camerlenghi, A., and Van Loon, A. J.: Contourite research: a field in full development, *Dev. Sediment.*, 60, 1–10, [https://doi.org/10.1016/S0070-4571\(08\)10001-2](https://doi.org/10.1016/S0070-4571(08)10001-2), 2008.
- Rebesco, M., Hernández-Molina, F. J., Van Rooij, D., and Wählin, A.: Contourites and associated sediments controlled by deep-water circulation processes: State-of-the-art and future considerations, *Mar. Geol.*, 352, 111–154, <https://doi.org/10.1016/j.margeo.2014.03.011>, 2014.
- Roberts, D. L., Neumann, F. H., Cawthra, H. C., Carr, A. S., Scott, L., Durugbo, E. U., Humphries, M. S., Cowling, R. M., Bamford, M. K., Musekiwa, C., and MacHutchon, M.: Palaeoenvironments during a terminal Oligocene or early Miocene transgression in a fluvial system at the southwestern tip of Africa, *Glob. Planet. Change*, 150, 1–23, <https://doi.org/10.1016/j.gloplacha.2017.01.007>, 2017.
- Rogers, J. and Rau, A.: Surficial sediments of the wave-dominated Orange River Delta and the adjacent continental margin off south-western Africa, *Afr. J. Mar. Sci.*, 28, 511–524, <https://doi.org/10.2989/18142320609504202>, 2006.
- Rommerskirchen, F., Condon, T., Mollenhauer, G., Dupont, L., and Schefuß, E.: Miocene to Pliocene development of surface and subsurface temperatures in the Benguela Current system, *Paleoceanography*, 26, 1–15, <https://doi.org/10.1029/2010PA002074>, 2011.
- Rowan, M. G., Peel, F. J., and Vendeville, B. C.: Gravity-driven fold belts on passive margins, in: *Thrust tectonics and hydrocarbon systems*, edited by: McClay, K. R., *Bulletin*, 82, 157–182, <https://doi.org/10.1306/61EECE28-173E-11D7-8645000102C1865D>, 2004.
- Scarselli, N., McClay, K., and Elders, C.: Seismic geomorphology of cretaceous megaslides offshore Namibia (Orange Basin): Insights into segmentation and degradation of gravity-driven linked systems, *Mar. Petrol. Geol.*, 75, 151–180, <https://doi.org/10.1016/j.marpetgeo.2016.03.012>, 2016.
- Séranne, M. and Anka, Z.: South Atlantic continental margins of Africa: A comparison of the tectonic vs climate interplay on the evolution of equatorial west Africa

- and SW Africa margins, *J. Afr. Earth Sci.*, 43, 283–300, <https://doi.org/10.1016/j.jafrearsci.2005.07.010>, 2005.
- Shanmugam, G.: Chapter 5 Deep-water Bottom Currents and their Deposits, in: *Developments in Sedimentology*, Vol. 60, Elsevier, 59–81, [https://doi.org/10.1016/S0070-4571\(08\)10005-X](https://doi.org/10.1016/S0070-4571(08)10005-X), 2008.
- Shanmugam, G.: Global case studies of soft-sediment deformation structures (SSDS): Definitions, classifications, advances, origins, and problems, *J. Palaeogeogr.*, 6, 251–320, <https://doi.org/10.1016/j.jop.2017.06.004>, 2017.
- Shumaker, L. E., Jobe, Z. R., and Graham, S. A.: Evolution of submarine gullies on a prograding slope: Insights from 3D seismic reflection data, *Mar. Geol.*, 393, 35–46, <https://doi.org/10.1016/j.margeo.2016.06.006>, 2017.
- Siesser, W. G.: Late Miocene origin of the Benguela upswelling system off northern Namibia, *Science*, 208, 283–285, <https://doi.org/10.1126/science.208.4441.283>, 1980.
- Siesser, W. G. and Dingle, R. V.: Tertiary sea-level movements around southern Africa, *J. Geol.*, 89, 83–96, <https://doi.org/10.1086/628618>, 1981.
- Silva, C. C., Marcolino, C. S., and Lima, F. D.: Automatic fault extraction using ant tracking algorithm in the Marlim South Field, Campos Basin, Paper presented at the 2005 SEG Annual Meeting, Houston, Texas, 6–11 November 2005, 857–860, <https://doi.org/10.1190/1.2148294>, 2005.
- Stramma, L. and Peterson, R. G.: Geostrophic transport in the Benguela Current region, *J. Phys. Oceanogr.*, 19, 1440–1448, [https://doi.org/10.1175/1520-0485\(1989\)019<1440:GTITBC>2.0.CO;2](https://doi.org/10.1175/1520-0485(1989)019<1440:GTITBC>2.0.CO;2), 1989.
- Uenzelmann-Neben, G., Tobias, W., Gruetzner, J., and Maik, T.: Transition from the Cretaceous ocean to Cenozoic circulation in the western South Atlantic – a twofold reconstruction, *Tectonophysics*, 716, 22–240 <https://doi.org/10.1016/j.tecto.2016.05.036>, 2017.
- van der Spuy, D.: Aptian source rocks in some South African Cretaceous basins, *Geol. Soc. Lond. Sp. Publ.*, 207, 185–202, <https://doi.org/10.1144/GSL.SP.2003.207.10>, 2003.
- van der Spuy, D. and Sayidini, B.: Offshore Namibia discovery signals bright future for South Africa oil and gas, *AAPG Explorer*, <https://explorer.aapg.org/story/>, last access: 31 March 2022.
- Viola, G., Kounov, A., Andreoli, M. A. G., and Mattila, J.: Brittle tectonic evolution along the western margin of South Africa: more than 500 Myr of continued reactivation, *Tectonophysics*, 514, 93–114, <https://doi.org/10.1016/j.tecto.2011.10.009>, 2012.
- Weigelt, E. and Uenzelmann-Neben, G.: Sediment deposits in the Cape Basin: Indications for shifting ocean currents?, *AAPG Bull.*, 88, 765–780, <https://doi.org/10.1306/01260403101>, 2004.
- Weigelt, E. and Uenzelmann-Neben, G.: Early Pliocene change of deposition style in the Cape Basin, south-eastern Atlantic, *Geol. Soc. Am. Bull.*, 119, 1004–1013, <https://doi.org/10.1130/B26110.1>, 2007a.
- Weigelt, E. and Uenzelmann-Neben, G.: Orbital forced cyclicity of reflector strength in the seismic records of the Cape Basin, *Geophys. Res. Lett.*, 34, 1–4, <https://doi.org/10.1029/2006GL028376>, 2007b.
- Wigley, R. A. and Compton, J. S.: Late Cenozoic evolution of the outer continental shelf at the head of the Cape Canyon, South Africa, *Mar. Geol.*, 226, 1–23, <https://doi.org/10.1016/j.margeo.2005.09.015>, 2006.
- Wildman, M., Brown, R., Watkins, R., Carter, A., Gleadow, A., and Summerfield, M.: Post break-up tectonic inversion across the southwestern cape of South Africa: New insights from apatite and zircon fission track thermochronometry, *Tectonophysics*, 654, 30–55, <https://doi.org/10.1016/j.tecto.2015.04.012>, 2015.
- Yilmaz, Ö.: Seismic data analysis: Processing, inversion, and interpretation of seismic data, *Soc. Expl. Geophys.*, Tulsa, 2001.
- Zachos, J., Pagani, M., Sloan, L., Thomas, E., and Billups, K.: Trends, rhythms, and aberrations in global climate 65 Ma to present, *Science*, 292, 686–693, <https://doi.org/10.1126/science.1059412>, 2001.



3D reflection seismic imaging of natural gas/fluid escape features in the deep-water Orange Basin of South Africa

N. G. Maduna¹ · M. S. D. Manzi¹ · J. E. Bourdeau^{2,3} · Z. Jinnah¹

Received: 17 December 2022 / Accepted: 2 May 2023
© The Author(s) 2023

Abstract

Many features indicative of natural gas and oil leakage are delineated in the deep-water Orange Basin offshore South Africa using 3D reflection seismic data. These features are influenced by the translational and compressional domains of an underlying Upper Cretaceous deep-water fold-and-thrust belt (DWFTB) system detaching Turonian shales. The origin of hydrocarbons is postulated to be from both: (a) thermogenic sources stemming from the speculative Turonian and proven Aptian source rocks at depth; and (b) biogenic sources from organic-rich sediments in the Cenozoic attributed to the Benguela Current upwelling system. The late Campanian surface has a dense population of > 950 pockmarks classified into three groups based on their variable shapes and diameter: giant (> 1500 m), crater (~ 700–900 m) and simple (< 500 m) pockmarks. A total of 85 simple pockmarks are observed on the present-day seafloor in the same area as those imaged on the late Campanian surface found together with mass wasting. A major slump scar in the north surrounds a ~ 4200 m long, tectonically controlled mud volcano. The vent of the elongated mud volcano is near-vertical and situated along the axis of a large anticline marking the intersection of the translational and compressional domains. Along the same fold further south, the greatest accumulation of hydrocarbons is indicated by a positive high amplitude anomaly (PHAA) within a late Campanian anticline. Vast economical hydrocarbon reservoirs have yet to be exploited from the deep-water Orange Basin, as evidenced by the widespread occurrence of natural gas/fluid escape features imaged in this study.

Keywords Deep-water Orange Basin · 3D reflection seismic data · Gas/fluid escape feature · Pockmarks · Mud volcano · PHAA anticline

Introduction

The southwest African passive margin has received much interest pertaining to the economical hydrocarbon systems found within the Orange and more southern Outeniqua basins (e.g., van der Spuy and Sayidini 2022). Deep-sea technological advances made by the petroleum industry since the 1970s have allowed the more distal regions of sedimentary basins to be explored. This has promoted interest in the study of complex geological structures known to either host or are indicative of gas/fluid migration. The expression of fluid and gas migration through the sedimentary column is shown by a variety of features such as: gravity collapse structures, mounds, mud volcanoes, surface and buried pockmarks, diapirs, cold seeps and polygonal faulting (Cartwright et al. 2007; Hartwig et al. 2012; Ho et al. 2012). These features are often associated with seismic anomalies such as positive high amplitude anomalies (PHAAs), bottom simulating

✉ N. G. Maduna
nombuso.maduna@gmail.com

M. S. D. Manzi
musa.manzi@wits.ac.za

J. E. Bourdeau
bourdeau.julie.e@gmail.com

Z. Jinnah
zubair.jinnah@wits.ac.za

¹ School of Geosciences, University of the Witwatersrand, Johannesburg, South Africa

² Geological Survey of Canada, 601 Booth Street, Ottawa, ON K1A 0E8, Canada

³ Wits Mining Institute, University of the Witwatersrand, Johannesburg, South Africa

reflectors (BSRs), and pipe and chimney venting structures (Løseth et al. 2011; Gay et al. 2003; Cartwright et al. 2007; Hustoft et al. 2010; Ho et al. 2012). Natural gas/fluid escape features identified offshore South Africa and Namibia in the shallow Orange Basin include seafloor and buried pockmarks (Hartwig et al. 2012), seismic chimneys (Ben-Avraham et al. 2002; Paton et al. 2007; Kuhlmann et al. 2010; Boyd et al. 2011), mud diapers and volcanoes (Ben-Avraham et al. 2002; Viola et al. 2005), reflecting the basin's underlying hydrocarbon system. Economical hydrocarbon reserves are proven in the Orange Basin, both in the shallow and deep-water environments (Boyd et al. 2011; Isiaka et al. 2017; van der Spuy and Sayidini 2022). This is reflected by the Namibian Kudu and South African Ibbhesi gas fields which are in production along the shelf, and the recent deep-water hydrocarbon finds in Namibia from the Graaf-1 appraisal and Venus-1X wildcat wells which are directly adjacent to this study (Fig. 1). Since the deep-water discoveries in Namibia are in proximity to this study, and the two regions are similar in geology, the potential for prolific hydrocarbon finds in the distal Orange Basin of South Africa is high.

The deep-water study area sits within a region of well-preserved Upper Cretaceous gravitational collapse structures, referred to as deep-water fold-and-thrust belts (DWFTBs) (Fig. 1; de Vera et al. 2010; Rowan et al. 2004; Nemcok et al. 2005; Paton et al. 2007). Key elements in the evolution of the Orange Basin have been constrained through various studies mostly using early 2D reflection seismic data, well logs, then much later 3D reflection seismic data (e.g., Light et al. 1993; Clemson et al. 1997; de Vera et al. 2010; Hartwig et al. 2012; Dalton et al. 2015, 2017; Collier et al. 2017; Baby et al. 2018; Mahlalela et al. 2021; Maduna et al. 2022). These studies describe events within the late stages of continental breakup, including the stratigraphy, structure and formation of gravitational collapse structures together with the hydrocarbon potential of the basin. The observations are however limited in South Africa since few studies have integrated the known hydrocarbon system with the natural fluid/gas features observed in relation to the underlying structure and stratigraphy of the passive margin, and even more so in the distal deep-water environments (e.g., Kuhlman et al. 2010; Mahlalela et al. 2021). Furthermore, in contrast to the Namibian extent, the deep-water Orange Basin remains underexplored in South Africa due to the sparsity of wells and limited 3D reflection seismic data coverage (Fig. 1; PASA 2017; van der Spuy and Sayidini 2022). The main aim of basin analysis is in understanding the basin's evolution which is centred around the tectonic setting under which the basin formed, its depositional environment, and the presence, accumulation, and extent of hydrocarbons. In this study we attempt to better constrain these elements

in the deep-water Orange Basin offshore South Africa. We use seismic attributes to resolve numerous natural gas/fluid escape features and describe their relationship to the underlying DWFTB system described in Maduna et al. (2022).

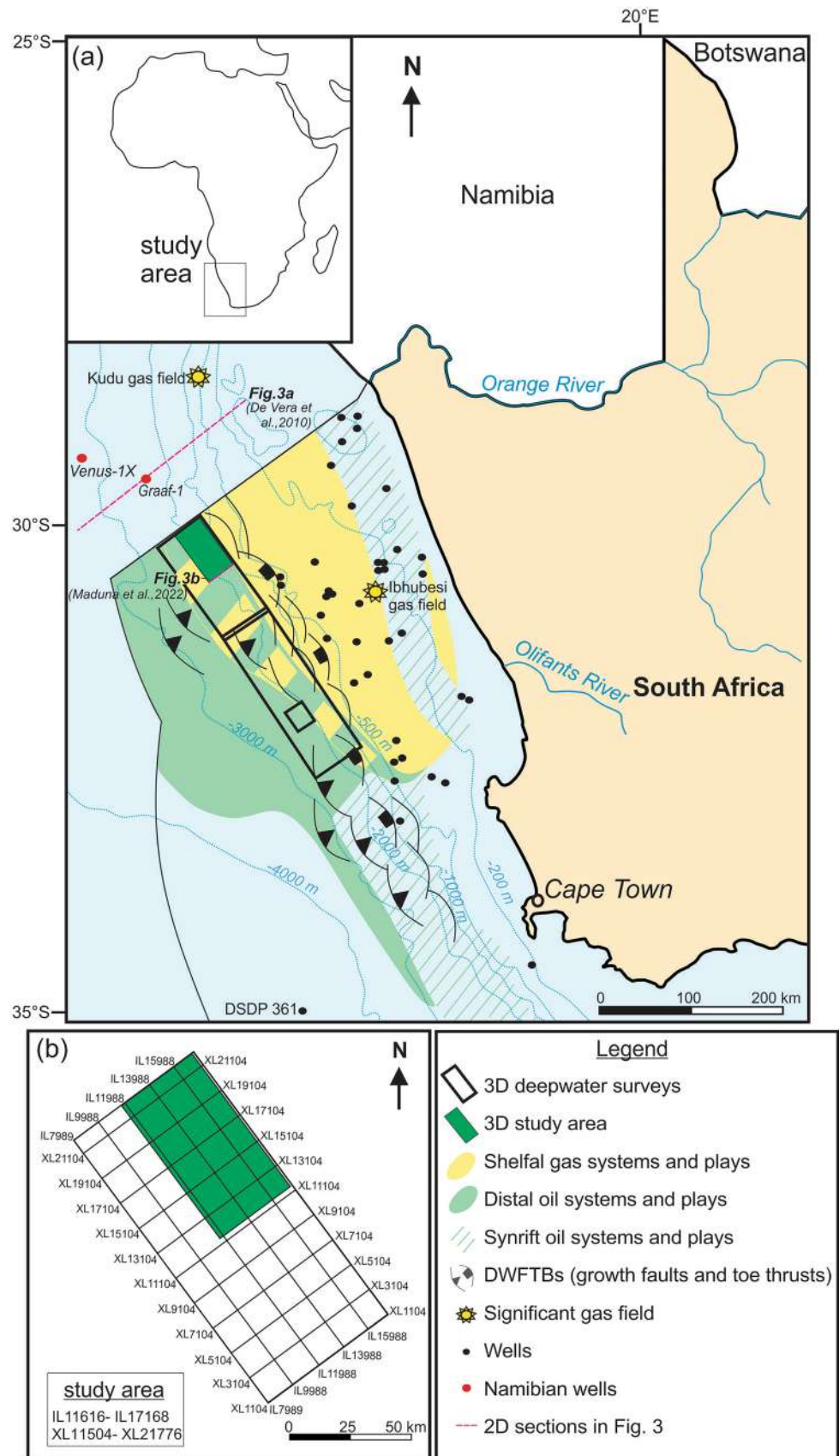
Regional setting

The study area is located in the deep-water Orange Basin offshore SW Africa between 1000 and 2000 m water depths (Fig. 1). The basin covers an overall area of ~160 000 km² with the southern and central extents located offshore western South Africa and the northern extent located offshore Namibia. The Cretaceous to present-day infill of the Orange Basin is derived from the South African Plateau (SAP) (or hinterland) with sediment transported by the Orange and Olifants rivers and their proto-equivalents since the Lower Cretaceous (Maslanyj et al. 1992; De Vera et al. 2010). The sedimentary succession is comprised of syn-rift sequences related to the break-up of Gondwana during the Late Jurassic, followed by drift (post-rift) sequences with the opening of the South Atlantic (Fig. 2; Light et al. 1993). In the southern Orange Basin, the maximum depositional thickness is ~3 km, while in the north, the sedimentary succession reaches ~7 km (Kuhlmann et al. 2010). The structural and stratigraphic evolution of the SW African margin has been analysed mostly using seismic data and well logs, including the study of sediment accumulation rates, solid phase volumes and thermo-chronometric datasets (e.g., Light et al. 1993; de Vera et al. 2010; Hirsch et al. 2010; Baby et al. 2018, 2020; Maduna et al. 2022).

Offshore structural framework

The pre-rift basement offshore SW Africa is comparable to the complex onshore Proterozoic to Early Paleozoic Pan African Gariep Belt (Clemson 1997; Frimmel et al. 2011; Mohammed et al. 2017). A 30 km wide, N–S orientated zone of pronounced flexure, known as the 'hinge line', has separated regions of uplift and subsidence since the Mesozoic in the pre-rift basement (Light et al. 1993; Clemson et al. 1997; Mohammed et al. 2017; Baby et al. 2018). The hinge line forms a critical boundary separating the margin's offshore and onshore morphologies (Light et al. 1993; Clemson et al. 1997; Aizawa et al. 2000) and its flexure reflects its progressive landward migration (Baby et al. 2018). The hinge line is offset by several NE–SW fracture zones (segment boundaries) which partitioned rifting during the break-up of Gondwana between the Middle to Late Jurassic (160 to 130 Ma) (Clemson et al. 1997). Seaward dipping reflectors (SDRs) observed in the upper

Fig. 1 Map of the SW African margin showing **a** known and predicted hydrocarbon systems, wells, position of sections in Fig. 3, and DWFTBs in the South African Orange Basin; and **b** location of the present study area in green



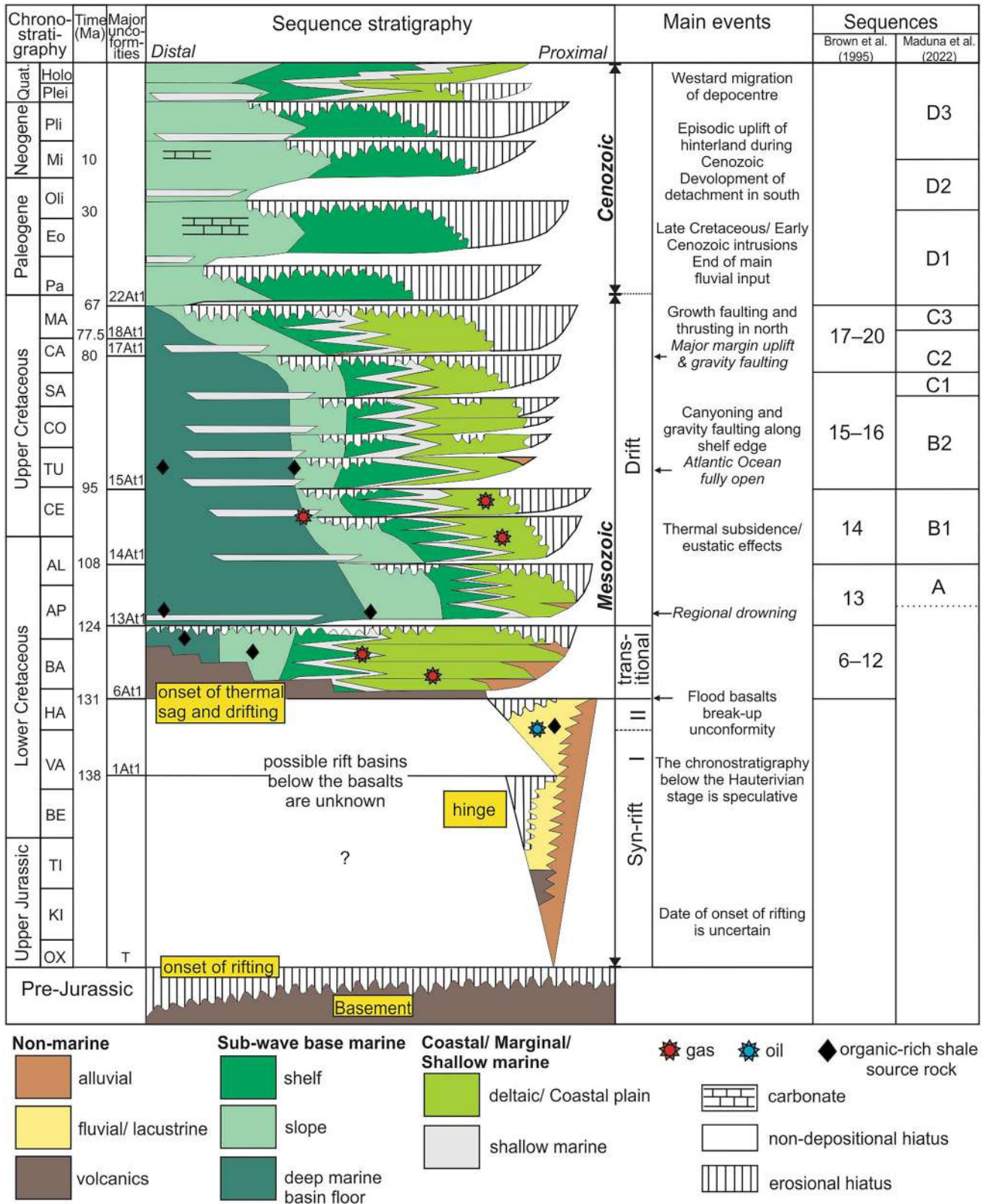


Fig. 2 Chronostratigraphy and sequence stratigraphy of the Orange Basin throughout the evolution of the margin using the stratigraphic nomenclature developed by PetroSA (previously Soeker) (Brown et al. 1995; PASA 2017)

basement lithologies of the SW African margin reflect the volcanic evolution of the passive margin during rifting (Clemson et al. 1997; Menzies et al. 2002; Séranne and Anka 2005). The SDRs form a thick > 3 km package comparable in age to the Parana-Etendeka Large Igneous Province at ~ 135 Ma (Koopman et al. 2016; Baby et al. 2018).

The zipper-like south to north opening of the South Atlantic Ocean occurred through right-lateral strike-slip motion along the NE–SW fracture zones (Light et al. 1993). Viola et al. (2012) places the opening of the South Atlantic Ocean at ~ 134 Ma, following ENE–WSW extension and rifting. The spreading oceanic ridge marks the onset of drift; the second major phase of margin evolution following the break-up of Gondwana (Séranne and Anka 2005; Granado et al. 2009). The spreading centre propagated northwards over a 40 my rift-drift transition period (Viola et al. 2012), with drift subdividing the margin into well-defined shelf, slope and basal environmental settings (Light et al. 1993). The oldest evidence of mid-oceanic ridge activity and the transition to oceanic crust occurs at the M3 magnetic anomaly, between the Hauterivian and Barremian sequences at 127 Ma (Séranne and Anka 2005). The Orange, Lüderitz and Walvis basins formed in zones of greatest subsidence between the Rio Grande Fracture Zone to the north and Aghulhas-Falkland Fracture Zone to the south (Light et al. 1993; Clemson et al. 1997; Séranne and Anka 2005). The smaller Cape and Outeniqua basins also formed south of the Orange Basin. The predominant structural grain and trend of all structural lineaments is NW–SE to NNW–SSE, following the regional foliation of the SW African margin (Light et al. 1993; Wildman et al. 2015).

Offshore stratigraphy

The presence of SDRs together with rotated and eroded extensional fault blocks in the syn-rift sequence are evidence of the tectonic control on sedimentation along the SW African margin during this time (Maslanyj et al. 1992; Light et al. 1993; Granado et al. 2009). The syn-rift sequence is comprised of isolated half-grabens infilled with interbedded Late Jurassic to Lower Cretaceous (late Hauterivian) siliciclastic and volcanoclastic sediments (Fig. 2; Jungslager 1999; Paton et al. 2008). The onset of drift began with the deposition of Lower Cretaceous to present-day post-rift clastic sediments above the Hauterivian break-up unconformity (Fig. 2; Light et al. 1993; Menzies et al. 2002; Granado et al. 2009; de Vera et al. 2010). Early drift sediments correspond to black shales and claystones, while late drift sediments are interbedded heterolithic shales and claystones (Dalton et al. 2017).

Sedimentation in the Upper Cretaceous was primarily driven by tectonics with climate and oceanic circulation playing little to no role as the difference in pole and equator temperatures were low (Maslanyj et al. 1992; Light et al. 1993; Granado et al. 2009; Uenzelmann-Neben et al. 2017).

In the Cenozoic sedimentation and facies distribution were strongly affected by oceanographic processes and climatic changes (Light et al. 1993; Weigelt and Uenzelmann-Neben 2004). The early Oligocene opening of the Drake Passage in the south created the cooler Antarctic Circumpolar Current and Atlantic meridional overturning circulation currents leading to the subsequent development of thermally stratified bottom and deep-water currents in the Miocene (Weigelt and Uenzelmann-Neben 2004; Uenzelmann-Neben et al. 2017). Southern-sourced bottom and deep-water currents responsible for depositional changes observed since the Miocene offshore SW Africa include the Antarctic Intermediate Water current, North Atlantic Deep Water, and deep Antarctic Bottom Water currents, together with the Benguela Coastal Current (Weigelt and Uenzelmann-Neben 2004). These thermally stratified countercurrents led to cold water upwelling of the Benguela Current in the Miocene intensifying at ~ 11 Ma (Diester-Haass et al. 2004; Rommerskirchen et al. 2011).

The post-rift stratigraphy of the Orange Basin has been well-described and subdivided in terms of several stratigraphic units/sequences separated by key stratigraphic markers/bounding surfaces (e.g., Emery et al. 1975; Bolli et al. 1978; Brown et al. 1995; Holtar and Forsberg 2000; Paton et al. 2008; Granado et al. 2009; De Vera et al. 2010; Kuhlmann et al. 2010; Dalton et al. 2017; Baby et al. 2018; Maduna et al. 2022). Several phases of uplift and denudation in the post-rift succession have enhanced gravitational processes within the basin, responsible for both crustal thinning and the inversion of extensional faults (e.g., Granado et al. 2009; De Vera et al. 2010; Hirsch et al. 2010; Brown et al. 2014; Wildman et al. 2015). Periods of elevated sedimentation rates are recorded mostly in the Upper Cretaceous (93.5–66 Ma), then later in the Oligocene (~ 30–25 Ma) successions (Baby et al. 2020). Elevated sedimentary flux in the Upper Cretaceous corresponds to a major uplift of the South African Plateau (De Vera et al. 2010; Hirsch et al. 2010), caused either by a dynamic topography as the African plate moved over the African Superplume found in the lower mantle, or via lithospheric delamination/metasomatism (Baby et al. 2020). Gravitational collapse structures (DWFTB systems) found in the Orange Basin (Fig. 3) formed in response to this major margin uplift together with seaward tilting, significantly eroding the inner margin (Paton et al. 2008; Granado et al. 2009; Hirsch et al. 2010; De Vera et al. 2010; Kuhlmann et al. 2010).

Aptian-, Turonian- and Cenomanian-aged maximum flooding surfaces are seaward-dipping, over-pressured shale detachments upon which gravitational sliding of DWFTB systems occur in the Orange Basin (Brown et al. 1995; Morley et al. 2011; Dalton et al. 2015; Baby et al. 2018; Maduna et al. 2022). A full system consists of a linked: (1) up-dip extensional domain with listric normal faults separating convex-upward growth strata; (2) central transional (or trans-lational) domain with complex overprinted extensional and

compressional tectonics; and (3) down-dip compressional domain where folds and thrust faults occur (Fig. 3; Rowan et al. 2004; Bilotti and Shaw 2005; Morley et al. 2011). Toe thrusting and folding occurs within an approximately 3 km thick section extending for up to 60 km in the direction of transport in the compressional domain (Morley et al. 2011).

The study of DWFTB systems has grown because of their association with economic hydrocarbon reserves in the distal folds of anticlines (compressional domain); for example, the northern Orange Basin in Namibia (van der Spuy and Sayidini 2022) and the Niger Delta (Bilotti and Shaw 2005; Corredor et al. 2005; Krueger and Gilbert 2009).

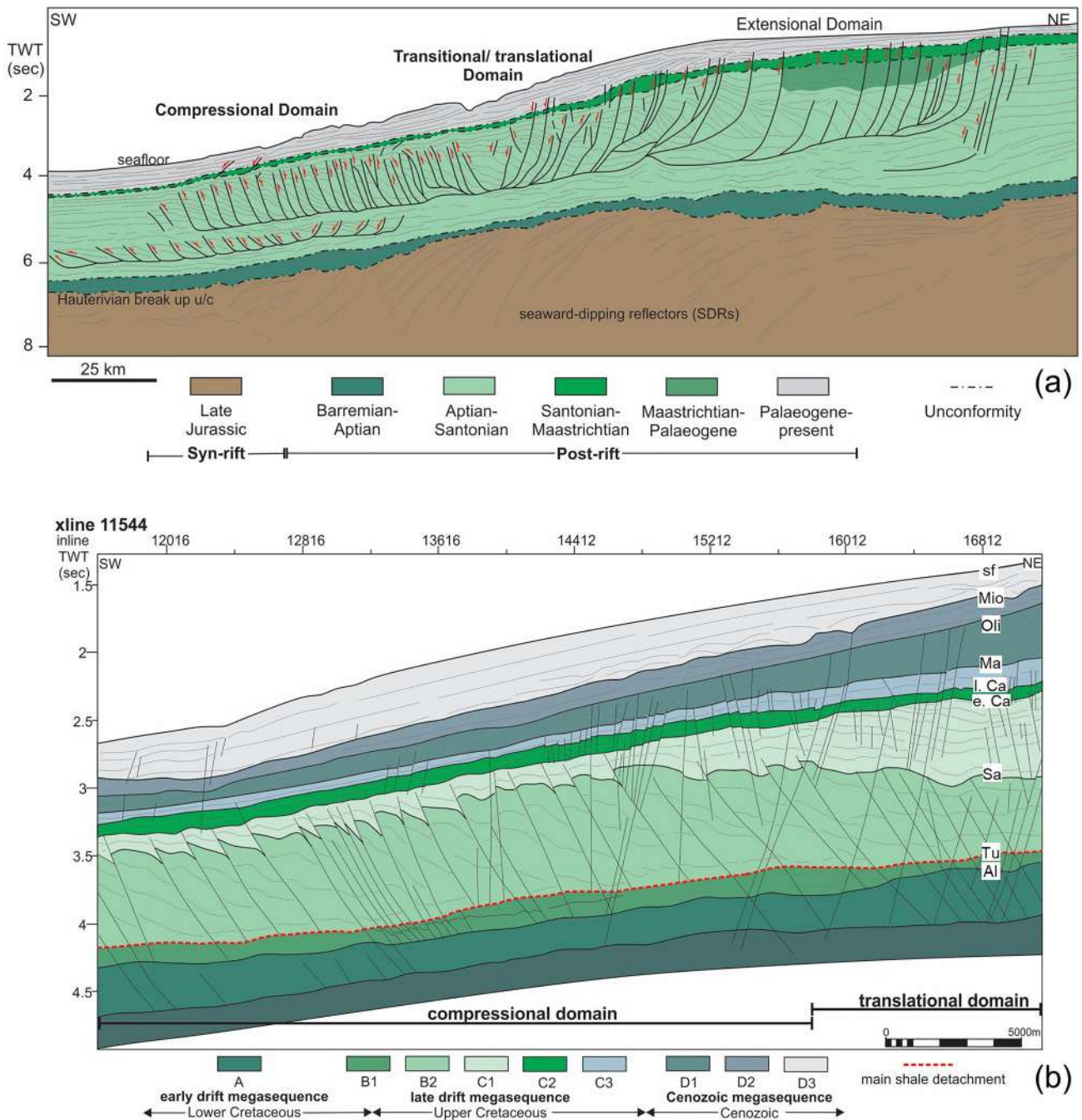


Fig. 3 2D seismic profiles through DWFTB systems of the Orange Basin showing; **a** a full DWFTB system comprised of an up-dip extensional, central transitional (or translational) and down-dip compressional domain (De Vera et al. 2010); and **b** the detailed translational

and compressional domains imaged in the present study area (Maduna et al. 2022). Abbreviations: *Al* Albian, *Tu* Turonian, *Sa* Santonian, *Ma* Maastrichtian, *e. Ca* early Campanian, *l. Ca* late Campanian, *Oli* Oligocene, *Mio* Miocene, and *sf* seafloor. Vertical exaggeration = 5

Hydrocarbon system

Exploration in the shallow shelf environments of the Orange Basin has confirmed several petroleum systems sourced from Barremian to Albian, and possibly Turonian shales (Aldrich et al. 2003; van der Spuy 2003). The two commercial hydrocarbon plays in the shallow proximal settings of the South African basin are the Ithubesi gas field (Fig. 1) and A-J oil syn-rift system (van der Spuy and Sayidini 2022). The Ithubesi gas field is sourced from the lower Aptian source shales located in the depocentre of the Orange Basin with reservoirs stratigraphically trapped in fluvial channel-fill sandstones (PASA 2017). A similar gas play in the shallow shelf regions is the Kudu gas field, offshore southern Namibia (Fig. 1). The Kudu gas field is sourced from Barremian shales with reservoirs stratigraphically trapped within aeolian sandstones (PASA 2017). These plays both have the potential of multi-TCF (trillion cubic feet) natural gas reserves. The only oil system found in the shallow shelf region occurs within the isolated A-J half-graben sourced from rich Hauterivian lacustrine shales (Jungslager 1999). Oil reservoirs are stratigraphically trapped within lake shoreline sandstones interbedded within the source rocks (PASA 2017). Results from the DSDP 361 borehole and a possible Turonian oil source rock imaged the Bredasdorp Basin, indicates that the Orange Basin becomes increasing oil-prone distally (Fig. 1; van der Spuy 2003; PASA 2017). This is proven in Namibia as recent significant light oil discoveries were made from Shell's Graff-1 appraisal well and TotalEnergies' Venus-1X wildcat well drilled between 2 and 3 km water depths with reservoirs speculated to be located in the significantly older Aptian to lower Albian sediments (Fig. 1; Heins 2022; van der Spuy and Sayidini 2022). Currently, South Africa's largest deep-water prospect is found within the southern Outeniqua Basin's Brulpadda blocks, hosting an average of one billion BOE (barrel of oil equivalent) of natural gas condensate (Feder 2019). Due to the harsh conditions imposed by the setting of the strong Agulhas current, however, not much progress has been made in drilling (L'Arvor et al. 2020).

Overview of natural gas/fluid escape features

The most well-known seafloor (or palaeo-seafloor) expressions of vertically focussed fluid flow in hydrocarbon systems include mud volcano systems and pockmarks. These surface expressions are linked to subsurface processes such as pipes and chimneys, formed within fracture zones, reflecting the focussed movement of gas, fluids and large sedimentary masses in the case of mud volcanoes (Mazzini and Etiope 2017).

Surface expression of natural gas/fluid flow

Mud volcanoes, first recognised and described in the 1970s, are unstable topographical features formed by rapid rates of relative methane expulsion, with rates high enough to remobilize sediment and fluids to the surface (Roberts et al. 2006; Judd and Hovland 2007; Andresen 2012). Mud volcanoes episodically vent a mixture of gas (large amounts of hydrocarbon gas and methane, and lesser amounts of CO₂, N₂ and He), oil, water, mud and rock fragments (constituents forming the mud breccia) in a process termed 'sedimentary volcanism' (Dimitriv 2002; Judd and Hovland 2007; Mazzini and Etiope 2017). Sedimentary volcanism is driven by the gravitative instability of buoyant shales and fluid overpressures, leading to hydrofracturing and the subsequent flow of fluids along permeable fractures (Mazzini and Etiope 2017). The most extensive mud volcanoes systems are found in the offshore environment since water-saturated conditions yield low viscosity flows (Mazzini and Etiope 2017). In compressional margins Judd and Hovland (2007) note that there is a relationship between earthquakes and mud volcanoes; a major earthquake may be triggered sedimentary volcanism, which may in turn trigger minor earthquakes. From satellite imagery and field observations, the distribution of mud volcanoes is shown to be often structurally controlled as they occur with normal faults, strike-slip faults, fault-related folds and along the axis of anticlines (Mazzini et al. 2009; Mazzini and Etiope 2017).

Pockmarks are elliptical or cone-shaped depressions in fine-grained sediment (Hovland and Judd 1988), and were first documented by King and MacLean (1970) on the Scotian shelf. Unlike the large vent feeding a mud volcano, the flux of gas-saturated mud in blowout pipes is moderate, and therefore insufficient to form a large edifice on the seafloor resulting in the formation of smaller pockmarks (Roberts et al. 2006; Cartwright 2007). The escape of fluids erupting to the surface is envisaged to be quite violent during the initial formation of pockmarks then followed by smaller seepages along the same migration pathway (Judd and Hovland 2007). The size of pockmarks varies depending on the grain size of sediments they are hosted in (Judd and Hovland 2007), and type and size of the underlying conduit. Numerous pockmarks have been described both in the shallow (Jungslager 1999; Kuhlman et al. 2010; Hartwig et al. 2012; Isiaka et al. 2017; Palan et al. 2020) and deep-water reaches (Mahlalela et al. 2021) of the Orange Basin on the palaeo-Cenozoic and current seafloors. In the shallow water reaches of the basin, seafloor pockmarks are associated with active faults (e.g., Jungslager 1999; Hartwig et al. 2012).

Subsurface expression of natural gas/fluid flow

The gas and fluid pathways responsible for the surface expression of gas/fluid escape features are created by discontinuities and unconformities primarily in the form of faults, faulted anticlines, salt diapirs and structural surfaces along the bedrock (Gay et al. 2003). A type of faulting system above hydrocarbon reservoirs in fine-grained sediment are polygonal faults describing a honeycombed hydraulic fracturing pattern in planform (Henriet et al. 1991; Cartwright 1994, 2007). Polygonal faults are often linked to pockmark formation acting as fluid migration pathways (Cartwright et al. 2003; Gay et al. 2006, 2007). Polygonal faults are attributed to mechanisms such as differential compaction and dewatering, overpressures, density inversion and dissolution-induced shear failure (Cartwright et al. 2003; Cartwright 2007, 2011).

Seismic chimneys and pipes are the most common subsurface processes reflecting the vertical movement of gas/fluids through fracture systems to the surface (Løseth et al. 2011; Gay et al. 2006, 2007; Cartwright et al. 2007). Chimneys indicate slow methane expulsion rates, while smaller pipes which lead to surface pockmarks are indicative of moderate methane expulsion rates (Roberts et al. 2006). According to Andresen (2012), a chimney is defined as a wide (sometimes narrow) vertical zone of focussed fluid flow characterised by low amplitude, disrupted or chaotic reflectors; and a pipe is defined as a narrow (< 300 m) vertical zone of focussed fluid flow mainly characterised by stacked, high amplitude anomalous reflectors. There are many hypotheses when it comes to the formation of seismic pipes and chimneys, discussed in detail by Cartwright and Santamarina (2015). Hypotheses include hydraulic fracturing and erosive fluidization (Brown 1990; Løseth et al. 2009, 2011; Cartwright et al. 2007), capillary invasion (Cathles et al. 2010), localized subsurface volume loss similar to the formation of mud volcano pathways (Roberts et al. 2006) and syn-sedimentary formation (Cartwright and Santamarina 2015). The most popular hypothesis of pipe and chimney formations is hydraulic fracturing caused by the combined effects of elevated pore fluid pressures with fluid-driven erosion (Cartwright 2007). Other subsurface processes include mud intrusions and mounds, domes, dewatering pipes, domes, diapirs and diatremes; all of which are referred to as piercement structures by Mazzini and Etiope (2017).

Data and methods

Seismic acquisition, processing, and interpretation

Three deep-water 3D seismic surveys have been conducted in the deep-water extents of the South African Orange

Basin (van der Spuy and Sayidini 2022). The first acquired in 2002 exhibited low signal-to-noise ratio; then, between 2012 and 2014, two large, higher-resolution 3D seismic surveys were conducted. This present study uses a portion of the northern-most 3D seismic dataset bordering the Namibian maritime licensing region (Fig. 1). Shell Global Solutions International commissioned the present study's high-resolution 3D seismic survey between 2012 and 2013 (Kramer and Heck 2014). The survey was conducted in a ~NNW to SSE orientation, covering a total area of ~8200 km² (Fig. 1b). However, in this study, we interpret the northernmost ~1800 km² portion of the full seismic dataset bordering Namibia.

Seismic acquisition was conducted onboard the *Dolphin Geophysical Polar Duchess* using the UTM Zone 33S, central meridian 15° map projection. The source used was an array of dual airguns 15 m in length with a separation of 100 m, volume of 4100 cubic inches, 25 m shot point interval (flip/flop) towed at 8 m depths. The group interval and group length for the 7950 m long streamers were both 12.5 m, with each of the 8 streamers being 7950 m in length, separated by 200 m. The data were recorded in SEG-D format with a record length of 7186 ms, sampled at a rate of 2 ms using a low-cut and high-cut frequency of 4.4 Hz at a 12 db/Oct slope and 214 Hz at a 341 db/Oct slope, respectively. Following pre-processing involving data conversion from SEG-D to SEG-Y output onboard the *Dolphin Geophysical Polar Duchess*, full seismic processing was carried out by the Netherlands Global Processing team using Shell's proprietary SIPMAP software. Processing was done at 4 ms from SEG-Y field tape data through surface-related multiple elimination (SRME) using 3D SRME and anisotropic Kirchhoff pre-stack depth migration (PSDM). The original acquisition grid for the inline and crossline was 6.25 m × 50 m, respectively. Following PSDM migration, the final crossline and inline cell size output is given as 25 × 25 m according to Shell's report for the study area (Kramer and Heck 2014). The full acquisition and step-by-step processing parameters are added as tables in the supplementary material.

In this study, the data are geologically interpreted using Schlumberger's Petrel software. The seismic data has a dominant frequency of 20 Hz and an average velocity of 2400 m/s (see Kuhlman et al. 2010). With a wavelength of 120 m, the vertical seismic resolution is calculated to be either 60 or 30 m based on the ½ and ¼ wavelength criteria, respectively (Yilmaz 2001). The horizontal resolution for migrated seismic data is defined by ½ the wavelength (i.e., 60 m for these data) (Herron 2011). However, this resolution is also dependent on the quality of the data, bin size or trace spacing and geometry of the survey (Lebedeva-Ivanova et al. 2018).

Application of seismic attributes

Seismic attributes were applied to the seismic data to image features below the vertical and horizontal resolution limits as in Manzi et al. (2013) and Schoole et al. (2020). Volumetric attributes applied to the full seismic dataset prior to seismic interpretation include variance, generalized spectral decomposition (GSD), envelope, sweetness and the iterative root mean square (RMS) amplitude. Since seismic attributes are sensitive to noise, structural smoothing was first applied to the full seismic volume to precondition the data and enhance the signal-to-noise (S/N) ratio (Randen et al. 2000). Variance was then applied to the structurally smoothed dataset. Variance is an attribute that highlights discontinuities by measuring local deviations in the seismic signal through a coherency analysis (Silva et al. 2005; Maselli et al. 2019). Envelope is the most popular trace attribute used to detect hydrocarbons as it highlights acoustic impedance contrasts in sandstone reservoirs as bright spots (Koson et al. 2014). The RMS amplitude (iterative) and sweetness attributes are highly correlated to envelope and are therefore also used to detect 'bright spots' (i.e., possible hydrocarbon reservoirs). The RMS amplitude (iterative) is a smoother, scaled estimate of the trace envelope (Koson et al. 2014). It computes the root mean square (RMS) iteratively on instantaneous trace samples over a user-specified vertical window. The sweetness attribute, defined as envelope divided by the square root of instantaneous frequency, is often used to image coarse-grained sandstone reservoirs. GSD uses the concept of unravelling the seismic waveform back to its pre-computed waveforms and constituent frequencies (Chopra and Marfurt 2005; Koson et al. 2014). Tuning the seismic data to specific frequencies allows subtle changes in lithology or flow barriers to be detected (Chopra and Marfurt 2005). The GSD attribute is also used as a direct hydrocarbon indicator, known to show gas charged reservoirs (Burnett et al. 2003; Naseer et al. 2017). Horizon-based attributes were applied once sufficient seismic interpretation had taken place on surfaces of interest. These include the edge detection, and influential data attributes; structural operations applied to the seafloor and late Campanian surfaces to highlight 3D geometric variations introduced by fault displacements and gas/fluid escape features. Edge detection extracts an edge model to enhance discontinuities by combining the dip and dip azimuth properties and normalizing these to the local noise of the surface (Randen et al. 2000; Manzi et al. 2012). Influential data is essential to ensuring sensible geometric form as it enhances areas of rapid 3D geometric variation. Prior to edge detection and surface smoothing, however, surface smoothing was first applied to filter out anomalous peaks and noise on each surface.

Seismic interpretation strategy

The seismic stratigraphy is described using Mitchum et al. (1977)'s classical approach whereby stratal termination patterns (downlap, onlap, toplap erosional truncation and concordance) separate the sedimentary succession into seismic facies or sequences with distinct internal reflection geometries (e.g., parallel, subparallel, divergent, prograding, chaotic, sigmoid, hummocky). The surfaces that separate these sequences are erosional or conformable stratigraphic markers created through the interaction of sedimentation and sea-level fluctuations as depositional regimes change (Caturanu 2006). The stratigraphic markers used in this study were chosen because of their dominant high amplitudes and lateral continuity observed throughout the seismic volume. Since no wells are present in the deep-water region, a direct well tie could not be performed on the dataset to calibrate the geological ages to the stratigraphy. Geological ages were assigned based on the comparison of previous Orange Basin studies with seismic data and well logs (e.g., Brown et al. 1995; de Vera et al. 2010; Kuhlmann et al. 2010; Hirsch et al. 2010; Baby et al. 2018). The stratigraphic markers identified in the Cretaceous are the Albian, Turonian, Santonian, early Campanian, late Campanian and Maastrichtian surfaces (Fig. 3b). According to the offshore stratigraphic nomenclature developed by PetroSA the stratigraphic markers in this study correspond to the 14At1, 15At1, possibly 16Dt, 17At1 and 22At1 unconformities, respectively (Fig. 2; Brown et al. 1995). In the Cenozoic succession we identified the Miocene and Oligocene erosional unconformities (Fig. 3b), which were also recognised by Baby et al. (2018). The sedimentary succession is subdivided into four megasequences (A–D) reflecting the three major phases of margin evolution early drift (A), late drift (B1–C3) and Cenozoic (D1–D3) (Fig. 3b) as in Dalton et al. (2017).

Results and interpretations

This study's seismic volume images the up-dip transitional and down-dip compressional domains of a Upper Cretaceous DWFTB system and the overlying Cenozoic succession between 1000 and 2000 m below sea level (mbsl) (Figs. 1, 3b and 4). The evidence for fluid and natural gas seepage in the seismic volume includes polygonal faults, pockmarks, a HPAA anticline and a mud volcano, well imaged on the late Campanian surface (Fig. 4). The structural framework associated with all these gas/fluid escape features include a combination of thrust faults, normal faults and oblique-slip faults associated with the Upper Cretaceous DWFTB system (Fig. 3b). Influential data (using two different colour tables) and edge detection were two key horizon-based attributes

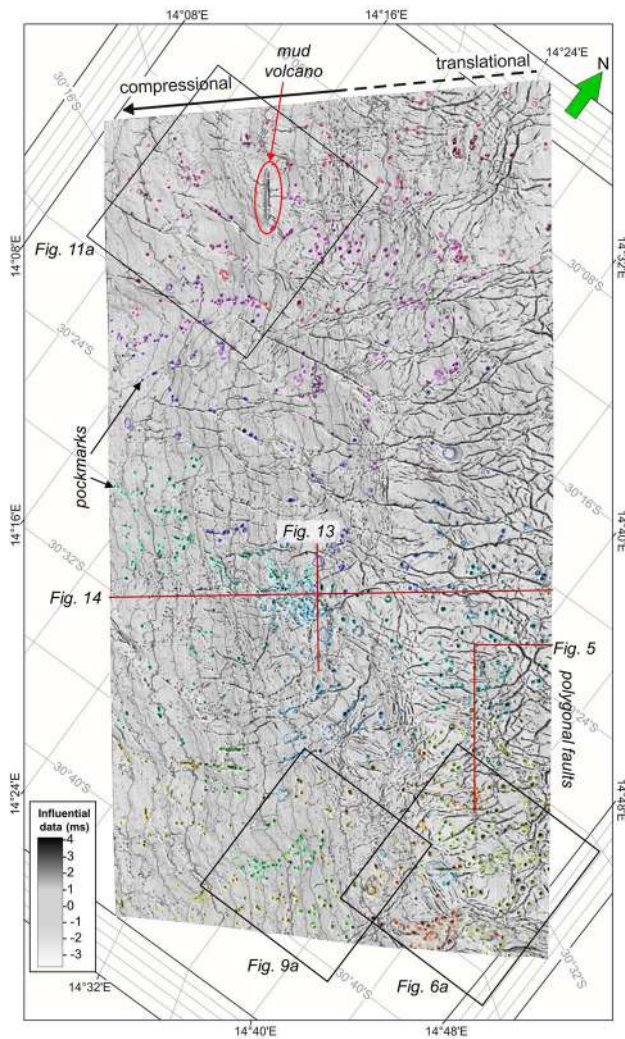


Fig. 4 3D late Campanian surface covering the full study area (Fig. 1) imaged with the influential data attribute (using a white–grey–black colour scale) to highlight features influencing the 3D form of the surface. The surface is highly pockmarked (pockmarks outlined by coloured polygons) with the greatest concentration of pockmarks occurring in the S (bottom left). Other features highlighted include polygonal faults in the E and SE, and an elongated mud volcano with few pockmarks surrounding it in the NW. Vertical exaggeration = 5

applied to better enhance all these features, together with the variance volumetric attribute enhancing discontinuities.

Late Campanian pockmarks

There are over 950 well-preserved, elliptical-shaped depressions characteristic of pockmarks on the late Campanian surface (Fig. 4). The most efficient horizon-based attribute used to image these pockmarks clearly on the whole surface was influential data using a white–grey–black colour table (see Fig. 4). Late Campanian pockmark formation is strongly associated with

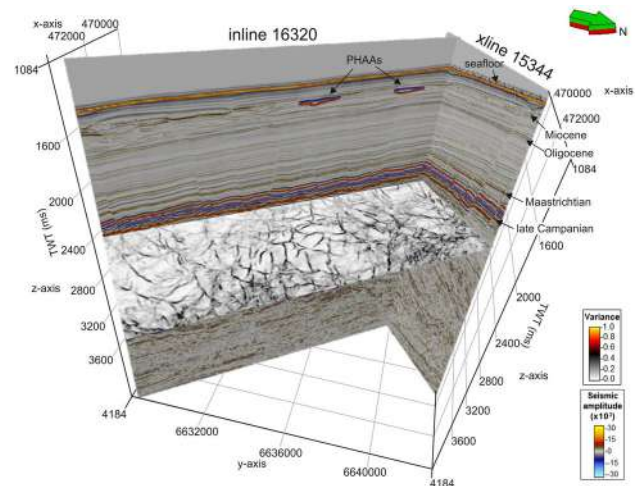


Fig. 5 3D view of an inline and crossline, together with the variance attribute timeslice (located just below the late Campanian surface) showing polygonal faults in cross section and their characteristic honey-combed pattern. PHAA positive high amplitude anomaly. Vertical exaggeration = 5

polygonal faulting in the eastern and southeastern sections of the study area, as many pockmarks of the surface are bound within them (Figs. 4, 5 and 6a). The variance time slice placed just above the translational domain of the Upper Cretaceous DWFTB system in Fig. 5 (southeastern portion of Fig. 4) displays the honey-combed pattern of polygonal faulting. Faults dip 45°, on average, and have variable dip directions accounting for the polygonal pattern seen in planform. Individual fault throws are 30–50 m and the distance between each fault (the size of each closed polygon cell) ranges from ~800 to 1200 m (Fig. 5). Most faults in the study area initiate from the Turonian shale detachment surface at depth and terminate around the late Campanian surface (Fig. 3b). Some of the faults in the eastern section of the study area, however, terminate at the Oligocene or Miocene surfaces (Cenozoic).

Pockmarks on the late Campanian surface were categorized into three different groups based primarily on their size and shape as: giant (8), crater (~20) and simple (>900) pockmarks. Giant pockmarks are greater than 1500 m in diameter with a ~1:16 depth-to-diameter ratio (Figs. 6 and 7). Crater pockmarks, named so because of their resemblance to simple crater meteorite impact structures, are mostly ~800 m in diameter with a 1:7 depth-to-diameter ratio. Crater pockmarks are linked to polygonal faults in the eastern section of the study area (Figs. 4, 5 and 6). Simple pockmarks are regular elliptical-shaped depressions with the smallest sizes (>500 m diameter and metre-scale deep). All the different types of pockmarks observed on the late Campanian surface are shown in Fig. 6 (a zoomed in portion of Fig. 4 in the SE). Figure 6a shows the association of different

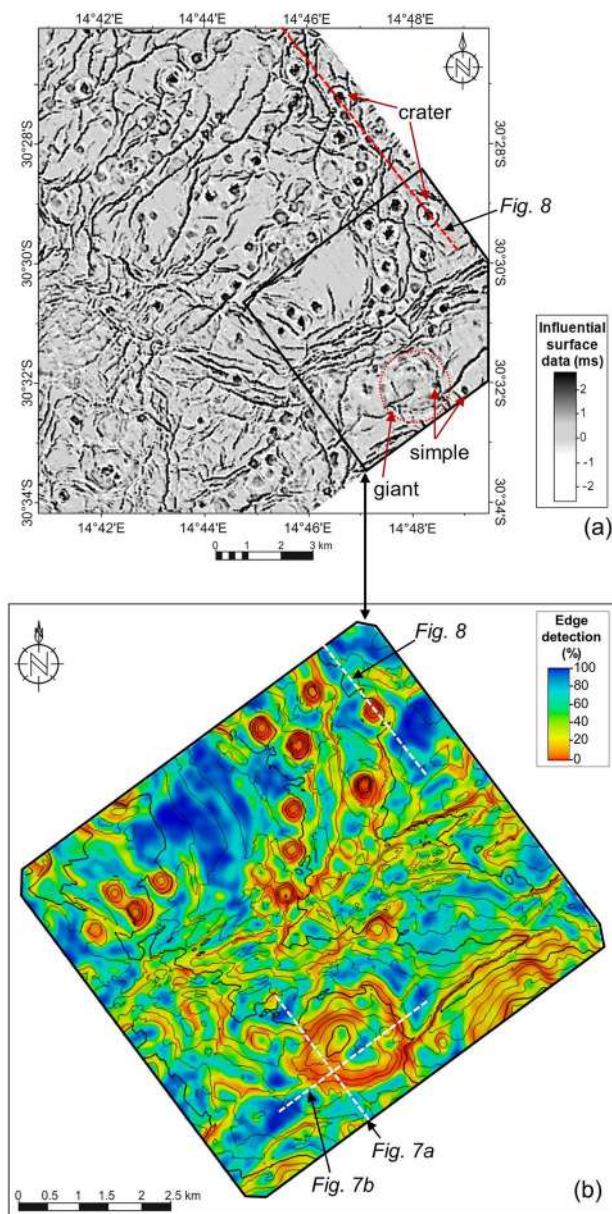


Fig. 6 Different types of pockmarks on the late Campanian surface shown using: **a** the influential data attribute (using a contrast black to white colour table), and **b** the edge detection attribute on a zoomed in section

types of pockmarks to surrounding faults and fractures, and Fig. 6b is a close-up using the edge detection attribute.

Giant pockmarks are the largest pockmarks identified in the study, being 1500–2000 m in diameter (Figs. 6 and 7) and ~120 ms TWT (c. 114 m) deep (TWT-depth conversion using velocities of $1900 \text{ m/s} \pm 10\%$; cf. Kuhlmann et al. 2010). There are a few (8) of these large, cone-shaped depressions throughout the study area (e.g., Fig. 6) often linked to wide chimneys at depth (Fig. 7a). An example of a giant pockmark is shown in Fig. 7. The inline in Fig. 7a

shows a large, dome-shaped anomaly of convex upwards deformed sediments leading up to the feature. This 1800 m wide zone of disrupted reflectors is a seismic chimney. The giant pockmark is bound between normal faults terminating above the Maastrichtian surface. Figure 7b, a crossline section, shows the pockmark's direct underlying stratigraphy is disrupted by normal faults. Smaller, simple pockmarks may occur within giant pockmarks as seen in Fig. 7b and the 3D image in Fig. 7c.

Pockmarks displaying a “crater-like” morphology in plan and cross-section (Figs. 6 and 8) are classified as crater pockmarks in this study. Crater pockmarks are 700–900 m in diameter (Fig. 6) and are approximately 120 ms TWT (c. 114 m) deep (TWT-depth conversion using velocities of $1900 \text{ m/s} \pm 10\%$; cf. Kuhlmann et al. 2010). They have slightly raised wing-shaped rims giving them their distinctive “simple crater-like” morphology (Fig. 8b, c). Compared to giant pockmarks (Fig. 7) they are more circular in plan view (Fig. 6b) and symmetrical in cross-section (Fig. 8a, b). Crater pockmarks are confined to the SE region of polygonal faulting above the transitional domain (Fig. 6). The crater pockmarks are situated directly in the centre of polygonal fault cells (Figs. 6a and 8b). Intriguingly, these pockmarks are not associated with large zones of disrupted reflectors directly beneath them but appear to be related to faults and fracture zones (Fig. 8).

Simple pockmarks are much smaller in size, most are metre-scale in depth and less than 300 m in diameter, displaying elliptical- to cone-shaped morphologies (Figs. 7a, b and 9a). Furthermore, they lack the outer wing-shaped rims and are distributed throughout the late Campanian surface, unlike crater pockmarks which are confined to polygonal faulted areas above the translational domain (Figs. 4, 6 and 9a). Many simple pockmarks occur along faults (Fig. 6a), and others occur either randomly in between faults or follow a trend in seemingly un-faulted regions indicating possible microfractures (Fig. 9a). While giant pockmarks are linked to seismic chimneys at depth (Fig. 7), both crater and simple pockmarks are linked to faults at depth which are often difficult to distinguish (Figs. 8 and 9c, d). Pockmarks do not appear to be linked to any pipes at depth (Fig. 8a), however, this may be due to possible pipe widths being below the seismic resolution limit.

Seafloor pockmarks and mass wasting

There are 85 pockmarks imaged on the seafloor with the greatest concentration occurring in the central and southern region of the study in the down-dip direction above compressional domain (Fig. 10). Seafloor pockmarks are similar to the late Campanian's simple pockmarks, although slightly larger in size, with most being ~400 m in diameter and less than 120 ms TWT (c. 114 m) deep (TWT-depth conversion

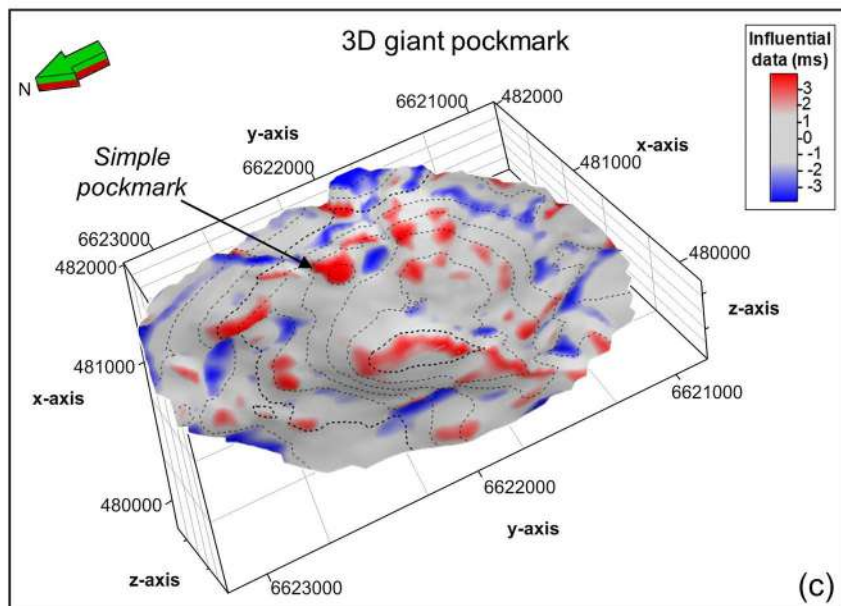
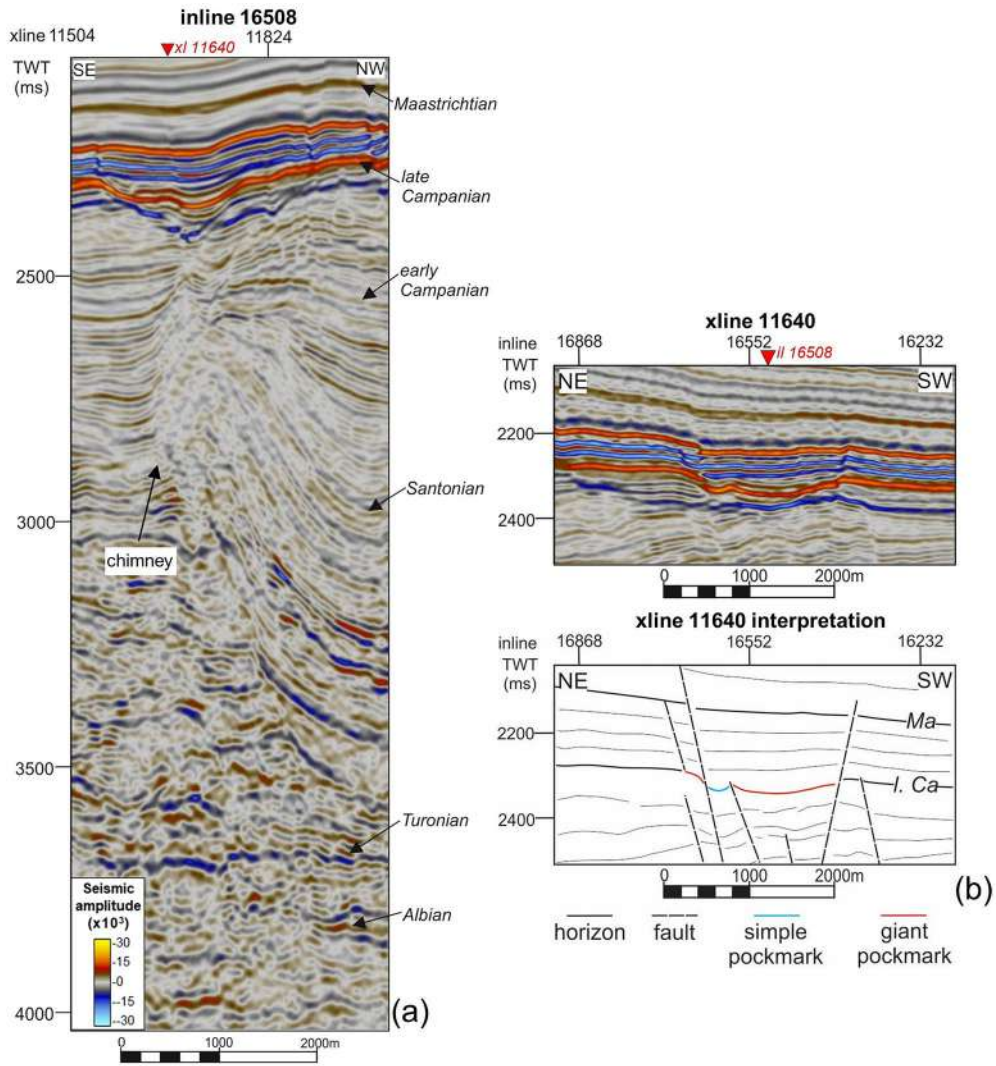


Fig. 7 Example of a giant pockmark with a smaller, simple pockmark enclosed within it; **a** inline section showing a chimney leading up to the giant pockmark, **b** crossline section and interpretation of the giant and simple pockmark, **c** 3D influential data view of the giant and simple pockmark using the standard red-grey-blue colour scale. Vertical exaggeration = 5

using velocities of $1900 \text{ m/s} \pm 10\%$; cf. Kuhlmann et al. 2010). Seafloor pockmarks are strongly influenced by the underlying stratigraphy with most occurring directly above those imaged on the late Campanian surface or following the same trend. An example of this is shown in Fig. 9a and b; fewer, larger pockmarks occur on the seafloor following the same NE-SW trend of those on the late Campanian surface. A conjoined simple pockmark pair on the late Campanian surface is shown to correspond to one large pockmark on the seafloor in the NW region of Fig. 9a and b. No other pockmarks are observed in the stratigraphy between the two surfaces, nor are there clearly distinguishable faults, pipes or chimneys leading up from the late Campanian to seafloor surfaces.

The only notable features observed between the late Campanian and seafloor surfaces, following the trend of both surfaces' pockmarks, are normal faults with some forming the sidewalls (gliding planes) of slides (Fig. 9c and d). The slides are coherent masses of sediment with little internal deformation. They are ~2–4 km in diameter with rotational slip occurring along the Miocene and Oligocene surfaces. In Fig. 9d original bedding planes are shown to have been rotated by the gliding plane of the slide. Some seafloor pockmarks are found within slides in the centre of the study area in the region directly above a late Campanian PHAA anticline (Fig.), and in the south (Figs. 9b, d and 10). Pockmarks associated with slides are larger in size (up to ~1500 m in diameter) and irregular in shape. The greatest mass wasting feature is seen in the NW; a large $> 26 \times 19 \text{ km}$ slump scar characterised by low amplitude, internally deformed reflectors (Figs. 10, 11b and 12a, b). The slump scar is not associated with any pockmarks on the seafloor but with a mud volcano detailed in the following section (Figs. 11 and 12).

Mud volcano

A NW–SE orientated topographical feature is found in the NW of the study area, with a positive relief of 50 ms TWT (c. 48 m) (TWT-depth conversion using velocities of $1900 \text{ m/s} \pm 10\%$; cf. Kuhlmann et al. 2010), a length of ~4200 m, and width of ~400 m (Figs. 11 and 12). This

feature is interpreted as an elongated mud volcano. The mud volcano is located within the centre of a large, 7400 m wide anticline from the Upper Cretaceous DWFTB system (Fig. 11b, c). The anticline marks the intersection between the DWFTB system's compressional and translational domains. The mud volcano conduit roots from the Turonian surface as a wide ~1800 m zone displaying chaotic internal reflections which then narrows into an internally chaotic vent (Figs. 11b, c and 12). Deformation into convex-downwards layers, defining the positive relief of the mud volcano, starts just below the crest of the anticline in Santonian sediments (Fig. 11c).

On the late Campanian surface, the influential data surface attribute reveals a few simple pockmarks surrounding the mud volcano (Fig. 11a) which are not as densely populated as those found in the south of the study area (Figs. 4, 6 and 9a). The mud volcano is situated within a large, slumped region on the seafloor (Fig. 10). Within here, an even deeper depression (slumping within a slump) occurs to the SE, adjacent to the length of the mud volcano characterized by chaotic internal reflections from the Miocene to seafloor surfaces (Fig. 12a, b). Very few faults surround the mud volcano (Fig. 11a). Perpendicularly orientated fractures appear to feed into the mud volcano vent using the influential data surface attribute on the late Campanian surface, as presented in Fig. 11a. Figure 12 is an inline section that cuts through the length of the mud volcano. Reflections within the elongate vent are acoustically dampened and show low amplitudes compared to its surroundings in the envelope attribute (Fig. 12b).

HPAA anticline

An anticline occurs along the late Campanian surface, appearing as an approximately 3.5 km (Fig. 13) by 4.2 km (Fig. 14) PHAA. The inline section presented in Fig. 13 shows the anticline is bound by faults dipping away from each other, depicting a horst structure. Four volume-based attributes known to detect the presence of hydrocarbons were used; iterative RMS, sweetness, generalized spectral decomposition (GSD) and envelope (Fig. 13a–d). The envelope attribute (Fig. 13d) best illustrated the presence of hydrocarbons with minimal loss in distinguishing strong reflections (surfaces and faults). Figure 14 shows the intersecting crossline section both normally (a) and using the envelope attribute (b) detecting the PHAA of the anticline and the overall interpretation (c). The outer edge from the crest of the anticline is likely the hydrocarbon spoil point which is bound by a fault (Fig. 14).

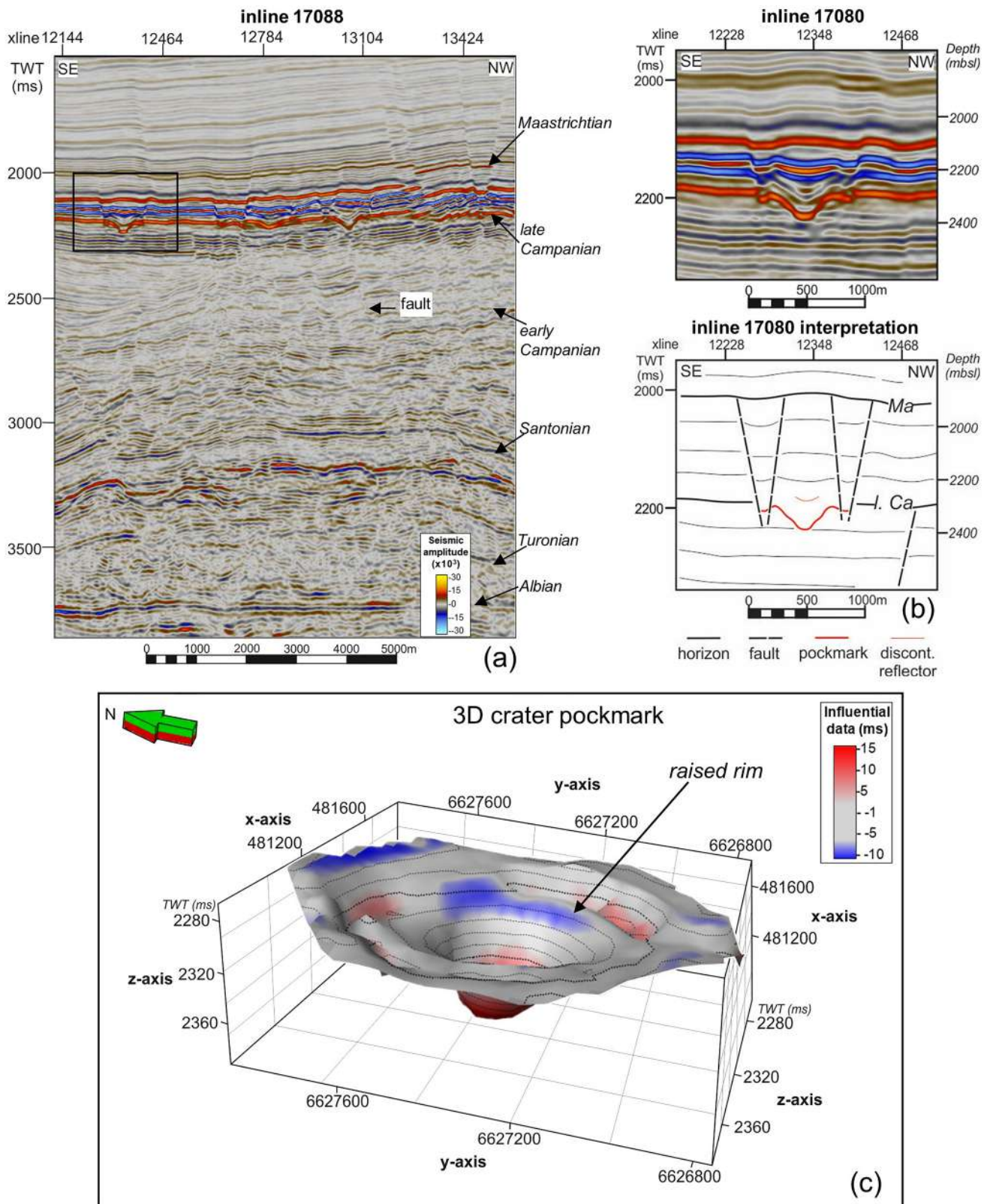


Fig. 8 Example of a crater-type pockmark; **a** inline section showing two crater pockmarks with one clearly showing a fault leading up to it, **b** zoomed-in inline section and interpretation of a crater pockmark,

c 3D influential data view of the crater pockmark using the standard red–grey–blue colour scale. Vertical exaggeration = 3

Like the previously described mud volcano (Fig. 11), the anticline located further S occurs at the intersection of the translational and compressional domains of an underlying Upper Cretaceous DWFTB system (Fig. 14). In the region directly above the anticline, large pockmarks and slumps occur on the seafloor, as shown in Fig. 10. Pockmarks also occur along Campanian surface along the anticline but are difficult to see as they are highly irregular in shape (Fig. 4), deviating from the regular elliptical shape. PHAAs are also found within the Turonian to Santonian sediments in the region immediately below the anticline (Figs. 13 and 14). Up-dip of the anticline in the NE section of the study, the seismic character of the late Campanian to Maastrichtian sediments becomes progressively higher in amplitude, resulting in another PHAA above the translational domain as shown in Fig. 14b.

Most faults initiate from the Turonian surface in the compressional domain which often merges with the Albian surface in the translational domain (Fig. 14c). Thrust faults in the compressional domain terminate at the early Campanian to late Campanian surfaces, while many normal and oblique slip faults from the translational domain terminate along the stratigraphically younger Maastrichtian, Oligocene and Miocene sequence boundaries (Fig. 14c). Many smaller faults begin within early Campanian to late Campanian sediments in the translational domain and terminate in Cenozoic sediments (Fig. 14c).

Discussion

The study of natural gas/fluid flow features is an underutilized tool in basin analysis that may explain various aspects of basin evolution including the timing of formation, main driving and trigger mechanisms, fluid source and migration pathways (Andresen 2012). Since the sedimentary succession is undisrupted by salt tectonics, the accumulation and distribution of hydrocarbons in the deep-water Orange Basin can be investigated. Gas/fluid escape features have been classified in several ways according to their geometry, lithology, surrounding geological impact, cause of formation or methane flux intensity (Roberts et al. 2006; Cartwright et al. 2007; Løseth et al. 2009; Huuse et al. 2010; Andresen 2012). The natural gas/fluid migration features observed in the study area include fluid migration conduits of faults and chimneys, and their surface expression as pockmarks, and a mud volcano on the late Campanian and seafloor surfaces. All these features are strongly controlled by

a Upper Cretaceous DWFTB system above or within which they occur (Maduna et al. 2022). The processes responsible for forming these gas/fluid escape features are based on the same common principles with one feature forming instead of another due to minor or major differences in influential factors such as the stress environment, sediment and fluid type, fluid concentration, or the influence of external triggers (Judd and Hovland 2007).

Upper Cretaceous DWFTB system

Only the up-dip translational and down-dip compressional domains are imaged in the seismic dataset, with gravitational sliding having occurred along a main overpressurized Turonian shale detachment surface (Fig. 3b). The compressional domain is characterized by fold and thrust belts recognized throughout the Orange Basin (Figs. 1 and 3) along the continental slope in many studies (e.g., Paton et al. 2008; de Vera et al. 2010; Scarselli et al. 2016; Mahlalela et al. 2021). The previously ill-defined translational domain is characterized by overprinted extensional (listric normal faults) and compressional (thrust faults) tectonics with the downslope translation of sediment accommodated by extensive oblique-slip faults segmenting thrust sheets along strike (Maduna et al. 2022). Known and postulated source rock intervals of the Orange Basin include the Hauterivian, Barremian, Aptian and Turonian shales (Fig. 2). The Turonian shale detachment surface is the youngest and most speculative source rock interval estimated to have reached oil and gas maturation between 85 and 16 Ma with temperatures ranging between 100 and 140 °C along the shelf (Hirsch et al. 2010). Results from well logs and basin modelling suggest oil maturation in the deep water where sediment is thickest (Aldrich et al. 2003; van der Spuy 2003; Paton et al. 2008; Hirsch et al. 2010; van der Spuy and Sayidini 2022). The widespread occurrence of subsurface and surface gas/fluid escape features serves as indirect evidence of elevated pore fluid pressures in the Upper Cretaceous. Fluid overpressures are mainly formed by the combined effects of volumetric expansion involved in hydrocarbon generation and maturation, tectonic stresses and disequilibrium compaction (Rowan et al. 2004; Bilotti and Shaw 2005). Other mechanisms include mechanical compaction (due to sudden mass movement events or gradual burial), dehydration reactions and the thermal effect of increasing temperature gradients in pore fluids (Mazzini and Etiope 2017).

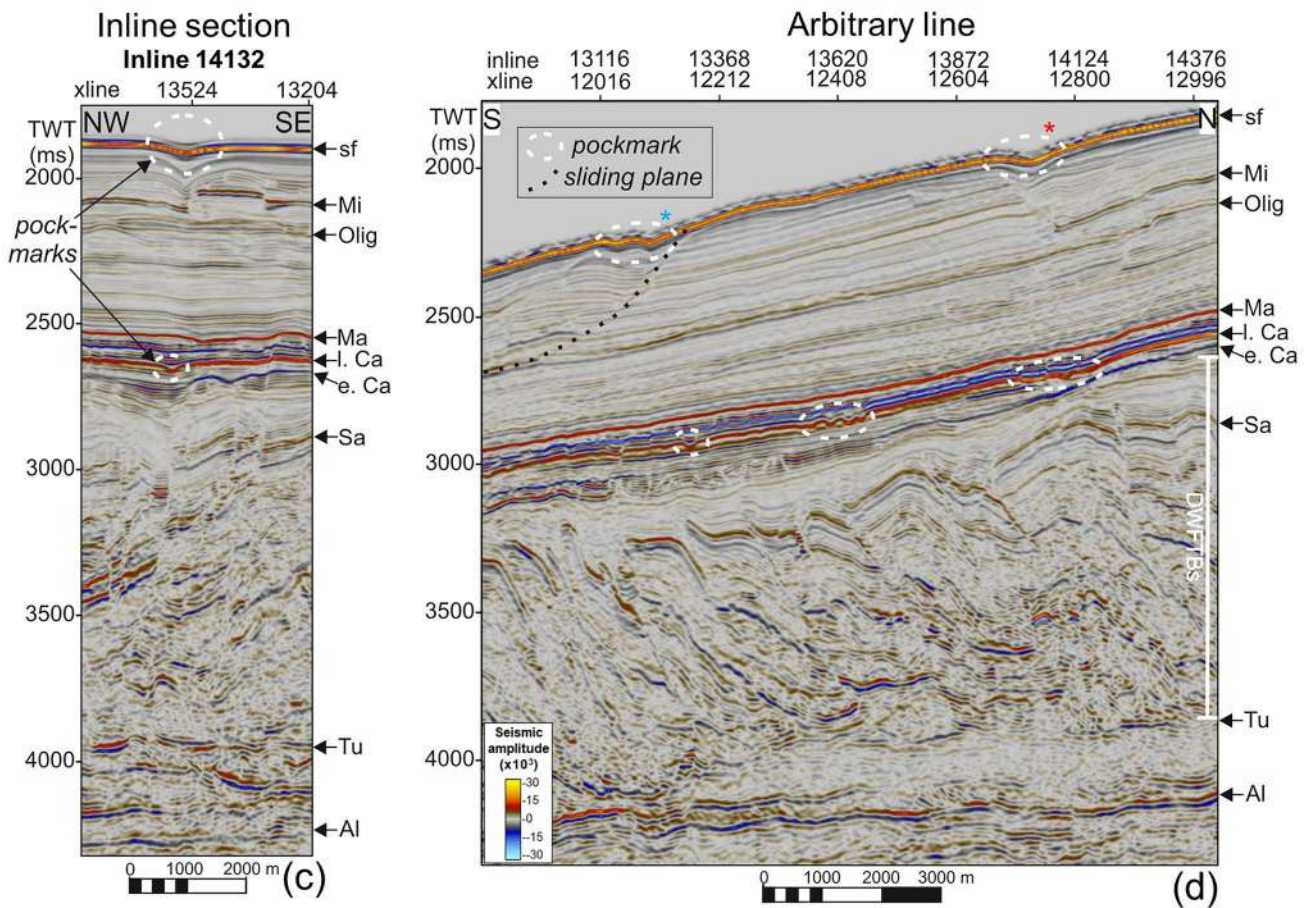
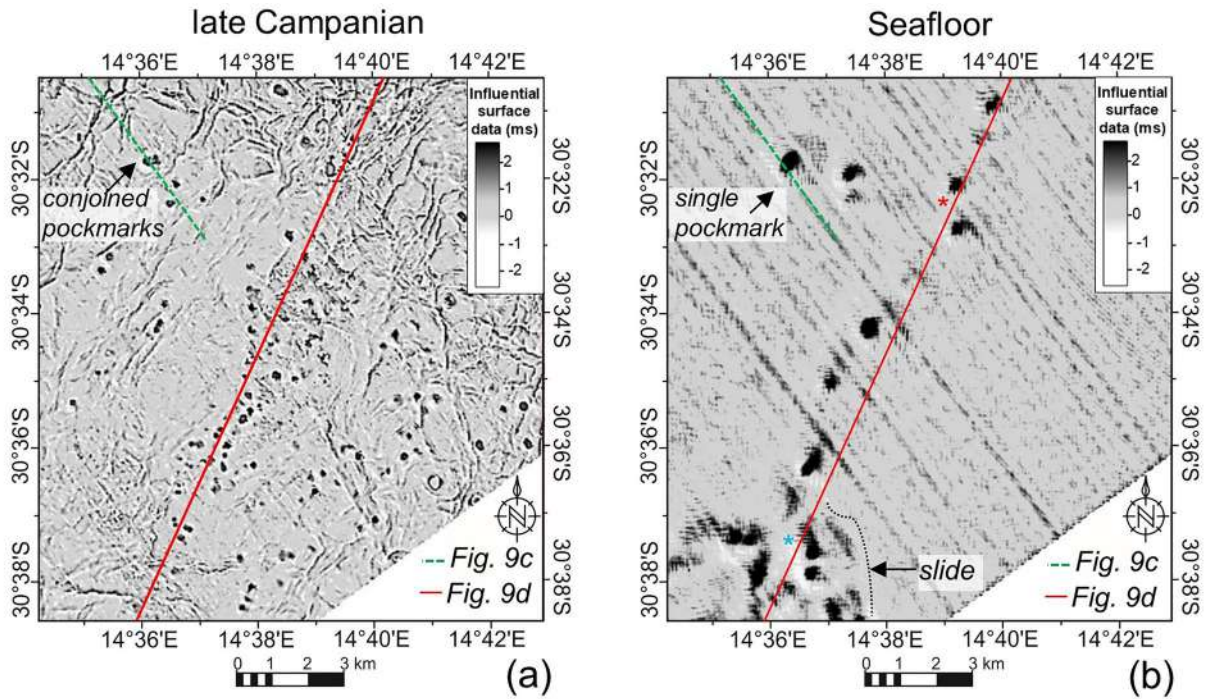


Fig. 9 Comparison of the **a** late Campanian and **b** seafloor surface's simple pockmarks using the influential data attribute. In **c** an inline section is shown cutting through a pair of conjoined pockmarks on the late Campanian surface corresponding to a single pockmark on the seafloor. In **d**) an arbitrary seismic line following the linear trend of the late Campanian and seafloor pockmarks is imaged, showing the structure between the two surfaces and the underlying DWFTBs in the compressional domain. Abbreviations: *Al* Albian, *Tu* Turonian, *Sa* Santonian, *Ma* Maastrichtian, *e. Ca* early Campanian, *l. Ca* late Campanian, *Oli* Oligocene, *Mio* Miocene, and *sf* seafloor. Vertical exaggeration = 5

The distribution of all subsurface and surface gas/fluid escape features in this study are strongly influenced by the underlying tectonics of the Upper Cretaceous DWFTB system. Most of the fluid migration pathways linked to pockmarks on the late Campanian surface originate from the Turonian shale detachment surface (Figs. 7, 8, 9 and 12). Polygonal faults and crater pockmarks on the late Campanian surface are confined in the SW region above the translational domain (Figs. 4, 5 and 6). Simple pockmarks on the late Campanian and seafloor surfaces are concentrated above the compressional domain (Figs. 4, 9 and 10). At the intersection of the translational and compressional domains, a late Campanian PHAA anticline is found in the center of the study together with irregular seafloor pockmarks in the area directly above it (Figs. 10, 13 and 14). The orientation and location of the elongated mud volcano in the NW also occurs at the intersection of the two domains (Fig. 13b).

Surface gas/fluid escape features

Pockmarks

According to Judd and Hovland (2007), the density of pockmarks is dependent on the thickness, strength and permeability of the surrounding sediments. The overall distribution of pockmarks in the N of the study area are not as dense as those in the S for both the late Campanian and seafloor surfaces (Figs. 4 and 10). This implies low permeabilities, meaning fewer migration pathways resulting in the sparse distribution of pockmarks in the north compared to the south of the study area. Pockmarks in the deep-water study have been influenced by faults and chimneys leading up to the late Campanian and seafloor surfaces. On the late Campanian surface, wide chimneys are linked to giant pockmarks (Fig. 7a), and faults are linked to simple and crater pockmarks (Figs. 8a and 9c, d). All pockmarks are associated with bright(er) spots within the already high amplitude

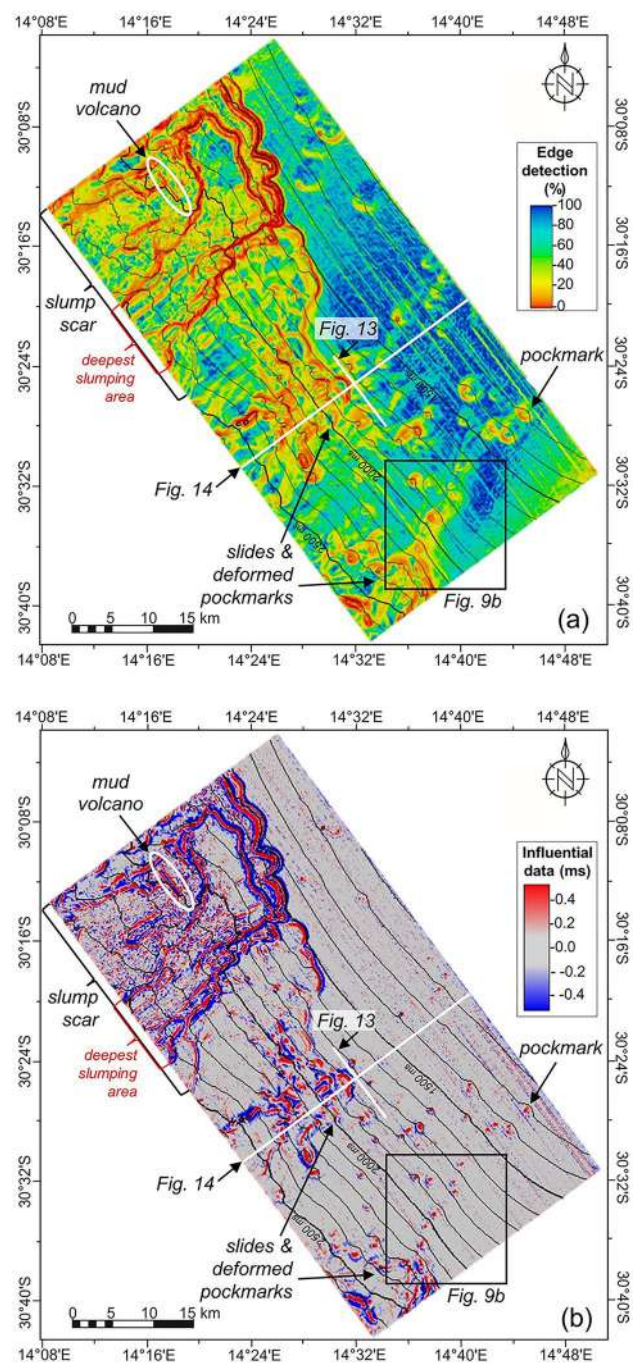


Fig. 10 Pockmarks and slumping features on the seafloor imaged using **a** the edge detection, and **b** influential surface data attributes. The greatest concentration of pockmarks occurs in the S and is often associated with slides (e.g., Fig. 9). The NW is dominated by a large slump scar and within the feature an elongated mud volcano outcrops to the surface

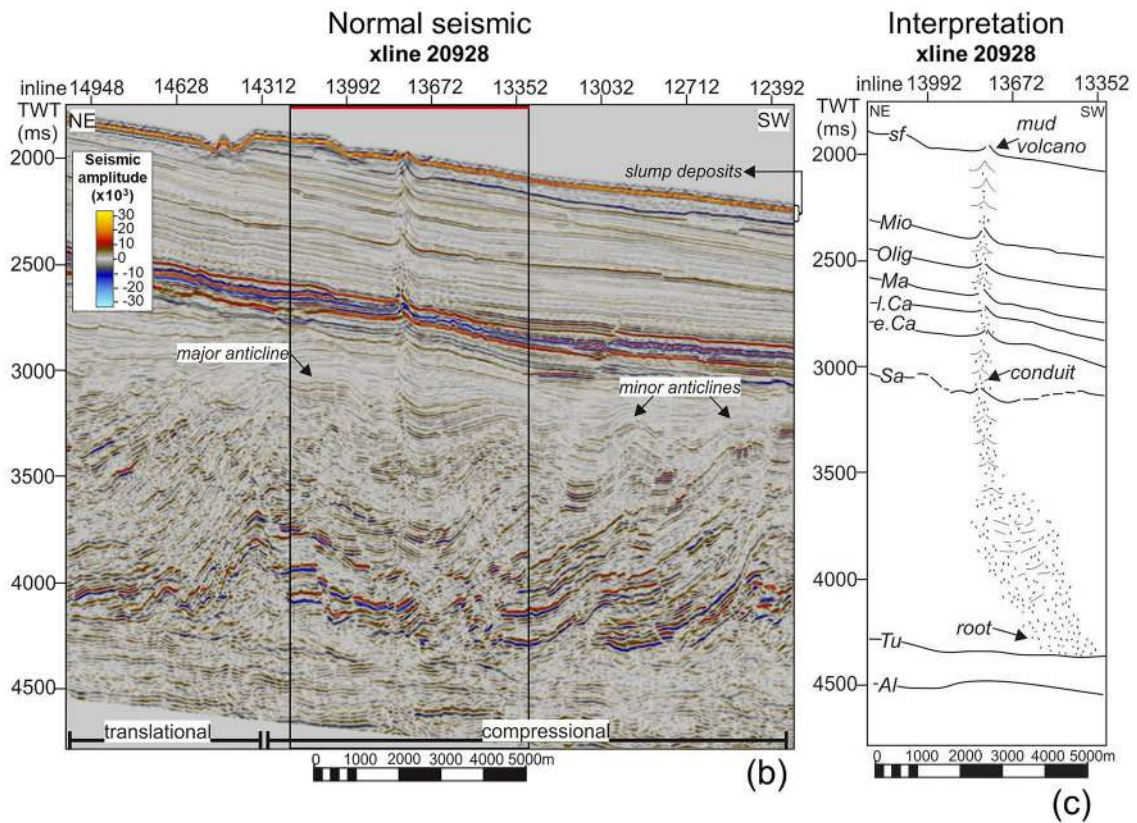
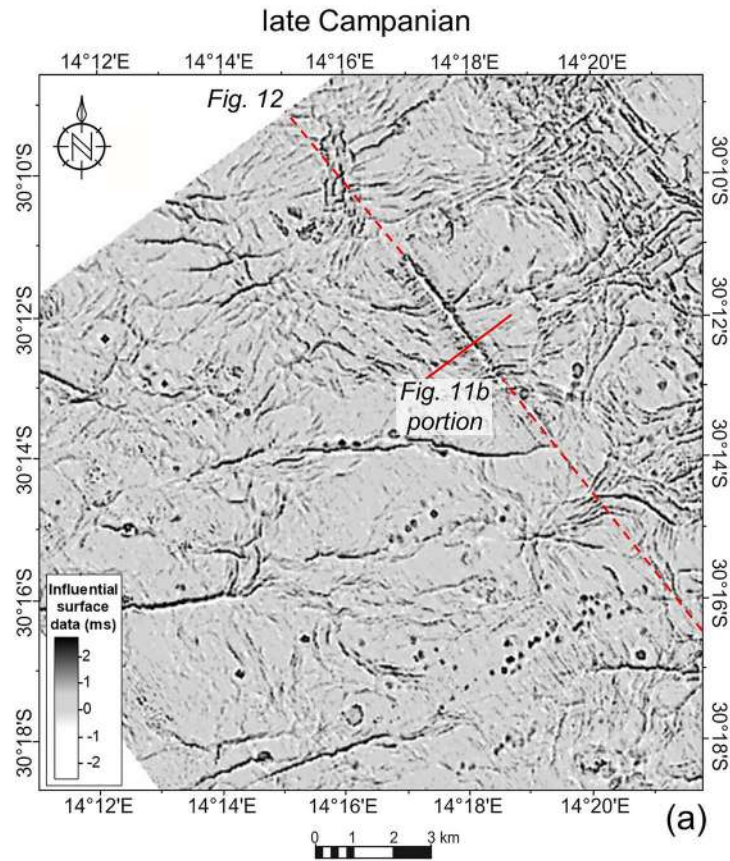


Fig. 11 Mud volcano system. The location of the elongated mud volcano is shown on the late Campanian surface in (a) surrounded by simple pockmarks (red solid line=xline position shown in b and c; red stippled line=inline position shown in Fig. 12). The cross-section width of the mud volcano is shown in (b) situated in the centre of the largest anticline around the intersection of the translational and compressional domains. The interpretation of the mud volcano plumbing system along its width is shown in (c)

late Campanian and seafloor surfaces they are found along. Although the cross sections in Fig. 9c and d do not show a distinct association between the two pockmarked surfaces, the fact that seafloor pockmarks occur in the same area or follow the same trend as those of the late Campanian mean that there is a relationship. A possible explanation is that a

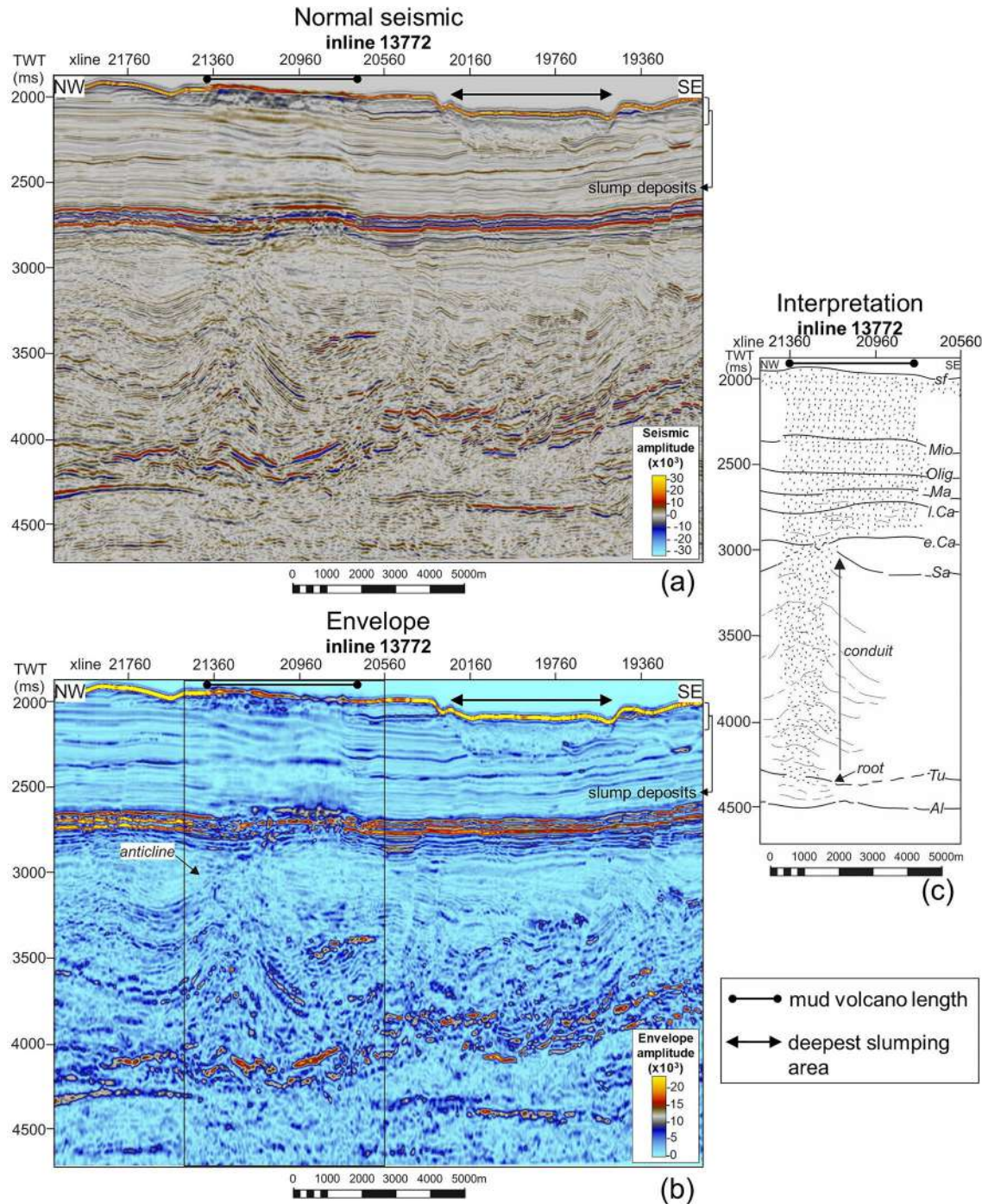


Fig. 12 Mud volcano system and slump scar. The cross-section length of an elongated mud volcano is shown in (a) situated in the centre of the largest anticline with a major slump scar adjacent to it. The envelope attribute in (b) shows acoustically dampened and disrupted

reflections within the mud volcano system and the slump deposit compared to their surroundings. The interpretation of the mud volcano plumbing system along its length is shown in (c)

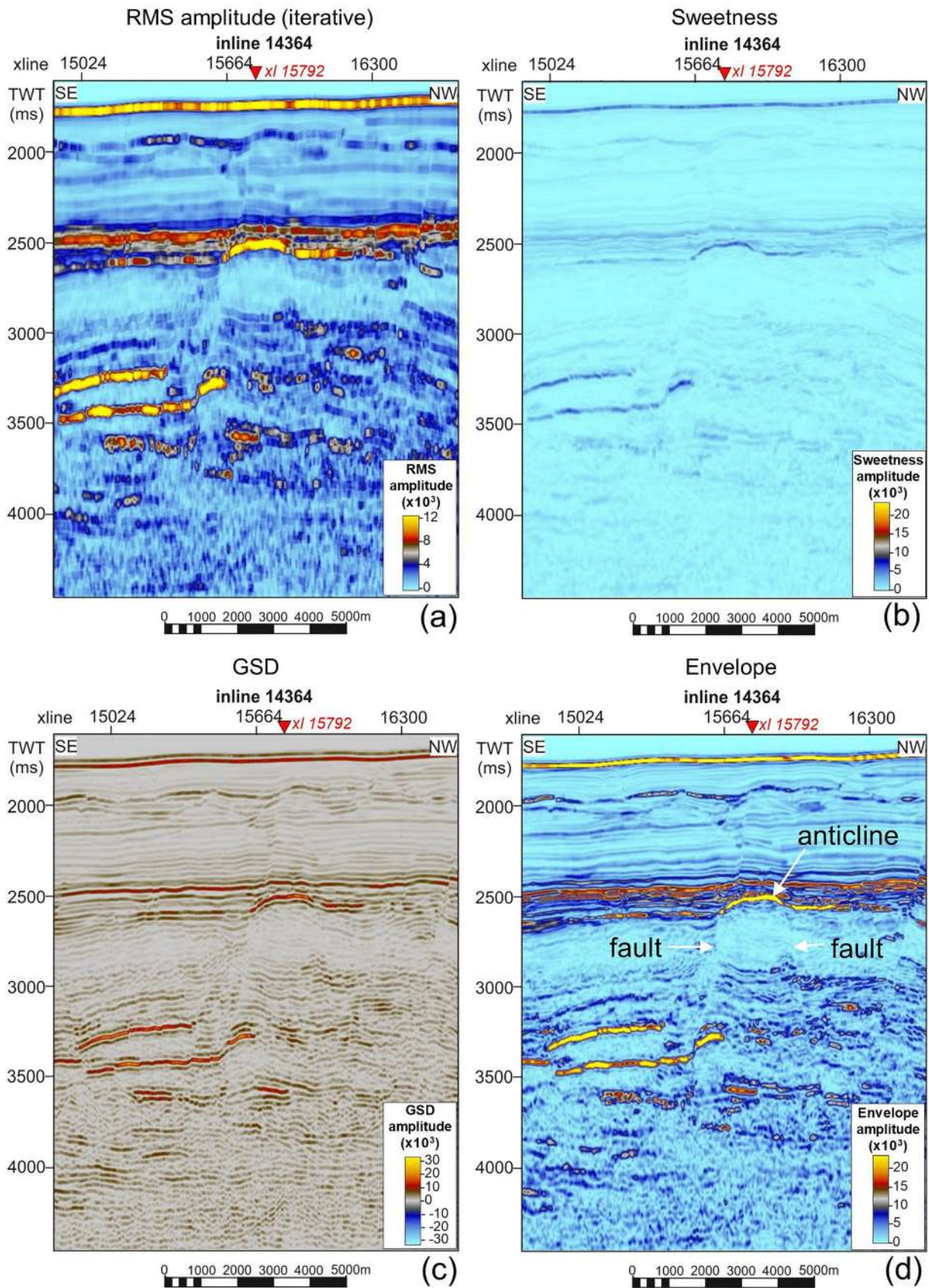


Fig. 13 Inline section of an anticline located within a horst structure shown using the: **a** RMS (iterative), **b** sweetness, **c** GSD and **d** envelope volumetric attributes. Although all volumetric attributes used indicate the presence and accumulation of hydrocarbons along the high amplitude feature, the envelope volumetric attribute in (**d**) highlights the anticline well without distorting the stratigraphy and structure of its surroundings compared to other volumetric attributes

fracture system is at play, with displacements being below the smallest vertical resolution limit of 30 m between the two surfaces and below the late Campanian. A few giant pockmarks have also identified in the Barents Sea associated with melting ice, and three in the North Sea with one being the approximate size of a football field (900 m wide and 450 m deep) (Judd et al. 1994; Judd and Hovland 2007). Judd and Hovland (2007) attribute the formation of these giant pockmarks to the process of explosive decompression, whereby high fluid overpressures penetrate the surface in extreme cases such as the elongated Lokbatan-type mud volcanoes. Since giant pockmarks indicate rapid rates of methane expulsion (Roberts et al. 2006; Judd and Hovland 2007), so are their connected subsurface chimneys (Fig. 7).

Crater pockmarks are confined to the SE, located centrally within cells of polygonal faults (Figs. 4 and 6). Polygonal faults are found between the Santonian to Miocene sediments, have variable strike orientations, small fault throws and lateral extensions, and high densities (Figs. 4, 5 and 6). The variable strike orientations indicate that they do not have a principal stress direction (Fig. 5) and were thus not formed by regional compressional or extensional tectonics, but rather hydraulic fracturing (Cartwright 2007). Andresen and Huuse (2011) informally termed pockmarks associated with polygonal faulting as ‘bulls-eye’ pockmarks because of their central location within the faults. These ‘bulls-eye’ pockmarks are found within Plio-Pleistocene sediments of the Lower Congo Basin and have large size ranges, measuring between 70 and 500 m in diameter and 20–50 m in depth. In contrast to the ones observed on the Late Campanian surface in this study, those of the Congo Basin occur as a stacked succession in the stratigraphy. The concentric arrangement of pockmarks within, rather than above, polygonal faults strongly suggests that crater pockmark formation predates polygonal faulting (Andresen and Huuse 2011).

On the late Campanian surface, simple pockmarks dominate in the SW to NW compressional domain region, occurring along faults, in linear belts unrelated to visible faults and conjoined composite clusters (Fig. 9a), within giant pockmarks (Figs. 6, 7b and 11a), and otherwise random distributions (Fig. 4). The few pockmarks observed on the seafloor have a strong spatial relationship to those on the late Campanian surface with most displaying a simple circular morphology in plan view (Figs. 9a, b and 10). Directly south of the present study, Mahlalela et al. (2021) describe a few simple pockmarks on the seafloor that are 700–1100 m in

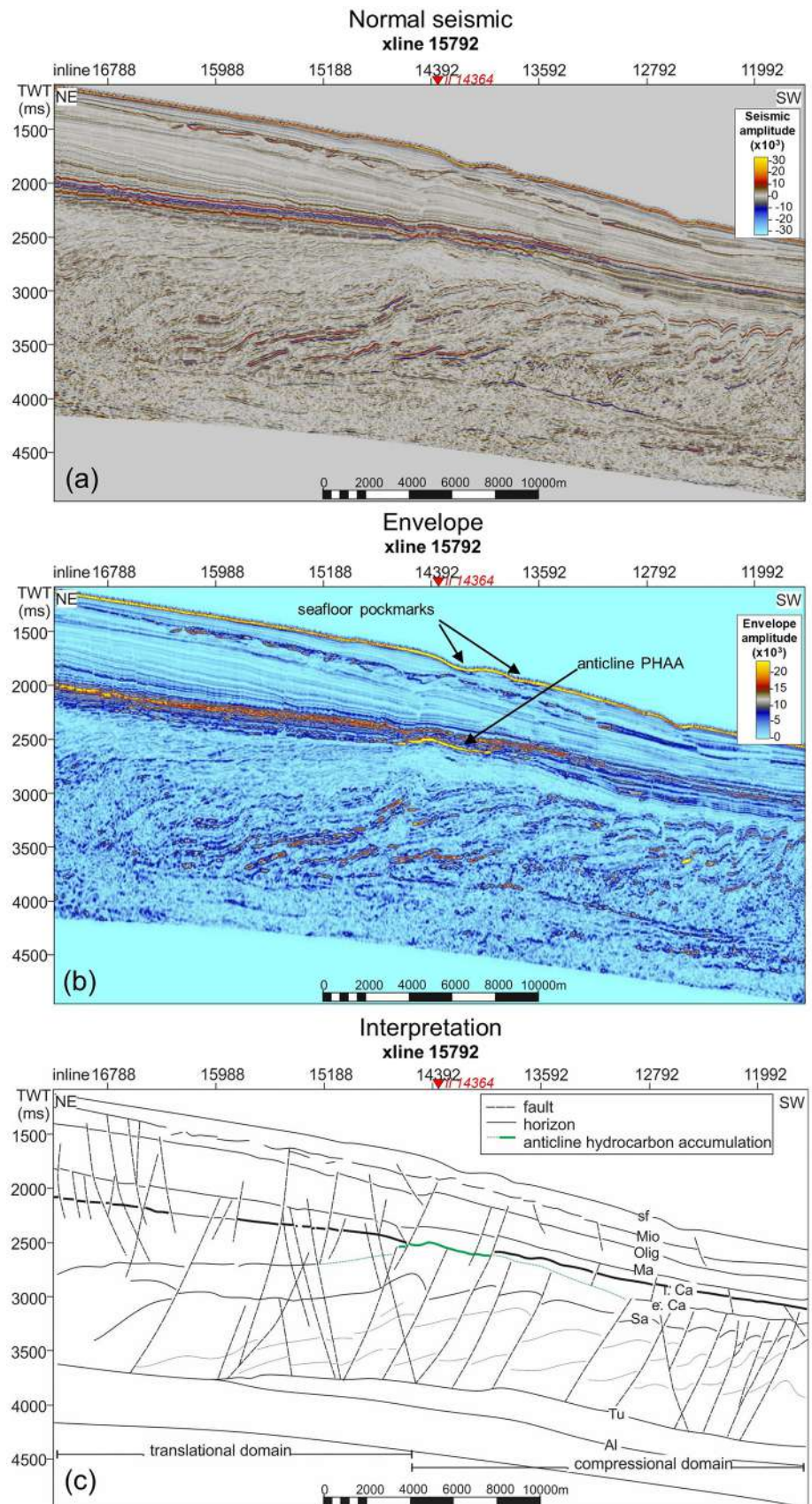
diameter with depressions 75–103 m deep. These pockmarks represent the same pockmark field observed on the seafloor surface in this study.

Mud volcano

The morphology of mud volcanoes is controlled by several dynamic and mechanical factors, including: the frequency and vigour of volcanism, width of the conduit, pre-existing local topography, erosion type (e.g., bottom currents, wind, rain), rate of basin subsidence and the thickness and character of the affected strata (Mazzini and Etiope 2017). Cone-shaped mud volcanoes, the most common morphology, are observed in the shallow reaches of the Orange Basin following a N/NNW trend which is strongly associated with active, near-vertical strike-slip faults, thus reflecting neo-tectonic activity (Ben-Avraham et al. 2002; Viola et al. 2005). According to Viola et al. (2005) the mud volcanoes are the offshore structural expression of the same stress field observed onshore Namaqualand, South Africa and central Namibia, where recent faulting created N/NNW and NW orientated lineaments. Both offshore and onshore structures follow the present-day stress field of SW Africa and are thus postulated to be attributed to the Wegener stress anomaly (since the greatest horizontal compressive stress is NW/NNW). The mud volcano observed in this deep-water study also trends NW, however, unlike those observed in the proximal Orange Basin, it is elongated in morphology. An onshore example of an elongated mud volcano is the Lokbatan located in Azerbaijan (Planke et al. 2003; Mazzini and Etiope 2017). The Lokbatan has provided the basis of what is known of elongated mud volcanoes worldwide since it is easily accessible. This elongated mud volcano is characterised by extremely explosive eruptions with the last recorded in 2001 ejecting mud breccia after a large initial burst of hot methane (Planke et al. 2003; Mazzini and Etiope 2017). The volume of the Lokbatan mud volcano is affected by the deflation of the underlying shallow chamber following each eruption (Planke et al. 2003).

In like manner as the Lokbatan mud volcano coinciding with the trend of an anticline axis (Mazzini and Etiope 2017), the elongated mud volcano in this study is also situated along the axis of a deep-seated anticline (Fig. 11b, c) and is therefore tectonically controlled. The anticline forms part of a Upper Cretaceous fold and thrust belt marking the intersection of the translational and down-dip compressional domains. Sedimentary volcanism is postulated to have begun in the Santonian (86–83 Ma) since deformation shown by convex pull-up reflectors starts within these sediments (Figs. 11 and 12). This age coincides with the start of the oil and gas maturation window at 85 Ma estimated by Hirsch et al. (2010) for the Turonian shale detachment surface from which the mud volcano roots from (Figs. 11 and

Fig. 14 Crossline section showing the stratigraphy and structure of the margin from an Upper Cretaceous DWFTB system underneath younger Cenozoic successions. The uninterpreted seismic section is shown in (a). The envelope volumetric attribute shown in (b) highlights the greatest accumulation of hydrocarbons as a PHAA defining an anticline, and c is the overall combined interpretation of the inline



12). The mud volcano gradually increased in height shown by stratigraphic surfaces leading up to the seafloor which could possibly indicate intense eruptions.

Source of hydrocarbons

Since pockmarks and mud volcanoes are found in a wide variety of settings, from passive to active margin settings, in compressional zones such as accretionary prisms, fold and thrust belt systems, deltaic settings and deep sedimentary basins related to active plate margins (e.g., Judd and Hovland 1988; Gay et al. 2003, 2006, 2007; Loncke et al. 2004; Hustoft et al. 2010; Andresen and Huuse 2011; Ho et al. 2012; Hartwig et al. 2012; Anka et al. 2014), the source of their hydrocarbon system varies greatly. From the synthesis of past studies in the shallow Orange Basin (Jungslager 1999; Ben-Avraham et al. 2002; Kuhlmann et al. 2010; Hartwig et al. 2012), we postulate the source of hydrocarbons in this study to also be of both thermogenic and biogenic (or microbial) origin. According to van der Spuy (2003) and Paton et al. (2007), thermogenic gas originates from the deep, thermally mature Aptian source shales which become progressively oil-prone distally (Jungslager 1999). Since the Turonian shale detachment surface is also a speculated source rock interval, thermogenic hydrocarbons may have been sourced from both the deep-seated Aptian (unobserved in this study) and Turonian shales in this study. Fluid migration pathways stemming from the Turonian surface, together with late Campanian pockmarks linked to them, may therefore consist of thermogenic hydrocarbons. Biogenic gas is believed to originate from younger, organic-rich sediments involved in the upwelling of the Benguela Current in the Cenozoic (Kuhlmann et al. 2010).

An increase in biogenic activity attributed to the Benguela current upwelling system is recorded in the late Miocene to early Pliocene sediments offshore SW Africa (Diester-Haass et al. 2004; Rommerskirchen et al. 2011). This period of upwelling coincides with the development of thermally stratified bottom and deep-water currents offshore SW Africa resulting in major depositional changes observed in the Miocene (Weigelt and Uenzelmann-Neben 2004; Maduna et al. 2022). Seafloor pockmarks in this study are postulated to consist of a mixture of both thermogenic and biogenic hydrocarbons since the faults feeding them initiate from within the Cenozoic sediments; at the Oligocene and Miocene surfaces (Fig. 9c, d). The dissociation of gas hydrates is another possible origin for the source of hydrocarbons. Ben-Avraham et al. (2002) related their mud volcanoes in the shallower extents of the Orange Basin to a gas hydrate stability zone (GHSTZ) at depth. There is no evidence to support this hypothesis in the present deep-water study since no bottom-simulating reflectors (BSR) or other definitive gas hydrate indicators are observed in the seismic volume.

Migration and accumulation of hydrocarbons

The distribution of surface and subsurface gas/fluid escape features shows the overall intensification of methane flux increases from the SE to the NW. In the SE, crater pockmarks on the late Campanian surface are associated with faults (moderate methane flux) (Figs. 4 and 6). In the NW, an elongated mud volcano (high methane flux) is found surrounded by a large slump scar on the seafloor (Figs. 4 and 10). Unlike the heavily faulted E, SE and central areas of the study, the NW has very few faults (Fig. 4). Consequently, instead of fluid flow pressures being distributed along many faults, one near-vertical fault-turned-vent took all the pressure, erupting gas, fluids and sediment to the palaeo- and current seafloors through an elongated mud volcano. Gas and fluids are postulated to have been escaping to the ocean/atmosphere since the Santonian when sedimentary volcanism began which may account for the lack of PHAAs within or surrounding the mud volcano (Figs. 11b and 12b). PHAAs are mostly found in the central and SW regions of the study (Figs. 5, 13 and 14). In addition to migrating upwards along fault surfaces, over-pressurized fluids may also travel through the permeable beds (e.g., Gay et al. 2006). This is seen in the centre of the study area where an anticline on the late Campanian surface displays a PHAA using the envelope attribute in Fig. 14b. The PHAA anticline is situated directly above the intersection of the compressional and translational domains and is bound within a horst structure (Figs. 13 and 14). Hydrocarbons are therefore both structurally (anticline and horst structure) and stratigraphically (late Campanian surface) trapped. As sedimentation progressed, hydrocarbons migrated upwards through the stratigraphy to the seafloor when later faults formed. Irregular pockmarks on the seafloor, directly above the PHAA anticline, may be explained by this continued seep of hydrocarbons disrupting their normal elliptical/cone-shaped depressions (Figs. 10 and 14).

Mass wasting features

Slides are observed in the S and centre of the study area, and a major slump scar is observed in the NW on the present-day seafloor (Fig. 10). Slides are known to be coherent masses with minor internal deformation as shown in this study (Fig. 9d), while slumps (a mass flow that is a magnitude higher in flow velocity) are characterised by more internal deformation as seen from the seafloor sediments in Figs. 11b and 12 (Posamentier and Martinsen 2011). These mass wasting features are closely related to gas/fluid escape features found on the seafloor; an elongated mud volcano is found in the centre of the slump scar in the NW (Figs. 10, 11 and 12) and pockmarks are found together with slides in the S (Figs. 9b, d and 10). Both mass wasting features occur

in the distal down-dip region where the slope dips steepest. Possible triggers for mass wasting on the seafloor and the underlying Upper Cretaceous DWFTB system (a different type of mass transport) include seismicity, rapid sedimentation rates upon a dipping slope, high internal pore fluid pressures and downslope undercutting (Séranne and Anka 2005; Rogers and Rau 2006; Kuhlmann et al. 2010). Another trigger mechanism for mass wasting in the Cenozoic is the interaction of opposite-flowing ocean currents along the SW African margin (Weigelt and Uenzelmann-Neben 2004).

High methane expulsion rates associated with sedimentary volcanism (Roberts et al. 2006) destabilized sediments surrounding the elongated mud volcano. This led to major slumping on the seafloor. The size of the slump scar is an indication of how much sediment was (and possibly still is) being remobilized in the underlying stratigraphy—greater than 26×19 km. Pockmarks formed under moderate hydrocarbon expulsion rates (Roberts et al. 2006) and consequently, instead of one large slump feature, they are associated with smaller slides which reflect lower flow velocities (Fig. 10). Slope instability leading to these mass wasting features along a dipping slope arise from discontinuities in the subsurface. These discontinuities are faults between the Oligocene to seafloor surfaces leading to pockmark formation and are the gliding planes of some slumps (Figs. 9c and d). Large and irregular seafloor pockmarks in association with slides (Fig. 10) reflect the progressive downslope flow of sediment in mass wasting, i.e., pockmarks grow in size as slides continue downslope along a gliding plane as seen in Fig. 9d. On the seafloor this implies that Cenozoic faults first led to pockmark formation, and some of these very same faults became gliding planes for mass sediment flows (slides). Cenozoic mass wasting features are also observed in the shallower regions of the Orange Basin caused by margin instability and gravity faulting as old, underlying faults were rejuvenated in the outer margin (e.g., Hirsch et al. 2010; Palan et al. 2020).

Conclusions

The 3D seismic data helped to view natural gas and fluid escape features which would previously have been missed or not fully resolved in a regular 2D survey. This study describes the occurrence of widespread natural gas/fluid escape features in relation to an underlying Upper Cretaceous DWFTB system in the deep-water Orange Basin. Together with the shallow water hydrocarbon systems in play, and encouraging deep-water discoveries in Namibia, the numerous gas/fluid escape features observed in this study point to a prolific hydrocarbon system in the deep-water

South African basin that is yet to be exploited. The following conclusions can be drawn with regards to the origin, distribution and occurrence of gas/fluid escape features, and its implications on the deep-water basin's hydrocarbon system:

- Hydrocarbons are biogenic and mostly thermogenic and in origin, sourced from nutrient-rich Cenozoic sediments and the speculated Turonian source rock, respectively, in addition to the thermogenic Aptian source shales.
- Methane expulsion rates increase from the SE to NW having culminated in an elongated mud volcano situated within an anticline axis of a Upper Cretaceous thrust belt marking the intersection of the translational and compressional domains. The tectonically controlled mud volcano is indicative of extreme overpressures, and thus, rapid rates of methane flux.
- On the seafloor, sediment instability resulted in major slumping in the NW due to sediment remobilization associated with mud volcanism, and smaller slides in the S associated with pockmarks.
- Hydrocarbons migrated in a NW direction following the underlying trend of a Upper Cretaceous thrust belt located at the intersection of the translational and compressional domains.
- The largest accumulation of hydrocarbons, and hence most favourable place to drill is in the region directly above the late Campanian anticline based on it appearing as a PHAA, and the presence of seafloor pockmarks directly above the area.

We recommend drilling to ground truth the observations made to get the exact stratigraphy, ages, depths, rates of gas expulsion and nature of the sediments. This will ultimately determine the economic viability of the deep-water Orange Basin's hydrocarbon system.

Supplementary Information The online version contains supplementary material available at <https://doi.org/10.1007/s11001-023-09523-2>.

Acknowledgements For funding the first author's doctoral, our sincerest thanks are extended to the National Research Foundation (NRF) of South Africa and the South African Council for Geoscience (CGS), respectively. We would also like to thank Shell and the Petroleum Agency of South Africa (PASA) for providing the 3D reflection seismic data, and Schlumberger for the Petrel software and support. We are furthermore grateful for the scientific discussions and insights provided by our friends and colleagues from the Wits Seismic Research Centre. The authors thank two anonymous reviewers whose comments have greatly improved the manuscript. The authors also thank Dr. Wu-Cheng Chi for editorial handling.

Author contributions All authors contributed to the conception and design of the manuscript. NGM conducted the research and wrote the manuscript draft; MSDM and ZJ supervised the main author's research; MSDM, ZJ, and JEB reviewed and edited the manuscript. All authors read and approved the final manuscript.

Funding Open access funding provided by University of the Witwatersrand. This study was funded by the National Research Foundation (NRF) of South Africa for the first author's doctoral under grant UID: 130186, and the South African Council for Geoscience (CGS) for the first author's master's degree.

Data availability The data are the property of Shell and may be purchased through the Petroleum Agency of South Africa's (PASA) online geoportal at https://geoportal.petroleumagencysa.com/Storefront/Viewer/index_map.html (last access: 9 November 2022).

Declarations

Competing interests The authors have no competing interests to declare that are relevant to the content of this manuscript.

Ethical approval Not applicable.

Consent to participate Not applicable.

Consent for publication All authors give consent for publication.

Open Access This article is licensed under a Creative Commons Attribution 4.0 International License, which permits use, sharing, adaptation, distribution and reproduction in any medium or format, as long as you give appropriate credit to the original author(s) and the source, provide a link to the Creative Commons licence, and indicate if changes were made. The images or other third party material in this article are included in the article's Creative Commons licence, unless indicated otherwise in a credit line to the material. If material is not included in the article's Creative Commons licence and your intended use is not permitted by statutory regulation or exceeds the permitted use, you will need to obtain permission directly from the copyright holder. To view a copy of this licence, visit <http://creativecommons.org/licenses/by/4.0/>.

References

- Aizawa M, Bluck B, Cartwright J, Milner S, Swart R, Ward J (2000) Constraints on the geomorphological evolution of Namibia from the offshore stratigraphic record. *Commun Geol Surv Namibia* 12:337–346
- Aldrich, J, Zilinski, R, Edman, J, Leu, W, Berge, T and Corbett, K (2003) Documentation of a new petroleum system in the South Atlantic. In AAPG Annual Convention Salt Lake City, p. 90013
- Andresen KJ (2012) Fluid flow features in hydrocarbon plumbing systems: What do they tell us about the basin evolution? *Mar Geol* 332:89–108. <https://doi.org/10.1016/j.margeo.2012.07.006>
- Andresen KJ, Huuse M (2011) 'Bulls-eye' pockmarks and polygonal faulting in the Lower Congo Basin: relative timing and implications for fluid expulsion during shallow burial. *Mar Geol* 279:111–127. <https://doi.org/10.1016/j.margeo.2010.10.016>
- Anka Z, Loegering M, di Primio R, Marchal D, Rodriguez J, Vallejo E (2014) Distribution and origin of natural gas leakage in the Colorado Basin, offshore Argentina Margin, South America: seismic interpretation and 3D basin modelling. *Geol Acta* 12:269–285. <https://doi.org/10.1344/GeologicaActa2014.12.4.1>
- Baby G, Guillocheau F, Morin J, Ressouche J, Robin C, Broucke O, Dall'Asta M (2018) Post-rift stratigraphic evolution of the Atlantic margin of Namibia and South Africa: implications for the vertical movements of the margin and the uplift history of the South African Plateau. *Mar Petrol Geol* 97:169–191. <https://doi.org/10.1016/j.marpetgeo.2018.06.030>
- Baby G, Guillocheau F, Braun J, Robin C, Dall'Asta M (2020) Solid sedimentation rates history of the Southern African continental margins: implications for the uplift history of the South African Plateau. *Terra Nova* 32:53–65. <https://doi.org/10.1111/ter.12435>
- Ben-Avraham Z, Smith G, Reshef M, Jungslager E (2002) Gas hydrate and mud volcanoes on the southwest African continental margin off South Africa. *Geology* 30:927–930. [https://doi.org/10.1130/0091-7613\(2002\)030%3c0927:GHAMVO%3e2.0.CO;2](https://doi.org/10.1130/0091-7613(2002)030%3c0927:GHAMVO%3e2.0.CO;2)
- Bilotti F, Shaw JH (2005) Deep-water Niger Delta fold and thrust belt modeled as a critical-taper wedge: the influence of elevated basal fluid pressure on structural styles. *AAPG Bull* 89:1475–1491. <https://doi.org/10.1306/06130505002>
- Bolli HM, Ryan WBF, Foresman JB, Hottman WE, Kagami H, Longoria JF, McKnight BK, Melguen M, Natland J, Proto-Decima F (1978) Cape basin continental rise sites 360 and 361. *Init Rep Deep Sea Drill Proj* 40:29–182
- Boyd D, Anka Z, di Primio R, Kuhlmann G, De Wit MJ (2011) Passive margin evolution and controls on natural gas leakage in the Orange Basin, South Africa. *South Afr J Geol* 114:415–432. <https://doi.org/10.2113/gssaj.114.3-4.415>
- Brown KM (1990) The nature and hydrogeological significance of mud diapirs and diatremes for accretionary systems. *J Geophys Res* 95:8969–8982. <https://doi.org/10.1029/JB095iB06p08969>
- Brown R, Summerfield M, Gleadow A, Gallagher K, Carter A, Beucher R, Wildman M (2014) Intracontinental deformation in southern Africa during the late cretaceous. *J Afr Earth Sci* 100:20–41
- Brown LF, Benson JM, Brink GJ, Doherty S, Jollands A, Jungslager EAH, Keenan JHG, Muntingh A, van Wyk NJS (1995) Sequence stratigraphy in offshore south african divergent basins: an atlas on exploration for cretaceous lowstand traps by soekor. *AAPG Studies in Geology*, Tulsa, p 191
- Burnett MD, Castagna JP, Méndez-Hernández E, Rodríguez GZ, García LF, Vázquez JTM, Avilés MT, Villaseñor RV (2003) Application of spectral decomposition to gas basins in Mexico. *Lead Edge* 22:1130–1134. <https://doi.org/10.1190/1.1634918>
- Cartwright JA (1994) Episodic basin-wide fluid expulsion from geopressured shale sequences in the North Sea basin. *Geology* 22:447–450. [https://doi.org/10.1130/0091-7613\(1994\)022%3c0447:EBWFEF%3e2.3.CO;2](https://doi.org/10.1130/0091-7613(1994)022%3c0447:EBWFEF%3e2.3.CO;2)
- Cartwright J (2007) The impact of 3D seismic data on the understanding of compaction, fluid flow and diagenesis in sedimentary basins. *J Geol Soc Lond* 164:881–893. <https://doi.org/10.1144/0016-76492006-14>
- Cartwright J (2011) Diagenetically induced shear failure of fine-grained sediments and the development of polygonal fault systems. *Mar Petrol Geol* 28:1593–1610. <https://doi.org/10.1016/j.marpetgeo.2011.06.004>
- Cartwright J, Santamarina C (2015) Seismic characteristics of fluid escape pipes in sedimentary basins: implications for pipe genesis. *Mar Petrol Geol* 65:126–140. <https://doi.org/10.1016/j.marpetgeo.2015.03.023>
- Cartwright J, Huuse M, Aplin A (2007) Seal bypass systems. *AAPG Bull* 91:1141–1166. <https://doi.org/10.1306/04090705181>
- Cartwright J, James D, Bolton A (2003) The genesis of polygonal fault systems: a review. *Subsurface sediment mobilization. Geol Soc Lond Spec Publ* 216:223–243. <https://doi.org/10.1144/GSL.SP.2003.216.01.15>
- Cathles LM, Su Z, Chen D (2010) The physics of gas chimney and pockmark formation, with implications for assessment of sea-floor hazards and gas sequestration. *Mar Petrol Geol* 27:82–91. <https://doi.org/10.1016/j.marpetgeo.2009.09.010>
- Cataneanu O (2006) Principles of sequence stratigraphy. Elsevier, Amsterdam, p 375
- Chopra S, Marfurt KJ (2005) Seismic attributes — A historical perspective. *Geophysics* 70:3SO–28SO. <https://doi.org/10.1190/1.2098670>

- Clemson J, Cartwright J, Booth J (1997) Structural segmentation and the influence of basement structure on the Namibian passive margin. *J Geol Soc* 154:477–482. <https://doi.org/10.1144/gsjgs.154.3.0477>
- Collier JS, McDermott C, Warner G, Gyori N, Schnabel M, McDermott K, Horn BW (2017) New constraints on the age and style of continental breakup in the South Atlantic from magnetic anomaly data. *Earth Planet Sc Lett* 477:27–40. <https://doi.org/10.1016/j.epsl.2017.08.007>
- Corredor F, Shaw JH, Bilotti F (2005) Structural styles in the deep-water fold and thrust belts of the Niger Delta. *AAPG Bull* 89:753–780. <https://doi.org/10.1306/02170504074>
- Dalton TJS, Paton DA, Needham T, Hodgson N (2015) Temporal and spatial evolution of deepwater fold thrust belts: Implications for quantifying strain imbalance. *Interpretation* 3:SAA59–SAA70. <https://doi.org/10.1190/INT-2015-0034.1>
- Dalton TJS, Paton DA, Needham DT (2017) Influence of mechanical stratigraphy on multi-layer gravity collapse structures: insights from the Orange Basin, South Africa. *Geol Soc Lond Sp Publ* 438:211–228. <https://doi.org/10.1144/SP4384>
- de Vera J, Granado P, McClay K (2010) Structural evolution of the Orange Basin gravity-driven system, offshore Namibia. *Mar Petrol Geol* 27:223–237. <https://doi.org/10.1016/j.marpetgeo.2009.02.003>
- Diester-Haass L, Meyers PA, Bickert T (2004) Carbonate crash and biogenic bloom in the late Miocene: evidence from ODP Sites 1085, 1086, and 1087 in the Cape Basin, southeast Atlantic Ocean. *Paleoceanography*. <https://doi.org/10.1029/2003PA000933>
- Dimitrov LI (2002) Mud volcanoes—the most important pathway for degassing deeply buried sediments. *Earth Sci Rev* 59:49–76. [https://doi.org/10.1016/S0012-8252\(02\)00069-7](https://doi.org/10.1016/S0012-8252(02)00069-7)
- Emery KO, Uchupi E, Bowin CO, Phillips J, Simpson ESW (1975) Continental margin off Western Africa: Cape St Francis (South Africa) to Walvis Ridge (South-West Africa). *AAPG Bull* 59:3–59. <https://doi.org/10.1306/83D91C09-16C7-11D7-8645000102C1865D>
- Feder J (2019) Offshore: making a comeback after the downturn. *J Pet Technol* 71:27–31. <https://doi.org/10.2118/0519-0027-JPT>
- Frimmel HE, Basei MS, Gaucher C (2011) Neoproterozoic geodynamic evolution of SW-Gondwana: a southern African perspective. *Int j Earth Sci Geol* 100:323–354. <https://doi.org/10.1007/s00531-010-0571-9>
- Gay A, Lopez M, Cochonot P, Sultan N, Cauquil E, Brigaud F (2003) Sinuous pockmark belt as indicator of a shallow buried turbiditic channel on the lower slope of the Congo Basin, West African Margin. *Geol Soc Lond Spec Publ* 216:173–189. <https://doi.org/10.1144/GSL.SP.2003.216.01.12>
- Gay A, Lopez M, Cochonot P, Séranne M, Levaché D, Sermondadaz G (2006) Isolated seafloor pockmarks linked to BSRs, fluid chimneys, polygonal faults and stacked Oligocene-Miocene turbiditic palaeochannels in the Lower Congo Basin. *Mar Geol* 226:25–40. <https://doi.org/10.1016/j.margeo.2005.09.018>
- Gay A, Lopez M, Berndt C, Seranne M (2007) Geological controls on focused fluid flow associated with seafloor seeps in the Lower Congo Basin. *Mar Geol* 244:68–92. <https://doi.org/10.1016/j.margeo.2007.06.003>
- Granado P, Vera JD, McClay KR (2009) Tectonostratigraphic evolution of the Orange Basin, SW Africa. *Trabajos de geología* 29:321–328
- Hartwig A, Anka Z, di Primio R (2012) Evidence of a widespread paleo-pockmarked field in the Orange Basin: an indication of an early Eocene massive fluid escape event offshore South Africa. *Mar Geol* 332–334:222–234. <https://doi.org/10.1016/j.margeo.2012.07.012>
- Heins WA (2022) Probing the frontier in Namibia. *First Break* 40:51–57. <https://doi.org/10.3997/1365-2397.fb2022037>
- Henriet JP, De Batist M, Verschuren J (1991) Early fracturing of Palaeogene clays, southernmost North Sea: relevance to mechanisms of primary hydrocarbon migration. *Spec Pub Eur Assoc Petrol* 1:217–227
- Herron DA (2011) Resolution. In: Latimer RB (ed) *First steps in seismic interpretation*. Soc Expl Geophys, Tulsa, pp 75–82
- Hirsch KK, Scheck-Wenderoth M, van Wees J-D, Kuhlmann G, Paton DA (2010) Tectonic subsidence history and thermal evolution of the Orange Basin. *Mar Petrol Geol* 2:565–584. <https://doi.org/10.1016/j.marpetgeo.2009.06.009>
- Ho S, Cartwright JA, Imbert P (2012) Vertical evolution of fluid venting structures in relation to gas flux, in the Neogene-Quaternary of the Lower Congo Basin, Offshore Angola. *Mar Geol* 332:40–55. <https://doi.org/10.1016/j.margeo.2012.08.011>
- Holtar E, Forsberg AW (2000) Postrift development of the Walvis Basin, Namibia: results for the exploration campaign in quadrant 1911. In: Mello MR, Katz BJ (eds) *Petroleum Systems of South Atlantic Margins*. AAPG Mem, Tulsa, pp 429–446
- Hovland M, Judd AG (1988) Seabed pockmarks and seepages: impact on geology, biology and the marine environment. Graham and Trotman Ltd, London, p 293
- Hustoft S, Bünz S, Mienert J (2010) Three-dimensional seismic analysis of the morphology and spatial distribution of chimneys beneath the Nyegga pockmark field, offshore mid-Norway. *Basin Res* 22:465–480. <https://doi.org/10.1111/j.1365-2117.2010.00486.x>
- Huuse M, Jackson CAL, Van Rensbergen P, Davies RJ, Flemings PB, Dixon RJ (2010) Subsurface sediment remobilization and fluid flow in sedimentary basins: an overview. *Basin Res* 22:342–360. <https://doi.org/10.1111/j.1365-2117.2010.00488.x>
- Isiaka AI, Durrheim RJ, Manzi MS, Andreoli MA (2017) 3D seismic analysis of the AK Fault, Orange Basin, South Africa: implications for hydrocarbon leakage and offshore neotectonics. *Tectonophysics* 721:477–490. <https://doi.org/10.1016/j.tecto.2017.10.011>
- Judd AG, Hovland M (2007) *Seabed fluid flow: impact on geology*. Cambridge University Press, Cambridge, Biology and the Marine Environment, p 475p
- Judd AG, Long D, Sankey M (1994) Pockmark formation and activity, UK block 15/25, North Sea. *B Geol Soc Denmark* 41:34–49
- Jungslager EH (1999) Petroleum habitats of the Atlantic margin of South Africa. *Geol Soc Lond Sp Publ* 153:153–168. <https://doi.org/10.1144/GSL.SP.1999.153.01.10>
- King LH, MacLean B (1970) Pockmarks on the Scotian shelf. *Geol Soc Am Bull* 81:3141–3148. [https://doi.org/10.1130/0016-7606\(1970\)81\[3141:POTSS\]2.0.CO;2](https://doi.org/10.1130/0016-7606(1970)81[3141:POTSS]2.0.CO;2)
- Koopmann H, Schreckenberger B, Franke D, Becker K, Schnabel M (2016) The late rifting phase and continental break-up of the southern South Atlantic: the mode and timing of volcanic rifting and formation of earliest oceanic crust. *Geol Soc Lond Sp Publ* 420:315–340. <https://doi.org/10.1144/SP420.2>
- Koson S, Chenrai P, Choowong M (2014) Seismic attributes and their applications in seismic geomorphology. *Bull Earth Sci Thai* 6:1–9
- Kramer EAJ, Heck L (2014) Orange basin 3D pre-processing and preSDM 2013 shell global solutions international BV. Rijswijk, Netherlands
- Krueger A, Gilbert E (2009) Deepwater fold-thrust belts: not all the beasts are equal. AAPG search and discovery article 30085. https://www.searchanddiscovery.com/documents/2009/30085_krueger/index.htm. Accessed 9 Nov 2022
- Kuhlmann G, Adams S, Campher C, van der Spuy D, di Primio R, Horsfield B (2010) Passive margin evolution and its controls on natural gas leakage in the southern Orange Basin, blocks 3/4, offshore South Africa. *Mar Petrol Geol* 27:973–992. <https://doi.org/10.1016/j.marpetgeo.2010.01.010>

- L'Arvor E, Maya T, Lattes P (2020) Seismic survey challenges offshore South Africa. In Second EAGE marine acquisition workshop 2020. EAGE Publications BV, pp 1–3
- Lebedeva-Ivanova N, Polteau S, Bellwald B, Planke S, Berndt C, Stokke HH (2018) Toward one-meter resolution in 3D seismic. *Lead Edge* 37:818–828. <https://doi.org/10.1190/tle37110818.1>
- Light MPR, Maslanyj MP, Greenwood RJ, Banks NL (1993) Seismic sequence stratigraphy and tectonics offshore Namibia. *Geol Soc Lond Sp Publ* 71:163–191. <https://doi.org/10.1144/GSL.SP.1993.071.01.08>
- Loncke L, Mascle J, Parties FS (2004) Mud volcanoes, gas chimneys, pockmarks and mounds in the Nile deep-sea fan (Eastern Mediterranean): geophysical evidences. *Mar Petrol Geol* 21:669–689. <https://doi.org/10.1016/j.marpetgeo.2004.02.004>
- Løseth H, Gading M, Wensaas L (2009) Hydrocarbon leakage interpreted on seismic data. *Mar Petrol Geol* 26:304–1319. <https://doi.org/10.1016/j.marpetgeo.2008.09.008>
- Løseth H, Wensaas L, Gading M (2011) Deformation structures in organic-rich shales. *AAPG Bull* 95:729–747. <https://doi.org/10.1306/09271010052>
- Maduna NG, Manzi MS, Jinnah Z, Bourdeau JE (2022) Strato-structural evolution of the deep-water Orange Basin: constraints from 3D reflection seismic data. *Solid Earth* 13:1755–1780. <https://doi.org/10.5194/se-13-1755-2022>
- Mahlalela V, Manzi MSD, Jinnah Z, Bourdeau JE, Durrheim RJ (2021) Structural characteristics and 3D seismic detection of gas migration pathways in the deep-water Orange Basin. *S Afr Mar Geophys Res* 42:8. <https://doi.org/10.1007/s11001-021-09428-y>
- Manzi MSD, Durrheim RJ, Hein KAA, King N (2012) 3D edge detection seismic attributes used to map potential conduits for water and methane in deep gold mines in the Witwatersrand basin, South Africa. *Geophysics* 77:W133–W147. <https://doi.org/10.1190/geo2012-0135.1>
- Manzi MSD, Hein KAA, King N, Durrheim RJ (2013) Neoproterozoic tectonic history of the Witwatersrand Basin and Ventersdorp Supergroup: new constraints from high-resolution 3D seismic reflection data. *Tectonophysics* 590:94–105. <https://doi.org/10.1016/j.tecto.2013.01.014>
- Maselli V, Kneller B, Taiwo OL, Iacopini D (2019) Sea floor bedforms and their influence on slope accommodation. *Mar Pet Geol* 102:625–637. <https://doi.org/10.1016/j.marpetgeo.2019.01.021>
- Maslanyj MP, Light MPR, Greenwood RJ, Banks NL (1992) Extension tectonics offshore Namibia and evidence for passive rifting in the South Atlantic. *Mar Petrol Geol* 9:590–601. [https://doi.org/10.1016/0264-8172\(92\)90032-A](https://doi.org/10.1016/0264-8172(92)90032-A)
- Mazzini A, Etiope G (2017) Mud volcanism: an updated review. *Earth Sci Rev* 168:81–112
- Mazzini A, Nermoen A, Krotkiewski M, Podladchikov Y, Planke S, Svensen H (2009) Strike-slip faulting as a trigger mechanism for overpressure release through piercement structures. Implications for the Lusi mud volcano. *Indonesia Mar Pet Geol* 26:1751–1765. <https://doi.org/10.1016/j.marpetgeo.2009.03.001>
- Menzies MA, Klempner SL, Ebinger CJ, Baker J (2002) Characteristics of volcanic rifted margins. In: Menzies MA, Klempner SL, Ebinger CJ, Baker J (eds) *Volcanic rifted margins*. Geological Society of America, Boulder, pp 1–14. <https://doi.org/10.1130/0-8137-2362-0.1>
- Mitchum RM, Vail PR, Thompson S (1977) Seismic stratigraphy and global changes of sea level: Part 2. The depositional sequence as a basic unit for stratigraphic analysis: Section 2. Application of seismic reflection configuration to stratigraphic interpretation. *AAPG Memoir*, Tulsa, pp 53–62
- Mohammed M, Paton D, Collier REL, Hodgson N, Negonga M (2017) Interaction of crustal heterogeneity and lithospheric processes in determining passive margin architecture on the southern Namibian margin. *Geol Soc Lond Sp Publ* 438:177–193. <https://doi.org/10.1144/SP438.9>
- Morley CK, King R, Hillis R, Tingay M, Backe G (2011) Deepwater fold and thrust belt classification, tectonics, structure and hydrocarbon prospectivity: a review. *Earth-Sci Rev* 104:41–91. <https://doi.org/10.1016/j.earscirev.2010.09.010>
- Naseer MT, Asim S (2017) Detection of cretaceous incised-valley shale for resource play, Miano gas field, SW Pakistan: spectral decomposition using continuous wavelet transform. *J Asian Earth Sci* 47:358–377. <https://doi.org/10.1016/j.jseaeas.2017.07.031>
- Nemčok M, Schamel S, Gayer R (2005) *Thrustbelts: Structural architecture, thermal regimes and petroleum systems*, 1st edn. Cambridge University Press, Cambridge, pp 1–541
- Palan K, Green AN, Andrews B, Sink K, Wiles EA (2020) A morphometric analysis of the fluid flow features of the southern Orange Basin South Africa. *Mar Geol*. <https://doi.org/10.1016/j.marpetgeo.2020.106145>
- Paton DA, di Primio R, Kuhlmann G, van der Spuy D, Horsfield B (2007) Insights into the petroleum system evolution of the southern Orange Basin, South Africa. *South Afr J Geol* 110:261–274. <https://doi.org/10.2113/gssajg.110.2-3.261>
- Paton DA, van der Spuy D, di Primio R, Horsfield B (2008) Tectonically induced adjustment of passive-margin accommodation space; influence on the hydrocarbon potential of the Orange Basin, South Africa. *AAPG Bull* 92:589–609. <https://doi.org/10.1306/12280707023>
- Petroleum Agency South Africa (PASA) (2017) Information and opportunities, Petroleum Agency South Africa, Cape Town, South Africa. https://www.petroleumagencyrsa.com/images/pdfs/Pet_expl_opp_broch_2017bw1.pdf. Accessed 9 Nov 2022
- Planke S, Svensen H, Hovland M, Banks DA, Jamtveit B (2003) Mud and fluid migration in active mud volcanoes in Azerbaijan. *Geo-Mar Lett* 23:258–268. <https://doi.org/10.1007/s00367-003-0152-z>
- Posamentier HW, Martinsen OJ, Shipp RC (2011) The character and genesis of submarine mass-transport deposits: insights from outcrop and 3D seismic data. *Mass-transport deposits in deepwater settings*. SEPM Special Publication, Tulsa, pp 7–38
- Randen T, Monsen E, Signer C, Abrahamson A, Hansen JO, Sæter T, Schlaf J (2000) Three-dimensional texture attributes for seismic data analysis. In: 2000 SEG Annual Meeting, pp 668–671. <https://doi.org/10.1190/1.1816155>
- Roberts HH, Hardage BA, Shedd WW, Hunt J Jr (2006) Seafloor reflectivity—An important seismic property for interpreting fluid/gas expulsion geology and the presence of gas hydrate. *Lead Edge* 25:620–628. <https://doi.org/10.1190/1.2202667>
- Rogers J, Rau A (2006) Surficial sediments of the wave-dominated Orange River Delta and the adjacent continental margin off south-western Africa. *Afr J Mar Sci* 28:511–524. <https://doi.org/10.2989/18142320609504202>
- Rommerskirchen F, Condon T, Mollenhauer G, Dupont L, Schefuß E (2011) Miocene to Pliocene development of surface and subsurface temperatures in the Benguela current system. *Paleoceanography* 26:1–15. <https://doi.org/10.1029/2010PA002074>
- Rowan MG, Peel FJ, Vendeville BC (2004) Gravity-driven fold belts on passive margins. In: McClay KR (ed) *Thrust tectonics and hydrocarbon systems*. AAPG Bull, Tulsa, pp 157–182
- Scarselli N, McClay K, Elders C (2016) Seismic geomorphology of cretaceous megaslides offshore Namibia (Orange Basin): Insights into segmentation and degradation of gravity-driven linked systems. *Mar Petrol Geol* 75:151–180. <https://doi.org/10.1016/j.marpetgeo.2016.03.012>
- Schoole L, Manzi MS, Zhang SE, Bourdeau JE (2020) An innovative seismic and statistical approach to understand 3D magmatic structures and ore deposits in the western Bushveld Complex. S

- Afr. Ore Geol Rev 126:103784. <https://doi.org/10.1016/j.oregeorev.2020.103784>
- Séranne M, Anka Z (2005) South Atlantic continental margins of Africa: a comparison of the tectonic vs climate interplay on the evolution of equatorial west Africa and SW Africa margins. *J Afr Earth Sci* 43:283–300. <https://doi.org/10.1016/j.jafrearsci.2005.07.010>
- Silva CC, Marcolino CS, and Lima FD (2005) Automatic fault extraction using ant tracking algorithm in the Marlim South Field, Campos Basin. Paper presented at the 2005 SEG Annual Meeting, Houston, Texas, 6–11 November 2005, 857–860. <https://doi.org/10.1190/1.2148294>
- van der Spuy D, Sayidini B (2022) Offshore Namibia discovery signals bright future for South Africa oil and gas. *AAPG Explorer*. <https://explorer.aapg.org/story/articleid/62613/offshore-namibia-discovery-signals-bright-future-for-south-africa-oil-and-gas>. Accessed 31 Mar 2022
- Uenzelmann-Neben G, Tobias W, Gruetzner J, Maik T (2017) Transition from the Cretaceous ocean to Cenozoic circulation in the western South Atlantic—a twofold reconstruction. *Tectonophysics* 716:22–240. <https://doi.org/10.1016/j.tecto.2016.05.036>
- van der Spuy D (2003) Aptian source rocks in some South African Cretaceous basins. *Geol Soc Lond Sp Publ* 207:185–202. <https://doi.org/10.1144/GSL.SP.2003.207.10>
- Viola G, Andreoli M, Ben-Avraham Z, Stengel I, Reshef M (2005) Offshore mud volcanoes and onland faulting in southwestern Africa: neotectonic implications and constraints on the regional stress field. *Earth Planet Sci Lett* 231:147–160. <https://doi.org/10.1016/j.epsl.2004.12.001>
- Viola G, Kounov A, Andreoli MAG, Mattila J (2012) Brittle tectonic evolution along the western margin of South Africa: more than 500 Myr of continued reactivation. *Tectonophysics* 514:93–114. <https://doi.org/10.1016/j.tecto.2011.10.009>
- Weigelt E, Uenzelmann-Neben G (2004) Sediment deposits in the Cape Basin: indications for shifting ocean currents? *AAPG Bull* 88:765–780. <https://doi.org/10.1306/01260403101>
- Wildman M, Brown R, Watkins R, Carter A, Gleadow A, Summerfield M (2015) Post break-up tectonic inversion across the southwestern cape of South Africa: New insights from apatite and zircon fission track thermochronometry. *Tectonophysics* 654:30–55. <https://doi.org/10.1016/j.tecto.2015.04.012>
- Yilmaz Ö (2001) *Seismic data analysis: Processing, inversion, and interpretation of seismic data*. Society of Exploration Geophysicists, Tulsa
- Publisher's Note** Springer Nature remains neutral with regard to jurisdictional claims in published maps and institutional affiliations.

8 A novel approach to fault interpretation using convolutional neural network: a case study of the deep-water Orange Basin, South Africa

3 ^a School of Geosciences, University of the Witwatersrand, 1 Jan Smuts Ave., Johannesburg, 2000, South Africa.

4 ^b Wits Mining Institute, University of the Witwatersrand, 1 Jan Smuts Ave., Johannesburg, 2000, South Africa.

5 ^c Geological Survey of Canada, 601 Booth Street, Ottawa, Ontario, K1A 0E8, Canada.

7 Corresponding author e-mail address: musa.manzi@wits.ac.za (M.S.D. Manzi)

9 ABSTRACT

10 The main method of 3D seismic interpretation is currently through manual and automatic picking of faults and
11 horizons along the inline, crossline, and time or depth slices of the seismic volume. Manual picking is subjective
12 and a time-consuming process that is highly dependent on the interpreter's expertise. Conventional automatic
13 picking methods, although useful in horizon tracking, are not good at accurately tracking faults across the seismic
14 volume and tend to produce unrealistic fault-horizon geometries. Seismic attributes are often used to enhance
15 subtle faults that are often missed in the original seismic amplitude volume. Recent advances in deep learning, a
16 subset of artificial intelligence, has allowed seismic interpreters to automatically detect features of interest from
17 the seismic volume using convolution neural networks (CNNs). In this study, we use a CNN called 'fault-net'
18 with a U-shaped architecture to automatically identify and delineate faults from a high-resolution, pre-stack time
19 migrated 3D seismic volume. The CNN model is compared to the chaos and variance volumetric seismic attributes
20 to determine its efficiency in the interpretation of 3D reflection seismic data. The seismic volume used is situated
21 along the continental slope offshore southwestern Africa, in the deep-water Orange Basin. The study area is known
22 to be strongly controlled by gravitational collapse features from the Late Cretaceous, referred to as deep-water
23 fold-and-thrust belts (DWFTBs). A DWFTB system has a highly complex fault framework system reflecting
24 extensional (normal faults), translational (oblique-slip faults) and compressional tectonics (thrust faults) from the
25 proximal to distal offshore environments. Prior to the application of the CNN and edge-enhancing seismic
26 attributes, the data were conditioned through structural smoothing, combining median and mean filters, to improve
27 the signal-to-noise ratio. A combination of synthetic and real seismic data were used to train the CNN fault
28 segmentation model before its application to the Orange Basin 3D seismic dataset. Although both methods imaged
29 the complex structures of the DWFTB system, the CNN-based approach of fault recognition proved to be more
30 effective as it (1) was more time-efficient and less biased, (2) produced a cleaner output, and (3) did not require a
31 high-powered desktop. Compared to the subjective conventional methods of fault recognition and interpretation
32 taking several months, the CNN-based method only took a couple of hours to run on the full dataset. The
33 volumetric seismic attributes had greater difficulty removing the effect of noise and other artifacts from the
34 seismic dataset despite both methods being conditioned in the same manner.

35 **Keywords:** Convolutional neural network (CNN), Seismic attributes, 3D seismics, Fault detection, Orange Basin.

37 **Highlights:**

- 38 1) Convolutional neural networks (CNNs), a deep learning tool, can be trained to specifically extract
39 discontinuities from 3D reflection seismic data.
- 40 2) Seismic attributes such as chaos and variance are sensitive to random and coherent noise in the seismic data.
- 41 3) The CNN-method is more efficient than traditional methods of fault delineation and interpretation as it is
42 more time-efficient, unbiased, produces a higher resolution output and does not require intensive hardware and
43 software.

44

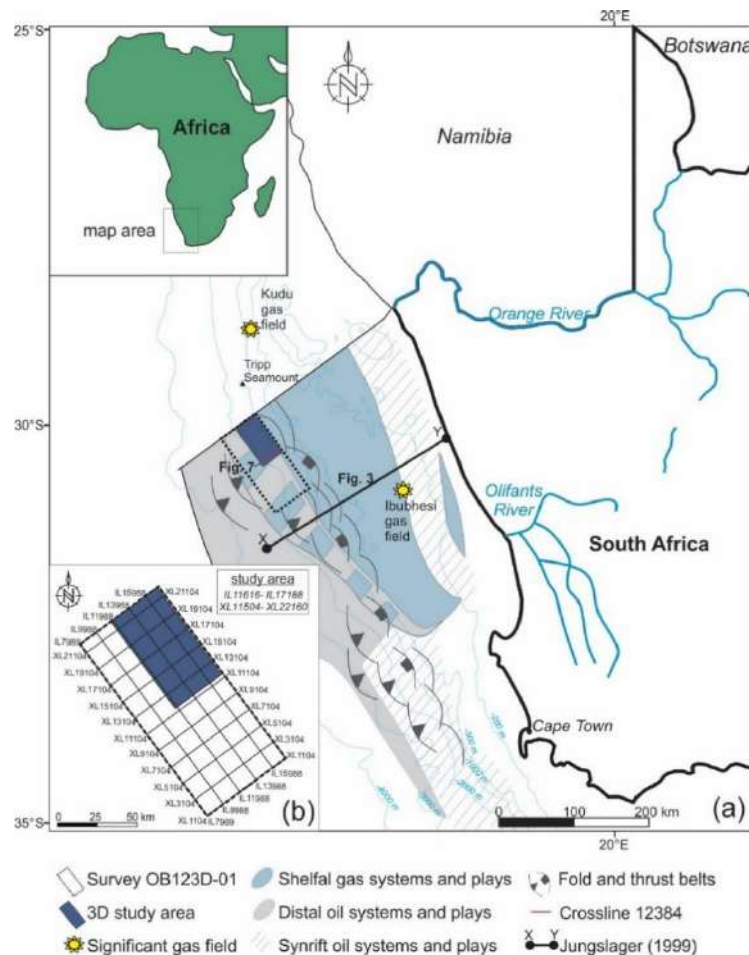
45 **1. Introduction**

46 The interpretation of reflection seismic data reveals important geological information pertaining to the
47 stratigraphy, structure, and reservoir characteristics of a basin. Fault mapping is an essential part of basin analysis
48 in building a structural framework to understand fluid and gas migration pathways. The correct interpretation of
49 a basin's structural framework is essential to the petroleum industry with regards to determining the placement of
50 production and appraisal wells, and estimating flow rates (Richards et al., 2015). Although today's conventional
51 methods of fault mapping using computer-based seismic interpretation software have come a long way from prior
52 paper-based interpretations (Cox et al., 2020), there are still some inherent problems such as subjectivity in manual
53 fault labelling, errors introduced by manual picking, sensitivity of seismic attributes to noise, and long run times
54 required for processing. As such, research into the use of convolutional neural networks (CNNs), a subclass within
55 deep learning (artificial intelligence), has rapidly evolved recently for fault detection (An et al., 2021; Dou et al.,
56 2022; Wei et al., 2022).

57 The importance of fault mapping for hydrocarbon exploration is of great significance in the offshore
58 environment as the sedimentary setting in marine environments is more conducive for the maturation of
59 hydrocarbons. Giant hydrocarbon reserves have yet to be discovered and exploited in the marine environment in
60 many parts of the world particularly in the distal deep-water regions which are largely underexplored. Several
61 regions are actively being explored or are in production for hydrocarbons offshore southern Africa (PASA, 2017).
62 One such area is the Orange Basin, located off the west coast of South Africa and Namibia (Fig. 1). The basin has
63 significant hydrocarbon reserves in the shallow shelf regions of South Africa and Namibia, and in the Namibian
64 deep-water environment (de Vera et al., 2010; van der Spuy and Sayidini, 2022). The deep-water Orange Basin
65 is strongly controlled by gravitational collapse structures, otherwise referred to as deep-water fold-and-thrust belt
66 (DWFTB) systems in Upper Cretaceous sediments (Mahlalela et al., 2021; Maduna et al., 2022). These systems
67 are structurally complex, and hence, very difficult to map accurately even with the use of conventional seismic
68 interpretation methods. Their study is important to the petroleum industry as most hydrocarbons are structurally
69 trapped within their folds (Morley et al., 2011).

70 The structural framework combines the interpretation of horizons and faults and their relationship to each
71 other. Faults are the result of tectonic forces acting on the subsurface, disrupting the continuity of stratigraphic
72 layers and may create or destroy reservoirs. Structural and stratigraphic traps for hydrocarbons are found in
73 favourable sedimentary units with migration pathways created by discontinuities in the form of structural surfaces
74 along a stratigraphic surface, salt diapirs, faults, and anticlines that are faulted (Gay et al., 2003). Fault extraction
75 from seismic data can be done using a variety of conventional methods including manual or expert opinion-based

76 methods using attributes as input (Dou et al., 2022). These approaches are variably successful and there are
 77 benefits and drawbacks associated with each method. Over the last three decades, automated mathematical
 78 analysis of seismic data gave rise to seismic attributes. Seismic attributes are quantitative measures of the seismic
 79 data used to visually enhance features of interest within the data such as faults, thin beds, and bright spots in
 80 hydrocarbon identification (Chopra and Marfurt, 2005, 2007). There are several seismic attributes used to delineate
 81 faults in seismic data including coherence, variance, chaos, semblance, entropy, and gradient magnitude (Marfurt
 82 et al., 1998, 1999; Randen et al., 2001; Hale, 2013).



83
 84 **Fig. 1.** Map of the SW African margin showing (a) the location of the Orange Basin with the hydrocarbon system
 85 play and position of deep-water fold and thrust belt systems along the continental slope. (b) location of the present
 86 study area in blue.

87 While folded strata are easily identifiable and interpretable, faults are more difficult to map using seismic
 88 data regardless of the areal extent the dataset covers, and even more so using 2D reflection seismic data compared
 89 to 3D data. The resolvability of a fault is controlled by the vertical resolution limit and signal-to-noise ratio of the
 90 seismic data. Caution is required in properly distinguishing faults from noise as faults are often marked by the
 91 absence of continuous reflections. Furthermore, other geological features (e.g., buried channels) may appear as
 92 low continuity regions unrelated to faulting (Hale, 2013). For this reason, seismic data are first conditioned to
 93 filter out noise prior to applying seismic attributes to delineate discontinuities. Manual fault picking (or labelling)

94 is a staple method of extracting faults from the seismic dataset from the original seismic amplitude volume using
95 the human visual-cognition systems capable of recognising spatial patterns. Although all computer-aided fault
96 extraction results are still compared to manually extracted faults, manual extraction presents a bias according to
97 the interpreter's pre-conceived expectation. This subjectiveness is one such drawback in fault mapping using
98 seismic interpretation software. Training and judgement will always vary between interpreters and all the
99 processes involved in fault mapping are time consuming. Since current seismic surveys result in large seismic
100 volumes, high-powered desktops with high-capacity RAM and a high-performance graphics card are required to
101 efficiently run every process for seismic interpretation.

102 The concept of 'big data' is becoming more pervasive as progressively larger datasets are rapidly
103 generated and archived by governmental, academic, and private entities (An et al., 2021). The exponential growth
104 of 'big data' has propelled the advancement of machine learning within the discipline of artificial intelligence.
105 Data modeling approaches have emerged as powerful tools, capable of emulating biological cognition with
106 remarkable precision. Deep learning is a class of algorithms within the field of machine learning that are
107 specifically capable of working with variably structured data such as images, videos, and other arbitrary data
108 tensors. Deep learning uses a connected mesh of artificial neural networks to model desirable relationships in data
109 that were used in training. Deep learning algorithms are different from shallow learning for spatial pattern
110 recognition, (e.g., random forest or support vector machine) in that feature generation, engineering and selection
111 are automated. This essentially replaces or augments human-based seismic interpretation. Deep learning is
112 therefore highly useful for features that are difficult to craft manually either because they are too complicated,
113 abstract, or high-dimensional. Faults, which are the displacement of otherwise continuous rock layers, are highly
114 abstract spatial features.

115 Deep learning differs functionally from shallow learning algorithms in that it integrates feature extraction
116 into the algorithm design. Automated feature extraction is highly useful for structurally complex data, of which,
117 seismic data are one type. A subclass of deep learning known as convolutional neural networks (CNNs) have
118 become increasingly popular in delineating and extracting complex fault systems and patterns from seismic data
119 (An et al., 2021; Dou et al., 2022; Wei et al., 2022). CNNs are designed to mimic biological vision (the convolution
120 layer) and perform automated feature generation and selection, followed by modelling. The delineation of
121 foreground objects from the general background is a task called 'image segmentation'. CNNs have been used to
122 perform image segmentation for many tasks, including tissue segmentation in biomedical imaging and more
123 recently, fault segmentation (or extraction) in seismic data. The machine learning task for fault segmentation is to
124 label image pixels as belonging to the object class of 'fault' and 'not fault'. In practice, the presence of faults can
125 be obtained from the seismic volume through labelling each pixel in the dataset provided as 0's (not containing a
126 fault) and 1's (containing a fault) for example, creating a probability map. Probability fault maps may help reduce
127 the risk of drilling in areas with high uncertainties and improve the efficiency of hydrocarbon exploration.

128 Here, the effectiveness of a CNN in segmenting faults is tested against conventional seismic attributes
129 using 3D reflection seismic data (pre-stack time migrated) from the deep-water Orange Basin region offshore SW
130 Africa (Fig. 1). The CNN-based approach uses the architecture presented in Dou et al. (2022). To address training
131 data sparsity, synthetic data generation was employed as a form of data augmentation following processing as an

132 adjustment of the method presented in [Wu et al. \(2016, 2019, 2020\)](#). The CNN was then tested on large seismic
133 datasets to learn complex fault patterns and relationships.

134

135 **2. Regional setting**

136 The Orange and Olifants river systems (together with their older proto-equivalents) are responsible for
137 the depositional sequences found in the Orange Basin, situated offshore SW Africa ([Gerrard and Smith, 1982](#);
138 [Muntingh and Brown, 1993](#); [de Vera et al., 2010](#)). The sequences attain a maximum thickness of 7 000 m in the
139 north and approximately 3 000 m in the south ([Gerrard and Smith, 1982](#); [Brown et al., 1995](#)). The basin originated
140 from the continental break-up of Gondwana. Sedimentary sequences are subdivided into: (1) the syn-rift
141 succession deposited during the Late Jurassic to late Hauterivian, and (2) the post-rift succession consisting of
142 late Hauterivian to current-day deposits ([Fig. 2](#)).

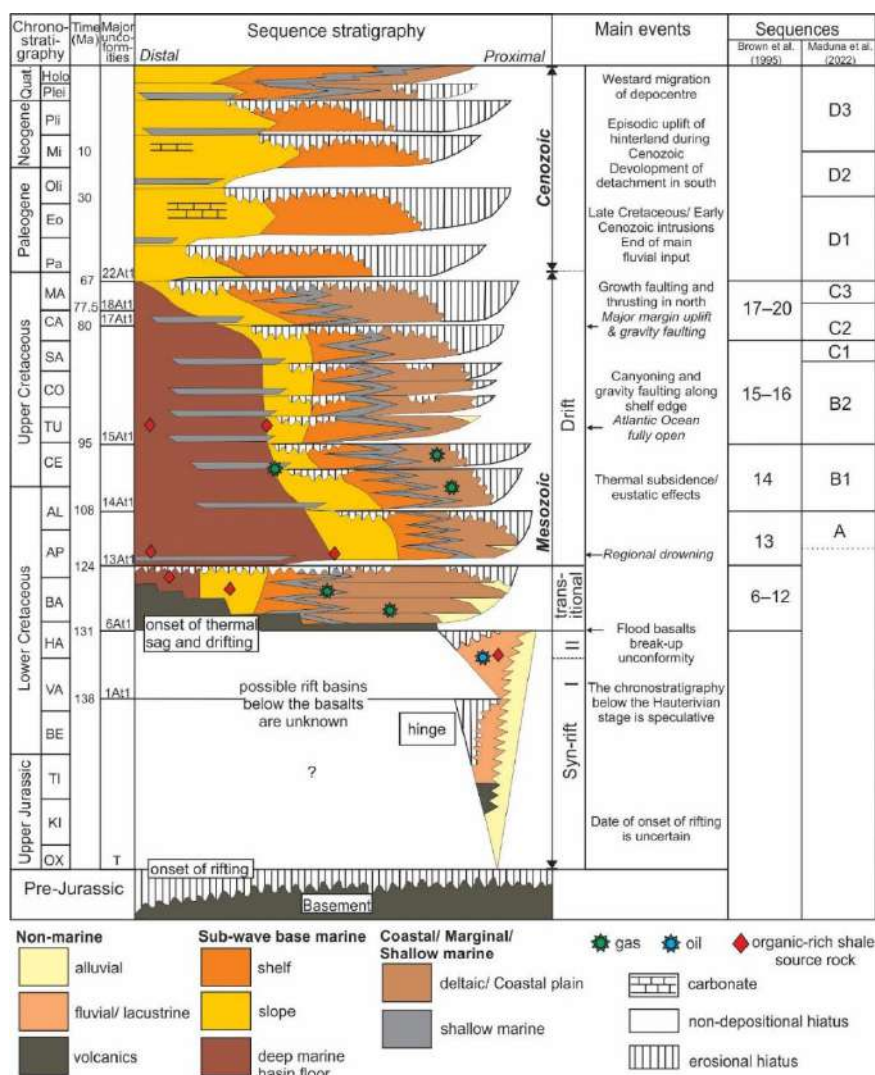
143 **2.1. Syn-rift succession**

144 The continental break-up of Gondwana occurred around 170–150 Ma as west Gondwana (composed of
145 South America and Africa) separated from east Gondwana (composed of New Zealand, Australia, India, and
146 Antarctica, forming margin-parallel orientated grabens and half-grabens ([Fig. 3](#); [Nürnberg and Müller, 1991](#);
147 [Broad et al., 2006](#); [Viola et al., 2012](#)). Siliciclastic lacustrine, fluvial sediments and minor volcanic flows were
148 deposited within these grabens. The megasequence is characterized by seaward dipping reflectors that are low in
149 frequency, high amplitude, discontinuous to continuous seismic reflections reflecting a volcanic rifted margin ([de](#)
150 [Vera et al., 2010](#); [Granado et al., 2009](#)). A regional break-up unconformity separates this succession from the
151 overlying post-rift clastic sediments by ([Light et al., 1993](#); [Granado et al., 2009](#)).

152 **2.2. Post-rift succession**

153 Many authors have described the Orange Basin's post-rift stratigraphy which is divided into several
154 depositional units separated by unconformity surfaces ([Fig. 2](#)) including [Brown et al. \(1995\)](#), [de Vera et al. \(2010\)](#),
155 [Dalton et al. \(2017\)](#), [Baby et al. \(2018\)](#), and [Maduna et al. \(2022\)](#). The post-rift megasequence composes the bulk
156 of sequences in the basin attaining a thickness of approximately 5 500 m ([Fig. 3](#); [McMillan, 2003](#); [Hartwig et al.,](#)
157 [2012](#)). At the base of the post-rift megasequence is a transitional zone of fluvial red-beds that are Barremian to
158 Aptian in age overlain by deltaic and marine sediments ([Gerrard and Smith, 1982](#); [McMillan, 2003](#)). [Maduna et](#)
159 [al. \(2022\)](#) divide the post-rift succession into 3 megasequences according to their age; the Mesozoic's Lower
160 Cretaceous (sequence A) and Upper Cretaceous (sequences B and C), and the Cenozoic (sequence D) ([Fig. 2](#)).
161 Sequences A and B are aggradational deltaic and fluvio-marine sediments overlain by pro-gradational organic-
162 rich marine shales ([Gerrard and Smith, 1982](#); [Brown et al., 1995](#); [McMillan, 2003](#)). An extensive deep-water fold-
163 and-thrust belt (DWFTB) system is detailed in [Maduna et al. \(2022\)](#) in the Upper Cretaceous sediments (sequences
164 B and C) formed by gravitational instability along the slope ([Fig. 3](#)). Gravitational instability formed because of
165 margin uplift and tilting which eroded the inner shelf leading to the accumulation of several pro-gradational
166 sequences ([Muntingh and Brown, 1993](#); [Brown et al., 1995](#)). The Cenozoic (sequence D) is characterized by a
167 thin (50–250 m thick) sequence of marine sediments deposited over the continental shelf, propagating into a
168 seaward-thickening wedge that extends from the continental margin ([McMillan, 2003](#)). Sedimentation and facies

169 distribution along the southwest African margin were greatly affected by climatic and oceanographic processes
 170 since the Miocene changing depositional styles (Diester-Haass et al., 1992; Weigelt and Uenzelmann-Neben,
 171 2004, 2007; Uenzelmann-Neben et al., 2017).



172

173 **Fig. 2.** Sequence and chrono-stratigraphy of the Orange Basin during the evolution of the SW African margin
 174 using the nomenclature proposed by Soeker (now PetroSA) for the stratigraphy (Brown et al., 1995; PASA, 2017).
 175 Abbreviations: Ox= Oxfordian; Ki= Kimmeridgian; Ti= Tithonian; Be= Berriasian; Va= Valanginian; Ha=
 176 Hauterivian; Ba= Barremian; Ap= Aptian; Al= Albian; Ce= Cenomanian; T= Turonian; Co= Coniacian; Sa=
 177 Santonian; Ca= Campanian; Ma= Maastrichtian; Pa= Palaeocene; Eo= Eocene; Oli= Oligocene; Mi= Miocene;
 178 and Pli= Pliocene.

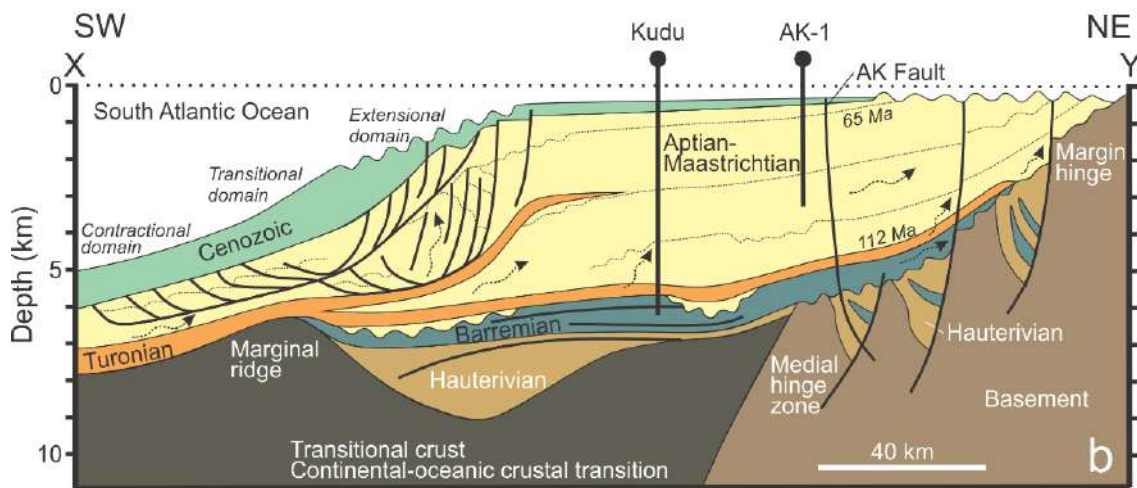
179

180 **2.3. Upper Cretaceous DWFTB systems of the Orange Basin**

181 DWFTB systems are formed by the gravitational collapse and subsequent contraction of sediment on a
 182 dipping detachment surface in deep-water environments (Rowan et al., 2004; Nemčok et al., 2005). Deep-water
 183 drilling has improved over the last two decades promoting interest into the study of DWFTBs because their distal

184 folds (anticlines) are often associated with hydrocarbons (e.g., [Corredor et al., 2005](#); [Benesh et al., 2014](#)). Well-
 185 preserved Upper Cretaceous DWFTB systems are found along the SW African coastline within the post-rift
 186 succession of the Orange Basin ([de Vera et al., 2010](#); [Scarselli et al., 2016](#); [Maduna et al., 2022, 2023](#)). They are
 187 linked tripartite systems comprising a down-dip compressional domain, middle transitional/translational domain,
 188 and an extensional domain up-dip towards the coastline ([Figs. 1c and 3](#); [Morley et al., 2011](#)). In the Orange Basin
 189 the extensional domain is characterized by steep, seaward dipping, listric growth faults proximal to the coastline
 190 ([de Vera et al., 2010](#)). The compressional domain is characterized by a ~3 km thick section of shallow, landward-
 191 dipping fold-and-thrust belts that are ~60 km wide with 1–5 km spacings between imbricate thrusts ([de Vera et](#)
 192 [al., 2010](#); [Morley et al., 2011](#)). Joining the two extensional and compressional tectonic regimes is a structurally
 193 complex transitional/translational domain with overprinted normal, thrust and oblique-slip faults ([Maduna et al.,](#)
 194 [2022](#)). The downslope translation of sediment was accommodated by oblique-slip faults that are =< 20 km in
 195 length segmenting thrust faults along-strike.

196



197

198 **Fig. 3.** Simplified stratigraphic cross-section of the margin. Image modified after [Jungslager \(1999\)](#). Refer to [Fig.](#)
 199 [1](#) for orientation of the cross-section.

200

201 According to [Morley et al. \(2011\)](#), since the Orange Basin's DWFTB systems are driven by near-field
 202 stresses and contain multiple, overpressured shale detachment surfaces, they classified as Type 1a DWFTB
 203 systems. Shale detachment surfaces of the Orange Basin include the Aptian-aged and Turonian-aged maximum
 204 flooding surfaces and source rock intervals, and the Cenomanian-aged maximum flooding surface ([Brown et al.,](#)
 205 [1995](#); [Jungslager 1999](#); [Aldrich et al., 2003](#); [van der Spuy et al., 2003](#); [Dalton et al., 2015](#)). Sediment from the
 206 upper portions of the Upper Cretaceous DWFTB systems in the extensional domain are reworked to form other
 207 mass flow deposits such as slides and slumps ([Kuhlmann et al., 2010](#); [Dalton et al., 2017](#)). Slides and slumps are
 208 also present in the Cenozoic succession overlying these mature DWFTB systems as faults have been rejuvenated
 209 into younger sequences with later margin instability ([Maduna et al., 2022](#)). All this reflects the strong influence
 210 that the underlying structure of the Upper Cretaceous DWFTB systems has (and possibly will always have) on
 211 depositional processes of the basin.

212

213 3. Data and methods

214 3.1. Seismic acquisition and processing

215 Between 2012 and 2014 a high-resolution 3D reflection seismic survey was conducted in the deep-water
 216 regions of the Orange Basin, situated offshore SW Africa (Fig. 1; Kramer and Heck, 2014). This study uses a 1
 217 800 km² portion of the full ~8 200 km² dataset bordering Namibian waters (Fig. 1). Full acquisition and processing
 218 parameters are summarized in Tables 1 and 2. Further details about the seismic design, acquisition, and processing
 219 of the data are detailed in Maduna et al. (2022; 2023).

220 The 3D seismic survey was conducted by the Dolphin Geophysical Polar Duchess (Kramer and Heck,
 221 2014) with the principal focus being to image the architectural elements of the deep-water Orange Basin to
 222 understand its evolution and determine its viability as an economic hydrocarbon system. The data were processed
 223 to produce a high-resolution, Kirchhoff pre-stack time migrated volume for detail structural interpretation. The
 224 machine learning and seismic attribute algorithms applied relied on the quality of the migrated seismic volume
 225 for precise and accurate structural interpretation. The study area’s seismic volume is ~6 km in depth (excluding
 226 upper and lower regions with no data), with an east–west extent of ~30 km and north–south extent of ~60 km.

227

228 **Table 1**

229 Seismic survey acquisition parameters (Kramer and Heck, 2014; Maduna et al., 2022).

Source	
<i>Source type</i>	Dual source
<i>Number of source arrays</i>	2
<i>Number of sub-arrays</i>	3
<i>Shot point interval</i>	25 m (flip/flop)
<i>Array separation</i>	100 m
<i>Array length</i>	15 m
<i>Source volume</i>	4 100 cu in
<i>Number of airguns / arrays</i>	30
<i>Operating pressure</i>	2 000 psi
<i>Source depth</i>	8 m
<i>Nominal common midpoint fold</i>	80
Recording	
<i>Recording format</i>	SEG-D
<i>Record length</i>	7 168 ms
<i>Recording filter delay</i>	None

<i>Sample rate</i>	2 ms
<i>Low cut filter hydrophone, slope</i>	4.4 Hz, 12 dB / octave
<i>Low cut filter geophone, slope</i>	Not applicable
<i>High cut filter both, slope</i>	214 Hz, 341 dB / octave
Sercel SSAS Sentinel, Sercel Seal-428	
<i>Number of streamers</i>	8
<i>Group interval</i>	12.5 m
<i>Group length</i>	12.5 m
<i>Number of hydrophones / groups</i>	1
<i>Number of geophones / groups</i>	1
<i>Streamer length</i>	7 950 m
<i>Streamer separation</i>	200 m
<i>Number of groups / streamers</i>	636
<i>Streamer depth</i>	10 – 15 m linear slant
<i>Nearest offset</i>	222 m

230

231 The pre-stack time migrated volume imaged high amplitude horizons with a frequency content of ~20
232 Hz. Considering the average P-wave seismic velocity of 2 400 m/s observed during processing, the dominant
233 frequency of the seismic data is ~120 m (e.g., [Kuhlmann et al., 2010](#); [Scarselli et al., 2016](#)). Based on the ½ and
234 ¼ wavelength criteria ([Yilmaz, 2001](#)), the vertical seismic resolution is calculated to either be 60 m or 30 m. The
235 horizontal resolution may be as small as ½ the wavelength in the marine environment for migrated data ([Herron,](#)
236 [2011](#)), and is therefore given as 60 m in this study. The geometry of the survey, proper bin size to avoid spatial
237 aliasing, fold of coverage, and source and receiver set-up also have an effect on vertical and horizontal resolution.

238 **Table 2**

239 Processing workflow (Kramer and Heck, 2014).

Dolphin Geophysical Polar Duchess team	
1	Conversion from SEG-D and navigation merge
2	Output to SEG-Y
Global Processing Team	
3	Conversion from SEG-Y to Shell's proprietary software (SIPMAP) format
4	Spherical spreading correction
5	Despike
6	Swell noise attenuation
7	Resample to 4 ms
8	Denoise
9	Linear noise attenuation
10	Deghosting
11	Seismic interference attenuation
12	Zero phasing
13	2D surface rendered multiple elimination prediction
14	3D surface-related multiple elimination prediction
15	LSQ matched subtraction
16	Multiplicity scaling for Kirchhoff migration
17	Phase deabsorption
18	Residual moveout analysis
19	RMO velocity model inversion and anisotropy scanning
20	Pre-migration signal enhancement
21	Kirchhoff pre-stack migration
22	Residual radon demultiplex
23	Amplitude deabsorption
24	Residual moveout correction
25	(Angle) stack
26	Time variant scaling (additional output volumes)
27	Archiving

240

241 **3.2. Data preparation for fault interpretation**

242 The quality of the 3D fault interpretation is dependent on the accuracy of the processing parameters (e.g.,
 243 migration techniques, velocity fields, and filtering operators) used during processing. Furthermore, the resolution
 244 of fault detection is primarily a function of the signal-to-noise ratio and the seismic dominant frequency of the

245 data. Since Earth is a low pass filter, high frequencies are easily attenuated causing the wavelength of the seismic
 246 signal to increase as a function of depth, resulting in poor detection of small faults at great depth. Although the
 247 processing steps undertaken for the deep-water Orange Basin 3D seismic data provided high-quality data, the
 248 conventional interpretation approaches (e.g., [Mahlalela et al., 2021](#)) did not allow for exploitation of the data to
 249 its full potential. For example, sub-seismic faults could not be fully identified on seismic sections. However,
 250 sophisticated seismic attribute analysis, such as chaos and variance, can be used to enhance the detection of these
 251 features in the data.

252 Seismic attributes play an important role in improving the quality and efficiency of fault interpretation
 253 in 3D structural interpretation ([Chopra and Marfurt, 2005, 2006](#); [Chopra and Marfurt, 2007](#); [Manzi et al., 2012](#);
 254 [Barnes, 2016](#)). However, the limitation of any seismic attribute is its sensitivity to coherent and incoherent noise.
 255 To enhance structural interpretation, this study introduces a novel approach to fault detection and interpretation,
 256 and it is divided into three steps including: (1) post-migrated data conditioning using smoothing operators, (2) the
 257 application of seismic attributes to conditioned data, and (3) the application of a CNN for fault extraction to the
 258 conditioned data. The workflow from data conditioning to conventional seismic attribute analysis and the deep-
 259 learning CNN is illustrated in [Fig. 4](#).

260 The seismic volume was initially conditioned using mean and median structural smoothing filters. This
 261 improved the quality of the data and enhanced the continuity of reflections throughout the seismic volume.
 262 Structural smoothing is guided by the computation of dip and azimuth to determine the local structure ([Randen et
 263 al., 2001](#)). The option of dip guided smoothing was selected whereby the local structure is smoothed parallel to
 264 its orientation using a Gaussian filter. To visually enhance the edges within the data the dip guided smoothing
 265 filter was chosen as it uses chaos as the edge enhancer. Gaussian filtering is then applied to the filter with the least
 266 chaos. The filter sizes (controlling the number of horizontal traces and vertical samples needed in the estimation
 267 of structural smoothing) were all set at 1.5 for orientation windows X, Y and Z corresponding to the crossline,
 268 inline and vertical sections, respectively. The structurally smoothed volume was used as input both for the
 269 computation of the variance and chaos attributes, and in the CNN for fault extraction.

270 The fault-net CNN model was trained over a 4 month period prior to being tested on the seismic volume of interest.
 271 In preparation for segmentation in machine learning, the original conditioned seismic volume was processed by
 272 discretizing it into smaller cubes of dimensions (e.g., 320 x 320 x 320) to enable faster processing. The discretised
 273 volume was checked for gaps, signal-to-noise ratios, and areas with high noise were interpolated to clean the
 274 volume. The geometry of the file was set according to the file header shown in [Table 3](#). The original data amplitude
 275 were a minimum of -33025.01, maximum of 32767.00, and delta of 65792.01 all normalised to ensure consistency
 276 with the convolutions.

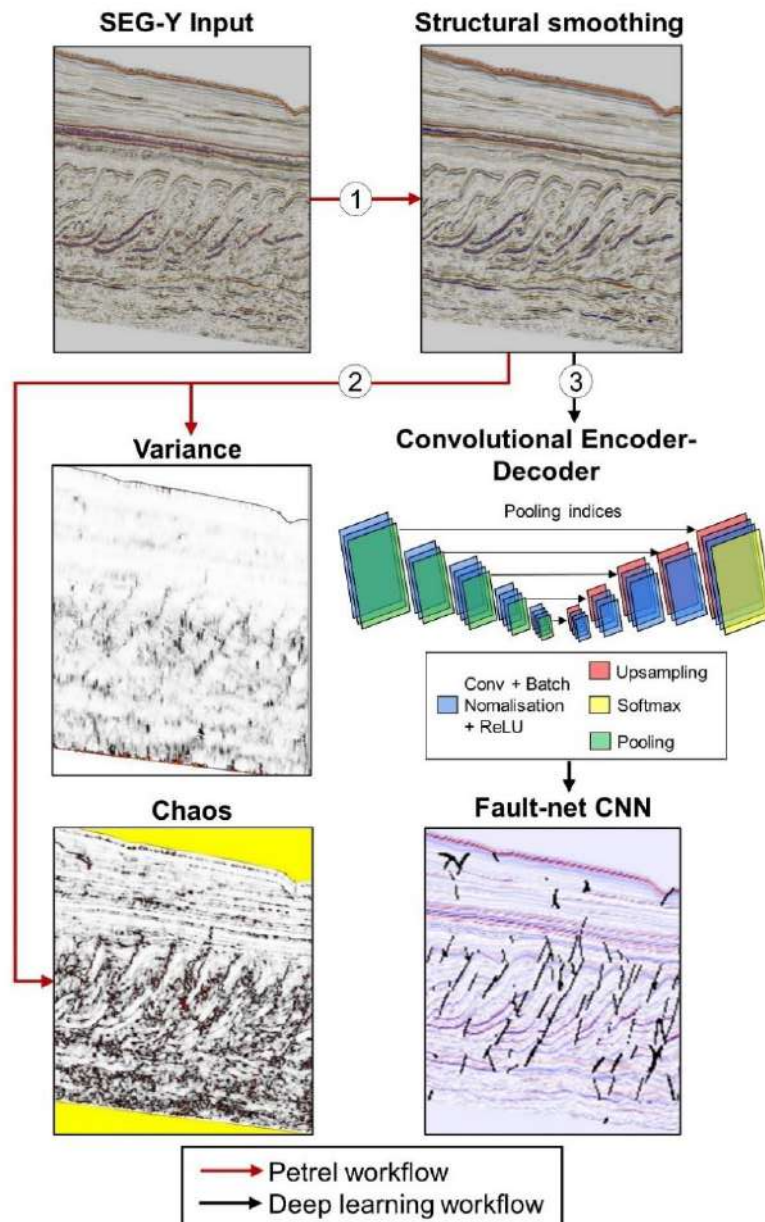
277 **Table 3**

278 Project file header used in geometry setup.

Project File Header		
Geometry	<i>First inline</i>	<i>Last inline</i>
	11616	17188

	<i>First crossline</i>	<i>Last crossline</i>	
	11504	22160	
Time	<i>Minimum</i>	<i>Maximum</i>	<i>Delta</i>
	-5726 ms	2 ms	5728
Coordinate Reference System of WGS_1984_UTM_Zone_33S, EPSG =32733			
	<i>Minimum</i>	<i>Maximum</i>	<i>Delta</i>
Latitude	30.42°27.6095"S	30.02°5.1435"S	0.40°22.4660"
Longitude	14.08°8.6564"E	14.50°37.7163"E	0.42°29.0599"
Trace	-5724	0	5724

279



280

281 **Fig. 4.** Workflow of fault detection from the 3D seismic volume using Petrel and a CNN in deep learning. The
 282 seismic volume was input into Petrel in SEG-Y format. Both (2) the edge detection attributes used in Petrel,
 283 together with (3) the CNN deep learning process were run on (1) the pre-conditioned, structurally smoothed data.

284

285 3.3. Conventional method of manually extracting faults

286 Initially, faults were manually picked along inlines, crosslines, time/depth slices, and arbitrary/random
 287 lines in both 2D and 3D. Variance and chaos are the two most popular volumetric seismic attributes applied to the
 288 seismic volume to delineate discontinuities. Depending on the interpreter’s desired output the variance and chaos
 289 algorithms may be run multiple times upon each other (e.g., [Silva et al., 2005](#); [Mahlalela et al., 2021](#); [Qi et al.,](#)
 290 [2019](#); [Maduna et al., 2022](#)). Since the application of seismic attributes are a time- and RAM-consuming process,
 291 all the algorithms used were first tested on a smaller, cropped portion of the dataset (including the structurally
 292 smoothed volume as mentioned earlier). The variance and chaos volumes were of great use in fault mapping to
 293 validate the presence and continuity of faults. Variance measures the local deviation of the seismic signal in the
 294 form of a coherency analysis and, regardless of high or low amplitude regions, will give the same response for the
 295 same seismic signature ([Silva et al., 2005](#)). Chaos measures the lack of organization from the seismic signal
 296 through statistical analysis of the dip and azimuth orientations ([Silva et al., 2005](#)). The only parameters required
 297 for chaos was the size of orientation windows X, Y and Z in filtering; all of which were set at 1.5. The parameters
 298 used for variance are in [Table 4](#).

299

300 **Table 4** Parameters used for variance in the study area.

<i>Variance parameters</i>	
<i>Inline range (filter length)</i>	3
<i>Crossline range (filter length)</i>	3
<i>Vertical smoothing (in samples)</i>	25
<i>Dip correction</i>	On
<i>Inline scale</i>	1.5
<i>Crossline range</i>	1.5
<i>Vertical scale</i>	1.5
<i>Plane confidence threshold</i>	0.6
<i>Dip guided smoothing</i>	Off

301

302 Following the application of volumetric seismic attributes, faults were picked in the seismic volume to
 303 create a fault framework; the first step in structural modelling. Faults are manually interpreted by first drawing a
 304 polyline on a seismic slice (inline/ crossline/ random/ arbitrary line) representing a fault surface in 2D. Polylines
 305 are drawn in 2D at every seismic slice chosen to follow the full trace of the fault in 3D. Fault polylines are adjusted
 306 manually to ensure that they follow the trace of the fault trace as accurately as possible. The process of picking
 307 and modelling faults took a period of over a year for the 1 800 km² study area as fault relationships needed defining
 308 and re-picking or re-evaluating to fit into the structural model overcoming certain software limitations imposed.

309 3.4. Deep learning-based method of fault extraction

310 The method used in this study is effectively an implementation of the method used in [Dou et al. \(2022\)](#)
311 which is an improvement on previous CNN-based fault segmentation methods to further suppress false negative
312 labels under the constraint of sparse 2D labels. The improvement is made by recognizing the effect of regional
313 versus distribution-based loss functions. Regional loss functions compute differences in the overlap of pixels
314 between a prediction and a ground truth. [Dou et al. \(2022\)](#) discovered that regional loss functions are more
315 effective at suppressing false negative labels and proposed the Mask Dice (MD) loss. The network architecture
316 was also modified, such that edge information is less degraded during propagation, because no coding process
317 occurs in the input of the network. A specific feature fusion block was used (Multi-Scale Compression Fusion) to
318 decouple the convolution process into feature selection and channel fusion separately. This prevents image details
319 from being weakened during fusion. The result is a new architecture named ‘fault-net’ by [Dou et al. \(2022\)](#). Due
320 to the preservation of edge features in fault-net, the complexity of the overall network could be substantially
321 reduced, resulting in a more specific configuration of the network that is suitable for fault segmentat. This also
322 improved performance characteristics of fault-net relative to earlier CNN-based approaches.

323 A combination of synthetic and real seismic data were used to train the fault-net CNN. The synthetic
324 data was generated using the principles in [Wu et al. \(2019\)](#) which helped overcome the sparsity of data training
325 in fault segmentation. In addition to the synthetic data, some labelled real seismic data acquired over offshore
326 Netherlands (F3), marine New Zealand (Kerry 3D), and Australia (Adele 3D), respectively ([Supplementary Data](#)).
327 Consistent with [Dou et al. \(2022\)](#), anomaly annotation was utilized to label faults in seismic images based on their
328 geometrical shape and size. We evaluated the performance of the proposed method by conducting experiments
329 based on the approach of [Dou et al. \(2022\)](#). The performance of our proposed method was compared with other
330 state-of-the-art methods, such as the Dice loss function, with and without anomaly annotation. A subset of faults
331 was manually selected to ground truth and validate the training and testing method in segmenting the network.
332 We used various metrics, including precision, recall, F1 score and segmentation error to evaluate the performance
333 of the proposed method. The workflow applied in this study was executed in the following order:

- 334 • **Data augmentation:** One of the critical factors that contributes to the success of U-Net in geological
335 fault segmentation is the quality of the training data. Labelled training data is often limited in geoscience
336 research and obtaining accurate ground truth labels for geological structures (e.g., faults) can be
337 challenging. To improve the generalisation and robustness of the segmentation network, synthetic data
338 augmentation is applied to increase the diversity of the training dataset. The data augmentation
339 techniques include rotation, scaling, flipping, and cropping ([Wu et al., 2019](#)).
- 340 • **Model training:** The proposed network was trained over four months on the synthetic seismic dataset
341 provided in [Wu et al. \(2019\)](#). It contains 100 training and 10 validation sets, 3D seismic data with
342 corresponding labels, respectively. The size of each sample is $128 \times 128 \times 128$ voxels. To mitigate the
343 data distribution differences or domain gap between the various training dataset and deployment seismic
344 volume which causes severe degradation in model generalisation, we have standardised the amplitudes
345 using z-score normalization. See [Supplementary Figure 1](#) for an example of training output using
346 Geoscience Australia’s Adele 3D seismic data.

- 347 • **Model evaluation:** The trained U-Net model is evaluated using the test dataset (Fig.5). The evaluation

348 metrics include precision, recall, F1 score, and segmentation error. The segmentation error is measured

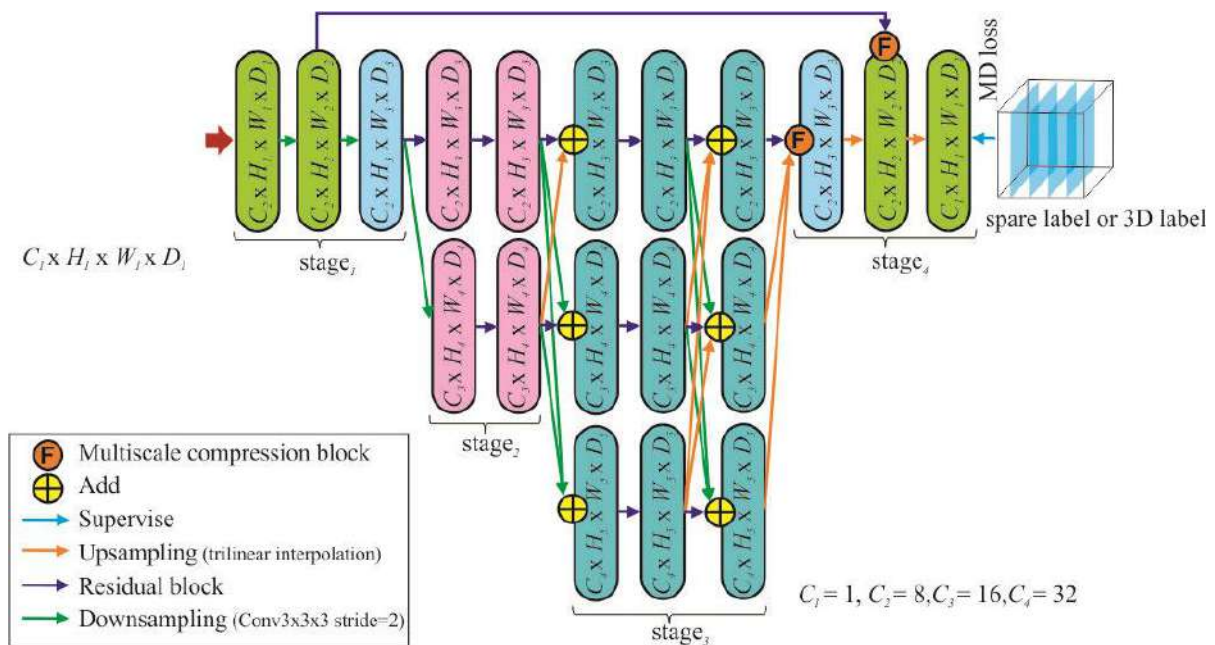
349 by comparing the predicted fault maps with the ground truth fault maps. The final model took 3 hours to

350 run on the study's seismic volume.
- 351 • **Post-processing:** Finally, post-processing techniques are applied to the predicted fault maps to remove

352 false positives and false negatives. These techniques include morphological operations, such as erosion

353 and dilation, and connected component analysis. Post-processing the seismic volume took 2 hours.

354



356 **Fig. 5.** Illustration of the U-Net fault-net architecture used in this study (modified after Dou et al., 2022).

357 4. Results and interpretations

358 The 1 800 km² seismic study images the post-rift Upper Cretaceous to Cenozoic Tertiary and Quaternary

359 sedimentary sequences of the deep-water Orange Basin (Figs. 6 and 7a). The Upper Cretaceous sedimentary

360 succession is dominated by the structurally complex translational and compressional domains of a DWFTB

361 system. To understand the regional structures of the study area, only the most extensive and prominent faults were

362 mapped out, belonging to a particular network or system arising from the DWFTB system. The reader is referred

363 to Maduna et al. (2022) for all the results and discussion of the structural framework (faults and horizons) obtained

364 using conventional methods as this study uses the same dataset. Here, we provide an overview of the results from

365 the fault framework, then lead to the conventional edge-enhancing methods used to aid in manually interpreting

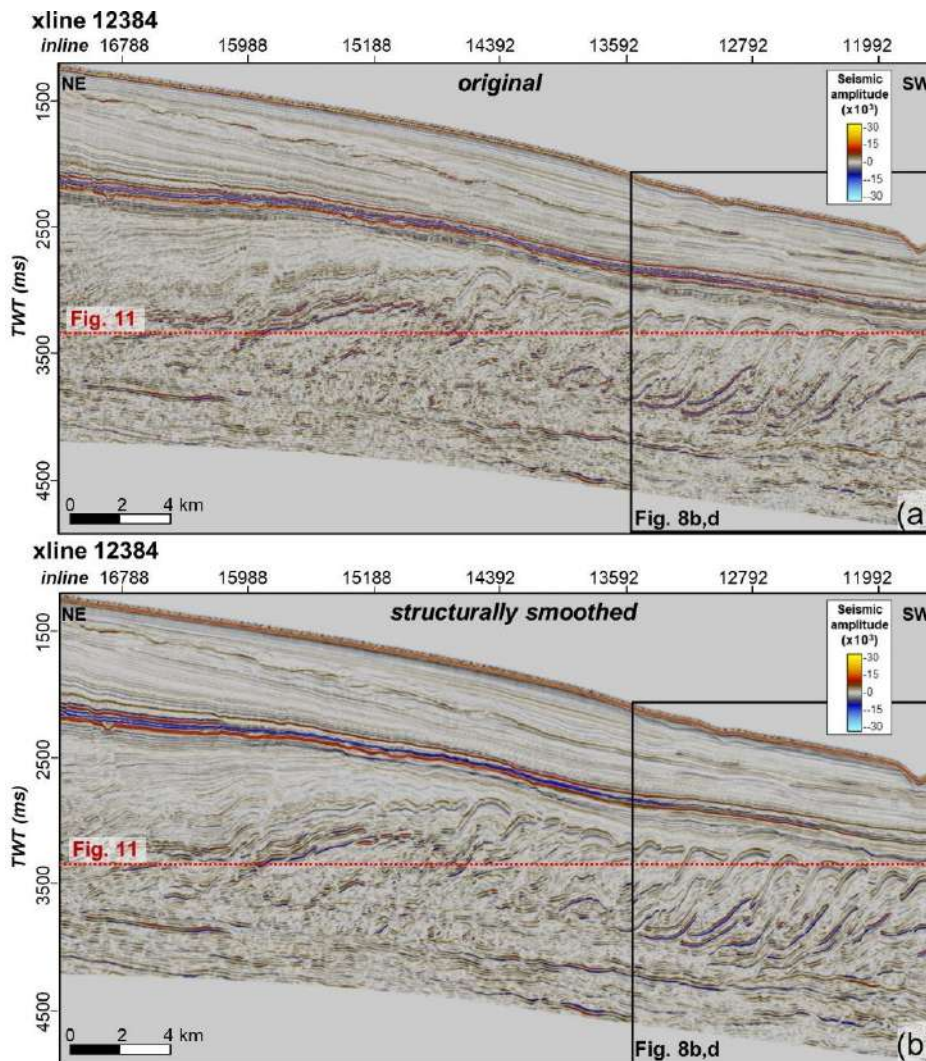
366 faults. Lastly, the results of machine learning are displayed as an emerging method for fault extraction.

367 4.1. Fault framework overview

368 The Orange Basin is comprises several sedimentary units bound by nine high amplitude stratigraphic

369 surfaces dominant throughout the study area (Fig. 6). These are the: (1) Albian, (2) Turonian, (3) Santonian, (4)

370 early Campanian, (5) late Campanian, and (6) Maastrichtian surfaces in the Upper Cretaceous; and the (7)
 371 Oligocene, and (8) Miocene surfaces in the Cenozoic, with the (9) present-day seafloor, altogether marking
 372 important geological events through time (Fig. 7a). Faults were distinguished in the seismic data from the
 373 observation of discontinuous surfaces showing upthrown and downthrown sections. These broken surfaces are
 374 mostly found in the Upper Cretaceous displaced by faults of the DWFTB system (Fig. 7a). Only large, first order
 375 faults greater than 2 km in lateral length were selected for the fault framework as the seismic volume is too heavily
 376 faulted to pick all and provide a regional understanding of the basin's tectonics. Approximately 500 faults were
 377 manually picked and selected for the fault framework (Figs. 7b and c).



378

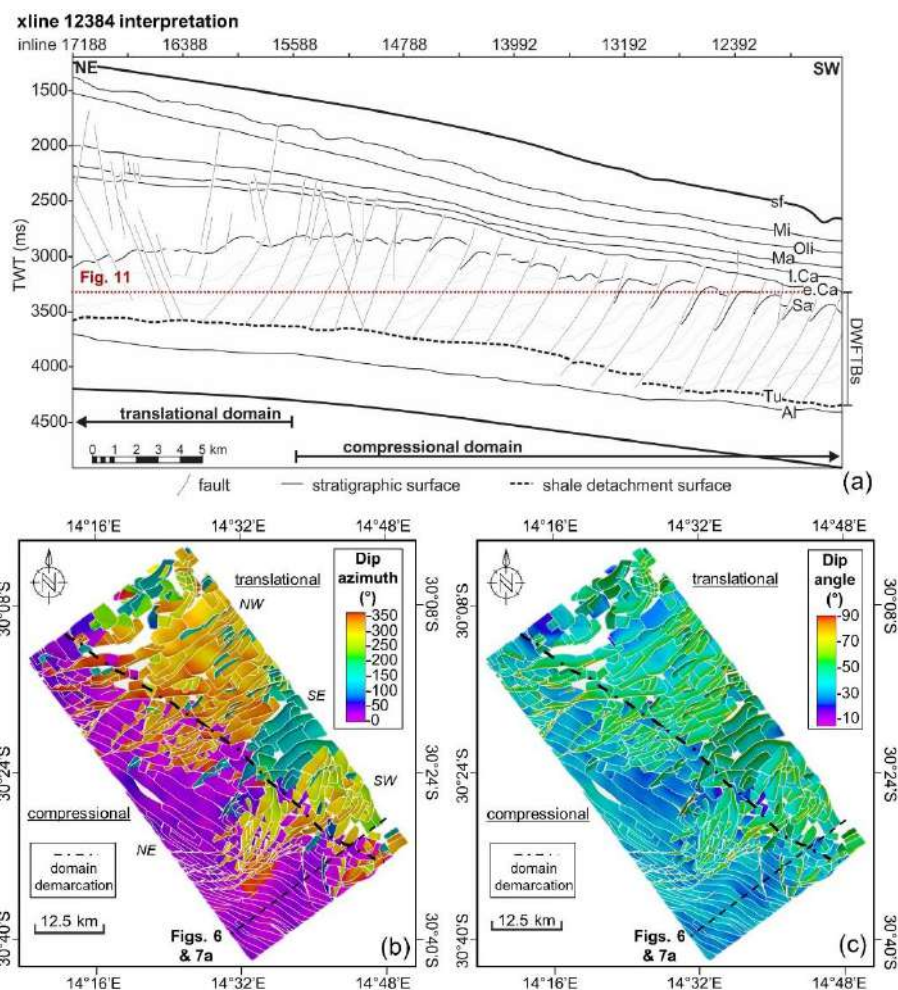
379 **Fig. 6.** Original seismic volume in (a) compared to the structurally smoothed volume in (b). Vertical exaggeration
 380 = 5.

381

382 Most faults detach against the Turonian-aged shales, the surface upon which 3 km of the Upper
 383 Cretaceous sedimentary succession slid downslope in gravitational collapse (Fig. 7a). Faults of the compressional
 384 domain mostly terminate at the early Campanian surface, while those in the up-dip translational domain terminate

385 within stratigraphically younger sequences within the Oligocene or Miocene. The type, geometry, and
 386 displacement characteristics of faults in the compressional domain and the translational domain differ greatly (Fig.
 387 7). The compressional domain is characterized by folded strata separated by ~2 km spaced, seaward-dipping
 388 imbricate thrust faults with 250 m displacements (Fig. 7a). Thrust faults are low in angle dipping between 22–45°
 389 NE with a NW–SE strike (Fig. 7b and c). The translational domain has a complex framework of faults from up-
 390 dip normal faults (extensional) to down-dip thrust faults (compressional), crosscut by normal-orientated oblique-
 391 slip faults. Normal faults have higher dip angles ranging between 50–70°, dipping to the NW, SE and SW, with a
 392 NE–SW strike and smaller, ~80 m, displacements (Fig. 7b and c). The translational domain and the compressional
 393 domain are linked by extensive oblique-slip faults that reach 20 km in length. Oblique-slip faults segment thrust
 394 sheets along strike as they are orientated perpendicular to the thrusts (striking NE-SW). Dip-slip offsets are ~80
 395 m on 135veragee while the magnitude of strike-slip displacement is variable with each segmented thrust sheet.
 396 Oblique-slip faults dip between 40–70° mostly to the NW and show a sinistral slip motion, while those dipping
 397 SE in the south show a dextral slip motion (Fig. 7b and c).

398



399

400 **Fig. 7.** Interpretation of the Orange Basin study area. (a) shows the interpretation of the crossline in Figure 5
 401 where stratigraphic sequences and surfaces are displaced by faults from the Upper Cretaceous DWFTB system.

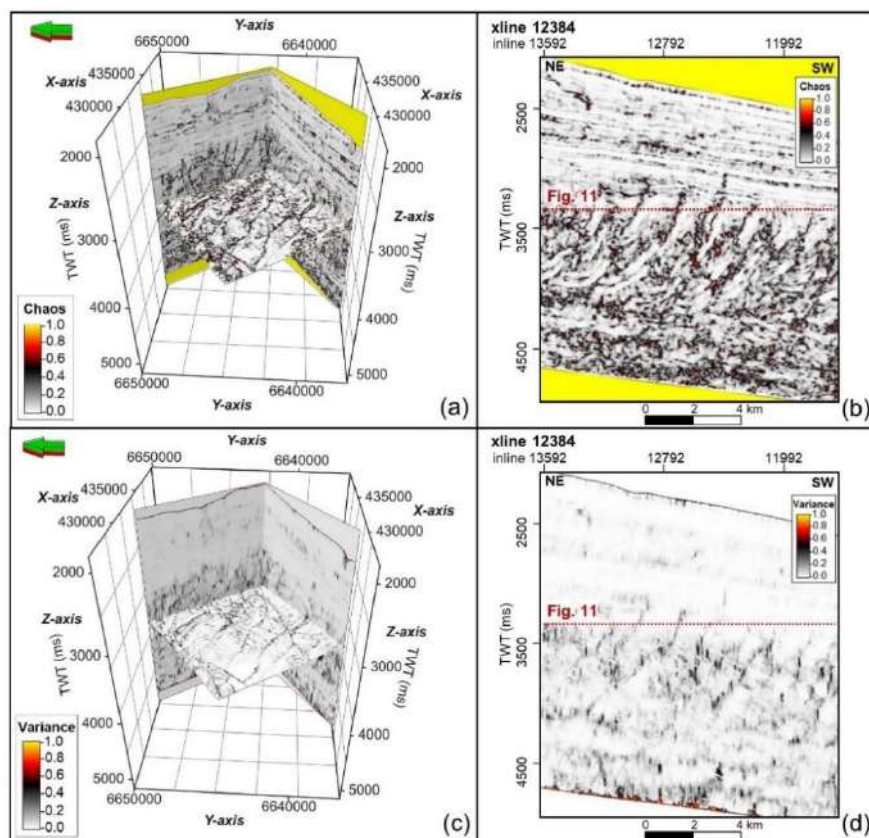
402 (b) and (c) show the plan view of the fault framework in dip azimuth and dip angle, respectively, as modified after
403 [Maduna et al. \(2022\)](#).

404

405 4.2. Conventional edge-enhancing methods for fault extraction

406 The fault framework in [Maduna et al. \(2022\)](#) was based on conventional methods of delineating and
407 interpreting faults. Chaos and variance were the most favourable edge-enhancing attributes to delineate faults in
408 the seismic volume ([Figs. 8, 10a and 11a](#)). Changes in seismic amplitude due to discontinuities result in high
409 chaos and variance values, while areas without discontinuities have low values ([Figs. 8, 10a and 11a](#)). Chaos
410 suffers from enhancing features too much, thus appearing ‘chaotic’, as noisy sections and some high amplitude
411 dipping surfaces are also enhanced ([Fig. 8a and b](#)). This is well seen in [Figures 8b and 10a](#) where some dipping
412 strata have been enhanced together with the more vertical faults of the DWFTB system making it difficult to
413 properly distinguish surfaces from faults. The variance volumes yield better results with regards to muting
414 stratigraphic surfaces, as shown in [Figure 8c and d](#). The faults in the variance vertical sections are however very
415 low in resolution and not as clear as chaos; faults appear over-muted ([Fig. 8c and d](#)). Faults are clearer and more
416 continuous in the variance time slice ([Fig. 11a](#)). For chaos, large- and small-scale discontinuities are viewed better
417 than variance in the vertical sections ([Figs. 8b, 10a and 11a](#)). The chaos horizontal time slice is poor in resolving
418 discontinuities particularly where faults cut through strong stratigraphic surfaces and at depth where the signal-
419 to-noise ratios were low ([Figs. 8a, b and 10a](#)).

420



421

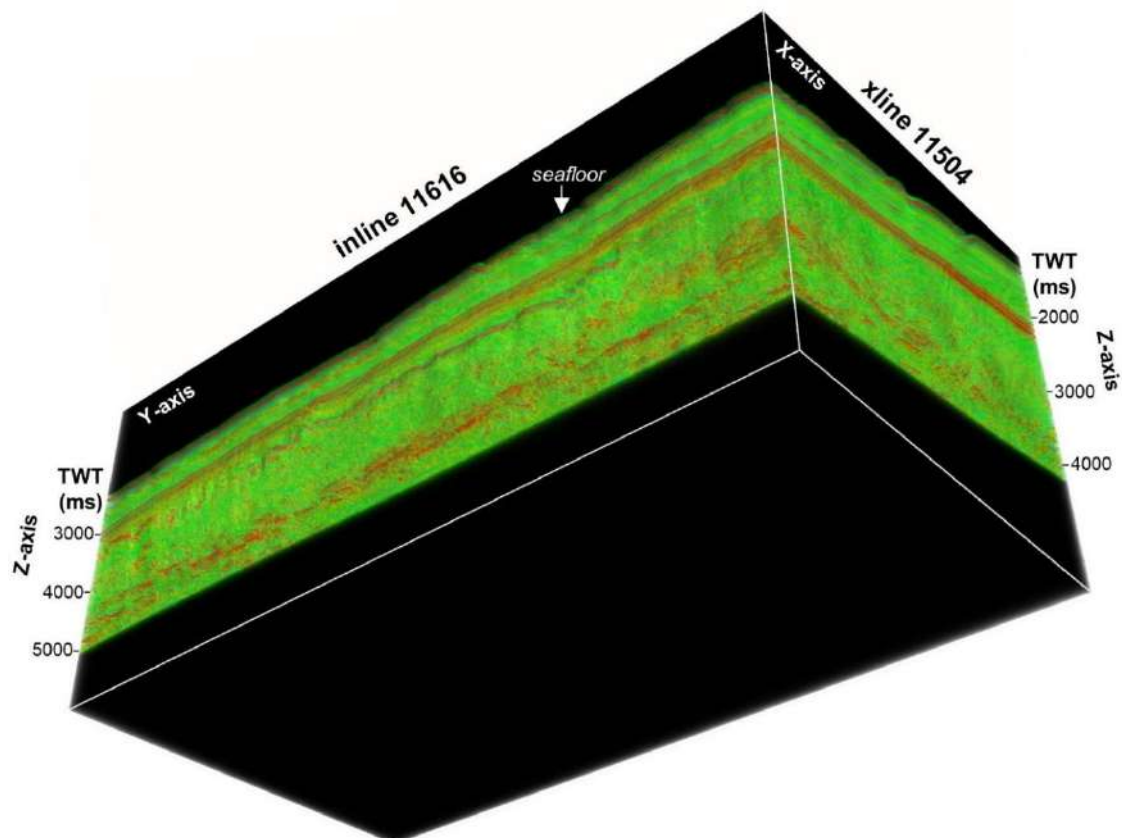
422 **Fig. 8.** Edge detection methods. (a) chaos in 3D, (b) chaos on crossline 12384, (c) variance in 3D, (d) variance on
423 crossline 12384. Vertical exaggeration = 5.

424

425 4.3. Deep learning-based method of fault extraction

426 Preparation of the seismic volume for fault segmentation using the fault-net architecture in deep learning
427 is shown in [Figure 9](#) with the black areas corresponding to no data, green corresponding to the sedimentary
428 successions, and red showing regions and surfaces that are high in amplitude. The volume was segmented to
429 identify and locate faults in the region. The predicted faults are shown in [Figures 10b, 11b](#) and [12](#), overlain upon
430 the original seismic volume. Some faults are parallel to the inline and crossline directions and may have otherwise
431 been missed from a single 2D vertical slice. To avoid this manual fault interpretation in 3D required additional
432 vertical sections called ‘arbitrary polylines’ to verify the consistency of an interpretation. Arbitrary polylines were
433 aligned normal to the strike orientation of faults to make them clearly identifiable in the seismic section for
434 picking. In comparison, the CNN still correctly detected and segmented faults from the seismic volume, regardless
435 of their orientation ([Figs. 10b, 11b](#) and [12](#)). Fault-net architecture predictions are consistent with the
436 discontinuities of manually interpreted faults using conventional methods in [Figure 7](#).

437

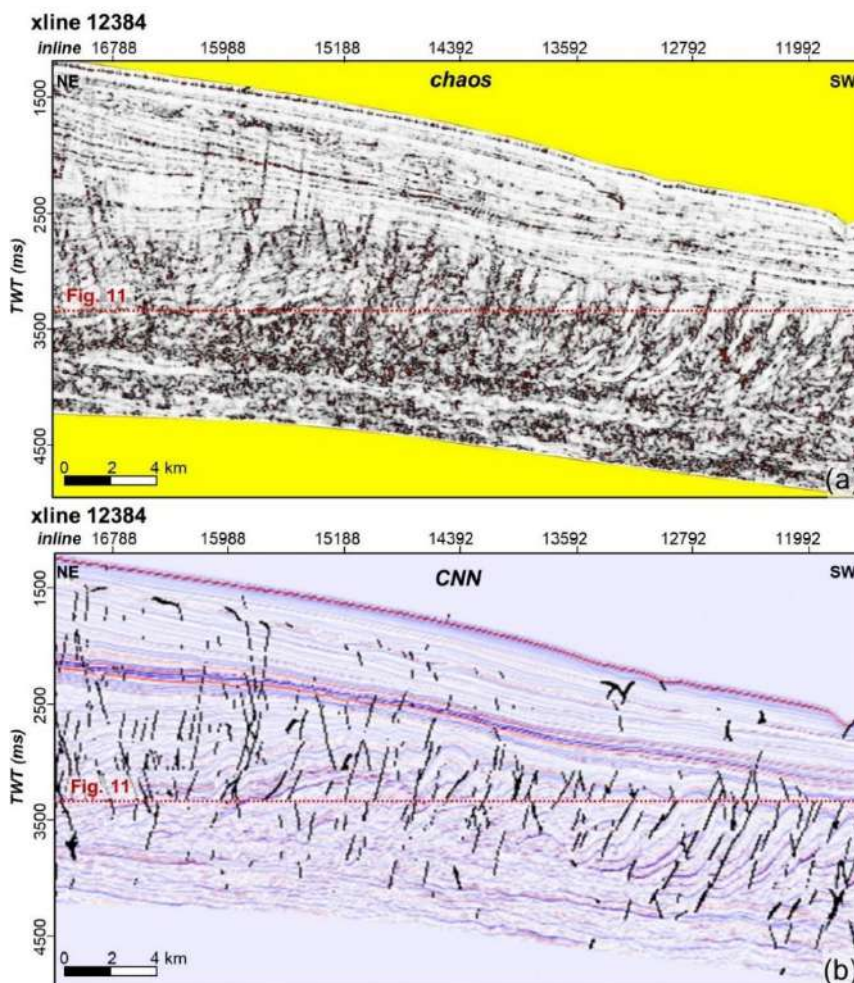


438

439 **Fig. 9.** Data preparation for fault segmentation in the CNN. The black areas at the top and bottom of the volume
440 indicate the absence of data or field noise. The red areas correspond to regions with stratigraphic significance,
441 while the green areas represent country rocks.

442
443
444
445
446
447
448
449
450
451
452
453
454
455
456
457

Figure 10 is a comparison of a chaos crossline to a fault-net architecture crossline. The CNN output provides a cleaner, less-distracted output highlighting faults as black solid lines without the influence of noise at depth (Fig. 10b), unlike the chaos volume (Fig. 10a). Although the influence of noise is reduced at depth, fault tips have not been fully segmented in the CNN (Fig. 10a). Types of faults (normal vs reverse) and fault displacements may be determined from the CNN volume because the output of faults is placed directly upon the original seismic volume (Fig. 10b). The chaos and variance edge-enhancing attributes do not show whether a fault displacement is normal or reverse (Figs. 8 and 10a). The sense of displacement can however be determined manually by displaying the manually interpreted faults on both the conventional amplitude and the CNN interpretation volumes. This is because the stratigraphic information of the horizons is largely removed particularly using the variance attribute (Fig. 8). Overall, the observation of the fault framework from the edge-enhanced and CNN volumes are consistent with the interpretation in Figure 7a; most faults initiate from the Turonian surface at depth, thrust faults of the compressional domain terminate in early to late Campanian sediments, while the translational domain's normal and oblique-slip faults terminate within stratigraphically younger Cenozoic sediments (Fig. 10).

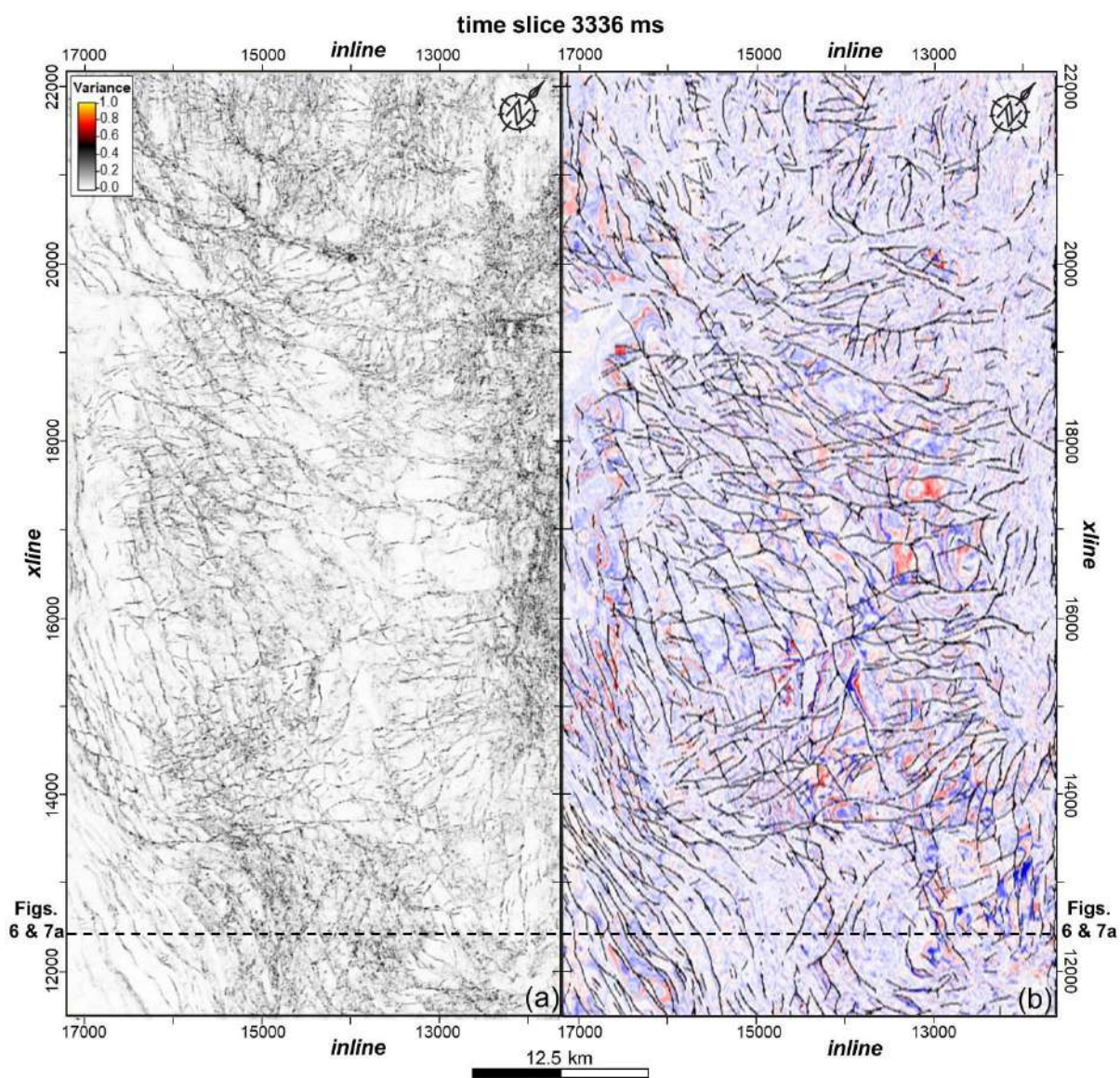


458
459

Fig. 10. Crossline section 12384 comparing structural lineaments in (a) the chaos compared to (b) the CNN output.

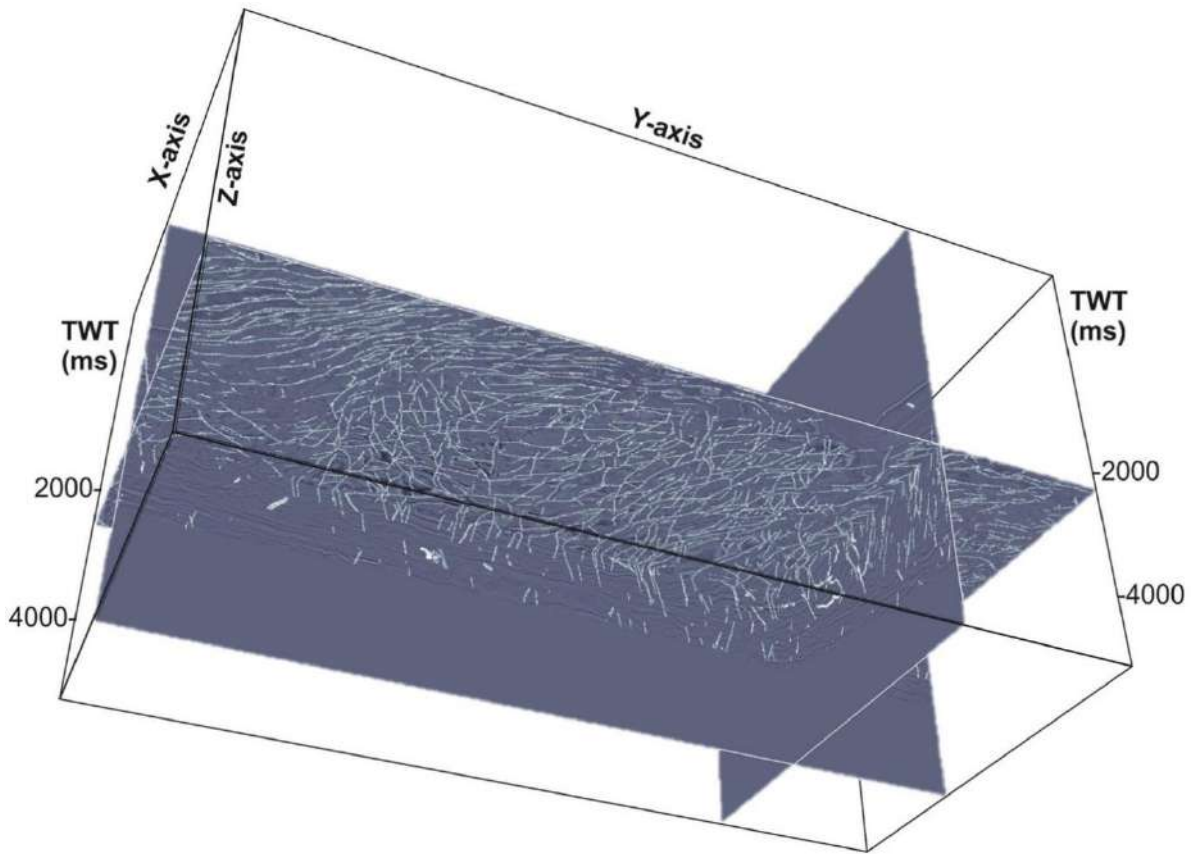
460
461
462
463
464
465
466
467
468
469
470

The overall pattern of the fault framework is best viewed on the horizontal time slice, and has such been shown in Figure 11, comparing the variance (a) and CNN output (b). The fault-net predicted fault locations (Fig. 11b) were generally consistent with variance (Fig. 11a) and the manually interpreted faults in Figure 7b and c. When interpreting the time slices alone, the only displacement characteristics that can be determined is the strike-slip component of oblique-slip faults where they segment compressional thrust sheets along strike (refer to Figs. 6b and c for the time slices in Fig. 11). Figure 11b shows that CNN model was able to identify additional faults that were not detected using the variance method. The visibility of faults is obscured by noise on the variance time slice as clearly seen in the northern and north-eastern areas (and other areas) in Figure 11a. The CNN output, however, has not been disrupted by noise in the dataset, and faults therefore appear clearly in all areas (Figs. 11b and 12).



471
472
473

Fig. 11. Time slice at 3336 ms comparing structural lineaments in (a) the variance volume compared to (b) the output of the CNN.



474

475 **Fig. 12.** 3D Fault-net model showing fault segmentation.

476

477 **5. Discussion**

478 The interpretation of reflection seismic data includes many steps and applications which depends on the
 479 level of detail the interpreter wants to image features in the subsurface. Understanding the fault framework system
 480 is a crucial step in determining the hydrocarbon prospectivity of a sedimentary basin. Faults impact the distribution
 481 and accumulation of potential hydrocarbons, creating migration pathways for the movement of hydrocarbons from
 482 the source rock to the reservoir until they are trapped and begin accumulating. The main criteria for identifying
 483 faults in a seismic section include the vertical displacement of reflectors, reflection discontinuity along a fault
 484 plane, and the abrupt termination of a seismic event (Duru et al., 2018). Faults are often missed in regular 2D
 485 seismic survey due to spatial limitations and the incorrect interpolation between 2D images (Richards et al., 2015).
 486 The deep-water Orange Basin study area has a complex fault framework system imaged using high-resolution,
 487 3D reflection seismic data.

488 Important geological and physical properties of a basin's structure, stratigraphy, and reservoir
 489 characteristics are revealed through the use seismic attributes that may otherwise be missed in a normal seismic
 490 volume (Chopra and Marfut, 2005; Brown, 2011). While volumetric attributes are applied in the initial stage of
 491 seismic interpretation, horizon/surface-based attributes may only be applied to a picked surface once sufficient
 492 manual interpretation has taken place. Using deep learning methods to recognize faults is rapidly evolving with
 493 the latest architectures being very computationally efficient. In this deep-water Orange Basin study, a new CNN-

494 based method of fault segmentation called ‘fault-net’ (developed by [Dou et al., 2022](#)) with a U-shaped architecture
495 is tested against conventional edge-enhancing volumetric attributes of chaos and variance following data
496 conditioning. The identification and delineation of faults using each method is discussed below, followed by the
497 implications for hydrocarbon exploration. A Late Cretaceous DWFTB system defines the bulk of the seismic
498 volume, and as such, the fault framework system identified using both the conventional edge-enhancement
499 attributes and the fault-net CNN stems from it.

500 **5.1. Comparison between 3D conventional methods and deep convolutional neural networks**

501 Faults are often highly variable in their geometry, connectivity, and orientation, making their
502 interpretation challenging. Various computer-based software platforms may be used to interpret reflection seismic
503 data and all have their limitations with regards to fault mapping ([Wu and Hale, 2016](#)). For example, certain fault
504 intersections such as offset scissor faults cannot be correctly modelled in other software packages, and defining
505 fault relationships is not a fully automated process. Fault interpretations therefore require tweaking with some
506 relationships needing to be manually forced to fit a fault framework model. Using the guidance of volumetric-
507 (variance), and surface-based (influential data and edge detection) attributes, [Maduna et al. \(2022\)](#) manually
508 mapped over 500 regional-scale faults in the deep-water study area ([Figs. 6b and c](#)) over a period of a year. This
509 conventional method of manual fault interpretation and extraction is heavily time-consuming and not without bias.

510 Research is ongoing in the application of deep learning tools/methods to seismology and specific
511 architectures for object labelling. Currently, there is a consensus on the use of CNNs with a U-shaped architecture
512 to automate image segmentation. This approach is based on the idea of semantic segmentation applied to faults in
513 seismic data. A trained deep learning model therefore labels faults on a per-pixel basis, treating the seismic volume
514 as a 3D image. An advantage of CNNs over conventional methods is a significantly reduced running time (several
515 months using the conventional method compared to several hours using the CNN method) and computational
516 power required to run processes ([Dou et al., 2022](#)). CNNs generate a fault output map based on the probability of
517 faults in a seismic volume ([Fig. 12](#)), providing valuable insights into the uncertainties associated with manual
518 fault interpretation, something that is unavailable using conventional methods. The fault-net CNN deep learning
519 model is highly efficient in that it can be trained on both small or large, and on real or synthetic datasets, and still
520 produce accurate results with more ease and less uncertainty. The uncertainties associated with fault interpretation
521 may be reduced using fault probability maps, helping geoscientists to better understand potential risks and
522 optimize drilling locations. For example, areas with many faults may be avoided or subject to more detailed
523 analysis before drilling. The use of probabilistic fault maps provides a more nuanced understanding of the fault
524 network and can be used to identify areas of high structural complexity.

525 The use of the variance and chaos edge-enhancing volumetric attributes ([Figs. 8, 10a and 11a](#)) improved
526 the recognition of faults compared to the uninterpreted seismic volume in [Figure 6](#). Apart from faults, chaos
527 enhances other features in seismic data such as channels, gas chimneys, and carbonate sediments appearing as
528 chaotic textures ([Randen et al., 2001](#)). When comparing the interpretation in [Figure 7a](#) with the chaos section in
529 [Figure 10a](#), the whole ~3 km thick succession defining the Upper Cretaceous DWFTB system is chaotic in texture
530 with the highest chaos values along Turonian and Albian surfaces. If the data were tuned by running the algorithm
531 on dip-guided windows at right angles to the dominant dip orientation, faults alone would be detected ([Randen et](#)

532 al., 2001). Other software packages, for example, do not however provide a dip-guided option when running
533 chaos, therefore resulting in a noisy output volume containing other features that are not necessarily faults such
534 as dipping surfaces (Figs. 8a, b and 10a).

535 Variance on the other hand does provide a dip correction and dip-guided smoothing option (Table 4),
536 and so, the effect of dipping surfaces may be removed from the output volume. This effect gives a poor, low-
537 resolution fault output in the vertical sections (Fig. 8c and d) compared chaos (Figs. 8a, b and 10a). Faults
538 delineated in variance's horizontal time slice are however much higher in resolution and are better in quality (Figs.
539 8c and 11a) which is the converse for the chaos volume (Fig. 8a). This may have to do with the way in which
540 variance is computed; as horizontal sub-slices (Randen et al., 2001). Both the chaos and variance volumes did not
541 operate well at depth because seismic resolution decreases with depth, resulting in noisy areas that may be
542 misinterpreted as being heavily fractured. Although structural lineaments indicating the presence of faults are
543 shown in the variance time slice in Figure 11a, it does not compare to the higher resolution output provided by
544 the CNN in Figure 11b. This is one of the key visible advantages of the CNN over conventional edge-enhancing
545 attributes; that it provides a cleaner, more continuous output, ignoring the effect of noise in the seismic dataset.
546 Seismic data can be affected by noise, artifacts, and other types of distortion, which can reduce the accuracy of
547 fault extraction. This is why pre-conditioning of the seismic data is essential to remove noise and correct for
548 distortions before training the CNN as was done in this study through structural smoothing (Fig. 6b).

549 Even though the conditioned volume (Fig. 6b) was used as input for both the chaos and variance edge-
550 enhancing attributes applied (Figs. 8, 10a and 11a) and the fault-net CNN (Figs. 10b, 11b and 12), the CNN output
551 fared much better in reducing the influence of noise and other artifacts in the dataset. Conversely, a limitation of
552 the fault-net CNN is that many small-scale faults at depth and the tips of faults were cleaned out from the output
553 model (Fig. 10b). This may be a minor limitation as the fault-net architecture may be further refined and trained
554 to recognise faults that are smaller in scale and displacement. Another limitation of the CNN-based approach of
555 fault segmentation is that the training process requires a large amount of labelled data, which may be difficult to
556 obtain in some cases. In regional studies (larger than the present 1 800 km² study), larger seismic datasets would
557 be required for training particularly in structurally more complex onshore areas. Furthermore, the fault labelling
558 process itself can be time-consuming, requiring a geoscience expert.

559 **5.2. Implications for hydrocarbon exploration**

560 The Orange Basin presents a prime study for hydrocarbon exploration. The basin is situated within an
561 overall extensional tectonic setting with compressional tectonics along the continental slope, thus accounting for
562 its structural complexity. The deep-water study area has all the makings of a prolific hydrocarbon system as it has
563 all necessary elements including source rocks, reservoir rocks, traps, and hydrocarbon migration pathways (Figs.
564 6 and 7a). Known source rock intervals identified in the Orange Basin occur within sediments of the Hauterivian
565 (Jungslager, 1999), Barremian to Aptian (van der Spuy, 2003) and Turonian (Aldrich et al., 2003) ages (Fig. 2).
566 Seen within the seismic volume is the Turonian-aged source rock interval acting as a primary shale detachment
567 surface for the Upper Cretaceous DWFTB system in this (Figs. 6 and 7a) and other orange Basin research (e.g.,
568 de Vera et al., 2010; Scarselli et al., 2016).

569 In the shallower reaches of the Orange Basin the two biggest hydrocarbon systems along the Namibian
570 (Kudu gas field) and South African (Ibubhesi gas field) shelves are stratigraphically trapped within aeolian and
571 fluvial channel-fill sandstone reservoirs (Jungslager, 1999). High sedimentation rates are recorded offshore SW
572 Africa during the Upper Cretaceous with major uplift and tilting of the margin (Hirsch et al., 2010; Baby et al.,
573 2020) resulting in the formation of DWFTB systems with the down-dip contraction of sediment (de Vera et al.,
574 2010). Sand was transported to the deeper reaches of the basin through canyons providing reservoirs for the
575 upward migration of hydrocarbons which are structurally trapped as channelized and ponded turbiditic sandstones
576 (PASA, 2017). Structural trapping may also be in the form of anticlines from distal folds of the compressional
577 domain as is the case for systems in the Niger Delta (Corredor et al., 2005; Benesh et al., 2014).

578 The most vital element for a petroliferous hydrocarbon system is the presence of hydrocarbon migration
579 pathways. Hydrocarbon migration pathways are described as the vertical movement of hydrocarbons from the
580 source to the reservoir until it becomes trapped (Dembicki, 2022). Apart from the stratigraphy, the distribution
581 and permeability of fractures play a crucial role in the migration of hydrocarbons, impacting the efficiency and
582 direction of fluid flow. The distribution of faults in the deep-water study area shown in Figure 7b and c is a
583 complicated system of up-dip normal, central oblique-slip, and down-dip thrust faults (Maduna et al., 2022).
584 Normal faulting is the downward vertical movement (dip-slip) of the hanging wall relative to the foot wall,
585 characteristic of extensional tectonics observed in rifted margins settings. Thrust faulting is the low-angle (<45°),
586 upward vertical movement (dip-slip) of the hanging wall relative to the foot wall, associated with compressional
587 tectonics. Oblique-slip faulting is a combination of both vertical (dip-slip) and horizontal (strike-slip) fault block
588 movement with the horizontal aspect, often associated with transform tectonic regimes.

589 Although both the edge-enhancing attributes and the CNN methods are capable of fault detection (Figs.
590 9, 10 and 12), the method that can distinguish normal faulting from thrust faulting with ease in the seismic volume
591 is the fault-net CNN (Figs. 10b and 12) which is a major advantage. The fault-net CNN outputs the presence of
592 faults together with the original seismic volume meaning that both the dip-slip and oblique-slip components of
593 faults may be determined directly from the output. This makes it possible to clearly see offset stratigraphic markers
594 without the need to constantly toggle back and forth between different views (or to overlay the different views)
595 which is required for the applied conventional seismic attributes.. To give a general estimate of vertical
596 displacement characteristics and determine fault types, the edge-enhancing attributes (Figs. 8 and 10a) need a
597 direct side-by-side (or overlay) comparison with the original/structurally smoothed seismic volume (Fig. 6) which
598 is an inaccurate, arduous, and time-consuming process. The purpose, and hence, inherent downfall of seismic
599 attributes is that they filter the data by focussing the attention on one specific component by removing others from
600 the dataset (Barnes, 2016) rather than highlighting the component of interest within the original seismic volume.

601 Maduna et al. (2023) identified features indicative of hydrocarbons in the deep-water study area including
602 a ~4 km elongated mud volcano, pockmarked surfaces, polygonal faults, and an anticline with a high positive
603 amplitude anomaly revealed using seismic attributes that are direct hydrocarbon indicators. Drilling is yet to
604 commence in the deep-water region to validate and determine the extent of hydrocarbons. Optimizing accurate
605 drilling locations first requires the seismic interpretation of the structural framework of which the distribution of
606 faults, acting as primary fluid migration pathways, is the most important. Results from the CNN-based approach

607 of segmenting faults compared to edge-enhancing seismic attributes show that deep learning tools are fast
608 becoming more advantageous than conventional methods of interpreting reflection seismic data.

609

610 **6. Conclusion**

611 The application of deep convolutional neural networks for 3D fault extraction from seismic data is a
612 promising and exciting approach for improving the efficiency and accuracy of fault interpretation in subsurface
613 structures, with profound implications for hydrocarbon exploration and target drilling. Our study demonstrated
614 the effectiveness of the U-Net architecture in accurately identifying and extracting faults from 3D seismic data in
615 the deep-water Orange Basin, offshore South Africa. The architecture can identify subtle fault features that may
616 be missed by human interpreters or conventional algorithms. This is a crucial step forward in our understanding
617 of the geological history and potential hydrocarbon resources in this region and beyond. The use of deep learning
618 CNNs for fault extraction can significantly reduce the time and subjectivity associated with manual interpretation
619 using conventional methods, allowing for more efficient and accurate identification of subsurface structures. All
620 conventional methods tend to suffer from noise-induced loss of performance and the computation of processes is
621 intensive. Furthermore, the fault map generated by the CNNs can help to quantify uncertainties in fault
622 interpretation, which is essential in improving the efficiency of hydrocarbon exploration by identifying areas of
623 high structural complexity and potential risks.

624 While there are limitations to the use of deep CNNs for 3D fault extraction, such as the need for high-
625 quality input data and a large amount of labelled data for training, the benefits of this approach are significant.
626 The application of deep learning techniques to seismic interpretation is an exciting area of research, and we
627 anticipate that further developments in this field will lead to more accurate and efficient identification of
628 subsurface structures, with profound implications for hydrocarbon exploration and target drilling. Overall, the
629 application of deep learning CNNs for 3D fault extraction from seismic data is a promising and revolutionary
630 approach that has the potential to improve our understanding of the geological history and potential hydrocarbon
631 resources in the deep-water Orange Basin, and other regions around the world.

632

633 **Acknowledgements**

634 Our sincerest thanks are extended to the National Research Foundation of South Africa and the South
635 African Council for Geoscience (CGS), respectively for funding the first author's (N.G Maduna) doctoral
636 research. We would also like to thank Shell and the Petroleum Agency of South Africa for providing the 3D
637 reflection seismic data, and Schlumberger for the Petrel software and support. We are furthermore grateful for the
638 scientific discussions and insights provided by our friends and colleagues from the Wits Seismic Research Centre.
639 The authors S.E. Zhang and J.E. Bourdeau would like to declare that: (1) the work was not undertaken under the
640 auspices of NRCAN as part of their employment responsibilities; (2) the work was conducted under the auspices
641 of the researcher's affiliation with an external institution; and (3) any views expressed therein are their personal
642 opinions and not those of NRCAN contribution number 20230156.

643

644 **Credit authorship contribution statement**

645 **Nombuso G. Maduna:** Conceptualization, Formal analysis, Methodology, Visualization, Writing – original draft,
646 Writing – review and editing. **Musa S.D. Manzi:** Data curation, Methodology, Supervision, Writing – Original
647 Draft, Writing – review and editing. **Glen T. Nwaila:** Methodology, Visualization, Writing – original draft,
648 Writing – review and editing. **Julie E. Bourdeau:** Visualization, Writing – original draft, Writing – review and
649 editing. **Zubair Jinnah:** Supervision. **Steven E. Zhang:** Methodology, Writing – original draft, Writing – review
650 and editing.

651

652 **Declaration of competing interest**

653 The authors declare that they have no known competing financial interests or personal relationships that could
654 have appeared to influence the work reported in this paper.

655 **Data availability**

656 The seismic data are the property of Shell and may be purchased through the Petroleum Agency of South
657 Africa's online geoportal at
658 https://geoportal.petroleumagencyrsa.com/Storefront/Viewer/index_map.html (last access: 9 November
659 2022).

660

661 **References**

662

663 Aldrich, J., Zilinski, R., Edman, J., Leu, W., Berge, T., Corbett, K., 2003. Documentation of a new petroleum
664 system in the South Atlantic. In: AAPG Annual Convention Salt Lake City, pp. 90013

665 An, Y., Guo, J., Ye, Q., Childs, C., Walsh, J., Dong, R., 2021. Deep convolutional neural network for automatic
666 fault recognition from 3D seismic datasets. *Comput. Geosci.* 153, 104776.
667 <https://doi.org/10.1016/j.cageo.2021.104776>.

668 Baby, G., Guillocheau, F., Braun, J., Robin, C., Dall'Asta, M., 2020. Solid sedimentation rates history of the
669 Southern African continental margins: Implications for the uplift history of the South African Plateau. *Terra Nova*
670 32, 53-65. <https://doi.org/10.1111/ter.12435>.

671 Baby, G., Guillocheau, F., Morin, J., Ressouche, J., Robin, C., Broucke, O., Dall'Asta, M., 2018. Post-rift
672 stratigraphic evolution of the Atlantic margin of Namibia and South Africa: Implications for the vertical
673 movements of the margin and the uplift history of the South African Plateau. *Mar. Petrol. Geol.* 97, 169–191.
674 <https://doi.org/10.1016/j.marpetgeo.2018.06.030>.

675 Barnes, A.E., 2016. Handbook of poststack seismic attributes. *Society of Exploration Geophysicists* 21, pp. 268.
676 <https://doi.org/10.1190/1.9781560803324>.

677 Benesh, N.P., Plesch, A., Shaw, J.H., 2014. Geometry, kinematics, and displacement characteristics of tear-fault
678 systems: An example from the deep-water Niger Delta. *AAPG Bull.* 98 465–482.
679 <https://doi.org/10.1306/06251311013>.

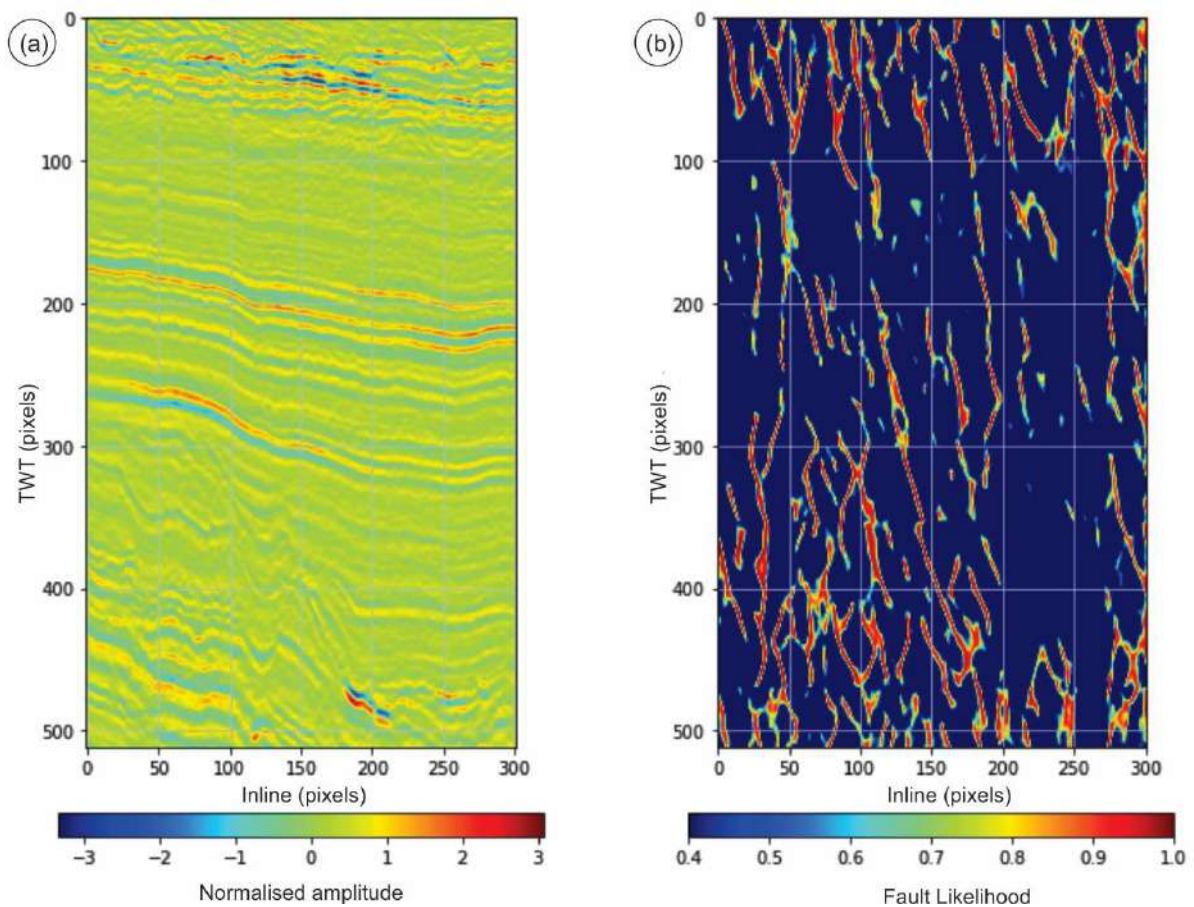
- 680 Broad, D., Jungslager, E., McLachlan I., Roux, J., 2006. Offshore Mesozoic Basins. In: Johnson, M.R.,
681 Anhaeusser, C.R., Thomas, R.J. (Eds.), *The Geology of South Africa*. Geological Society of South Africa and
682 Council for Geoscience, Johannesburg, pp. 553–571.
- 683 Brown, L., Benson, J., Brink, G., Doherty, S., Jollands, A., Jungslager, E., Keenen, J.H.G., Muntingh, A., van
684 Wyk, N.J.S., 1995. Sequence stratigraphy on offshore South African divergent basins: An atlas on exploration for
685 Cretaceous lowstand traps. Soekor (Pty) Ltd., AAPG Studies in Geology.
- 686 Brown, A.R., 2011. Interpretation of Three-Dimensional Seismic Data. Society of Exploration Geophysicists and
687 the American Association of Petroleum Geologists, USA, 646 pp.
- 688 Chopra, S., Marfurt, K.J., 2005. Seismic attributes – A historical perspective. *Geophysics* 70, 3SO-28SO.
689 <https://doi.org/10.1190/1.2098670>.
- 690 Chopra, S., Marfurt, K.J., 2007. Seismic Attributes for Prospect Identification and Reservoir Characterization.
691 Society of Exploration Geophysicists, 481 pp. <https://doi.org/10.1190/1.9781560801900>.
- 692 Corredor, F., Shaw, J.H., Bilotti, F., 2005. Structural styles in the deep-water fold and thrust belts of the Niger
693 Delta. *AAPG Bull.* 89, 753–780. <https://doi.org/10.1306/02170504074>.
- 694 Cox, D.R., Newton, A.M., Huuse, M., 2020. An introduction to seismic reflection data: Acquisition, processing
695 and interpretation. In: *Regional Geology and Tectonics*, pp. 571-603. [https://doi.org/10.1016/B978-0-444-
696 64134-2.00020](https://doi.org/10.1016/B978-0-444-64134-2.00020).
- 697 Dalton, T.J.S., Paton, D.A., Needham, D.T., 2017. Influence of mechanical stratigraphy on multi-layer gravity
698 collapse structures: insights from the Orange Basin, South Africa. *Geol. Soc. Lond. Sp. Publ.* 438, 211–228.
699 <https://doi.org/10.1144/SP4384>.
- 700 Dalton, T.J.S., Paton, D.A., Needham, T., Hodgson, N., 2015. Temporal and spatial evolution of deepwater fold
701 thrust belts: Implications for quantifying strain imbalance. *Interpretation* 3, SAA59–SAA70.
702 <https://doi.org/10.1190/INT-2015-0034.1>.
- 703 de Vera, J., Granado, P., McClay, K., 2010. Structural evolution of the Orange Basin gravity-driven system,
704 offshore Namibia. *Marine Petrol. Geol.* 27, 223–237. <https://doi.org/10.1016/j.marpetgeo.2009.02.003>.
- 705 Dembicki, H., 2020. *Practical Petroleum Geochemistry for Exploration and Production*. Elsevier Inc., Amsterdam,
706 The Netherlands, 332 pp.
- 707 Diester-Haass, L., Meyers, P.A., Bickert, T., 2004. Carbonate crash and biogenic bloom in the late Miocene:
708 Evidence from ODP Sites 1085, 1086, and 1087 in the Cape Basin, southeast Atlantic Ocean. *Paleoceanogr.*
709 *Paleoclimatology* 19, PA1007. <https://doi.org/10.1029/2003PA000933>.
- 710 Dou, Y., Li, K., Zhu, J., Li, T., Tan, S., Huang, Z., 2022. MD Loss: Efficient Training of 3-D Seismic Fault
711 Segmentation Network Under Sparse Labels by Weakening Anomaly Annotation. *IEEE Trans. Geosci. Remote*
712 *Sens.* 60, 1-14. <https://doi.org/10.1109/TGRS.2022.3196810>.
- 713 Duru, C.A., Ugwu, S.A., Nwankwoala, H.O., 2018. Velocity modeling for structural traps evaluation and
714 interpretation of TM-Field in Niger Delta. *Int. J. Geol. Earth Sci.* 4, 1-13.
715 <https://doi.org/10.5829/idosi.weasj.2018.67.85>.
- 716 Gay, A., Lopez, M., Cochonat, P., Sultan, N., Cauquil, E., Brigaud, F., 2003. Sinuous pockmark belt as indicator
717 of a shallow buried turbiditic channel on the lower slope of the Congo Basin, West African Margin. *Geol. Soc.*
718 *Lond. Spec. Publ.* 216, 173-189. <https://doi.org/10.1144/GSL.SP.2003.216.01.12>.
- 719 Gerrard, T., Smith, G.C., 1982. Post-Paleozoic succession and structure of the southwestern African continental
720 margin. In: Watkins, J.S., Drake, C.L., (Eds.), *Studies in Continental Margin Geology*, AAPG Memoir 34, pp.
721 49–74.
- 722 Granado, P., Vera, J.D., McClay, K.R., 2009. Tectonostratigraphic evolution of the Orange Basin, SW Africa.
723 *Trabajos de geología* 29, 321-328.

- 724 Hale, D., 2013. Methods to compute fault images, extract fault surfaces, and estimate fault throws from 3D seismic
725 images. *Geophysics* 78, O33-O43. <https://doi.org/10.1190/GEO2012-0331.1>.
- 726 Hartwig, A., Anka, Z., di Primio, R., 2012. Evidence of a widespread paleo-pockmarked field in the Orange Basin:
727 An indication of an early Eocene massive fluid escape event offshore South Africa. *Mar. Geol.* 332–334, 222–
728 234. <https://doi.org/10.1016/j.margeo.2012.07.012>.
- 729 Herron, D.A. 2011. Resolution. In: Latimer, R.B. (Ed.) *First Steps in Seismic Interpretation*. Society of
730 Exploration Geophysicists, pp. 75–82.
- 731 Hirsch, K.K., Scheck-Wenderoth, M., van Wees, J.-D., Kuhlmann, G., Paton, D.A., 2010. Tectonic subsidence
732 history and thermal evolution of the Orange Basin. *Mar. Petrol. Geol.* 27, 565-584.
733 <https://doi.org/10.1016/j.marpetgeo.2009.06.009>.
- 734 Jungslager, E., 1999. Petroleum habitats of the Atlantic margin of South Africa. In: Cameron, N., Bate, R., Clure,
735 V. (Eds.) *The Oil and Gas Habitats of the South Atlantic*. Geological Society, London, pp. 153–168.
736 <https://doi.org/10.1144/GSL.SP.1999.153.01.10>.
- 737 Kramer, E.A.J., Heck, L., 2014. Orange basin 3D pre-processing and preSDM 2013. Shell Global Solutions
738 International BV, Risjswijk, Netherlands.
- 739 Kuhlmann, G., Adams, S., Campher, C., van der Spuy, D., di Primio, R., Horsfield, B., 2010. Passive margin
740 evolution and its controls on natural gas leakage in the southern Orange Basin, blocks 3/4, offshore South Africa.
741 *Marine Petrol. Geol.* 27, 973–992. <https://doi.org/10.1016/j.marpetgeo.2010.01.010>.
- 742 Light, M.P.R., Maslanyj, M.P., Greenwood, R.J., Banks, N.L., 1993. Seismic sequence stratigraphy and tectonics
743 offshore Namibia. *Geol. Soc. Lond. Sp. Publ.* 71, 163–191. <https://doi.org/10.1144/GSL.SP.1993.071.01.08>.
- 744 Maduna, N.G., Manzi, M.S., Jinnah, Z., Bourdeau, J.E., 2022. Strato-structural evolution of the deep-water
745 Orange Basin: constraints from 3D reflection seismic data. *J. Geophys. Res. Solid Earth* 13, 1755-1780.
746 <https://doi.org/10.5194/se-13-1755-2022>.
- 747 Maduna, N.G., Manzi, M.S.D., Bourdeau, J.E., Jinnah, Z., 2023. 3D reflection seismic imaging of natural gas/fluid
748 escape features in the deep-water Orange Basin of South Africa. *Mar. Geophys. Res.* 44, 17.
749 <https://doi.org/10.1007/s11001-023-09523-2>.
- 750 Mahlalela, V., Manzi, M.S.D., Jinnah, Z., Bourdeau, J.E., Durrheim, R.J., 2021. Structural characteristics and 3D
751 seismic detection of gas migration pathways in the deep-water Orange Basin, South Africa. *Mar. Geophys. Res.*
752 42, 8. <https://doi.org/10.1007/s11001-021-09428-y>.
- 753 Manzi M.S.D., Hein K.A.A., King N., Durrheim R.J., 2013. Neoproterozoic tectonic history of the Witwatersrand
754 Basin and Ventersdorp Supergroup: new constraints from high-resolution 3D seismic reflection data.
755 *Tectonophysics* 590, 94–105. <https://doi.org/10.1016/j.tecto.2013.01.014>.
- 756 Marfurt, K.J., Kirilin, R.L., Farmer, S.L., Bahorich, M.S., 1998. 3-D seismic attributes using a semblance-based
757 coherency algorithm. *Geophysics* 63, 1150–1165. <http://doi.org/10.1190/1.1444415>.
- 758 Marfurt, K.J., Sudhaker, V., Gersztenkorn, A., Crawford, K.D., Nissen, S.E., 1999. Coherency calculations in the
759 presence of structural dip. *Geophysics* 64, 104–111. <http://doi.org/10.1190/1.1444508>.
- 760 McMillan, I.K., 2003. Foaminiferally defined biostratigraphic episodes and sedimentation patterns of the
761 Cretaceous drift succession (Early Barremian to Late Maastrichtian) in seven basins on the South African and
762 southern Namibian continental margin. *S. Afr. J. Sci.* 99, 537–576.
- 763 Morley, C.K., King, R., Hillis, R., Tingay, M., Backe, G., 2011. whi fold and thrust belt classification, tectonics,
764 structure and hydrocarbon prospectivity: A review. *Earth-Sci. Rev.* 104, 41–91.
765 <https://doi.org/10.1016/j.earscirev.2010.09.010>.
- 766 Muntingh, A., Brown, L.F.Jr., 1993. Sequence stratigraphy of petroleum plays, post-rift Cretaceous rocks (Lower
767 Aptian to Upper Maastrichtian), Orange Basin, western offshore, South Africa, In: Weimer, P., Posamentier, H.

- 768 (Eds.) Siliciclastic Sequence Stratigraphy: Recent Developments and Applications, AAPG Memoir 58, pp. 71–
769 98.
- 770 Nemčok, M., Schamel, S., Gayer, R., 2005. Thrustbelts: Structural Architecture, Thermal Regimes and
771 Petroleum Systems, 1st edn. Cambridge University Press, Cambridge, 541 pp.
- 772 Nürnberg, D., Müller, R.D., 1991. The tectonic evolution of the South Atlantic from Late Jurassic to present.
773 Tectonophysics 191, 27–53. [https://doi.org/10.1016/0040-1951\(91\)90231-G](https://doi.org/10.1016/0040-1951(91)90231-G).
- 774 Paton, D.A., van der Spuy, D., di Primio, R., Horsfield, B., 2008. Tectonically induced adjustment of passive-
775 margin accommodation space; influence on the hydrocarbon potential of the Orange Basin, South Africa. AAPG
776 Bull. 92, 589–609. <https://doi.org/10.1306/12280707023>.
- 777 Petroleum Agency South Africa (PASA), 2017. Information and opportunities, Petroleum Agency South Africa,
778 Cape Town, South Africa.
779 https://www.petroleumagencyrsa.com/images/pdfs/Pet_expl_opp_broch_2017bw1.pdf (accessed 9
780 November 2022).
- 781 Qi, J., Lyu, B., AlAli, A., Machado, G., Hu, Y., Marfurt, K., 2019. Image processing of seismic attributes for
782 automatic fault extraction. Geophysics 84, O25–O37. <https://doi.org/10.1190/GEO2018-0369.1>.
- 783 Randen, T., Pedersen, S.I., Sønneland, L., 2001. Automatic extraction of fault surfaces from three-dimensional
784 seismic data. In: 81st Annual International Meeting, SEG, Expanded Abstracts, pp. 551–554.
- 785 Richards, F.L., Richardson, N.J., Bond, C.E., Cowgill, M., 2015. Interpretational variability of structural traps:
786 implications for exploration risk and volume uncertainty. Geol. Soc. Lond. Spec. Publ. 421, 7–27.
787 <http://dx.doi.org/10.1144/SP421.13>.
- 788 Rowan, M.G., Peel, F.J., Vendeville, B.C., 2004. Gravity-driven fold belts on passive margins. In: McClay, K.R.
789 (Ed.) Thrust Tectonics and Hydrocarbon Systems. AAPG Bull. 82, 157–182.
790 <https://doi.org/10.1306/61EECE28-173E-11D7-8645000102C1865D>.
- 791 Scarselli, N., McClay, K., Elders, C., 2016. Seismic geomorphology of cretaceous megaslides offshore Namibia
792 (Orange Basin): Insights into segmentation and degradation of gravity-driven linked systems. Mar. Petrol. Geol.
793 75, 151–180. <https://doi.org/10.1016/j.marpetgeo.2016.03.012>.
- 794 Silva, C.C., Marcolino, C.S., Lima, F.D., 2005. Automatic fault extraction using ant tracking algorithm in the
795 Marlim South Field, Campos Basin. In: 2005 SEG Annual Meeting, Houston, Texas, pp. 857–860.
796 <https://doi.org/10.1190/1.2148294>.
- 797 Uenzelmann-Neben G., Tobias W., Gruetznert J., Maik T., 2017. Transition from the Cretaceous Ocean to
798 Cenozoic circulation in the western South Atlantic – a twofold reconstruction. Tectonophysics 716, 22–240.
799 <https://doi.org/10.1016/j.tecto.2016.05.036>.
- 800 van der Spuy, D., 2003. Aptian source rocks in some South African Cretaceous basins. Geol. Soc. Lond. Sp. Publ.
801 207, 185–202. <https://doi.org/10.1144/GSL.SP.2003.207.10>.
- 802 van der Spuy, D., Sayidini, B., 2022. Offshore Namibia discovery signals bright future for South Africa oil and
803 gas. AAPG Explorer. [https://explorer.aapg.org/story/articleid/62613/offshore-namibia-discovery-
804 signals-bright-future-for-south-africa-oil-and-gas](https://explorer.aapg.org/story/articleid/62613/offshore-namibia-discovery-signals-bright-future-for-south-africa-oil-and-gas) (accessed 31 March 2022).
- 805 Viola, G., Kounov, A., Andreoli, M.A.G., Mattila, J., 2012. Brittle tectonic evolution along the western margin
806 of South Africa: more than 500 Myr of continued reactivation. Tectonophysics 514, 93–114.
807 <https://doi.org/10.1016/j.tecto.2011.10.009>.
- 808 Wei, X.L., Zhang, C.X., Kim, S.W., Jing, K.L., Wang, Y.J., Xu, S., Xie, Z.Z., 2022. Seismic fault detection using
809 convolutional neural networks with focal loss. Comput. Geosci. 158, 104968.
810 <https://doi.org/10.1016/j.cageo.2021.104968>.
- 811 Weigelt, E., Uenzelmann-Neben, G., 2007. Early Pliocene change of deposition style in the Cape Basin,
812 southeastern Atlantic. Geol. Soc. Am. Bull. 119, 1004–1013. <https://doi.org/10.1130/B26110.1>.

- 813 Weigelt, E., Uenzelmann-Neben, G., 2004. Sediment deposits in the Cape Basin: Indications for shifting ocean
814 currents?. AAPG Bull. 88, 765–780. <https://doi.org/10.1306/01260403101>.
- 815 Wu, X., Hale, D., 2016. 3D seismic image processing for faults. Geophysics 81, IM1–IM11.
816 <http://doi.org/10.1190/geo2015-0380.1>.
- 817 Wu, X., Liang, L., Shi, Y., Fomel, S., 2019. FaultSeg3D: Using synthetic data sets to train an end-to-end
818 convolutional neural network for 3D seismic fault segmentation. Geophysics 84, IM35–IM45
819 <http://doi.org/10.1190/GEO2018-0646.1>.
- 820 Wu, X., Liang, L., Shi, Y., Geng, Z., Fomel, S., 2020. Deep learning for local seismic image processing: Fault
821 detection, structure-oriented smoothing with edge-preserving, and slope estimation by using a single
822 convolutional neural network. In: SEG International Exposition and Annual Meeting 2019, pp. 2222–2226.
823 <http://doi.org/10.1190/segam2019-3215251.1>.
- 824 Wu, X., Luo, S., Hale, D., 2016. Moving faults while unfaulting 3D seismic images. Geophysics 81, IM25–IM33.
825 <https://doi.org/10.1190/geo2015-0381.1>.
- 826 Yilmaz, Ö., 2001. Seismic Data Analysis: Processing, Inversion, and Interpretation of Seismic data, vol. 1. In:
827 Doherty, S.M. (Ed.) Society of Exploration Geophysicists, 24 pp.
- 828

829 **Supplementary Figure**



830

831 Figure S1. Example of seismic image training results showing “Fault Likelihood”.

832

833 **Supplementary Data**

834 Link to dataset 1: Offshore Netherlands (F3) - <https://terranubis.com/datainfo/F3-Demo-2020>

835 Link to dataset 2: Marine New Zealand (Kerry 3D) -

836 http://s3.amazonaws.com/open.source.geoscience/open_data/newzealand/Taranaiki_Basin/Keri_3D/Kerry3D.segy

837 [gy](http://s3.amazonaws.com/open.source.geoscience/open_data/newzealand/Taranaiki_Basin/Keri_3D/Kerry3D.segy)

838 Link to dataset 3: Australia (Adele 3D) -

839 https://zenodo.org/record/4299758/files/Adele_seismic_survey_NW%20australia_bind%20cube_fault_detection

840 [.segy?download=1](https://zenodo.org/record/4299758/files/Adele_seismic_survey_NW%20australia_bind%20cube_fault_detection)

841

842

843

9 Discussion

By examining features in the deep-water Orange Basin, insights have been gained pertaining to the timing of basin formation, the driving mechanisms behind geological processes, and reservoir characteristics of the hydrocarbon system. This chapter discusses the findings of the research separated here into three main topics: (1) the deep-water Orange Basin's hydrocarbon system, (2) seismic attributes and convolutional neural networks, and (3) the evolution of the deep-water Orange Basin. The first discussion topic covers [Chapter 7](#)'s published manuscript entitled “*3D reflection seismic imaging of natural gas/fluid escape features in the deep-water Orange Basin of South Africa*” ([Maduna et al., 2022](#)). The second discussion topic covers a portion of the manuscript in [Chapter 7](#) (seismic attributes used for hydrocarbon exploration) and [Chapter 8](#)'s submitted manuscript entitled “*A novel approach to fault interpretation using a convolutional neural network: a case study of the deep-water Orange Basin, South Africa*” ([Maduna et al., 2023b](#)). The third discussion topic covers [Chapter 6](#)'s manuscript entitled the “*Strato-structural evolution of the deep-water Orange Basin: constraints from 3D reflection seismic data*” ([Maduna et al., 2023a](#)). This third discussion topic further expands on the evolutionary model combining all observations made in the research.

9.1 The deep-water Orange Basin's hydrocarbon system

The study of natural gas/fluid flow features in basin analysis presents a valuable and underutilized tool for understanding various aspects of basin evolution. Numerous natural gas and fluid escape features are observed in the deep-water Orange Basin reflecting the underlying hydrocarbon system. A schematic illustration of the important elements defining the hydrocarbon system is presented in [Fig. 9.1](#) showing source rock intervals and surfaces displaying numerous natural gas and fluid escape features.

9.1.1 Elements of a prolific hydrocarbon system

The Orange Basin study area has the makings of a prolific hydrocarbon system in that it contains the following important elements outlined below.

9.1.1.1 Source rock

- The source of hydrocarbons in the deep-water Orange Basin are believed to be of both thermogenic and biogenic origin ([Jungslager, 1999](#); [Ben-Avraham et al., 2002](#); [Kuhlmann et al., 2010](#); [Hartwig et al., 2012](#)). The Turonian shales are the thermogenic source imaged in the study area which is also the main detachment surface of the DWFTB system, while the biogenic source are organic-rich sediments in the Miocene attributed to the Benguela Upwelling System ([Fig. 9.1](#)). The shallow shelf region of the Orange Basin reached gas maturation as shown by the presence of the commercial Ibhusesi and Kudu gas fields ([Aldrich et al., 2003](#); [van der Spuy, 2003](#); [Paton et al., 2008](#)). Basin modelling studies and Namibian well logs located adjacent to the present study area ([Fig. 1.1](#)) show that oil maturation was reached in the deep-water regions of the basin ([Hirsch et al., 2010](#); [van der Spuy and Sayidini, 2022](#)). [Hirsch et al. \(2010\)](#) estimate the Turonian source rock interval to have undergone oil maturation between 85 Ma and 16 Ma with temperatures ranging from 100–140°C.

9.1.1.2 Migration pathways

- The main factors responsible for the migration and accumulation of hydrocarbon in the deep-water Orange Basin are the basin's geothermal gradient and the burial history (Jungslager, 1999; Hirsch et al., 2010). A basin's geothermal gradient plays a significant role in the maturation of organic matter, affecting the timing and extent of hydrocarbon generation. Additionally, the burial history of the sedimentary succession determines the depth and pressure conditions, which further impact the migration pathways of fluids.
- The Orange Basin study area is dominated by tectonics of the of the Late Cretaceous DWFTB system with normal, thrust, and oblique-slip faulting. Large-scale thrusts in the down-dip compressional domain are segmented by oblique-slip faults extending from the up-dip translational domain. The architecture of the faults, including their orientation and connectivity played a crucial role in the distribution and intensity of gas and fluid escape features observed as over-pressurized fluids are known to migrate along fault surfaces and through permeable beds (Gay et al., 2006).

9.1.1.3 Reservoir rocks and trapping mechanisms

- High sedimentation rates with margin uplift and tilting during the Late Cretaceous resulted in the formation of DWFTB systems offshore SW Africa (de Vera et al., 2010; Hirsch et al., 2010; Baby et al., 2020). Terrestrial sand transported into the deeper regions of the Orange Basin created ideal hydrocarbon reservoirs. While the traps in the shallower shelf regions are primarily stratigraphic (Jungslager, 1999), those of the deep-water study are predominantly structural, confined within anticlines formed by folding in the compressional domain. According to PASA (2017) structural trapping may also occur in the form of ponded turbiditic, and channelized sandstones seen in other shallower parts of the Orange Basin.

9.1.2 Natural gas and fluid escape features of the Orange Basin

The interplay of tectonics and sedimentation has had a profound effect on the formation of natural gas and fluid escape features which serve as indirect evidence of elevated pore fluid pressures. Fluid overpressures primarily arise due to tectonic stresses, disequilibrium compaction, and volumetric expansion (Rowan et al., 2004; Bilotti and Shaw, 2005). Sediment loading from gravitational collapse, coupled with volumetric expansion during the generation and maturation of hydrocarbon in the Late Cretaceous, led to fluid overpressures in the deep-water Orange Basin. The surface expression of hydrocarbon migration is evidenced by distinct features in the study area which have affected the stability of the evolving margin. These features include (1) pockmarked surfaces, (2) polygonal faults, and (3) a mud volcano. Although they are not natural gas and fluid escape features, other features of interest are (4) the products of mass flow processes closely associated with hydrocarbon migration to the seafloor. The distribution of all these features in the study area is illustrated in Fig. 9.1. Apart from Fig. 9.1, this subsection cites figures from Chapter 7 in Maduna et al. (2023a).

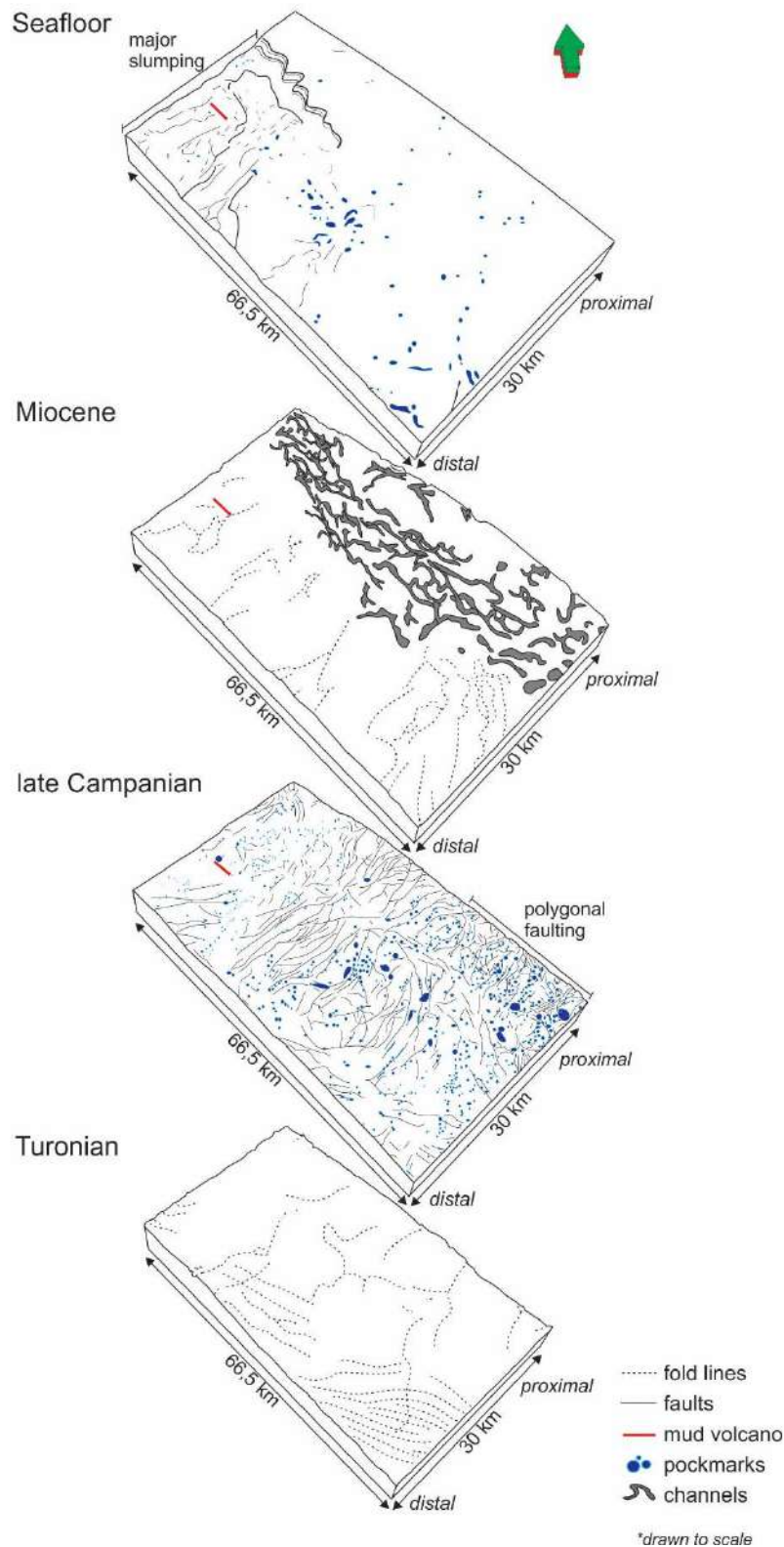


Figure 9.1 Schematic diagram of the deep-water Orange Basin illustrating the distribution and relationship of natural gas and fluid escape features observed in the study area. The Turonian shales are a thermogenic source rock interval. An explosive hydrocarbon expulsion event in the late Campanian created numerous pockmarks. The Miocene is a biogenic source rock interval and is marked by slope-parallel, sinuosoidal channels. An episodic release of hydrocarbons from the Miocene surface created pockmarks on the seafloor.

9.1.2.1 Pockmarked surfaces

a) Late Campanian

- Over 950 pockmarks are observed on the late Campanian surface (Figs. 4, 6-9; Maduna et al., 2023a) classified into three categories based on their shape and diameter: (1) giant pockmarks (>1 500 m in diameter) are linked to wide chimneys at depth arising from fault propagation folds and thrusts, (2) crater pockmarks (~700–900 m in diameter) are centrally located within postdating polygonal fault cells, and (3) simple pockmarks (<500 m in diameter) within giant pockmarks, as conjoined composite clusters, along fault surfaces, in linear belts unrelated to faulting, and otherwise random distributions. While only 8 giant and 20 crater pockmarks are observed on the paleo-surface, simple pockmarks are the most numerous with over 900 occurrences.
- The surfaces directly below and directly above the late Campanian do not show any pockmarks. The numerous distribution of pockmarks on this one surface is attributed to an explosive release of overpressurized fluids during the late Campanian triggered by faults arising from the DWFTB system. The source of hydrocarbons is thus likely from deep-seated thermogenic shales identified in the Aptian (unimaged in this study) (van der Spuy, 2003) and Turonian (Aldrich et al., 2003).

b) Present-day seafloor

- The present-day seafloor displays 85 pockmarks that are simple in morphology (Fig. 10; Maduna et al., 2023a). Most seafloor pockmarks are in the same vicinity or are aligned similarly to those on the buried late Campanian surface. Notably, there are no visible pipes or faults connecting the pockmarks between the late Campanian and seafloor surfaces (unless faults are below the seismic resolution limit). This suggests that the source of hydrocarbons on the seafloor is not from the same thermogenic source as the late Campanian. Seafloor pockmarks were likely formed from an episodic release of biogenic hydrocarbons arising from organic-rich Miocene sediments.

9.1.2.2 Polygonal faults

- The combination of compressional and extensional tectonics in the translational domain created a platform honeycombed pattern of faults (Fig. 6; Maduna et al., 2023a). These are known as polygonal faults formed by hydraulic fracturing in fine-grained hydrocarbon reservoirs (Henriet et al., 1991; Cartwright, 1994, 2007). Polygonal faults served as preferential fluid migration pathways contributing to the formation of concentric crater-like pockmarks on the late Campanian surface. These were referred to as “bull’s-eye” pockmarks by Andresen and Huuse (2011) because of their central location within polygonal fault cells (in planform) also seen in this research.

9.1.2.3 Mud volcano

- A 4.2 km long mud volcano occurs on the present-day seafloor postulated to have initially erupted (sedimentary volcanism) during the Santonian (Figs. 10, 11, and 12; Maduna et al., 2023a). Its shape and elongated morphology indicate that it is tectonically controlled (Mazzini and Etiope, 2017). The seismic data image its near-vertical vent to root from the Turonian shale detachment surface, and that it is situated along the axis of a large anticline marking the intersection of the translational domain and the compressional domain (Fig. 11; Maduna et al., 2023a).

- Mud volcanoes are indicative of extremely high rates of methane expulsion while pockmarks of moderate to high rates of methane expulsion (Roberts et al., 2006; Cartwright, 2007). The prevailing idea suggests that larger surface expressions of gas/fluid expulsion correlate with higher methane flux intensity. Methane flux intensity in the late Campanian is therefore shown to increase from the southeast to the northwest where the mud volcano is situated.

9.1.2.4 Mass flow products

- Mass flow processes formed a major slump system and smaller slides on the seafloor (Fig. 10; Maduna et al., 2023a). Although they are not natural gas and fluid escape features, they are closely related to them as hydrocarbons seeping to the seafloor affected the stability of Cenozoic to seafloor sediments. High methane expulsion rates associated with sedimentary volcanism led to major slumping on the seafloor forming a large slump system covering an area of $>26 \times 19$ km around the elongated mud volcano.
- Moderate to high methane expulsion rates forming seafloor pockmarks also affected the stability of surrounding sediments resulting in smaller slides. Features associated with the mass flow of sediment are triggered by events such as earthquakes, turbidity currents, or rapid changes in sedimentation rates (Rogers and Rau, 2006). The dynamics of mass flow processes can be highly complex, involving a combination of factors leading to sediment destabilization.

9.2 Seismic attributes and convolutional neural networks

Seismic attributes are invaluable in the exploration and production of hydrocarbons, particularly in deep-water settings where seismic data can be challenging to interpret. Seismic attributes played a crucial role in resolving and understanding the various features and structures described in the deep-water Orange Basin study. They are conventional techniques in seismic interpretation that enhance specific aspects of interest within the seismic dataset by applying various algorithms. While this approach remains effective in seismic interpretation software, the emergence of big data concepts has led a shift towards machine learning algorithms, particularly convolutional neural networks (CNNs), which can automatically detect features of interest. In this section, the seismic attributes applied to the seismic dataset are first briefly outlined (for more detailed descriptions, please refer to Chapter 4's Methodology). Edge-enhancing seismic attributes are then compared to a convolutional neural network's performance in interpreting the basin's fault framework system.

9.2.1 Seismic attributes

In the context of the deep-water research, seismic attributes have played a crucial role in resolving and interpreting features and structures that might have been otherwise difficult to distinguish. By applying various filters to the seismic dataset, these attributes highlighted the following aspects: (1) stratigraphic boundaries and faults, and (2) the potential hydrocarbon system.

9.2.1.1 Seismic attributes for stratigraphic and structural interpretation

- Structural smoothing was first applied to the full seismic volume to precondition the dataset. The structurally smoothed seismic volume was used as input for both the chaos and variance edge-

enhancement attributes, and the fault-net CNN. This full workflow is illustrated in Fig. 4 of Chapter 8 (Maduna et al., 2023b).

- Relative acoustic impedance was the volume-based seismic attribute applied to enhance the stratigraphy of seismic volume. Nine stratigraphic surfaces corresponding to major geological events along the SW African margin (Brown et al., 1995; PASA, 2017) were identified in the study (see Chapter 9.3).
- Surface-based attributes of confidence classification (applied to picked horizon interpretations), anomaly identifier, edge detection, and influential data were applied to the seismic volume seen in Chapter 6 (Maduna et al., 2022). They played a vital role in enhancing the stratigraphic interpretation process by detecting any anomalies and identifying geological boundaries related to faulting.

9.2.1.2 Seismic attributes for hydrocarbon exploration

- Specific volume-based attributes were used to interpret the hydrocarbon potential of deep-water study in Chapter 7 (Maduna et al., 2023a) including generalised spectral decomposition, envelope, sweetness, and the iterative root-mean-square amplitude. These are known as direct hydrocarbon indicators as they reveal the presence of hydrocarbons as positive high amplitude anomalies in seismic data.
- Positive high amplitude anomalies are predominantly concentrated in the central and southwest regions of the study area (Figs. 12 and 13; Maduna et al., 2023a). Notably, the most substantial hydrocarbon accumulation is in the region directly above a late Campanian anticline with the most extreme amplitudes. Surrounding this anticline, the area exhibits irregular and deformed pockmark shapes on both late Campanian and seafloor surfaces (Figs. 4 and 10; Maduna et al., 2023a). The anticline with the positive high amplitude anomaly is situated directly above the intersection of the translational domain and the compressional domain. It is further south of the elongated mud volcano that also occurs at the intersection of the two domains.

9.2.2 The comparison of edge-enhancement attributes with a fault-net CNN

Despite the effectiveness of seismic attributes, the field of seismic interpretation has undergone a transformation with the rise of big data concepts and advancements in machine learning. CNNs, a type of deep learning algorithm, have gained prominence due to their ability to automatically learn and recognize patterns from large datasets. In seismic interpretation, CNNs have demonstrated significant potential in automatically detecting and characterizing geological features. These algorithms excel at feature extraction and pattern recognition, making them well-suited for tasks such as fault detection, horizon picking, and seismic facies classification (Wu et al., 2019; An et al., 2021; Dou et al., 2022; Wei et al., 2022). In this research, conventional edge-enhancement attributes (variance and chaos) were compared to a CNN called fault-net (Dou et al., 2022) for detecting faults in the deep-water Orange Basin. Although both methods improve the understanding of structures in the subsurface, they each have their strengths and limitations described in Table 9.1.

9.2.2.1 Edge-enhancement seismic attributes

- Edge-enhancement seismic attributes are conventional techniques used in seismic interpretation to accentuate features with sharp changes or boundaries in seismic data and are therefore highly effective in delineating faults. The two edge-enhancement seismic attributes applied were of chaos and variance

following structural smoothing. Chaos highlights various features with chaotic textures, such as faults, channels, gas chimneys, and carbonates (Randen et al., 2001). Variance emphasizes regions with high variations in seismic amplitudes (Silva et al., 2005).

Table 9.1 The advantages and disadvantages of conventional edge-enhancement attributes (variance and chaos) compared to the fault-net convolutional neural network.

	Conventional edge-enhancement attributes	Fault-net convolutional neural network
<i>Advantages</i>	<ul style="list-style-type: none"> • Relatively straightforward in application and do not require extensive data training. • Enhances geological structures with complex orientations and shapes well. 	<ul style="list-style-type: none"> • Has the ability to learn and adapt to new data or complex relationships patterns from large volumes of labelled seismic data. • Offer a more automated, time-efficient approach without the subjectiveness arising from manual intervention. • Can handle seismic data with noise, distortions, and other artifacts resulting in cleaner and more accurate fault extraction outputs. • Fault output map is output together with the original seismic volume and so offset stratigraphic markers can be clearly seen. • Required less computation power
<i>Disadvantages</i>	<ul style="list-style-type: none"> • Limited to enhancing specific types of features (e.g., faults, channels) and are not as versatile in detecting other geological elements. • Do not effectively handle noise and other artifacts present in the seismic data, potentially leading to misinterpretations. • Requires a lot of manual intervention which is subjective and time-consuming. • Rule-based and lack the ability to learn and adapt to new data or complex relationships. • Fault displacements cannot be determined from the output volume alone as it does not include the stratigraphic information. • Required high computation power and long run times for the large dataset. 	<ul style="list-style-type: none"> • Fault segmentation requires a substantial amount of accurately labelled training data, which may be challenging to obtain, especially in large-scale regional studies. • Data training and designing the architecture demands expertise in data science and machine learning. • Struggles with the detection of small-scale faults or subtle features at depth, potentially requiring further model refinement and training.

9.2.1.2 Fault-net convolutional neural network

- CNNs are a class of deep learning algorithms widely used for image recognition and segmentation tasks. In seismic interpretation, CNNs have shown significant potential for automatically detecting and characterizing geological features.
- The approach employed in this research essentially adapts the fault-net method introduced by [Dou et al. \(2022\)](#), which represents an improvement over earlier CNN-based fault segmentation approaches ([Ronneberger et al., 2015](#); [Zhou et al., 2018](#); [Wang et al., 2020](#)).
- Both synthetic and real seismic data were utilized to train the fault-net CNN before preparing the 3D seismic volume for extracting faults. The synthetic data was generated based on the principles outlined in [Wu et al. \(2019\)](#), which effectively addressed the scarcity of training data for fault segmentation. After conditioning the seismic data through structural smoothing, the fault-net CNN was applied for extracting faults.

With regards to the Orange Basin's fault framework system (explained in the section below), the fault-net CNN applied validates the structural interpretations made using the chaos and variance edge-enhancement attributes. The transition towards machine learning-based approaches, like CNNs, has not replaced the use of seismic attributes but may rather complement them. Researchers and geoscientists now have access to a broader range of tools to tackle various challenges in seismic interpretation.

9.3 Evolution of the deep-water Orange Basin

The seismic volume images nine major stratigraphic surfaces representing significant geological events along the SW African margin ([Brown et al., 1995](#); [PASA, 2017](#)). These are the Late Cretaceous Albian (14At1), Turonian surface (15At1), Santonian (16Dt1), early Campanian (17At1), late Campanian (18At1), and Maastrichtian (22At1) surfaces; and the Cenozoic Oligocene, Miocene, and seafloor surfaces ([Table 4.8](#); [Fig. 4.18](#)). A conceptual model for the structural evolution of the deep-water Orange Basin was given in [Fig. 12 of Chapter 6 \(Maduna et al., 2022\)](#). The model is elaborated upon from the final structural model created shown in [Figs 4.19 and 4.20](#) of the methodology.

9.3.1 Late Cretaceous evolution

a) Albian–Turonian (~103–93 Ma)

- Between the late Albian to early Turonian, well-defined shelf, slope, and basinal depositional elements of the Orange Basin began to form during retrogradation ([Fig. 2.4](#); [Light et al., 1993](#); [Baby et al., 2018](#)). A progressively deepening basin with increased sedimentation rates is evidenced by gravitational collapse features between the Albian and Turonian shown in this research ([Figs. 6 and 12a](#); [Maduna et al., 2022](#)). These features are small-scale (~ 20 m wide folds) fold-and-thrust belts detaching the Albian surface at depth. They are situated in localized areas below the compressional domain of the kilometre-scale Late Cretaceous DWFTB system (described more in [point b](#)).
- The Turonian is one of the main surfaces of interest in this research as a regional scale DWFTB system, dominating the entirety of the Late Cretaceous succession seismically imaged, mostly detaches upon it

(Fig. 6; Maduna et al., 2022). The absence of the Turonian shale detachment surface in certain areas of the research is attributed to surface thinning as the overlying succession of sediment slid downslope during gravitational collapse (Fig. 8; Maduna et al., 2022). Turonian shales are known as a thermogenic source of hydrocarbon in the Orange Basin, together with the older Albian and deeper, unimaged Aptian shales (Aldrich et al., 2003; van der Spuy, 2003).

b) *Turonian–Santonian (~93–85 Ma)*

- All features and structures observed in the Late Cretaceous succession of this research are related to the up-dip translational and down-dip compressional domains of a gravitational collapse system along the continental slope (Figs. 5 and 6; Maduna et al., 2022). Analogue models such as the study of Cobbold and Szatmari (1991) and Wu et al. (2015) have been effective in investigating the formation of gravitational collapse systems. These models show that during gravitational collapse deltas spread radially outward forming an arcuate shape in plan view for delta tops (up-dip extensional domain) and toe thrusts (down-dip compressional domain). Toe thrusts are segmented by extensional shear (oblique-slip) faults formed within the translational domain (Wu et al., 2015).
- Gravitational sliding upon the Turonian shale detachment surface led to the remarkable formation of kilometre-scale fold-and-thrust belts in the distal regions of the Orange Basin which characterizes the compressional domain (Figs. 6 and 9; Maduna et al., 2022). The compressional domain is linked to the more proximal translational domain via extensive oblique-slip faults (Figs. 5 and 11; Maduna et al., 2022). The oblique-slip faults acted as lateral ramps segmenting thrust sheets along strike (mostly perpendicularly) to redistribute strain during sediment loading. Although the extent of the present dataset does not extend to the up-dip shelfal regions, other studies prove the existence of a proximal extensional domain characterized by listric growth faults (e.g., de Vera et al., 2010).
- A key observation made of the translational domain in this research is that it is a zone containing overprinted features of both extensional and compressional tectonics linked by oblique-slip tear faults (Figs. 5 and 11; Maduna et al., 2022). The 5% of missing strain observed between the extensional and compressional end member domains of DWFTB systems is likely found in the structurally complex translational domain supporting the observation of Dalton et al. (2017b) regarding internal strain redistribution. The slight to variable differences in the dip-slip and strike-slip components of oblique-slip faults (Figs. 5c and 7; Maduna et al., 2022) implies a syn-kinematic relationship of sedimentation with faulting to redistribute strain. The arcuate shape of the fault framework in plan view and their clockwise change in strike (SE–SW–NW–NE) from south to north (Fig. 5b) are an exemplary, real-world example of gravitational collapse through radial spreading observed in analogue models (Cobbold and Szatmari, 1991; Wu et al., 2015).
- In Dalton et al. (2017a) Orange Basin study, deformation to create fold-and-thrust belts in stratigraphically older sequences is modelled to postdate deformation of the stratigraphically younger sequence. This is a plausible scenario whereby progressive up-dip extension forced listric growth faults to propagate downwards onto a stratigraphically lower detachment surface for the redistribution of strain, which in turn led to distal down-dip compression on a lower detachment surface. In this research, however, that scenario cannot be concluded upon as the extensional domain of the DWFTB system is not imaged in the seismic dataset. A second scenario proposed here is that the underlying Albian–

Turonian fold-and-thrust belts pre-date the larger, kilometre-scale fold-and-thrust belts as is the case for Australian Ceduna sub-basin (Ahmed et al., 2022). The second scenario proposed is based on the fact that the structural styles of these two fold-and-thrust belt systems are not exactly the same; the Albian–Turonian fold-and-thrust belts only occur in localized areas and are smaller in height and fold spacing due to the small supply of sediment to the basin (compared to later times in the Late Cretaceous). There furthermore appears to be evidence of crosscutting relationships supporting the second scenario. This remains speculative, however, and has not been discussed in this research as the seismic resolution of features within the Albian–Turonian sequence is too low to effectively investigate.

c) *Santonian–Maastrichtian (~85–67 Ma)*

- Deformation by downslope gravitational collapse ended in the early Campanian proven by the change in fold geometry between the Santonian and late Campanian sequences. Thrust faults of the DWFTB system terminated around the early to late Campanian, while normal and oblique-slip faults of the proximal translational domain were reactivated terminating in younger Cenozoic sequences. The intricate fault framework system of the Late Cretaceous DWFTB system provided essential pathways for the migration of hydrocarbons from the Turonian source rock to the reservoir rocks above, eventually becoming structurally trapped and accumulating within anticlines.
- An elongated mud volcano emerged during the Santonian separating the two domains observed and has remained active till present. During the late Campanian a major gas and fluid expulsion event occurred forming widespread pockmarks on the paleo-seafloor. Along the same anticlinal ridge where the mud volcano formed furtherer south, hydrocarbons accumulated in a late Campanian anticline imaged as a positive high amplitude anomaly in the seismic volume. Mud volcanism and late Campanian pockmark formation, coinciding with the Turonian interval’s oil maturation window according to Hirsch et al. (2010), were triggered by fault reactivation during progressive gravitational collapse and contraction.
- The Maastrichtian marks the end of the Late Cretaceous and beginning of the Cenozoic. In this work, the thick surface is shown to separate underlying Late Cretaceous progradational sequences from the overlying Cenozoic retrogradational sequences.

9.3.2 Cenozoic evolution

d) *Oligocene (~30–25 Ma)*

- Canyoning in the Oligocene was caused by a major sea-level fall recognised along the SW African margin from continental uplift (Siesser and Dingle, 1981; Séranne and Anka, 2005). Sediments were eroded by downslope turbidity currents to form a large slope-perpendicular canyon cutting Oligocene right down to the Maastrichtian strata.

e) *Miocene (~12–10 Ma)*

- The influence of newly formed ocean currents started to play a vital role in the erosional and depositional systems of the Orange Basin from the Miocene. The formation of the opposite-flowing North Atlantic Deep Water and Antarctic Bottom Water bottom currents (Weigelt and Uenzelmann-Neben, 2004) formed slope-parallel, sinusoidal channels at the interface of the two bottom currents observed on the Miocene surface (Fig. 9.1). The preservation of the sinusoidal channels was aided by the intensification of the Benguela Upwelling System at ~11 Ma together with an arid climate decreasing sediment supply

offshore (Diester-Haass et al., 2004; Rommerskirchen et al., 2011). Organic-rich sediments from the upwelling system are a likely biogenic source of hydrocarbons for the natural gas and fluid escape features observed on the seafloor.

f) *Miocene–present (~12–0 Ma)*

- Slope instability formed a large slump scar and slides on the seafloor with their base within Oligocene to Miocene sediments. These mass wasting features are associated with the migration of fluid and/or gas to the seafloor. The slump scar reflects the underlying extent of sediment remobilization in the region of the elongated mud volcano imaged in the study. Another smaller gas and fluid expulsion event occurred resulting in pockmarks on the seafloor which occur together with slides. Vast economic hydrocarbon reservoirs in the deep-water Orange Basin are indicated by the extensive presence and wide distribution of all these natural gas and fluid escape features.

9.4 Future considerations and recommendations

Additional research is required with more high-resolution seismic sections including imagery of the proximal extensional domain of the Late Cretaceous DWFTB system identified in this research. Drilling is recommended in the South African deep-water region of the Orange Basin, particularly in regions displaying positive high amplitude anomalies, to validate the presence of hydrocarbons and evaluate the economical prospectivity of the basin. A comprehensive geochemical study is required that includes biomarker and stable isotope analyses, and fluid inclusion studies to distinguish between thermogenic and biogenic hydrocarbons. Understanding the temporal and spatial evolution of gravitational collapse and natural gas and fluid escape features in the Orange Basin requires a multidisciplinary approach, combining geological, geophysical, and geochemical data. The combination of high-resolution seismic surveys, borehole data, and core samples are crucial for thoroughly reconstructing the geological history of the Orange Basin. These comprehensive datasets are indispensable for evaluating the region's potentially abundant hydrocarbon systems.

For deep-learning, as CNNs are known to excel not only in pattern recognition but also in feature extraction, an improvement of the fault-net CNN would be the ability to extract and export only the fault patches in 3D with x, y, and z coordinates readable in other hydrocarbon or mineral exploration software. Currently, the CNN outputs fault images upon the original input seismic volume which is not useable in other software formats. In addition to this, the fault-net algorithm may be further improved in its effectiveness by reducing the time required for model training. This may be shortened from a few days to a few hours, minutes, and eventually possibly even a few seconds.

10 Concluding remarks

All depositional elements observed in the deep-water Orange Basin study were created by the interplay and change in tectonic, climatic, and oceanographic regimes affecting the southwest African passive margin between the Mesozoic's Late Cretaceous to Cenozoic. The deep-water Orange Basin's evolutionary model may serve multiple purposes, as it can be used as (a) an analogue to enhance comprehension of the structural interpretation of DWFTB systems on a global scale, (b) a significant example of how oceanographic circulation and climate impacted mid-Cenozoic sedimentation, and (c) compelling evidence that substantial economic hydrocarbon reservoirs within the basin remain untapped and await exploitation. The following conclusions are drawn from each aspect:

- a) Prior to this research, there was a scarcity of data for tectonics within the translational domain of DWFTB systems not only in the Orange Basin, but also worldwide. This is due to the domain's structural complexity which was often poorly resolved using spatially insufficient 2D and lower resolution 3D reflection seismic data. Translational tectonics are a gradual transition of proximal normal faulting (extensional tectonics) to distal thrust faulting (compressional tectonics) accommodated by oblique-slip faulting segmenting thrust sheets along strike all the way into the down-dip compressional domain.
- b) Sedimentation patterns in the Miocene were strongly controlled by the change in oceanographic circulation offshore southwest Africa changing climatic conditions and driving upwelling. Sinusoidal channel-like features orientated parallel to the margin were formed by the erosive interaction of the concurrent, opposite-flowing North Atlantic Deep Water and Antarctic Intermediate Water Ocean currents coinciding with the intensification of the Benguela Upwelling System.
- c) Alongside the active shelfal hydrocarbon systems and promising deep-water discoveries in Namibia, the extensive presence of natural gas and fluid escape features identified in this research serves as evidence for a highly productive hydrocarbon plumbing system in action. Significant natural gas and fluid escape features include pockmarked surfaces (late Campanian and seafloor surfaces), an elongated mud volcano, and a Late Campanian anticline with a positive high amplitude anomaly.
- d) The application of seismic attributes to the research enhanced the overall accuracy and precision of the final geological model generated. Numerous structural and stratigraphic features that may have otherwise been missed in the original seismic volume, were enhanced by the application of volume- and surface-based seismic attributes.
- e) The application of the fault-net CNN as a tool for fault extraction presents a promising machine learning approach in interpreting reflection seismic data. Some key benefits of using the CNN include automation, faster analysis, and the ability to handle massive datasets more efficiently than relying solely on conventional seismic attributes. By leveraging both the CNN approach and traditional seismic attributes in seismic data interpretation, geoscientists can make better-informed decisions in hydrocarbon exploration and reservoir management. This integration of cutting-edge technology and established methods holds the potential to significantly improve the accuracy and productivity of geological analysis, ultimately leading to more successful exploration and production outcomes.

11 References

- Aizawa, M, Bluck, B, Cartwright, J, Milner, S, Swart, R, and Ward, J (2000) Constraints on the geomorphological evolution of Namibia from the offshore stratigraphic record. *Communications of the Geological Survey of Namibia* 12(2000): 337–346
- Ahmed, B, McClay, K, Scarselli, N, and Bilal, A (2022) New insights on the gravity-driven deformation of late Albian–early Turonian stacked delta collapse systems in the Ceduna sub-basin, Bight Basin, southern margin of Australia. *Tectonophysics* 823, p.229184. <https://doi.org/10.1016/j.tecto.2021.229184>.
- Aldrich, J, Zilinski, R, Edman, J, Leu, W, Berge, T and Corbett, K (2003) Documentation of a new petroleum system in the South Atlantic. In *American Association of Petroleum Geologists Annual Convention Salt Lake City*, p. 90013
- An, Y, Guo, J, Ye, Q, Childs, C, Walsh, J, Dong, R (2021) Deep convolutional neural network for automatic fault recognition from 3D seismic datasets. *Computers and Geosciences* 153: 104776. <https://doi.org/10.1016/j.cageo.2021.104776>
- Baby, G, Guillocheau, F, Morin, J, Ressouche, J, Robin, C, Broucke, O, and Dall’Asta, M (2018) Post-rift stratigraphic evolution of the Atlantic margin of Namibia and South Africa: Implications for the vertical movements of the margin and the uplift history of the South African Plateau. *Marine Petroleum Geology* 97: 169–191. <https://doi.org/10.1016/j.marpetgeo.2018.06.030>
- Baby, G, Guillocheau, F, Braun, J, Robin, C and Dall’Asta, M (2020) Solid sedimentation rates history of the Southern African continental margins: Implications for the uplift history of the South African Plateau. *Terra Nova* 32: 53-65. <https://doi.org/10.1111/ter.12435>
- Barnes, AE (2016) *Handbook of Poststack Seismic Attributes*, Society of Exploration Geophysicists 21, 268 p. <https://doi.org/10.1190/1.9781560803324>
- Ben-Avraham, Z, Smith, G, Reshef, M and Jungslager, E (2002) Gas hydrate and mud volcanoes on the southwest African continental margin off South Africa. *Geology* 30(10): 927-930. [https://doi.org/10.1130/0091-7613\(2002\)030<0927:GHAMVO>2.0.CO;2](https://doi.org/10.1130/0091-7613(2002)030<0927:GHAMVO>2.0.CO;2)
- Boyd, D, Anka, Z, di Primio, R., Kuhlmann, G and De Wit, MJ (2011) Passive margin evolution and controls on natural gas leakage in the Orange Basin, South Africa. *South African Journal of Geology* 114(3–4): 415-432. <https://doi.org/10.2113/gssajg.114.3-4.415>
- Brown, AR (2011) Interpretation of three-dimensional seismic data. *American Association of Petroleum Geologists and Society of Exploration Geophysicists, Tulsa, Oklahoma, USA*, 646
- Brown, LF, Benson, JM, Brink, GJ, Doherty, S, Jollands, A, Jungslager, EAH, Keenan, JHG, Muntingh, A, and van Wyk, NJS (1995) *Sequence Stratigraphy in Offshore South African Divergent Basins: An Atlas on Exploration for Cretaceous Lowstand Traps by Soekor (Pty) Ltd.* American Association of Petroleum Geologists Studies in Geology 41, 191 p.
- Brown, R, Summerfield, M, Gleadow, A, Gallagher, K, Carter, A, Beucher, R, and Wildman, M (2014) Intracontinental deformation in southern Africa during the Late Cretaceous, *Journal of African Earth Sciences* 100: 20–41
- Butler, RWH and Paton, DA (2010) Evaluating lateral compaction in deepwater fold and thrust belts: How much are we missing from “nature’s sandbox”? *GSA Today* 20(3): 4–10, <https://doi.org/10.1130/GSATG77A.1>
- Cartwright, J, Huuse, M and Aplin, A (2007) Seal bypass systems. *American Association of Petroleum Geologists Studies Bulletin* 91(8): 1141-1166. <https://doi.org/10.1306/04090705181>
- Catuneanu, O (2002) Sequence stratigraphy of clastic systems: concepts, merits, and pitfalls. *Journal of African Earth Sciences*, 35(1): 1-43. [https://doi.org/10.1016/S0899-5362\(02\)00004-0](https://doi.org/10.1016/S0899-5362(02)00004-0)
- Catuneanu, O (2006) *Principles of Sequence Stratigraphy*, Elsevier, Amsterdam, p. 375

- Catuneanu, O, Abreu, V, Bhattacharya, JP, Blum, MD, Dalrymple, RW, Eriksson, PG, Fielding, CR, Fisher, WL, Galloway, WE, Gibling, MR, Giles, KA, Holbrook, JM, Jordan, R, Kendall, CGSC, Macurda, B, Martinsen, OJ, Miall, AD, Neal, JE, Nummedal, D, Pomar, L, Posamentier, HW, Pratt, BR, Sarg, JF, Shanley, KW, Steel, RJ, Strasser, A, Tucker, ME, Winker, C (2009) Towards the standardization of sequence stratigraphy. *Earth-Science Reviews*, 92(1-2) : 1–33. <http://dx.doi.org/10.1016/j.earscirev.2008.10.003>
- Chopra, S and Marfurt, KJ (2005) Seismic attributes — A historical perspective. *Geophysics* 70: 3SO-28SO. <https://doi.org/10.1190/1.2098670>
- Chopra, S and Marfurt, KJ (2007) Seismic Attributes for Prospect Identification and Reservoir Characterization. Society of Exploration Geophysicists and European Association of Geoscientists and Engineers 481. <https://doi.org/10.1190/1.9781560801900>.
- Clemson, J, Cartwright, J, and Booth, J (1997) Structural segmentation and the influence of basement structure on the Namibian passive margin. *Journal of the Geological Society*, 154(3): 477–482. <https://doi.org/10.1144/gsjgs.154.3.0477>
- Cobbold, PR and Szatmari, P (1991) Radial gravitational gliding on passive margins. *Tectonophysics*, 188(3-4): 249-289. [https://doi.org/10.1016/0040-1951\(91\)90459-6](https://doi.org/10.1016/0040-1951(91)90459-6)
- Compton, JS and Wiltshire, JG (2009) Terrigenous sediment export from the western margin of South Africa on glacial to interglacial cycles. *Marine Geology*, 266(1-4): 212–222. <https://doi.org/10.1016/j.margeo.2009.08.013>
- Corredor, F, Shaw, JH, and Bilotti, F (2005) Structural styles in the deep-water fold and thrust belts of the Niger Delta. *American Association of Petroleum Geologists Bulletin* 89(6): 753–780. <https://doi.org/10.1306/02170504074>
- Dalton, TJS, Paton, Douglas A, Needham, T, and Hodgson, N (2015) Temporal and spatial evolution of deepwater fold thrust belts: Implications for quantifying strain imbalance. *Interpretation* 3: SAA59–SAA70. <https://doi.org/10.1190/INT-2015-0034.1>
- Dalton, TJS, Paton, DA, and Needham, DT (2017) Influence of mechanical stratigraphy on multi-layer gravity collapse structures: insights from the Orange Basin, South Africa. *Geological Society, London, Special Publications*, 438(1): 211–228. <https://doi.org/10.1144/SP4384>
- Dalton, TJS, Paton, DA, Oldfield, SJ, Needham, DT and Wood, AM (2017) The importance of missing strain in deep water fold and thrust belts. *Marine and Petroleum Geology* 82: 163-177. <https://doi.org/10.1016/j.marpetgeo.2017.01.013>
- de Vera, J, Granado, P, and McClay, K (2010) Structural evolution of the Orange Basin gravity-driven system, offshore Namibia. *Marine and Petroleum Geology* 27(1): 223–237. <https://doi.org/10.1016/j.marpetgeo.2009.02.003>
- Diester-Haass, L, Meyers, PA and Rothe, P (1992) The Benguela Current and associated upwelling on the southwest African Margin: a synthesis of the Neogene-Quaternary sedimentary record at DSDP sites 362 and 532. *Geological Society, London, Special Publications* 64(1): 331-342. <https://doi.org/10.1144/GSL.SP.1992.064.01.22>
- Diester-Haass, L, Meyers, PA, and Bickert, T (2004) Carbonate crash and biogenic bloom in the late Miocene: Evidence from ODP Sites 1085, 1086, and 1087 in the Cape Basin, southeast Atlantic Ocean. *Paleoceanography* 19. <https://doi.org/10.1029/2003PA000933>
- Dondurur, D (2018). *Acquisition and processing of marine seismic data*. Elsevier.
- Dou, Y, Li, K, Zhu, J, Li, T, Tan, S, and Huang, Z (2022) MD Loss: Efficient Training of 3-D Seismic Fault Segmentation Network Under Sparse Labels by Weakening Anomaly Annotation. *IEEE Transactions on Geoscience and Remote Sensing* 60: 1-14. <https://doi.org/10.1109/TGRS.2022.3196810>
- Gay, A, Lopez, M, Cochonat, P, Sultan, N, Cauquil, E and Brigaud, F (2003) Sinuous pockmark belt as indicator of a shallow buried turbiditic channel on the lower slope of the Congo Basin, West African Margin. *Geological Society, London, Special Publications* 216(1): 173-189. <https://doi.org/10.1144/GSL.SP.2003.216.01.12>

- Granado, P, Vera, JD, and McClay, KR (2009) Tectonostratigraphic evolution of the Orange Basin, SW Africa, *Trabajos de geología*, 29
- Hartwig, A, Anka, Z, and di Primio, R (2012) Evidence of a widespread paleo-pockmarked field in the Orange Basin: An indication of an early Eocene massive fluid escape event offshore South Africa. *Marine Geology* 332–334: 222–234. <https://doi.org/10.1016/j.margeo.2012.07.012>
- Herron, DA (2011) Resolution. In: Latimer, R.B. (Ed.), *First steps in seismic interpretation*. Society of exploration geophysicists, Tulsa, pp. 75–82.
- Ho, S., Cartwright, J.A. and Imbert, P. (2012) Vertical evolution of fluid venting structures in relation to gas flux, in the Neogene-Quaternary of the Lower Congo Basin, Offshore Angola. *Marine Geology* 332: 40-55. <https://doi.org/10.1016/j.margeo.2012.08.011>
- Holtar, E and Forsberg, AW (2000) Postrift development of the Walvis Basin, Namibia: results for the exploration campaign in quadrant 1911. In: *Petroleum Systems of South Atlantic Margins*. American Association of Petroleum Geologists *Memoirs* 73: 429–446.
- Hustoft, S, Bünz, S and Mienert, J, (2010) Three-dimensional seismic analysis of the morphology and spatial distribution of chimneys beneath the Nyegga pockmark field, offshore mid-Norway. *Basin Research* 22(4):465-480. <https://doi.org/10.1111/j.1365-2117.2010.00486.x>
- Jungslager, EH (1999) Petroleum habitats of the Atlantic margin of South Africa. Geological Society, London, *Special Publications* 153(1): 153–168. <https://doi.org/10.1144/GSL.SP.1999.153.01.10>
- King, RC and Morley, CK (2017) Wedge geometry and detachment strength in deepwater fold-thrust belts. *Earth-Science Reviews* 165: 268–279. <https://doi.org/10.1016/j.earscirev.2016.12.012>
- Koopmann, H, Schreckenberger, B, Franke, D, Becker, K and Schnabel, M (2016) The late rifting phase and continental break-up of the southern South Atlantic: the mode and timing of volcanic rifting and formation of earliest oceanic crust. Geological Society, London, *Special Publications* 420(1): 315-340. <https://doi.org/10.1144/SP420.2>
- Koson, S, Chenrai, P and Choowong, M (2014) Seismic attributes and their applications in seismic geomorphology. *Bulletin of Earth Sciences of Thailand* 6(1): 1-9.
- Kramer EAJ, Heck L (2014) Orange Basin 3D Pre-processing and preSDM 2013 Shell Global Solutions International BV, Netherlands, Risjswijk
- Krueger, A and Gilbert, E (2009) Deepwater fold-thrust belts: Not all the beasts are equal. *American Association of Petroleum Geologists Search and Discovery Article* 30085. <https://www.searchanddiscovery.com/documents/2009/30085krueger/index.htm> (last access: 9 November 2022)
- Kuhlmann, G, Adams, S, Campher, C, van der Spuy, D, di Primio, R, and Horsfield, B (2010) Passive margin evolution and its controls on natural gas leakage in the southern Orange Basin, blocks 3/4, offshore South Africa. *Marine Petroleum Geology* 27(4): 973–992. <https://doi.org/10.1016/j.marpetgeo.2010.01.010>
- Lebedeva-Ivanova, N, Polteau, S, Bellwald, B, Planke, S, Berndt, C, Stokke, HH (2018). Toward one-meter resolution in 3D seismic. *Leading Edge* 37(11): 818–828. <https://doi.org/10.1190/tle37110818.1>
- Levell, B, Argent, J, Doré, AG and Fraser, S (2010) Passive margins: overview. In *Petroleum Geology: From Mature Basins to New Frontiers – Proceedings of the 7th Petroleum Geology Conference*. Geological Society of London 7(1): 823–830. <https://doi.org/10.1144/0070823>
- Light, MPR, Maslanyj, MP, Greenwood, RJ, and Banks, NL (1993) Seismic sequence stratigraphy and tectonics offshore Namibia. Geological Society of London *Special Publications* 71(1): 163–191. <https://doi.org/10.1144/GSL.SP.1993.071.01.08>
- Maduna, NG, Manzi, MS, Jinnah, Z and Bourdeau, JE (2022) Strato-structural evolution of the deep-water Orange Basin: constraints from 3D reflection seismic data. *Solid Earth* 13(1): 1755-1780. <https://doi.org/10.5194/se-13-1755-2022>

- Maduna, NG, Manzi, MSD, Bourdeau, JE and Jinnah, Z (2023) 3D reflection seismic imaging of natural gas/fluid escape features in the deep-water Orange Basin of South Africa. *Marine Geophysical Research* 44(17):1–28. <https://doi.org/10.1007/s11001-023-09523-2>
- Maduna, NG, Manzi, MSD, Nwaila, G, Zhang, SE, Bourdeau, JE and Jinnah, Z (2023) A novel approach to fault interpretation using a convolutional neural network: a case study of the deep-water Orange Basin, South Africa. Manuscript submitted for publication.
- Mahlalela, V, Manzi, MSD, Jinnah, Z, Bourdeau, JE, and Durrheim, RJ (2021) Structural characteristics and 3D seismic detection of gas migration pathways in the deep-water Orange Basin, South Africa. *Marine Geophysical Research* 42:1–17. <https://doi.org/10.1007/s11001-021-09428-y>
- Manzi, MSD, Hein, KAA, King, N, and Durrheim, RJ (2013) Neoproterozoic tectonic history of the Witwatersrand Basin and Ventersdorp Supergroup: New constraints from high-resolution 3D seismic reflection data. *Tectonophysics* 590: 94–105. <https://doi.org/10.1016/j.tecto.2013.01.014>
- Maselli, V, Kneller, B, Taiwo, OL, and Iacopini, D (2019) Sea floor bedforms and their influence on slope accommodation. *Marine Petroleum Geologists* 102: 625–637. <https://doi.org/10.1016/j.marpetgeo.2019.01.021>
- Maslanyj, MP, Light, MPR, Greenwood, RJ, and Banks, NL (1992) Extension tectonics offshore Namibia and evidence for passive rifting in the South Atlantic. *Marine Petroleum Geology* 9(6): 590–601. [https://doi.org/10.1016/0264-8172\(92\)90032-A](https://doi.org/10.1016/0264-8172(92)90032-A)
- Mazzini, A, Nermoen, A, Krotkiewski, M, Podladchikov, Y, Planke, S, Svensen, H (2009) Strike-slip faulting as a trigger mechanism for overpressure release through piercement structures. Implications for the Lusi mud volcano, Indonesia. *Marine Petroleum Geology* 26(9): 1751–1765 <https://doi.org/10.1016/j.marpetgeo.2009.03.001>
- Menzies, MA, Klemperer, SL, Ebinger, CJ, and Baker, J (2002) Characteristics of volcanic rifted margins, in: *Volcanic Rifted Margins*. Geological Society of America Special Paper 362: 1–14. <https://doi.org/10.1130/0-8137-2362-0.1>
- Miller, DE, Yates, RJ, Jerardino, A, and Parkington, JE (1995) Late Holocene coastal change in the southwestern Cape, South Africa. *Quaternary International* 29–30: 3–10. [https://doi.org/10.1016/1040-6182\(95\)00002-Z](https://doi.org/10.1016/1040-6182(95)00002-Z)
- Miller, KG, Kominz, MA, Browning, JV, Wright, JD, Mountain, GS, Katz, ME, Sugarman, PJ, Cramer, BS, Christie-Blick, N and Pekar, SF (2005) The Phanerozoic record of global sea-level change. *Science* 310(5752): 1293–1298. <https://doi.org/10.1126/science.1116412>
- Miller, RM (2008) *The Geology of Namibia: Upper Palaeozoic to Cenozoic*. Ministry of Mines and Energy, Geological Survey Namibia 3: 1600 p.
- Mitchum, RM, Vail, PR, Thompson, S (1977) Seismic stratigraphy and global changes of sea level: Part 2. The depositional sequence as a basic unit for stratigraphic analysis: Section 2. Application of seismic reflection configuration to stratigraphic interpretation. *American Association of Petroleum Geologists Memoir* 53–62
- Mohammed, M, Paton, D, Collier, REL, Hodgson, N, and Negonga, M (2017) Interaction of crustal heterogeneity and lithospheric processes in determining passive margin architecture on the southern Namibian margin. Geological Society, London, Special Publications 438(1): 177–193. <https://doi.org/10.1144/SP438.9>
- Morley, CK, King, R, Hillis, R, Tingay, M, and Backe, G (2011) Deepwater fold and thrust belt classification, tectonics, structure and hydrocarbon prospectivity: A review. *Earth-Science Reviews* 104(1–3): 41–91. <https://doi.org/10.1016/j.earscirev.2010.09.010>
- Palan, K, Green, AN, Andrews, B, Sink, K and Wiles, EA (2020) A morphometric analysis of the fluid flow features of the southern Orange Basin, South Africa. *Marine Geology* 423: 14 pp. <https://doi.org/10.1016/j.margeo.2020.106145>
- Paton, DA, di Primio, R, Kuhlmann, G, van der Spuy, D, and Horsfield, B (2007) Insights into the Petroleum System Evolution of the southern Orange Basin, South Africa. *South African Journal of Geology* 110(2–3): 261–274. <https://doi.org/10.2113/gssajg.110.2-3.261>

- Paton, DA, van der Spuy, D, di Primio, R, and Horsfield, B (2008) Tectonically induced adjustment of passive-margin accommodation space; influence on the hydrocarbon potential of the Orange Basin, South Africa. *American Association of Petroleum Geologists Bulletin* 92(5): 589–609. <https://doi.org/10.1306/12280707023>
- Pepper, AS and Corvi, PJ (1995) Simple kinetic models of petroleum formation. Part I: oil and gas generation from kerogen. *Marine Petroleum Geology* 12(3):291-319. [https://doi.org/10.1016/0264-8172\(95\)98381-E](https://doi.org/10.1016/0264-8172(95)98381-E)
- Peterson, RG and Stramma, L (1991) Upper-level circulation in the South Atlantic Ocean. *Progress in Oceanography* 26(1): 1–73. [https://doi.org/10.1016/0079-6611\(91\)90006-8](https://doi.org/10.1016/0079-6611(91)90006-8)
- Petroleum Agency South Africa (PASA) (2017) Information and opportunities, Petroleum Agency South Africa, Cape Town, South Africa. https://www.petroleumagencysa.com/images/pdfs/Pet_expl_opp_broch_2017bw1.pdf (last access: 9 November 2022)
- Pretorius, I, Piketh, SJ and Burger, RP (2015) The impact of the South African energy crisis on emissions. *WIT Transactions on Ecology and the Environment* 198:255-264
- Randen, T, Monsen, E, Signer, C, Abrahamsen, A, Hansen, J O, Sæter, T, and Schlaf, J (2000) Three-dimensional texture attributes for seismic data analysis, in: *SEG Technical Program Expanded Abstracts 2000*, SEG Technical Program Expanded Abstracts 2000: 668–671. <https://doi.org/10.1190/1.1816155>
- Rogers, J and Rau, A (2006) Surficial sediments of the wave-dominated Orange River Delta and the adjacent continental margin off south-western Africa. *African Journal of Marine Science* 28(3-4): 511–524. <https://doi.org/10.2989/18142320609504202>
- Rommerskirchen, F, Condon, T, Mollenhauer, G, Dupont, L, Schefuß, E (2011) Miocene to Pliocene development of surface and subsurface temperatures in the Benguela Current system. *Paleoceanography* 26(3): 1–15. <https://doi.org/10.1029/2010PA002074>
- Ronneberger, O, Fischer, P, and Brox, T (2015) U-net: Convolutional networks for biomedical image segmentation. In *International Conference on Medical Image Computing and Computer-Assisted Intervention*. Springer, pp. 234-241. https://doi.org/10.1007/978-3-319-24574-4_28
- Rowan, MG, Peel, FJ, and Vendeville, BC (2004) Gravity-driven fold belts on passive margins, in K R McClay, ed, *Thrust tectonics and hydrocarbon systems*. American Association of Petroleum Geologists Bulletin 82: 157–182. <https://doi.org/10.1306/61EECE28-173E-11D7-8645000102C1865D>
- Séranne, M and Anka, Z (2005) South Atlantic continental margins of Africa: A comparison of the tectonic vs climate interplay on the evolution of equatorial west Africa and SW Africa margins. *Journal of African Earth Sciences* 43(1-3): 283–300. <https://doi.org/10.1016/j.jafrearsci.2005.07.010>
- Silva, CC, Marcolino, CS, and Lima, FD (2005): Automatic fault extraction using ant tracking algorithm in the Marlim South Field, Campos Basin. Paper presented at the 2005 SEG Annual Meeting, Houston, Texas, 6–11 November 2005, pp. 857–860. <https://doi.org/10.1190/1.2148294>
- Spicer, RA and Corfield, RM (1992) A review of terrestrial and marine climates in the Cretaceous with implications for modelling the ‘Greenhouse Earth’. *Geological Magazine* 129(2): 169-180. <https://doi.org/10.1017/S0016756800008268>
- Uenzelmann-Neben, G, Tobias, W, Gruetzner, J, Maik, T (2017) Transition from the Cretaceous Ocean to Cenozoic circulation in the western South Atlantic— a twofold reconstruction. *Tectonophysics* 716: 22–240. <http://dx.doi.org/10.1016/j.tecto.2016.05.036>
- van der Spuy, D (2003) Aptian source rocks in some South African Cretaceous basins. *Geological Society, London, Special Publications* 207(1): 185–202. <https://doi.org/10.1144/GSL.SP.2003.207.10>
- van der Spuy, D, and Sayidini, B (2022) Offshore Namibia discovery signals bright future for South Africa oil and gas. *American Association of Petroleum Geologists Explorer*. <https://explorer.aapg.org/story/articleid/62613/offshore-namibia-discovery-signals-bright-future-for-south-africa-oil-and-gas>, last access: 31 March 2022

- Viola, G, Andreoli, M, Ben-Avraham, Z, Stengel, I, Reshef, M (2005) Offshore mud volcanoes and onland faulting in southwestern Africa: neotectonic implications and constraints on the regional stress field. *Earth and Planetary Science Letters* 231(1-2): 147–160. <https://doi.org/10.1016/j.epsl.2004.12.001>
- Viola, G, Kounov, A, Andreoli, MAG and Mattila, J (2012) Brittle tectonic evolution along the western margin of South Africa: more than 500 Myr of continued reactivation. *Tectonophysics* 514: 93-114. <https://doi.org/10.1016/j.tecto.2011.10.009>
- Wang, J, Sun, K, Cheng, T, Jiang, B, Deng, C, Zhao, Y, Liu, D, Mu, Y, Tan, M, Wang, X, and Liu, W (2020) Deep high-resolution representation learning for visual recognition. *IEEE transactions on pattern analysis and machine intelligence* 43(10):3349-3364. <https://doi.org/10.1109/TPAMI.2020.2983686>
- Wei, XL, Zhang, CX, Kim, SW, Jing, KL, Wang, YJ, Xu, S, and Xie, ZZ (2022) Seismic fault detection using convolutional neural networks with focal loss. *Computers and Geosciences* 158: 104968. <https://doi.org/10.1016/j.cageo.2021.104968>
- Weigelt, E, and Uenzelmann-Neben, G (2004) Sediment deposits in the Cape Basin: Indications for shifting ocean currents?. *American Association of Petroleum Geologists Bulletin* 88(6): 765–780. <https://doi.org/10.1306/01260403101>
- Weigelt, E and Uenzelmann-Neben, G (2007a) Early Pliocene change of deposition style in the Cape Basin, southeastern Atlantic. *Geological Society of America Bulletin* 119(7–8): 1004–1013. <https://doi.org/10.1130/B26110.1>
- Weigelt, E and Uenzelmann-Neben, G (2007b) Orbital forced cyclicity of reflector strength in the seismic records of the Cape Basin. *Geophysics Research Letters* 34(1). <https://doi.org/10.1029/2006GL028376>
- Wigley, RA and Compton, JS (2006) Late Cenozoic evolution of the outer continental shelf at the head of the Cape Canyon, South Africa. *Marine Geology* 226(1–2): 1–23. <https://doi.org/10.1016/j.margeo.2005.09.015>
- Wildman, M, Brown, R, Watkins, R, Carter, A, Gleadow, A, and Summerfield, M (2015) Post break-up tectonic inversion across the southwestern cape of South Africa: New insights from apatite and zircon fission track thermochronometry. *Tectonophysics* 654: 30–55. <https://doi.org/10.1016/j.tecto.2015.04.012>
- Wu, JE, McClay, K and Frankowicz, E (2015) Niger Delta gravity-driven deformation above the relict Chain and Charcot oceanic fracture zones, Gulf of Guinea: Insights from analogue models. *Marine and Petroleum Geology* 65: 43-62. <https://doi.org/10.1016/j.marpetgeo.2015.03.008>
- Wu, X, Liang, L, Shi, Y, Fomel, S (2019) FaultSeg3D: Using synthetic data sets to train an end-to-end convolutional neural network for 3D seismic fault segmentation. *Geophysics* 84(3): IM35–IM45 <http://dx.doi.org/10.1190/GEO2018-0646.1>
- Yilmaz, Ö (2001) *Seismic data analysis: Processing, inversion, and interpretation of seismic data*. Society of exploration geophysicists, Tulsa
- Zhang, B, Tong, Y, Du, J, Hussain, S, Jiang, Z, Ali, S, Ali, I, Khan, M and Khan, U (2022) Three-dimensional structural modeling (3D SM) and joint geophysical characterization (JGC) of hydrocarbon reservoir. *Minerals* 12(3): 363. <https://doi.org/10.3390/min12030363>
- Zhou, Z, Rahman Siddiquee, MM, Tajbakhsh, N and Liang, J (2018). Unet++: A nested u-net architecture for medical image segmentation. In *Deep Learning in Medical Image Analysis and Multimodal Learning for Clinical Decision Support*. Cham, Switzerland. Springer, pp. 3–11. https://doi.org/10.1007/978-3-030-00889-5_1

Seismic analysis of the Orange Basin; from a deepwater fold-and-thrust-belt to Cenozoic mass transport systems

Nombuso Maduna, Zubair Jinnah, Musa Manzi

School of Geosciences, University of the Witwatersrand, Johannesburg, South Africa

Traditionally, deepwater fold-and-thrust belts (DWFTBs) have been of great importance to the petroleum industry as vast reserves of hydrocarbons are associated with their anticlines. Well-preserved DWFTB systems are found in the South Atlantic with several occurring off the western coast of South Africa in the Orange Basin. Previous studies have mainly focussed on the 2D seismic interpretation of the Orange Basin, which is naturally limited or confined to shallow waters. In this study, the availability of high-resolution, 3D seismic reflection data has allowed us to constrain the strato-structural architecture of the deepwater Orange Basin from a Cretaceous DWFTB system to the overlying Cenozoic deposits.

The 3D seismic data show the imaging of the structurally complex transitional domain and a portion of the compressional domain, containing the fold-and-thrust belt system, upon a main, seaward-dipping, basal shale detachment surface. The strong seismic marker forms the oldest of the seven seismic reflections observed in the study area, identified at the base of lithological units. These are the: Turonian, Santonian and Maastrichtian Cretaceous horizons; and the Palaeocene, Oligocene and Miocene Cenozoic horizons, including the seafloor. Multiple shale detachment surfaces partially accommodate slip in the DWFTB system. Gravitational slip initially occurs along the main Turonian shale detachment surface until the DWFTB system becomes locked. Stress in the system is then redistributed through the downward propagation of thrust faults onto a lower shale detachment accommodating further slip and essentially creating a younger, underlying set of folds and thrusts. With progressive sediment deposition, stress and strain are constantly redistributed in the basin to give rise to a complex range of geometries. This affects the timing and locus of sedimentation as evidenced through the complicated fault networking system, which are possible conduits for hydrocarbon migration. Some of these faults have been reactivated, extending from the main Turonian shale detachment surface in the transitional domain and terminating between the Oligocene and Miocene stratigraphic horizons which are unconformity surfaces. These two horizons correspond with the major Oligocene and lesser Miocene sea-level lowstands, previously described in great detail for southwestern Africa's shallow marine to coastal settings, and are characterised by: one large submarine canyon truncating the base of the Palaeocene on its seaward trajectory; and a smaller series of concentrated incipient canyons, respectively. The Cenozoic mass transport system and deposits are thus strongly influenced not only by relative sea-level fluctuations but also by the underlying geometry of the Cretaceous DWFTB system. The present morphology of the seafloor indicates that slumping still occurs due to sediment instability along the seaward-dipping continental slope.

Evolution of the Orange Basin; Cretaceous Deepwater Fold-and-Thrust Belts to Cenozoic Mass Transport Systems

Introduction

Traditionally, deep-water fold-and-thrust belts (DWFTBs) have been of great importance to the petroleum industry as vast reserves of hydrocarbons are associated with their anticlines (Morley et al., 2011). Well-preserved DWFTB systems are found in the South Atlantic's passive margin with several occurring off the western coast of South Africa in the Orange Basin. The extensional and compressional domain of DWFTB systems has been well-studied due to the simplicity of the former and known hydrocarbon potential of the latter (e.g. Paton et al., 2007, 2008; De Vera et al., 2010; Baby et al., 2018). Apart from the study of Dalton et al. (2017), a paucity of data exists for the more structurally complex transitional region and how DWFTBs affect the overlying sedimentary successions through time. Understanding the architectural elements of southern Africa's passive margin, and the tectonic evolution of the DWFTB systems contained within, is therefore important in building on the scientific knowledge known of what occurs in these settings worldwide and in further constraining prospective sites for petroleum exploration in similar settings.

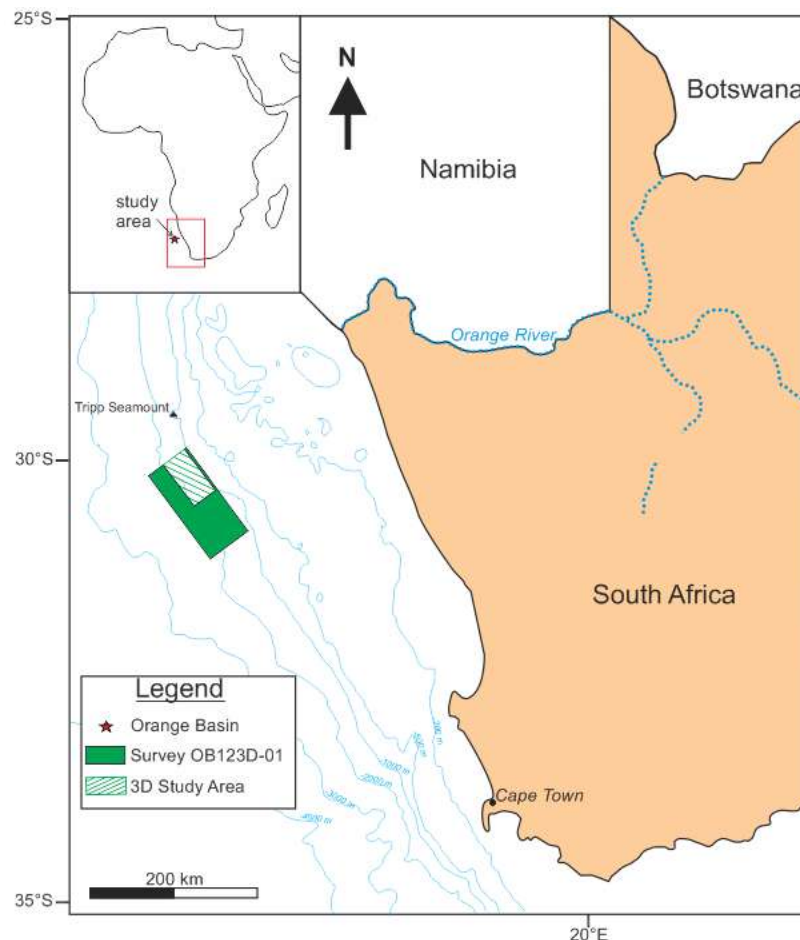


Figure 1 Map showing the location of the 3D study area within the deep-water Orange Basin.

The focus of this study is on an 1800 km² 3D seismic block in the deep-water Orange Basin, located along the continental slope between water depths of 1000 m and 2000 m within PASA's (Petroleum Agency South Africa) survey area OB123D-01 (Figure 1). Previous studies have mainly focused on the 2D seismic interpretation of the Orange Basin, which is naturally limited. In this study, the availability of high-resolution, 3D seismic reflection data has allowed us to constrain the strato-structural architecture of the deep-water Orange Basin from a Cretaceous DWFTB system to the overlying Cenozoic deposits.

Methodology

Seismic processing was carried out by the Netherlands Global Processing team through geometry setup, SEG-D to SEG-Y data conversion, trace editing, picking of first breaks, noise attenuation, velocity analysis, stacking, deconvolution, and migration. Following the corrections and editing involved in processing, a project for 3D seismic interpretation was created using Schlumberger's 2018 Petrel Exploration and Petroleum Software package. The complete Petrel workflow used is shown in Figure 2.

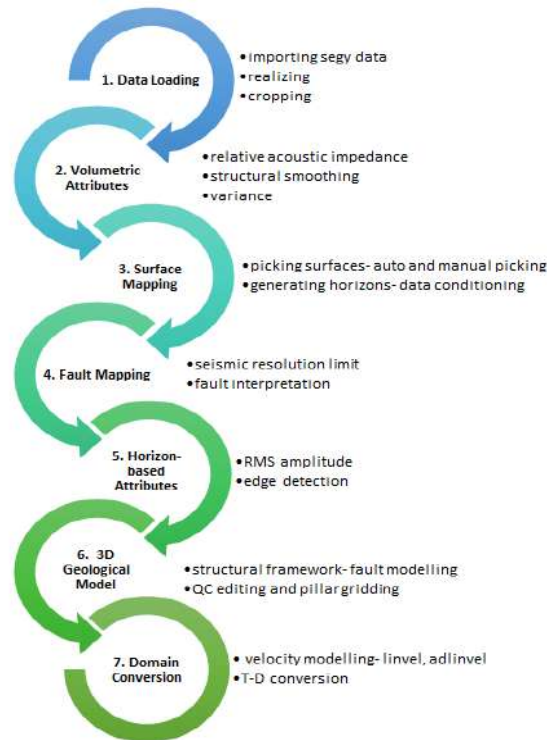


Figure 2 Methodology of the Petrel workflow..

Cretaceous DWFTB system

The 3D seismic data show the imaging of the structurally complex transitional domain and a portion of the compressional domain, containing the fold-and-thrust belt system, upon a main, seaward-dipping, basal shale detachment surface. The strongest seismic reflections mark the Turonian, Santonian and Maastrichtian Cretaceous stratigraphic horizons; and the Paleocene, Oligocene and Miocene Cenozoic stratigraphic horizons, including the seafloor. Multiple shale detachment surfaces are known to partially accommodate slip in the Orange Basin's DWFTB system (Dalton et al., 2017). This is observable in the study area as shown in Figure 3. Gravitational slip initially occurs along the main Turonian shale detachment surface until the DWFTB system becomes locked. Stress in the system is then redistributed through the downward propagation of thrust faults onto a lower shale detachment accommodating further slip and essentially creating a younger, underlying set of folds and thrusts. With progressive sediment deposition, stress and strain are constantly redistributed in the basin to give rise to a complex range of geometries. This affects the timing and locus of sedimentation as evidenced through the complicated fault networking system, which are possible conduits for hydrocarbon migration.

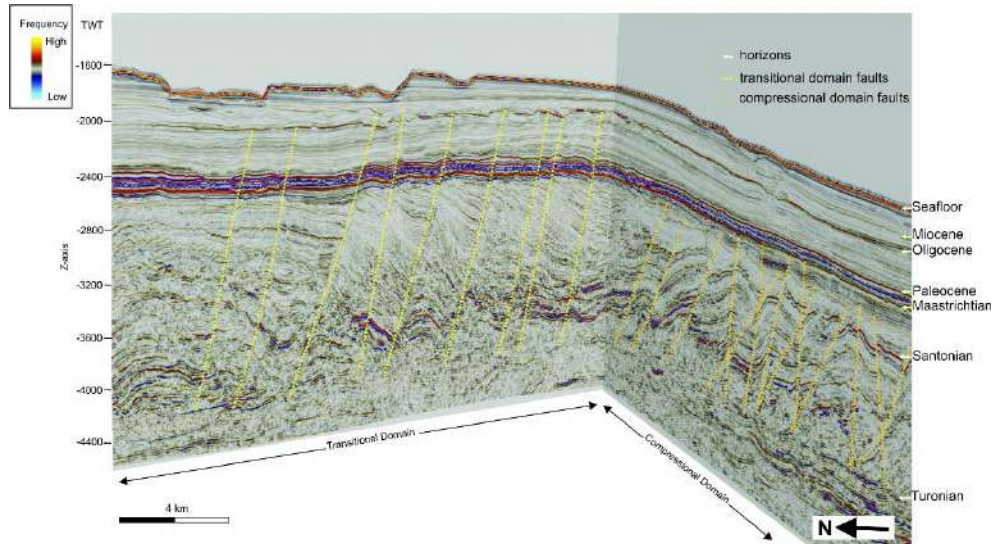


Figure 3 Strato-structural framework of the deep-water Orange Basin showing major stratigraphic horizons and faults within the transitional and compressional domains.

Cenozoic deposits

Some faults within the transitional domain have been reactivated, extending from the main Turonian shale detachment surface to terminate between the Oligocene and Miocene stratigraphic horizons; unconformity surfaces corresponding to relative sea-level falls (Figure 2; Figure 3). Evidence of the major Oligocene and lesser Miocene sea-level lowstands, most commonly observed in the shallow marine to coastal settings of the southwest African coastline (e.g. Baby et al., 2018; Kirkpatrick et al., 2018), is shown in the study by: one main, large Oligocene submarine canyon truncating the base of the Paleocene on its seaward trajectory; and a smaller series of cross-cutting and concentrated Miocene incipient canyons along the continental slope, respectively (Figure 4). The Cenozoic mass transport systems and deposits are thus strongly influenced not only by relative sea-level fluctuations, but also by the dipping slope and underlying geometry of the Cretaceous DWFTB system as faults are reactivated with progressive sedimentation in the transitional domain.

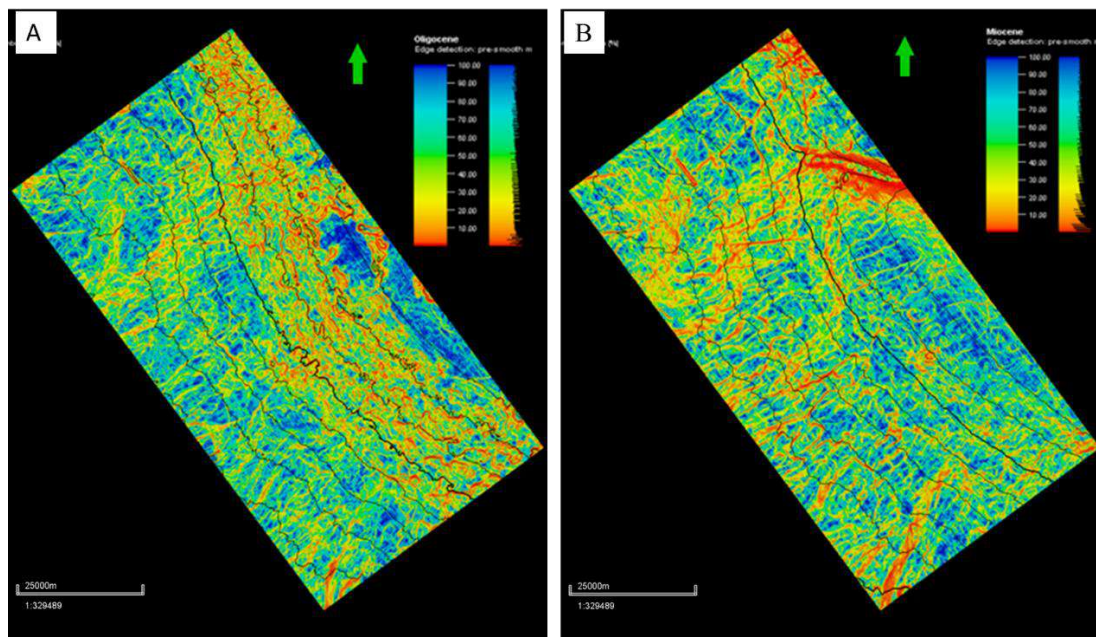


Figure 4 Edge detection attribute enhancing faults and features on the Oligocene (A) and Miocene (B) surfaces. A. Note the canyon to the NE section; B. Note the smaller, sinuous cross-cutting canyon.

Conclusions

This study has shown the different structural effects that the transitional and compressional domains of DWFTB systems have on the evolution of overlying deposits with progressive sedimentation. Understanding the complex fault networking system associated with DWFTB systems is crucial in determining the migration and possible concentration of vast hydrocarbons in structural and stratigraphic traps.

Acknowledgements

We would like to greatly thank the following for making this study possible: National Research Foundation (NRF) for sponsoring the studies of the main author; Shell for providing seismic data; Schlumberger for the use of its software, and the Wits Seismic Research Centre for the use of its resources.

References

- Baby, G., Guillocheau, F., Morin, J., Ressouche, J., Robin, C., Broucke, O., & Dall'Asta, M. [2018] Post-rift stratigraphic evolution of the Atlantic margin of Namibia and South Africa: Implications for the vertical movements of the margin and the uplift history of the South African Plateau. *Marine and Petroleum Geology*, **97**, 169-191.
- Dalton, T. J. S., Paton, D. A., & Needham, D. T. [2017] Influence of mechanical stratigraphy on multi-layer gravity collapse structures: insights from the Orange Basin, South Africa. *Geological Society*, London, Special Publications, **438**(1), 211-228.
- De Vera, J., Granado, P., & McClay, K. [2010] Structural evolution of the Orange Basin gravity-driven system, offshore Namibia. *Marine and Petroleum Geology*, **27**(1), 223-237.
- Kirkpatrick, L.H. and Green, A.N. [2018] Antecedent geologic control on nearshore morphological development: The wave dominated, high sediment supply shoreface of southern Namibia. *Marine Geology*, **403**, 34-47.
- Morley, C. K., King, R., Hillis, R., Tingay, M., & Backe, G. [2011] Deepwater fold and thrust belt classification, tectonics, structure and hydrocarbon prospectivity: A review. *Earth-Science Reviews*, **104**(1-3), 41-91.
- Paton, D. A., Di Primio, R., Kuhlmann, G., Van Der Spuy, D., & Horsfield, B. [2007] Insights into the petroleum system evolution of the southern Orange Basin, South Africa. *South African Journal of Geology*, **110**(2-3), 261-274.
- Paton, D. A., van der Spuy, D., di Primio, R., & Horsfield, B. [2008] Tectonically induced adjustment of passive-margin accommodation space; influence on the hydrocarbon potential of the Orange Basin, South Africa. *American Association of Petroleum Geologists Bulletin*, **92**(5), 589-609.

Constraining the temporal evolution of the deep-water Orange Basin using high-resolution 3D seismic reflection data

Introduction

The gravitational collapse and subsequent contraction of sedimentary sequences in the deep ocean forms deep-water fold-and-thrust belts (DWFTBs); distal sedimentary wedges of interrelated folds, and thrust faults created over a sloping detachment surface (de Vera et al., 2010). Well-preserved DWFTB systems are found within the Orange Basin, offshore the SW African coastline (Figure 1). At present, there is a great paucity of data for the central transitional domain of these systems due to its structural complexity and how it has been poorly seismically imaged (mainly 2D). This is in stark contrast to the linked up-dip extensional and down-dip compressional domains of the tripartite system, which have been well-studied due to the simplicity of the former and known hydrocarbon potential of the latter (e.g., Paton et al., 2007). In this study we use high-resolution 3D reflection seismic data from the Orange Basin to provide an in-depth examination of the transitional domain from a buried DWFTB system (Figure 1). We define its relationship to the down-dip compressional domain and assess how both domains have structurally affected the younger deposits with progressive sedimentation. From these observations we create a model describing not only the evolution of one DWFTB system, but also that of the overlying passive margin sediments as it played a significant role in its deformation.

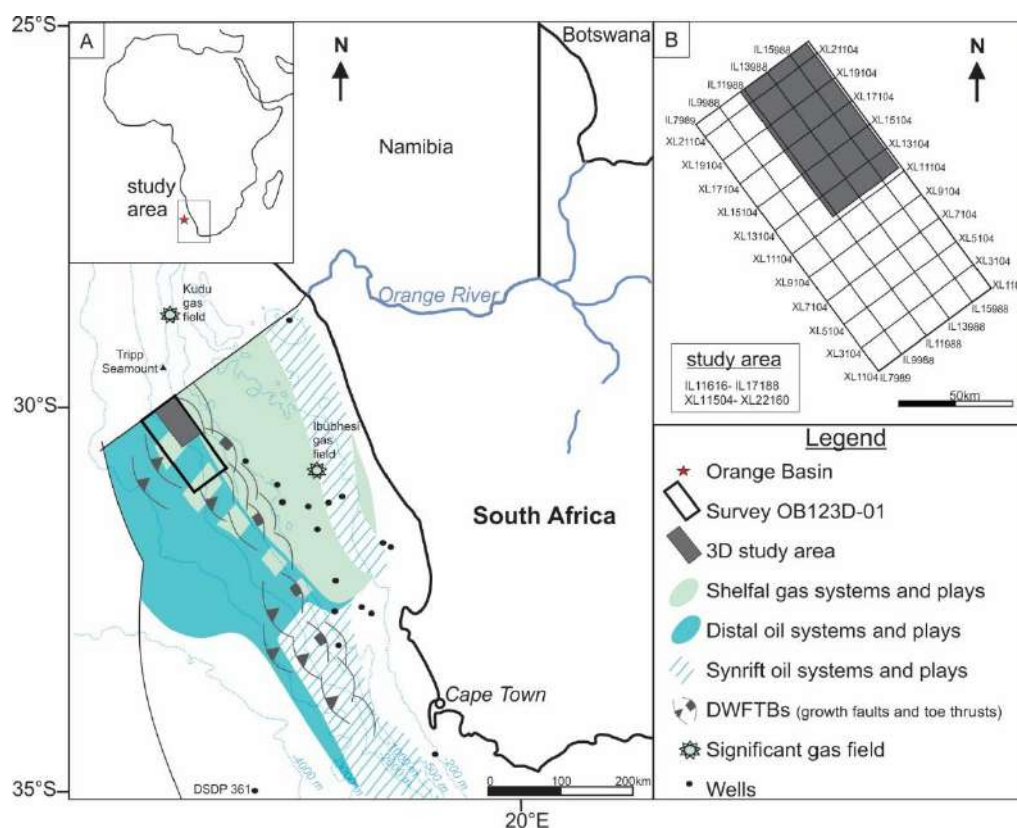


Figure 1 Map of the Orange Basin study area offshore the South African coastline. (a) Known and predicted petroleum systems and plays, the position of DWFTBs and wells (adapted from Jungslager, 1999). (b) Location of the present study.

Methods

Shell Global Solutions International commissioned a ~ 8 200 km² high-resolution 3D seismic survey between 2012–2013 in the deep-water Orange Basin, and this study focusses on a ~1 800 km² portion (Figure 1). Seismic processing was carried out by the Netherlands Global Processing team through geometry setup, SEG-D to SEG-Y data conversion, trace editing, picking of first breaks, noise attenuation, velocity analysis, stacking, deconvolution, and migration. In this study the data are

geologically interpreted using the Petrel Schlumberger software. The complete interpretation workflow used is shown in Figure 2.

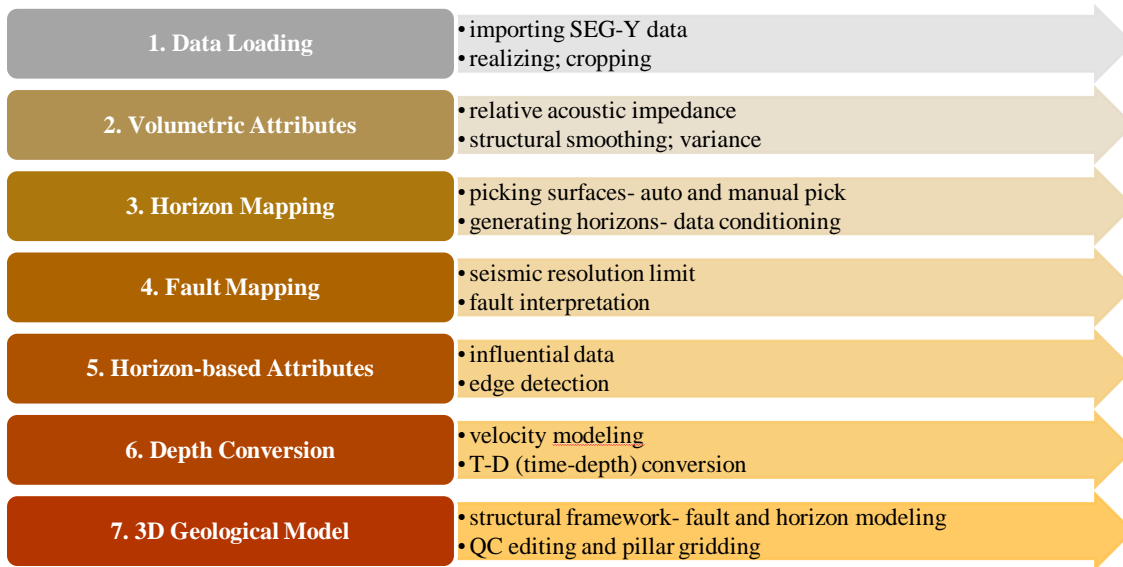


Figure 2 Interpretation workflow used to build this study's geological model in the Petrel software.

Results and Discussion

The study area lies along the South African continental slope between water depths of 1 000 to 2 000 m (Figure 1). We identified nine key seismic stratigraphic markers in this study. From oldest to youngest these are the: 1) Albian, and uninterpreted 2) Turonian shale detachment surfaces (SDSs); the 3) Santonian, 4) early Campanian, 5) late Campanian, 6) Maastrichtian, 7) Oligocene and 8) Miocene unconformities; and 9) the seafloor (Figure 3). The sedimentary succession comprises several sequences displaced by a complex structural framework of faults including overlapping thrust, normal and oblique-slip faults (Figure 4). The full seismic volume images the compressional and transitional domains of a Late Cretaceous DWFTB system (Figure) together with the overlying Cenozoic sediments.

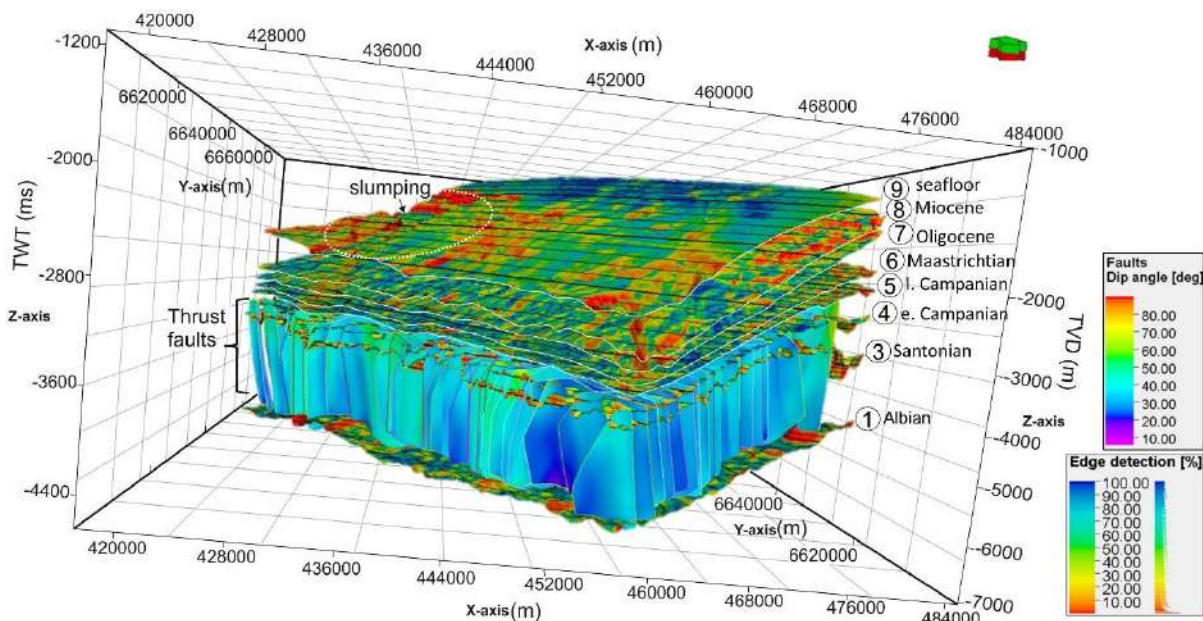


Figure 3 3D view showing all horizons in edge detection, and the dip of all thrust faults interpreted in the study area. Abbreviations: e= early, l= late. VE= 10.

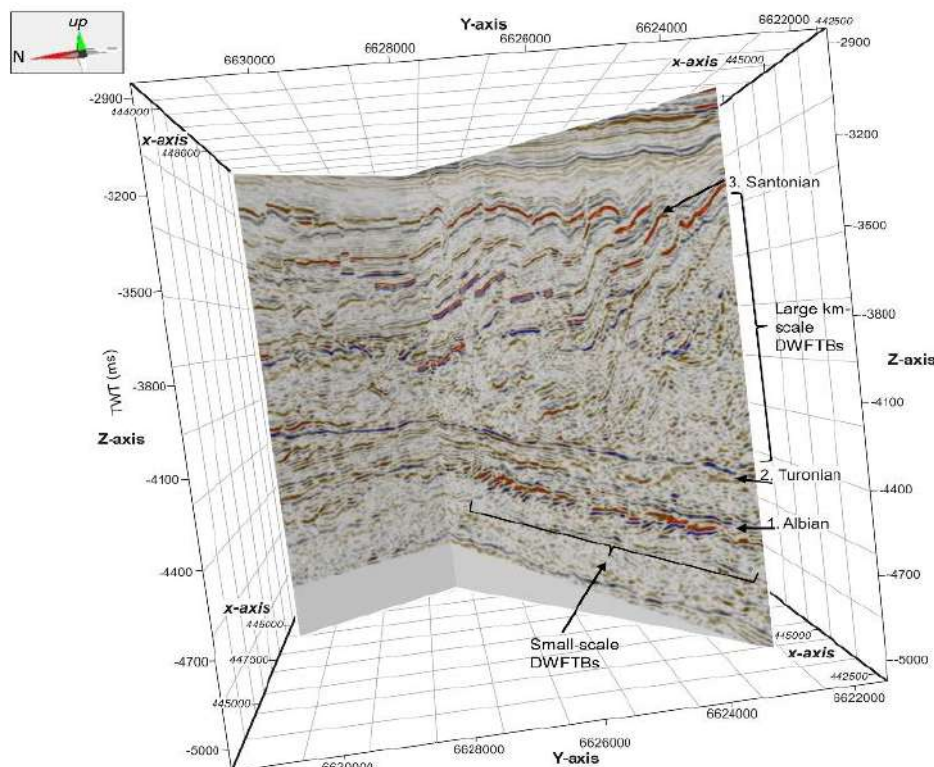


Figure 4 3D view showing an extensive, kilometre-scale DWFTB system detaching the Turonian SDS, and an underlying localized set of secondary, small-scale DWFTBs upon the Albian SDS. VE= 5.

We present an evolutionary model for the deep-water Orange Basin (Figure 5) using the stratigraphic and structural observations made in the present study, and previous literature on the tectonic history of the basin (e.g., Paton et al., 2007; De Vera et al., 2010; Hirsch et al., 2010; Dalton et al., 2017). The following sequence of events is proposed in the evolution of the Orange Basin from the formation of a Late Cretaceous DWFTB system, to its control on overlying Cenozoic sedimentation:

- Turonian:** margin uplift in the Late Cretaceous caused sea-level fall, and an increase in sedimentation rates.
- Turonian–Coniacian:** listric normal faulting in the up-dip extensional domain led to the formation of large fold-and-thrust belts in the down-dip compressional domain (Figure 4). Gravitational slip first occurred along the upper Turonian SDS where faults initially detach.
- Santonian–late Campanian:** as deformation continued, sediments became highly strained, and stress was redistributed through: 1) the downward propagation of listric normal faults to a lower Albian SDS encouraging gravitational slip to continue, and the formation of smaller scale DWFTBs down-dip (Figure 4); and 2) concurrent oblique-slip faulting along-strike the thrust sheets, laterally segmenting the deformed Late Cretaceous sediments.
- Oligocene:** a major sea-level fall past the shelf break led to the formation of a large Oligocene canyon constrained above the buried transitional domain. It was caused by an erosive downslope turbidity current.
- Miocene:** sea-level fall with margin uplift led to the formation of multiple crosscutting and sinusoidal channels in the Miocene constrained above the buried transitional domain. It was caused by the slope-parallel erosive action of bottom currents possibly related upwelling of the Benguela Current at ~10 Ma.
- Present:** Slope instability caused present-day slumping of seafloor sediments (Figure 3).

Conclusions

The strato-structural evolution of the Orange Basin has been investigated with an in depth look at structures within the structurally complex transitional domain of a DWFTB system which itself is often poorly constrained. This study has shown the difference in structural styles and effects of a Late

Cretaceous transitional and compressional domain and how they have influenced mass transport complexes of the Cenozoic.

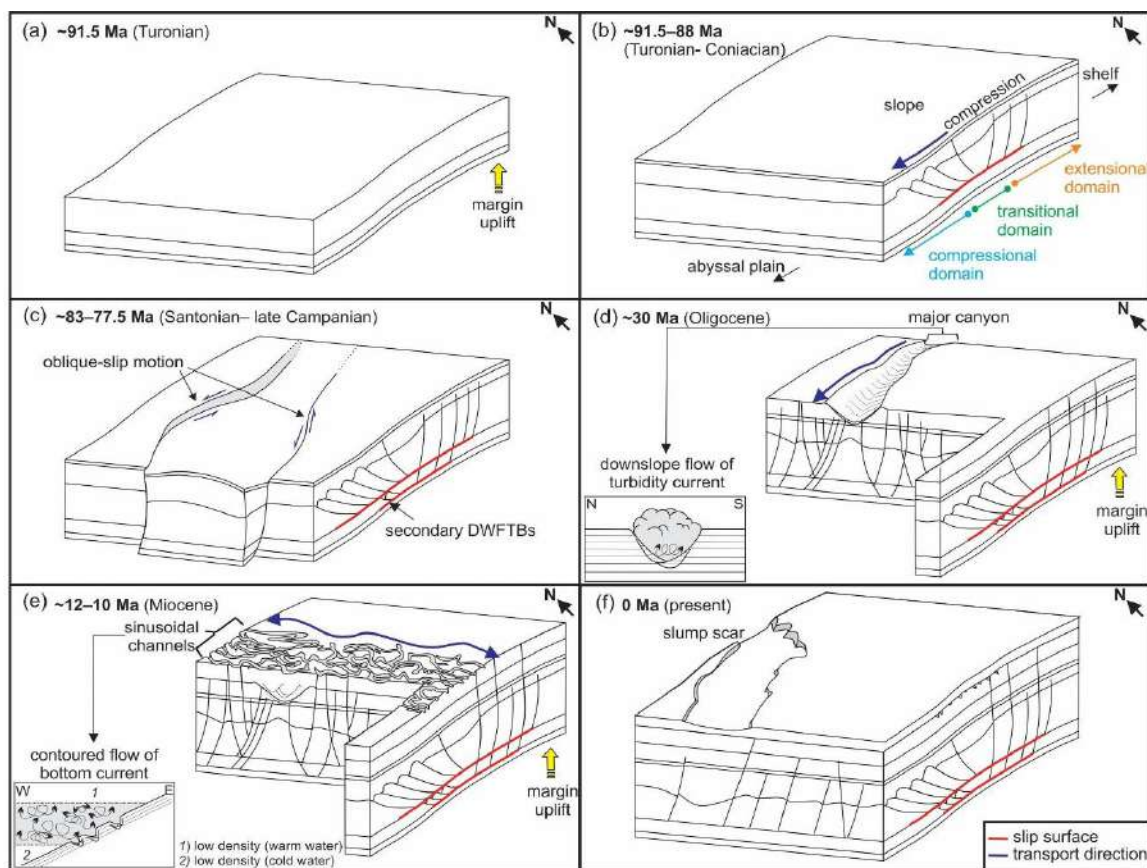


Figure 5 Temporal evolutionary model of the deep-water Orange Basin from a Late Cretaceous DWFTB system to Cenozoic mass-transport systems.

Acknowledgements

We would like to thank the National Research Foundation (NRF) and the Council for Geoscience (CGS) for funding the first author's research. Our thanks are also extended to Shell South Africa for providing the 3D reflection seismic data, Schlumberger for the Petrel software and support, and our colleagues from the Wits Seismic Research Centre for the scientific discussions had and invaluable inputs made.

References

- Dalton, T. J. S., Paton, D. A., & Needham, D. T. [2017] Influence of mechanical stratigraphy on multi-layer gravity collapse structures: insights from the Orange Basin, South Africa. *Geological Society, London, Special Publications*, **438**(1), 211-228.
- De Vera, J., Granado, P., & McClay, K. [2010] Structural evolution of the Orange Basin gravity-driven system, offshore Namibia. *Marine and Petroleum Geology*, **27**(1), 223-237.
- Hirsch, K. K., Scheck-Wenderoth, M., van Wees, J.-D., Kuhlmann, G., and Paton, D. A. [2010] Tectonic subsidence history and thermal evolution of the Orange Basin, *Marine and Petroleum Geology*, **27**, 565-584.
- Paton, D. A., Di Primio, R., Kuhlmann, G., Van Der Spuy, D., & Horsfield, B. [2007] Insights into the petroleum system evolution of the southern Orange Basin, South Africa. *South African Journal of Geology*, **110**(2-3), 261-274.

Temporal evolution of the deep-water Orange Basin using high-resolution 3D seismic reflection data

N.G. Maduna¹, M.S.D. Manzi¹, Z.J. Jinnah¹

1. University of the Witwatersrand, South Africa,
nombuso.maduna@gmail.com

BIOGRAPHY

The first author, Nombuso Maduna, is a Geology PhD student at the University of the Witwatersrand researching the offshore evolution of the deep-water Orange Basin, South Africa, using seismic reflection data. Her supervisors, the second and third authors of this paper, are researchers and lecturers at the University of the Witwatersrand. Geophysicist Prof. Musa Manzi specializes in reflection seismology, and geologist Dr. Zubair Jinnah specializes in sedimentology.

SUMMARY

In this study we examined the temporal evolution of the underexplored South African deep-water Orange Basin, using high-resolution 3D reflection seismic data; from the translational and compressional domains of a buried Late Cretaceous deep-water fold-and-thrust belt (DWFTB) system to the Cenozoic mass transport processes it has affected.

The translational domain is characterized by overprinted features of both extensional and compressional tectonics since crosscutting relationships are observed in the structural framework. Extensive, DWFTBs occur in the compressional domain underlain by smaller, localized sets of DWFTBs in older sediments. Thrust sheets are displaced by extensive oblique-slip faults, laterally extending from the translational domain. The presence of multiple shale detachment surfaces gave rise to a range of complex structural styles as faults were encouraged to propagate.

Cenozoic canyon-channel systems were influenced by the underlying structure and geometry of the translational domain as evidenced by faults propagating upwards to the Oligocene and Miocene erosional surfaces. A large turbidity-current-formed, submarine canyon occurs the Oligocene, while bottom currents created multiple smaller, sinusoidal channel-like features in the Miocene. Using Schlumberger's Petrel E& P software package we observed how the underlying stratigraphy and structural framework of the Orange Basin has and always will control its evolution.

Key words: Orange Basin, reflection seismic data, DWFTB system, structural framework

INTRODUCTION

The gravitational collapse and subsequent contraction of sedimentary sequences in the deep ocean forms deep-water fold-and-thrust belts (DWFTBs); distal sedimentary wedges of interrelated folds, and thrust faults created over a sloping detachment surface (de Vera et al., 2010). Well-preserved DWFTB systems are found within the Orange Basin, offshore the SW African coastline (Figure 1). At present, there is a great paucity of data for the central translational domain of these systems due to its structural complexity and how it has been poorly seismically imaged (mainly 2D). This is in stark contrast to the linked up-dip extensional and down-dip compressional domains of the tripartite system, which have been well-studied due to the simplicity of the former and known hydrocarbon potential of the latter (e.g., Paton et al., 2007). In this study we use high-resolution 3D reflection seismic data from the Orange Basin to provide an in-depth examination of the translational domain from a buried DWFTB system (Figure 1). We define its relationship to the down-dip compressional domain and assess how both domains have structurally affected the younger deposits with progressive sedimentation. From these observations we create a model describing not only the evolution of one DWFTB system, but also that of the overlying passive margin sediments as it played a significant role in its deformation.

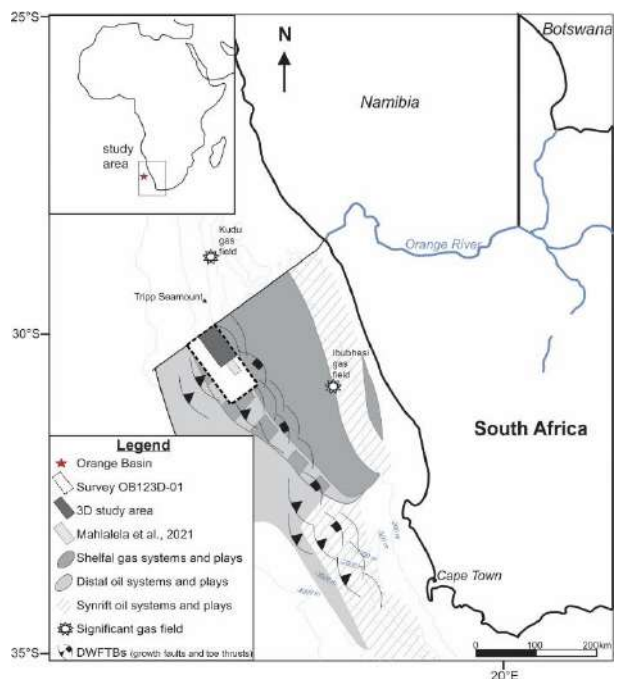


Figure 1. Map of the Orange Basin study area offshore the South African coastline. (a) Known and predicted petroleum systems and plays, the position of DWFTBs and wells (adapted from Jungslager, 1999). (b) Location of the present study.

METHODOLOGY

Shell Global Solutions International commissioned a ~ 8 200 km² high-resolution 3D seismic survey between 2012–2013 in the deep-water Orange Basin, and this study focusses on a ~1 800 km² portion (Figure 1). Seismic processing was carried out by the Netherlands Global Processing team through geometry setup, SEG-D to SEG-Y data conversion, trace editing, picking of first breaks, noise attenuation, velocity analysis, stacking, deconvolution, and migration. In this study the data are geologically interpreted using the Petrel Schlumberger software. The complete interpretation workflow used is shown in Figure 2.

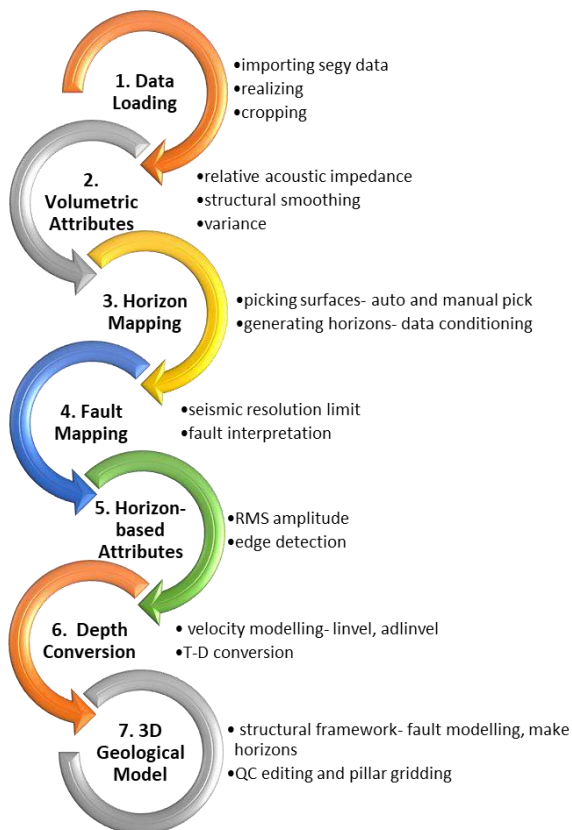


Figure 2. Interpretation workflow used to build this study’s geological model in the Petrel software.

RESULTS AND DISCUSSIONS

The study area lies along the South African continental slope between water depths of 1 000 to 2 000 m (Figure 1). We identified nine key seismic stratigraphic markers in this study. From oldest to youngest these are the: 1) Albian, and uninterpreted 2) Turonian shale detachment surfaces (SDSs); the 3) Santonian, 4) early Campanian, 5) late Campanian, 6) Maastrichtian, 7) Oligocene and 8) Miocene unconformities; and 9) the seafloor (Figure 3). The sedimentary succession comprises several sequences displaced by a complex structural framework of faults including overlapping thrust, normal and oblique-slip faults (Figure 4). The full seismic volume images the compressional and translational domains of a Late

Cretaceous DWFTB system (Figure) together with the overlying Cenozoic sediments.

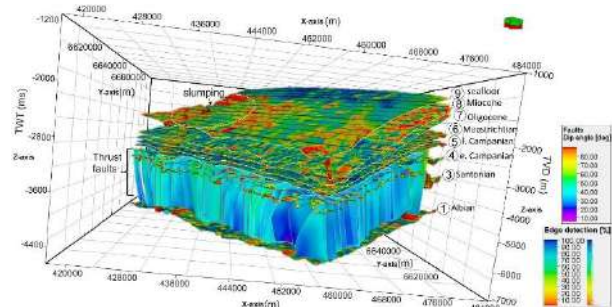


Figure 3. 3D view showing all horizons in edge detection, and the dip of all thrust faults interpreted in the study area. Abbreviations: e= early, l= late. VE= 10.

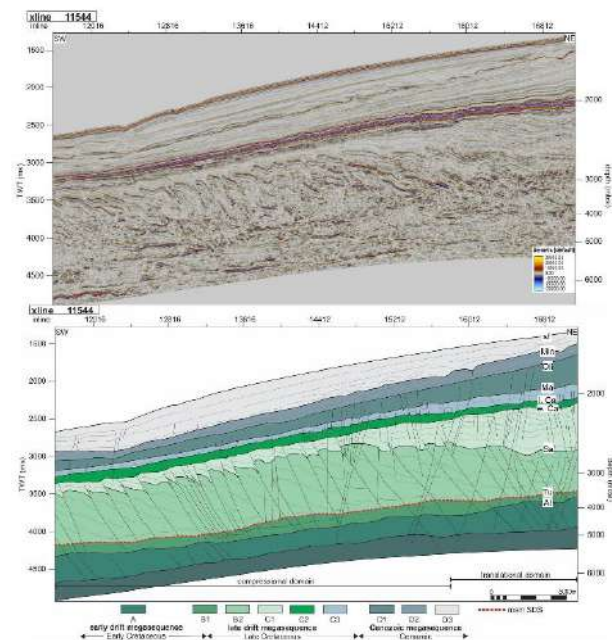


Figure 4. 2D view of uninterpreted and interpreted sections of crossline 11544 showing the translational domain and the compressional domain with faults detaching the Turonian SDS (VE= 5). SDS= shale detachment surface, Al= Albian, Tu= Turonian, Sa= Santonian, e. Ca= early Campanian, l. Ca= late Campanian, Ma= Maastrichtian, Olig= Oligocene, Mio= Miocene, sf= seafloor.

We present an evolutionary model for the deep-water Orange Basin (Figure 5) using the stratigraphic and structural observations made in the present study, and previous literature on the tectonic history of the basin (e.g., Paton et al., 2007; De Vera et al., 2010; Hirsch et al., 2010; Dalton et al., 2017). The following sequence of events is proposed in the evolution of the Orange Basin from the formation of a Late Cretaceous DWFTB system, to its control on overlying Cenozoic sedimentation:

- a) **Turonian:** margin uplift in the Late Cretaceous caused sea-level fall, and an increase in sedimentation rates.
- b) **Turonian–Coniacian:** listric normal faulting in the up-dip extensional domain led to the formation of large fold-and-thrust belts in the down-dip compressional domain (Figure 4). Gravitational slip first occurred along the upper Turonian SDS where faults initially detach.
- c) **Santonian–late Campanian:** as deformation continued, sediments became highly strained, and stress was redistributed through 1) the downward propagation of listric normal faults to a lower Albian SDS encouraging gravitational slip to continue, and the formation of smaller scale DWFTBs down-dip (Figure 4); and 2) concurrent oblique-slip faulting along-strike the thrust sheets, laterally segmenting the deformed Late Cretaceous sediments.
- d) **Oligocene:** a major sea-level fall past the shelf break led to the formation of a large Oligocene canyon constrained above the buried translational domain. It was caused by an erosive downslope turbidity current.
- e) **Miocene:** sea-level fall with margin uplift led to the formation of multiple crosscutting and sinusoidal channels in the Miocene constrained above the buried translational domain. It was caused by the slope-parallel erosive action of bottom currents possibly related upwelling of the Benguela Current at ~10 Ma.
- f) **Present:** Slope instability caused present-day slumping of seafloor sediments (Figure 3).

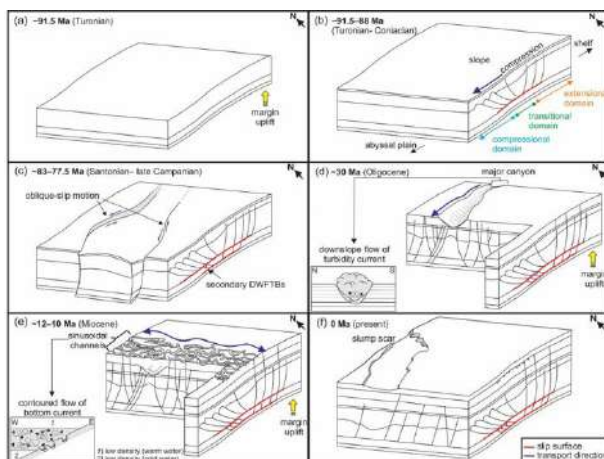


Figure 5. Temporal evolutionary model of the deep-water Orange Basin from a Late Cretaceous DWFTB system to Cenozoic mass-transport systems.

CONCLUSIONS

The strato-structural evolution of the Orange Basin has been investigated with an in depth look at structures within the structurally complex translational domain of a DWFTB system which itself is often poorly constrained.

This study has shown the difference in structural styles and effects of a Late Cretaceous translational and compressional domain and how they have influenced mass transport complexes of the Cenozoic.

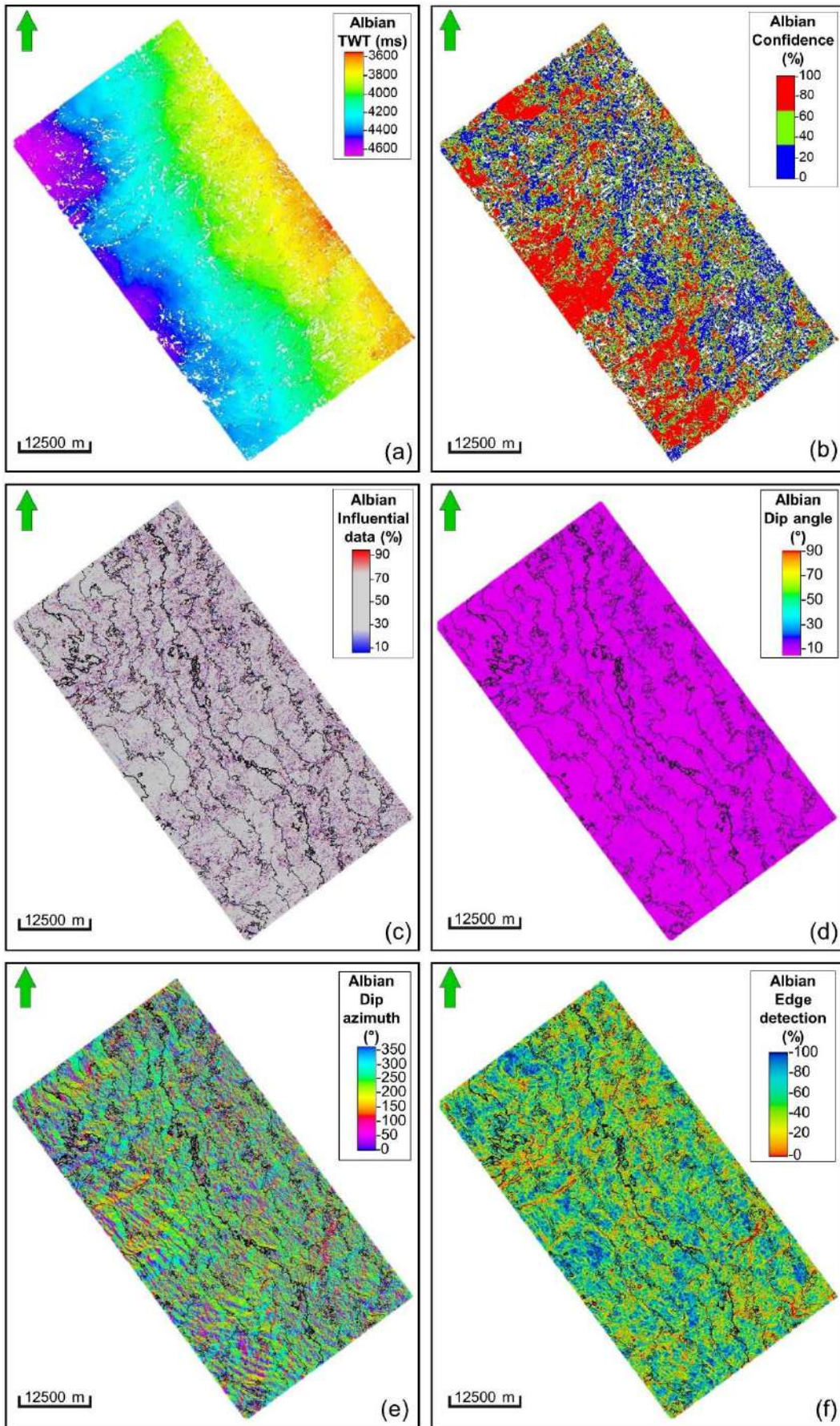
ACKNOWLEDGMENTS

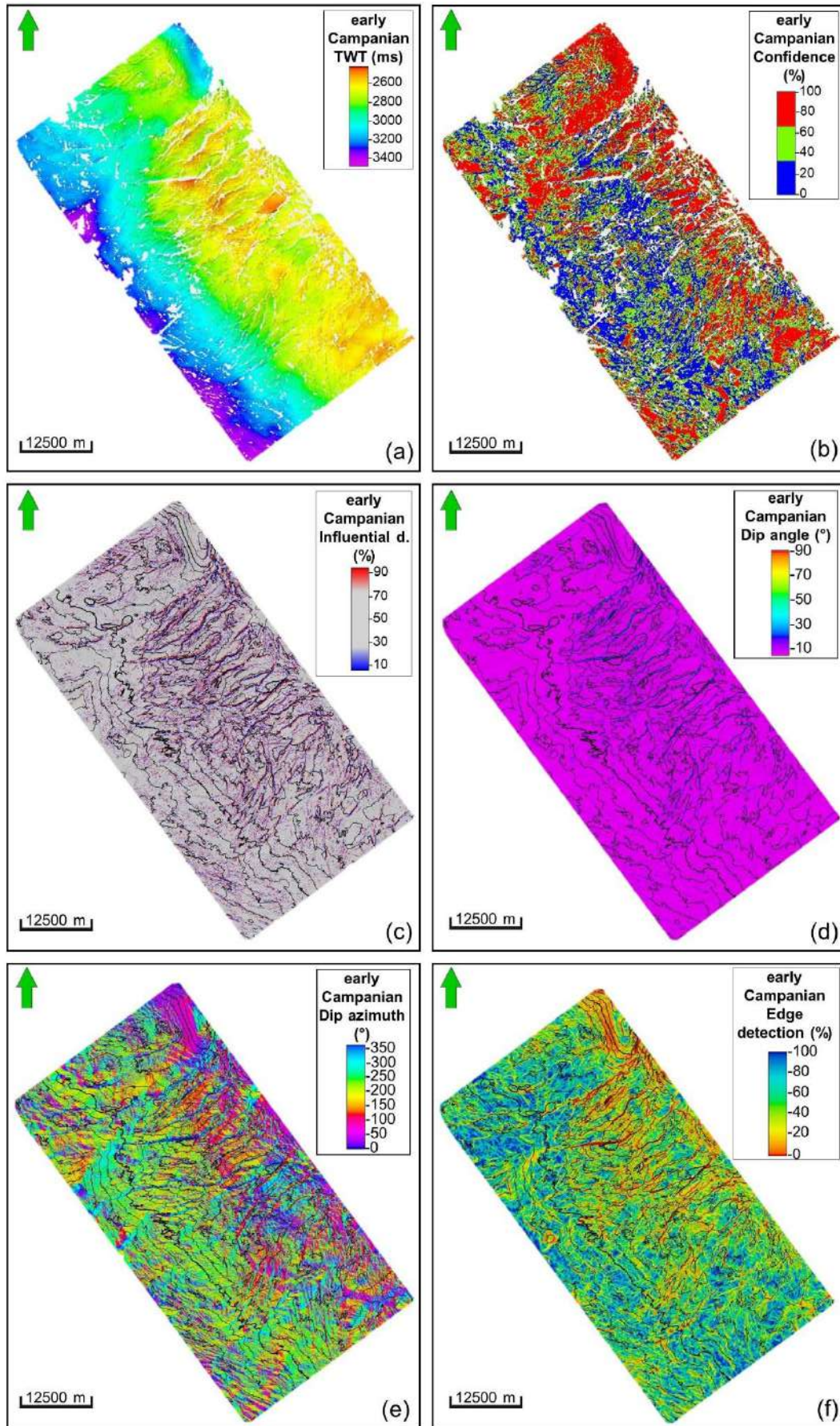
We would like to thank the National Research Foundation (NRF) and the Council for Geoscience (CGS) for funding the first author's research. Our thanks are also extended to Shell South Africa for providing the 3D reflection seismic data, Schlumberger for the Petrel software and support, and our colleagues from the Wits Seismic Research Centre for the scientific discussions had and invaluable inputs made.

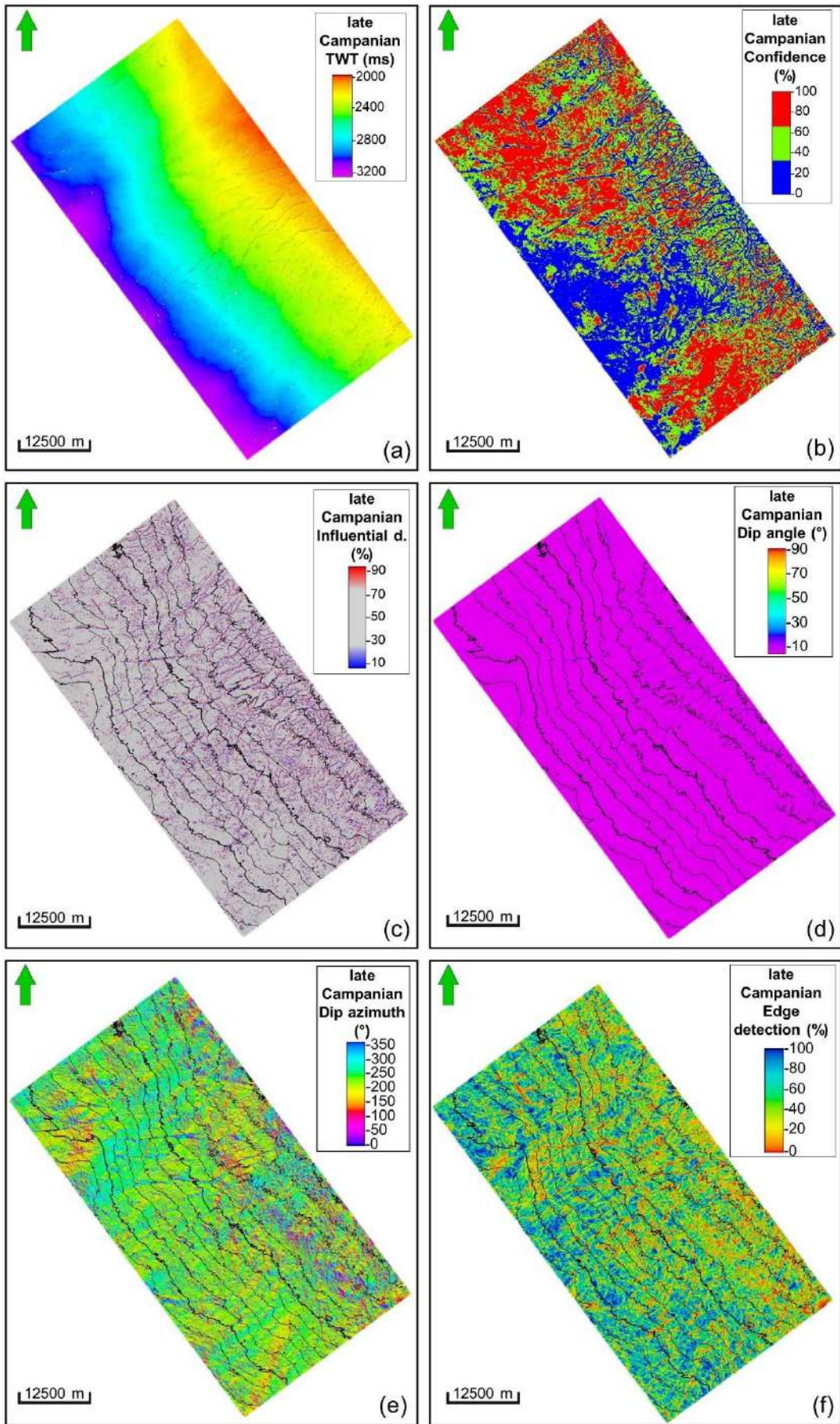
REFERENCES

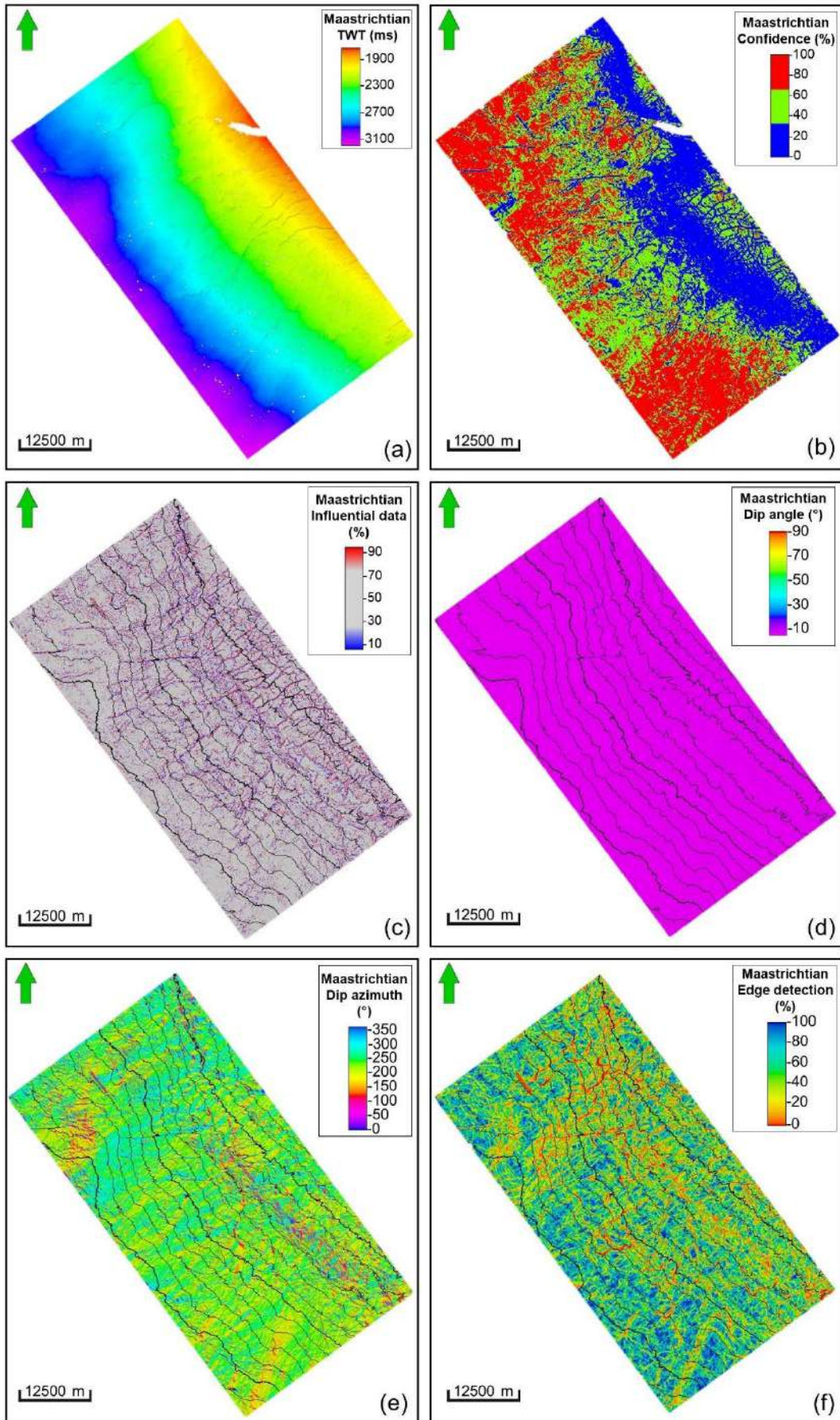
- Dalton, T. J. S., Paton, D. A., & Needham, D. T., 2017, Influence of mechanical stratigraphy on multi-layer gravity collapse structures: insights from the Orange Basin, South Africa. *Geological Society, London, Special Publications*, 438(1), 211-228.
- De Vera, J., Granado, P., & McClay, K., 2010, Structural evolution of the Orange Basin gravity-driven system, offshore Namibia. *Marine and Petroleum Geology*, 27(1), 223-237.
- Hirsch, K. K., Scheck-Wenderoth, M., van Wees, J.-D., Kuhlmann, G., and Paton, D. A., 2010, Tectonic subsidence history and thermal evolution of the Orange Basin, *Marine and Petroleum Geology*, 27, 565–584.
- Jungslager, E.H., 1999, Petroleum habitats of the Atlantic margin of South Africa. *Geological Society, London, Special Publications*, 153(1), pp.153-168.
- Paton, D. A., Di Primio, R., Kuhlmann, G., Van Der Spuy, D., & Horsfield, B., 2007, Insights into the petroleum system evolution of the southern Orange Basin, South Africa. *South African Journal of Geology*, 110(2-3), 261-274.

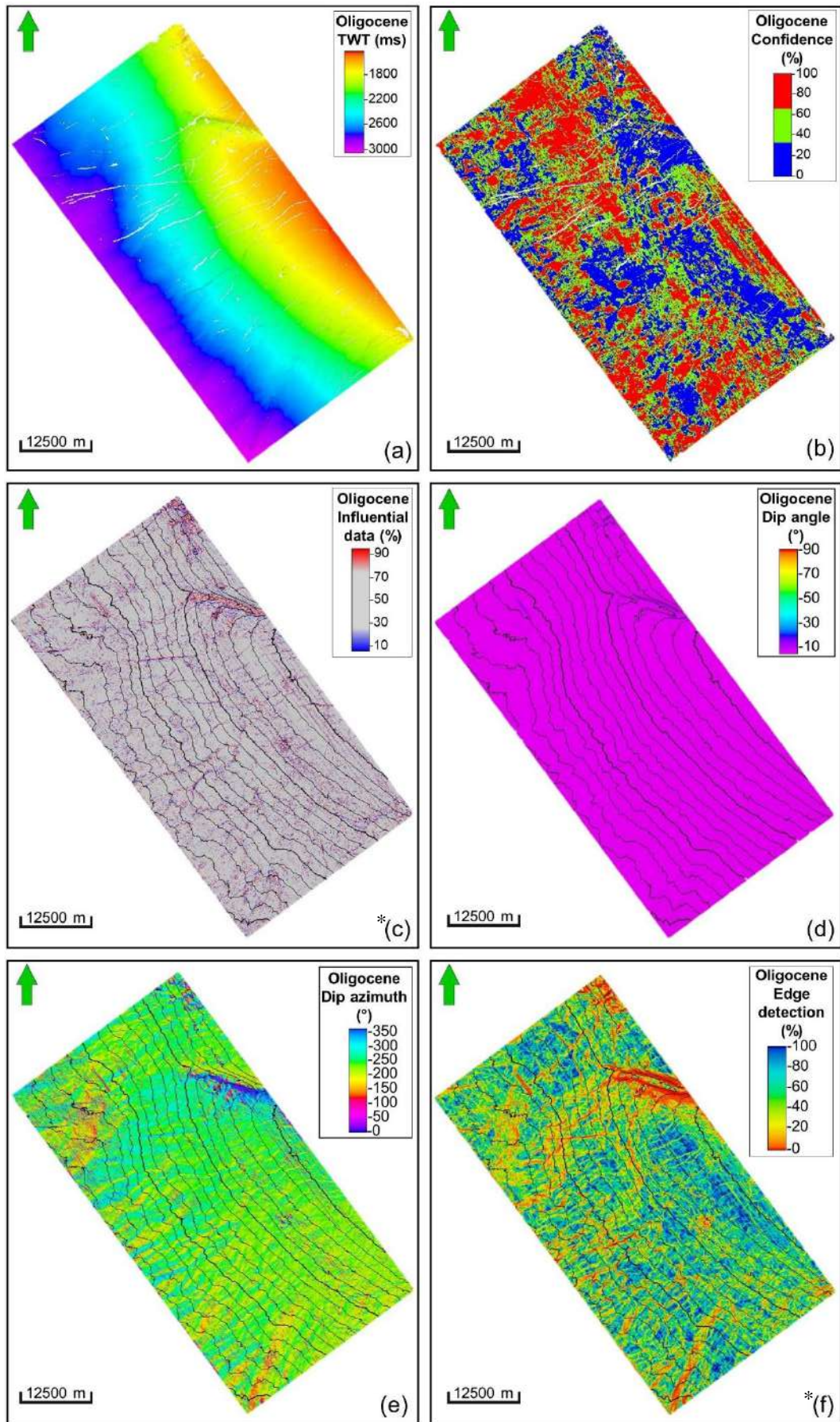
Appendix B
Horizon mapping attributes



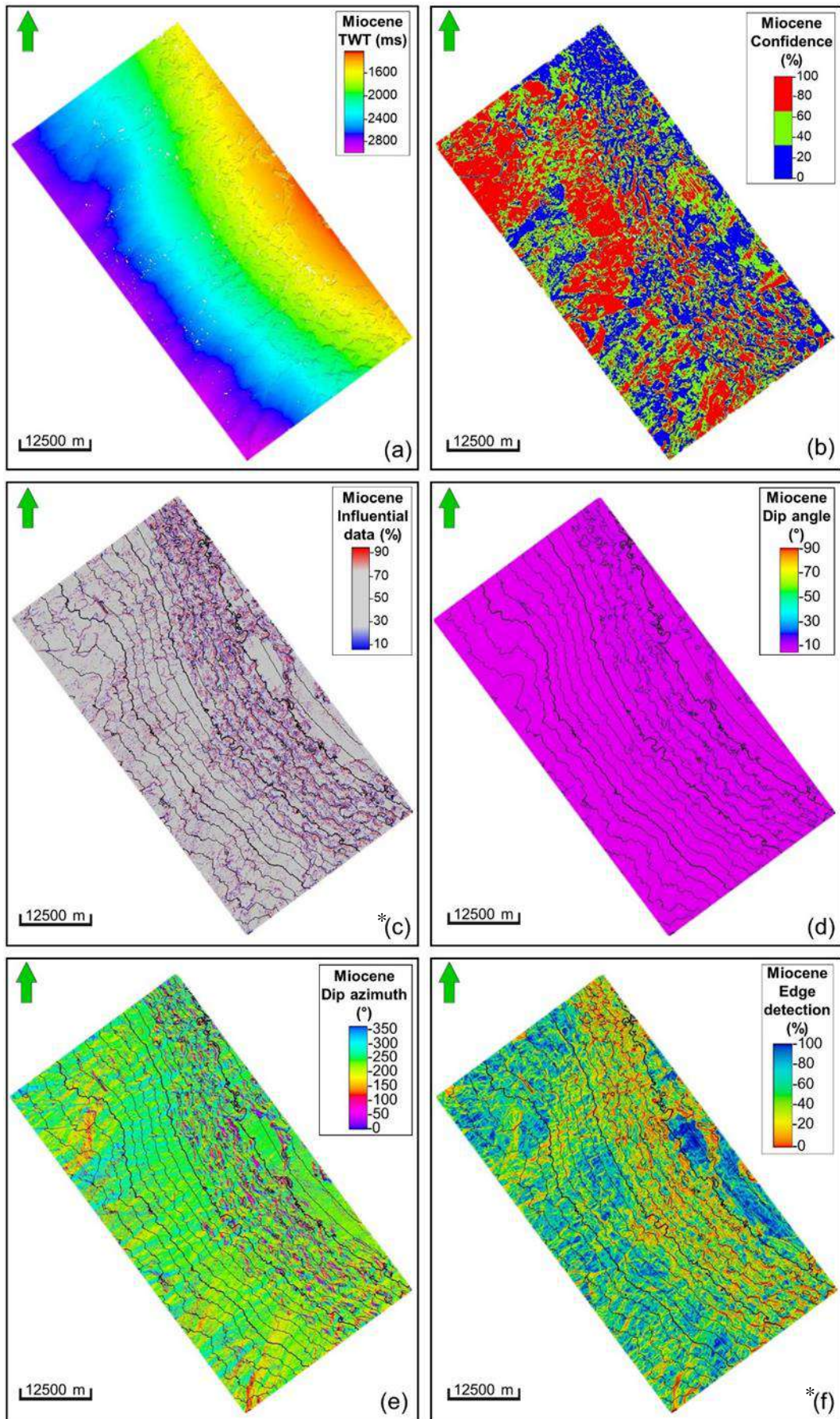




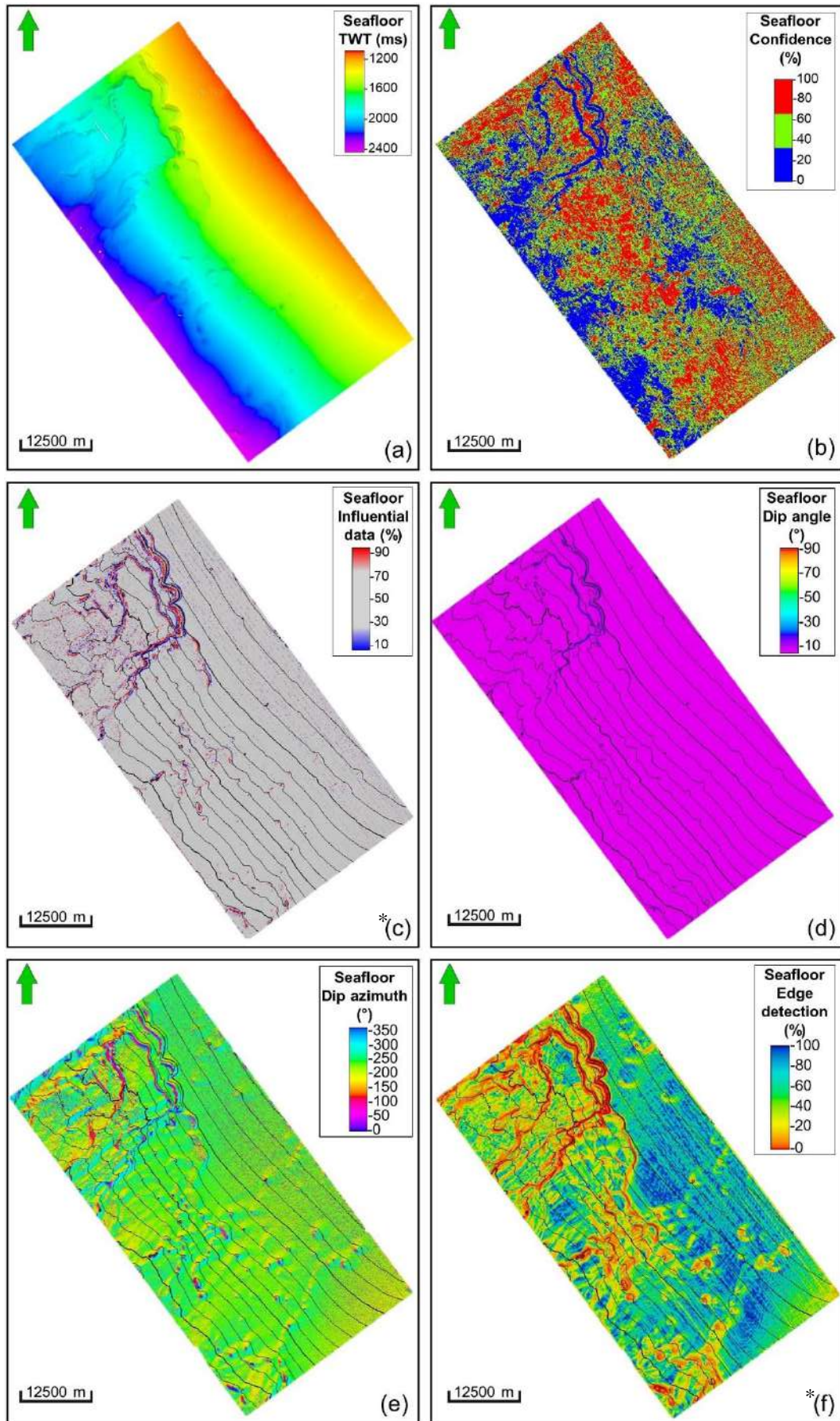




*Note: images (c) and (f) are adapted after Figs. 10a and b of Maduna et al. (2022).



*Note: images (c) and (f) are adapted after Figs. 10c and d of Maduna et al. (2022).



*Note: images (c) and (f) are adapted after Figs. 10a and b of Maduna et al. (2023).